



# Detection of metastable He2\* molecules in helium plasma

Bartosz Glowacz

## ► To cite this version:

Bartosz Glowacz. Detection of metastable He2\* molecules in helium plasma. Atomic Physics [physics.atom-ph]. Université Paris 6 Pierre et Marie Curie; Jagiellonian University, 2011. English. NNT: . tel-01360241

**HAL Id: tel-01360241**

**<https://theses.hal.science/tel-01360241>**

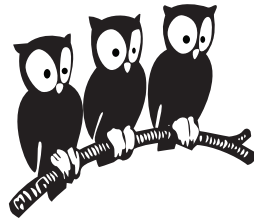
Submitted on 5 Sep 2016

**HAL** is a multi-disciplinary open access archive for the deposit and dissemination of scientific research documents, whether they are published or not. The documents may come from teaching and research institutions in France or abroad, or from public or private research centers.

L'archive ouverte pluridisciplinaire **HAL**, est destinée au dépôt et à la diffusion de documents scientifiques de niveau recherche, publiés ou non, émanant des établissements d'enseignement et de recherche français ou étrangers, des laboratoires publics ou privés.



Distributed under a Creative Commons Attribution - NonCommercial - NoDerivatives 4.0 International License



**THÈSE de DOCTORAT de l'UNIVERSITÉ PARIS VI**

Spécialité : Physique Atomique

présentée par

**Bartosz GŁOWACZ**

pour obtenir le grade de DOCTEUR de l'UNIVERSITÉ PARIS VI

---

**Detection of metastable  $\text{He}_2^*$   
molecules in helium plasma**

---

**Soutenue le 19 septembre 2011**

devant le jury composé de :

<b>M.</b>	<b>Jerzy KONIOR</b>	Uniwersytet Jagielloński Kraków	Examineur
<b>M.</b>	<b>Jakub ZAKRZEWSKI</b>	Uniwersytet Jagielloński Kraków	Examineur
<b>M.</b>	<b>Stanisław CHWIROT</b>	Uniwersytet Mikołaja Kopernika Toruń	Rapporteur
<b>Mme.</b>	<b>Corinne BOURSIER</b>	Université Pierre et Marie Curie	Examinatrice
<b>Mme.</b>	<b>Genevieve TASTEVIN</b>	Laboratoire Kastler Brossel	Examinatrice
<b>M</b>	<b>Tomasz DOHNALIK</b>	Uniwersytet Jagielloński Kraków	Directeur de thèse
<b>M.</b>	<b>Pierre-Jean NACHER</b>	Laboratoire Kastler Brossel	Directeur de thèse

---

<b>Mme.</b>	<b>Nelly BONIFACI</b>	G2E Lab Grenoble	Rapporteuse
<b>M.</b>	<b>Jarosław KOPERSKI</b>	Uniwersytet Jagielloński Kraków	Rapporteur

## Detection of metastable $\text{He}_2^*$ molecules in helium plasma

**Abstract:** Metastable  $\text{He}_2^*$  molecules, ubiquitous in helium systems, consist of a metastable  $\text{He}^*$  ( $2^3\text{S}_1$ ) and a ground-state He atoms. Their detection through the optical transition  $a^3\Sigma_u^+(\nu = 0) - e^3\Pi_g(\nu = 0)$  has been performed in He plasma ( $P=8\text{-}267$  mbar) with a tunable cw laser at 465 nm, based on the sum frequency generation of 923 and 937 nm in the PP-KTP crystal. The laser has been characterized for its wavelength tuning and efficiency of nonlinear conversion. Absorption rates provide direct access to  $\text{He}_2^*$  number densities, based on quantitative spectroscopic data obtained for the probed rotational branches. Studies mainly involve  $^3\text{He}_2^*$  but its isotopologues are also studied in isotopic mixtures and pure  $^4\text{He}$  gas.  $\text{He}_2^*$  absorption spectra yield rotational temperatures close to the gas temperatures. In addition to the spin-statistics-driven line intensities alternation, an alternation of  $^3\text{He}_2^*$  line shapes occurs indicative of the underlying structure of the rotational states. Time evolution of absorption signals has been recorded in discharge afterglow providing quantitative information about dynamics and relative abundances of the metastable species. The  $\text{He}_2^*$  density varies for strong laser excitation of  $\text{He}^*$  at 1083 nm, as formation rate from the  $2^3\text{P}$  state is 100-times higher. Simultaneous absorption measurements on atoms and molecules during the metastability exchange optical pumping (MEOP) experiments has been performed to study the potential contribution of  $\text{He}_2^*$  to the laser-enhanced  $^3\text{He}$  nuclear relaxation observed in MEOP. Preliminary results has shown expected increase in molecular density that is so far mild in comparison with the spectacular enhancement of  $^3\text{He}$  nuclear relaxation rate.

**Keywords:** helium, metastable molecule, molecular spectra, blue laser, sum frequency generation, optical pumping.

## Détection de molécules métastables $\text{He}_2^*$ dans un plasma d'hélium

**Résumé:** Les molécules métastables  $\text{He}_2^*$ , dans lesquelles un atome métastable  $\text{He}^*$  ( $2^3\text{S}_1$ ) et un atome dans l'état fondamental sont liés, sont fréquemment rencontrées dans les fluides d'hélium. Leur détection via la transition optique à 465 nm  $a^3\Sigma_u^+(\nu = 0) - e^3\Pi_g(\nu = 0)$  a été faite dans des plasmas d'He ( $P=8\text{-}267$  mbar) avec un laser continu accordable, utilisant une addition de fréquences (lasers à 923 et 937 nm) dans un cristal de PP-KTP. Des mesures d'absorption donnent accès aux densités de  $\text{He}_2^*$  à partir des données spectroscopiques obtenues pour les niveaux rotationnels étudiés, principalement pour  $^3\text{He}_2^*$ , mais aussi dans les mélanges isotopiques et dans  $^4\text{He}$  pur. Les spectres d'absorption moléculaire montrent une bonne thermalisation des niveaux rotationnels. En plus de l'alternance attendue (statistique) des intensités des raies, une alternance de formes de raies a été observée dans  $^3\text{He}_2^*$ , révélant la structure sous-jacente des niveaux rotationnels. Des mesures d'absorption en post-décharge fournissent des données quantitatives sur la cinétique et les densités des espèces métastables. Lors d'une excitation intense à 1083 nm, la densité de  $\text{He}_2^*$  augmente car le taux formation à partir de l'état  $2^3\text{P}$  est 100 fois plus fort qu'à partir de  $\text{He}^*$ . Des mesures d'absorption par les atomes et par les molécules métastables ont été faites lors d'expériences de pompage optique (par échange de métastabilité, POEM) pour étudier la contribution potentielle des molécules à la relaxation induite par le pompage observée en POEM. Seule une augmentation modérée des densités moléculaires a été observée, bien moindre que l'augmentation spectaculaire simultanément observée pour les taux de relaxation nucléaire.

**Mots clés:** helium, molécule métastable, spectre moléculaire, laser bleu, addition de fréquences optiques, pompage optique.

## Detekcja molekuł metastabilnych $\text{He}_2^*$ w plazmie helowej

**Streszczenie:** Molekuły metastabilne  $\text{He}_2^*$  - ekscymery, składają się z atomu helu w stanie podstawowym oraz  $\text{He}^*$ -atomu w stanie metastabilnym ( $2^3\text{S}_1$ ). Dla ich optycznej detekcji, poprzez przejście  $a^3\Sigma_u^+(\nu = 0) \rightarrow e^3\Pi_g(\nu = 0)$ , zbudowany został układ laserowy, bazujący na nieliniowym procesie sumowania częstości 923 i 937 nm w kryształach PP-KTP. Laser przestrzajalny, pracujący w trybie ciągłym, emituje na długości fali 465 nm, odpowiadającej wybranemu przejściu molekularnemu. Rozdzielone składowe rotacyjne przejścia zostały wykorzystane do pomiarów wartości absorpcji w plazmie helowej radiowych częstości w zakresie ciśnień gazów 8-267 mbar. Badania objęły przede wszystkim molekuły  $^3\text{He}_2^*$ , ale także izotopologię  $^4\text{He}_2^*$  oraz  $(^3\text{He}-^4\text{He})^*$  obecne w mieszaninie izotopowej gazowego helu. Zarejestrowane widma absorpcyjne pozwoliły na wyznaczenie temperatur rotacyjnych bliskich temperaturze gazów. Dodatkowo dla  $^3\text{He}_2^*$  zaobserwowano, obok, wynikającej z własności statystycznych, alternacji intensywności linii, także alternację ich kształtów, związaną z istnieniem struktury stanów rotacyjnych. Ewolucja czasowa gęstości molekuł podczas periodycznej 100% amplitudowej modulacji wzbudzenia plazmy dostarcza ilościowych informacji na temat dynamiki i względnej abundancji metastabilnych atomów i molekuł.

Gęstość  $\text{He}_2^*$  wzrasta, gdy atomy  $\text{He}^*$  w plazmie zostają wzbudzone do stanu  $2^3\text{P}$  przy użyciu światła 1083 nm, używanego w procesie pompowania optycznego z wymianą metastabilności (MEOP). Jest to efektem stukrotnego wzrostu szybkości tworzenia się  $\text{He}_2^*$  podczas zderzeń trójciałowych, gdy w zderzeniach z dwoma atomami helu w stanie podstawowym bierze udział atom helu w stanie  $2^3\text{P}$ , zamiast  $2^3\text{S}_1$ . W przeprowadzonych jednoczesnych pomiarach gęstości atomów i molekuł metastabilnych podczas eksperymentu MEOP helu-3 pod ciśnieniem 32 mbar, w zależności od mocy lasera pompującego, zanotowano niewielki wzrost koncentracji  $\text{He}_2^*$  w porównaniu ze znacznym wzrostem relaksacji polaryzacji jądrowej.

**Słowa-klucze:** hel, molekula metastabilna, widmo molekularne, niebieski laser, sumowanie częstości, pompowanie optyczne.

# Podziękowania...

## Remerciements...

## Acknowledgements...

Dziękuję mojemu promotorowi prof. dr hab. Tomaszowi Dohnalikowi za umożliwienie pracy w swojej Grupie podczas realizacji projektu doktorskiego, za opiekę naukową i moralne wsparcie, jak również za propozycję studiów w trybie międzynarodowym i nieocenioną pomoc w ich organizacji wiążącej się z wieloma zawiłościami formalnymi.

Je remercie mon directeur de thèse français - Pierre-Jean Nacher, pour m'avoir accueilli dans son groupe du Laboratoire Kastler Brossel, une école du meilleur niveau en physique expérimentale. Je lui adresse des remerciements particuliers pour ses conversations scientifiques toujours productives et pour avoir su répondre clairement à toutes mes questions. J'apprécie également son aide précieuse pour l'organisation de mes séjours à Paris (des formalités de l'Université Pierre et Marie Curie aux questions de logement).

Un grand merci également à Geneviève Tastevin, ma deuxième directrice de thèse française, bien que non officielle, pour son immense contribution scientifique dans la réalisation de ce projet et son investissement dans les expériences, l'analyse des données et la rédaction de ce manuscrit. Merci pour ses leçons de régularité et d'auto-critique scientifique ainsi que son aide qui a rendu ma vie à Paris plus simple.

Serdeczne podziękowania dla polskich recenzentów za zainteresowanie moją pracą i wysiłek włożony w jej lekturę i ocenę - prof. dr hab. Stanisławowi Chwirotowi oraz prof. dr hab. Jarosławowi Koperskiemu - także za cenne wskazówki dotyczące fizyki molekuł.

Remerciements à ma rapportrice française C.R. Nelly Bonifaci pour évaluer ma dissertation.

Oczywiście dziękuję wszystkim współpracownikom w Grupie polskiej:

Tadkowi Pałaszowi, za cenne dyskusje i wskazówki dotyczące elementów układu eksperymentalnego;

Guilhemowi Collier, za wspólne godziny spędzone nad dyskusjami dla zrozumienia zagadnień teoretycznych metody MEOP, za rozjaśniające umysł podpowiedzi i niezliczone tłumaczenia tekstów na język francuski;

Ani Nikiel, z którą współpraca podczas eksperymentów pompowania optycznego była wielką przyjemnością. Dziękuję jej za otwartość, zawsze wyciągniętą pomocną dłoń, mimo wielu własnych problemów i za wspaniałe relacje koleżeńskie;

Zbyszkowi Olejniczakowi i Mateuszowi Suchankowi, za współpracę w Grupie i cenne dyskusje nie tylko w zakresie tematu pracy.

Also many thanks to all the colleagues met at LKB:

Kajum Safiullin - who had begun and now is finishing his PhD in parallel with me, for sharing the common fate of graduate student abroad and for his friendship, ever lasting smile on the face and good word every time;

Cavin Talbot - for his australian-english lessons and common attendance to french classes at ENS. I appreciate also his hints and discussions about optical part of the experiments as well as non-scientific meetings together with his family;

Emmanuel Baudin - pour son aide inestimable dans les contacts (au-delà de la barrière de la langue) avec le Crous et l'administration de l'université française pendant l'inscription aux études chaque année et pour ses conseils scientifiques;

Marion Batz - for any scientific help when this dissertation was being written as well as experiments and data analysis had been performed, especially when they had concerned the MEOP of which she had become the specialist. Thanks also for good word every time we met and spiritual support until the very end. Danke schön!

Dziękuję także za okazaną życzliwość i pomoc Danusi Myrek, Józefowi Fladze, Stanisławowi Pajce, Piotrowi Klockowi oraz Jerzemu Olejniczakowi.

Merci aussi aux personnels technique et administratif du LKB : Linda Krikorian, Thierry Tardieu et Christophe Bernard pour l'aide administrative et de même Jean-Michel Isac et Saysavanh Souramasing pour le support technique de l'atelier qui ne m'a jamais longtemps fait attendre lors de commandes d'éléments pour le montage expérimental.

W szczególny sposób dziękuję moim Rodzicom i Rodzinie za pomoc i wsparcie podczas wszystkich lat studiów magisterskich i doktoranckich.

Dziękuję z całego serca mojej dziewczynie Justynie Mika za wiarę we mnie, otuchę, cierpliwość, wytrwałość i zrozumienie podczas długich miesięcy rozłąki związanych z pobytami w Paryżu.

# Contents

<b>Contents</b>	<b>I</b>
<b>List of Figures</b>	<b>IV</b>
<b>List of Tables</b>	<b>VIII</b>
<b>1 Introduction</b>	<b>1</b>
<b>2 The He<sub>2</sub>* metastable molecule</b>	<b>7</b>
2.0.1 Binding between two He atoms . . . . .	7
2.0.2 Formation rates for He <sub>2</sub> * . . . . .	8
2.1 Theoretical description of molecular dimer . . . . .	10
2.1.1 Approximations of V(R) potential . . . . .	12
2.1.2 Electronic molecular states . . . . .	15
2.1.3 Symmetries of the rotational levels and transition selection rules . . . . .	21
2.2 Intensities of the rotational lines of $a^3\Sigma_u^+$ (0)- $e^3\Pi_g$ (0) transition and molecular densities . . . . .	26
<b>3 Blue laser setup</b>	<b>31</b>
3.1 Second Harmonic Generation in PP-KTP . . . . .	33
3.1.1 Quasi-phase-matching . . . . .	34
3.1.2 Conversion efficiency . . . . .	36
3.1.3 Matching tolerances . . . . .	42
3.2 465 nm laser setup - description . . . . .	45
3.2.1 Laser setup components . . . . .	45
3.2.1.1 Laser diodes . . . . .	45
3.2.1.2 Nonlinear PP-KTP crystal . . . . .	46
3.2.2 Setup for SFG - construction scheme . . . . .	46
3.2.3 Laser output wavelength tuning . . . . .	48
3.3 Laser performance - experimental results . . . . .	50
3.3.1 Output power and efficiency . . . . .	50
3.3.2 Tuning range and matching conditions . . . . .	52
3.3.2.1 Laser wavelength calibration . . . . .	52
3.3.2.2 Matching conditions . . . . .	54
3.3.3 Matching tolerances in the experiment . . . . .	59
3.4 Summary and conclusions . . . . .	62



<b>4</b>	<b>Absorption measurements on helium molecule - experimental results</b>	<b>65</b>
4.1	Experimental setup . . . . .	65
4.1.1	Cell and rf discharge . . . . .	66
4.1.2	Laser frequency scans. Acquisition scheme . . . . .	67
4.1.3	Frequency scans recordings procedure . . . . .	68
4.1.4	Measurements of the density decay times . . . . .	69
4.2	Data processing and data reduction . . . . .	70
4.2.1	Processing of the recorded data files in numerical lock-in software . . .	70
4.2.2	Absorption line profile position determination . . . . .	72
4.2.3	Absorbance and demodulated signal relations . . . . .	73
4.2.3.1	100% square modulation . . . . .	73
4.2.3.2	Partial sine amplitude modulation . . . . .	74
4.3	Absorption lines shape . . . . .	74
4.4	Position of absorption lines . . . . .	87
4.4.1	Isotopic mixture cell - recordings of multiple lines . . . . .	87
4.5	Intensities of absorption lines . . . . .	96
4.5.1	Rotational temperature determination from relative absorption rates . .	96
4.5.2	Dynamics of helium molecule . . . . .	100
4.5.2.1	Molecular and atomic density decay curves . . . . .	101
4.5.2.2	Atomic and molecular coupled rate equations . . . . .	103
4.6	Summary and conclusions . . . . .	106
<b>5</b>	<b>Investigations on Metastability Exchange Optical Pumping dynamics with blue laser</b>	<b>109</b>
5.1	Basics of MEOP . . . . .	109
5.2	Achievements in MEOP in standard and non-standard conditions . . . . .	112
5.3	MEOP angular momentum budget and laser induced relaxation . . . . .	113
5.4	Description of MEOP experiment with blue light transmission measurement on molecular helium . . . . .	115
5.4.1	Design of the MEOP experimental setup . . . . .	116
5.4.1.1	General constraints . . . . .	116
5.4.1.2	Nuclear polarization measurement method choice - pros and cons . . . . .	116
5.4.1.3	Blue laser in MEOP setup . . . . .	118
5.4.2	MEOP experimental setup - realization . . . . .	118
5.4.3	Acquisition scheme and measurements protocols . . . . .	121
5.4.3.1	Acquisition scheme and recorded signals . . . . .	121
5.4.3.2	Measurements protocol . . . . .	122
5.5	Experimental data reduction and processing . . . . .	125
5.5.1	Polarization build-up and decay curve for $M_{eq}$ and $T_{decay}$ determination .	125
5.5.2	Metastable atoms number density determination . . . . .	127
5.6	Experimental results of MEOP with molecular density measurements . . . . .	129
5.6.1	Discharge intensity . . . . .	129
5.6.2	Results of MEOP - nuclear polarization values . . . . .	131
5.6.3	Light induced relaxation and molecular absorption rates at $M_{eq}$ . . . . .	132

5.6.4	Atomic and molecular metastable species density change with polarization . . . . .	135
5.7	Absorption measurements in presence of OP pump beam at $M = 0$ . . . . .	136
5.8	Summary and the conclusions . . . . .	138
<b>6</b>	<b>Conclusion and outlook</b>	<b>139</b>
<b>A</b>	<b>Reference data on molecular helium a-e transition spectral lines</b>	<b>141</b>
<b>B</b>	<b>Principle of laser absorption technique</b>	<b>145</b>
<b>C</b>	<b>Sellmeier equation and dispersion coefficients for PP-KTP</b>	<b>149</b>
<b>D</b>	<b>Constants</b>	<b>151</b>
	<b>Bibliography</b>	<b>153</b>

# List of Figures

1.1	Schematic diagram of Metastability Exchange Optical Pumping process. . . . .	2
2.1	Potential curve of two interacting helium atoms . . . . .	8
2.2	Potential curves for He <sub>2</sub> molecule [GB70]. Red - potential curve for $a^3\Sigma_u^+$ state, blue - potential curve for $e^3\Pi_g$ state. The potential curve of the ground state $X^1\Sigma_g^+$ (18 ev below the $a^3\Sigma_u^+$ ) has been omitted on the diagram and the energy of the first ( $v = 0, N = 0$ ) ro-vibrational level of $a^3\Sigma_u^+$ state has been taken as 0 of the ordinate scale on the left; 0 of the right ordinate scale in electron volts is based on the lowest level in $X^2\Sigma_u^+$ of He <sub>2</sub> <sup>+</sup> . The transition and its wavelength value for the atomic $2^3S - 2^3P$ transition has been marked on the right side. . . . .	9
2.3	Hund's coupling (b). Detailed description in the text. . . . .	17
2.4	Scheme of rotational sublevels of $a^3\Sigma_u^+$ and $e^3\Pi_g$ states of <sup>4</sup> He <sub>2</sub> . . . . .	19
2.5	Scheme of rotational sublevels of $a^3\Sigma_u^+$ and $e^3\Pi_g$ states of <sup>3</sup> He <sub>2</sub> . . . . .	20
3.1	Schematic drawing of PP-KTP crystal. . . . .	35
3.2	Simulated curves of Boyd-Kleinman focusing factor . . . . .	38
3.3	Change of the $\sigma = \sigma_m$ in function of $\xi$ . . . . .	39
3.4	Optimization of Boyd-Kleinman focusing factor $h(\sigma_m, \xi)$ in terms of $\xi$ parameter . . . . .	40
3.5	Change of the $h(\sigma, \xi)$ function FWHM with $\xi$ . . . . .	41
3.6	Laser set-up . . . . .	47
3.7	Change of the laser diodes feeding current value with external voltage applied to the power supply controller . . . . .	48
3.8	Infra red laser diodes wavelength tuning with the external voltage driven feeding current. . . . .	49
3.9	Settings of the 937 nm laser diode current providing compensation of $\lambda_b$ wavelength change with variation of the $T_{LD}$ . . . . .	53
3.10	The relation between the published wavelength of absorption line maximum [DR50, BG71] and corresponding laser diodes temperature. . . . .	54
3.11	Evolution of the wavelength-to-driving voltage for control of LD current coefficient ( $\frac{d\lambda}{dV}$ ) in the laser diodes temperature range. . . . .	55
3.12	Infra-red laser diodes wavelength tuning within $T_{LD}$ 10-40°C range. . . . .	56
3.13	Crystal matching temperature and laser diodes temperature matching points fulfilling quasi-phase-matching conditions within available operating range. The parameters of the linear fit allows to write the functional dependency between both temperatures as follows: $T_{cr} = 19.7(5) + 1.03(2) * T_{LD}$ . . . . .	57
3.14	Crystal matching temperature versus output blue wavelength - $\lambda_b$ . . . . .	58

3.15	Phase-matched wavevectors difference ( $\Delta k$ ) for fundamental beam wavelength in 930-931.5 nm range . . . . .	58
3.16	The phase-matching curves for the crystal (a) and laser diodes (b) . . . . .	60
3.17	$\sqrt{P_b}$ dependency on crystal temperature ( $T_{cr}$ ) as a matching parameter. . . . .	61
3.18	$\sqrt{P_b}$ dependency on laser diode temperature ( $T_{LD}$ ) as a matching parameter. . . . .	62
4.1	Optical setup scheme for absorption measurements on molecules (with use of 465 nm laser) and atoms (with use of 1083 nm laser) . . . . .	66
4.2	Scheme of the acquisition setup for the absorption frequency scans using voltage (triangle course of the $V(t)$ function) control of 937 nm laser diode current . . . . .	67
4.3	Diagram of $2^3S_1$ and $2^3P$ states of $^3\text{He}$ and $^4\text{He}$ with possible optical transitions signed as $C_1$ to $C_9$ and $D_0$ to $D_2$ respectively [NL85]. The examples of the absorption spectrum corresponding to these diagrams is given on the fig.5.2 . . . . .	69
4.4	(a) Demodulated signal for transmitted blue laser (black solid curve) with laser diode current control triangle voltage (red dashed curve) in function of the recording time. The record last 1.5 period of the voltage triangular function allowing comparison of the line profiles and positions reproducibility with the negative (solid black) and positive (solid red) voltage slope (b). . . . .	72
4.5	Comparison of the molecular absorption lineshapes of Q branch of two isotopologues $^3\text{He}_2^*$ and $^4\text{He}_2^*$ . . . . .	75
4.6	Odd-N numbered Q-branch transitions lineshapes change with the gas pressure . . . . .	77
4.7	Line profiles comparison for Q(1) and Q(2) lines . . . . .	78
4.8	Lorentzian half width of Voigt profiles for Q(2) transition absorption lines at 8.66.7,128 and 267 mbar pressure of $^3\text{He}$ . . . . .	80
4.9	Even-N numbered Q branch line profiles for 8 mbar pure $^3\text{He}$ cell . . . . .	81
4.10	Even-N numbered Q branch line profiles for 66.7 mbar pure $^3\text{He}$ cell . . . . .	82
4.11	Even-N numbered Q branch line profiles for 128 mbar pure $^3\text{He}$ cell . . . . .	83
4.12	Even-N numbered Q branch line profiles for 266 mbar pure $^3\text{He}$ cell . . . . .	84
4.13	Lineshapes comparison between the only well-resolved lines of $(^3\text{He}-^4\text{He})^*$ and Q(2) line of $^3\text{He}_2^*$ . . . . .	85
4.14	Three frequency scans including more than one molecular line . . . . .	88
4.15	Frequency scans of close lying $^3\text{He}_2^*$ and $^4\text{He}_2^*$ molecular lines for which one is overlapping with an absorption line of the hetero nuclear isotopologue $(^3\text{He}-^4\text{He})^*$ . . . . .	89
4.16	Frequency scan for which well resolved absorption lines of $^3\text{He}_2^*$ , $^4\text{He}_2^*$ and $(^3\text{He}-^4\text{He})^*$ are present. . . . .	90
4.17	Example of the frequency scan containing only two absorption lines, the registered $^{33}\text{Q}(1)$ (Q(1) of $^3\text{He}_2^*$ ) and one of the hetero nuclear dimer . . . . .	91
4.18	Frequency scan of unresolved triplet - two absorption lines of the $(^3\text{He}-^4\text{He})^*$ molecule and one of $^4\text{He}_2^*$ overlapped with $^{34}\text{Q}(2)$ . . . . .	91
4.19	Frequency scans of partially overlapped absorption lines doublets for $^3\text{He}_2^*$ and $(^3\text{He}-^4\text{He})^*$ . . . . .	92
4.20	Frequency scans of the R(0) lines doublet of $^3\text{He}_2^*$ and $(^3\text{He}-^4\text{He})^*$ ( $^{33}\text{R}(0)$ and $^{34}\text{R}(0)$ ). . . . .	93
4.21	Positions of all the helium molecule isotopologues $^3\text{He}_2^*$ , $^4\text{He}_2^*$ and $(^3\text{He}-^4\text{He})^*$ absorption lines observed using the $a^3\Sigma_u^+(0) - e^3\Pi_g(0)$ transition around 465 nm. Overlapping of the lines indicated using the information in the Table 4.9 . . . . .	95

4.22	Comparison of the linear fits to the $\ln\left(\ln T / \ln T_{Q(2)}\right)$ on $\Delta F = F(N) - F(2)$ dependency . . . . .	98
4.23	Comparison of the rotational temperatures between two isotopologues $^3\text{He}_2^*$ and $^4\text{He}_2^*$ at the pressure of 66.7 mbar. . . . .	100
4.24	Comparison of the linear fits to the $\ln\left(\ln T / \ln T_{Q(2)}\right)$ on $\Delta F = F(N) - F(2)$ dependency for three helium molecular isotopologues present in 1:1 $^3\text{He}$ and $^4\text{He}$ isotopic mixture gas at 66.7 mbar pressure. . . . .	101
4.25	Time decay curves of atomic (red lines) and molecular (black lines) densities relative to the steady state values (plasma discharges are switched off at Time=0 on the graphs) . . . . .	102
4.26	Impact of gas pressure on the atomic (a) and molecular (b) densities time evolutions. . . . .	103
4.27	Comparison of the decay curves for three isotopologues of $\text{He}_2^*$ . . . . .	104
4.28	Comparison of the time evolutions of atomic $^3\text{He}$ and $^4\text{He}$ densities in the 1:1 isotopic mixture cell at 66.7 mbar . . . . .	104
5.1	Schematic diagram of Metastability Exchange Optical Pumping process. . . . .	110
5.2	Calculated absorption spectra of $^3\text{He}^*$ (a) and $^4\text{He}^*$ (b) at 300 K, pressure 32 mbar and null magnetic field B. Doppler and pressure broadening effects has been taken into account. The lines designation is given according to well established nomenclature [NL85]. Notice the frequency scale and overlapping of $C_8$ and $C_9$ lines with $D_2$ and $D_1$ if absorption spectroscopy in isotopic mixture gas is performed. . . . .	112
5.3	Arrangement of the optical elements for MEOP with simultaneous measurement of 465 nm laser transmission mounted on a single breadboard 120x30 cm. . . . .	119
5.4	Block scheme of the measurement and acquisition system. . . . .	121
5.5	Protocol A - absorption measurement at $M=0$ . . . . .	123
5.6	Time chart of the IR and blue probe beams course in presence of the OP light. . . . .	124
5.7	Build up and decay of polarization as a function of time for the MEOP experiment performed with protocol B. . . . .	126
5.8	Example of polarization decay curve plotted both with semi-log scale. . . . .	127
5.9	Discharge stability during 4 h series of the MEOP measurements in 32 mbar cell expressed as a stability of $T_{decay}$ value . Regime of strong discharge (40% of IR probe, $C_8$ absorption). Presented data results from the exponential fits to the 15 s decay recordings in the absence of pump beam within protocol C. With the line, the $T_{decay}$ value is presented obtained from B-protocol recording where recording of the decay lasts 90 s. All the values from protocol C recordings agree within the error bars with the B-protocol value. . . . .	130
5.10	Values of $^3\text{He}$ nuclear polarization in steady-state, obtained in the MEOP for various absorbed OP light powers for two discharge regimes . . . . .	132
5.11	Log-log plot of laser-induced relaxation rates $\Gamma_{laser}$ as a function of the absorbed OP beam power at $M = M_{eq}$ . . . . .	133

5.12	Values of $-\ln(T_{blue})$ for 465 nm laser light tuned to Q(2) molecular transition measured at $M_{eq}$ (32 mbar cell, blue light absorbance in MEOP experiment performed with $C_8$ at 0.82 mT), as a function of the absorbed IR pump laser power. Red triangles / black squares - data for "strong" / "weak" discharges. Graph (a): the absolute absorbances of 465 nm light ( $-\ln(T_{blue}) \propto N_M$ - molecular density). With solid black/red/blue lines the linear fits for comparable absorption power ranges are shown in case of both discharge regimes: ("weak" full range up to 0.3 W)/("strong" up to 0.4 W)/("strong" up to 0.2 W) of absorbed pump laser power. Graph (b): Changes in absorbances (therefore in $N_M$ ) in respect to the measured value in absence of the OP beam ( $\ln(T_{blue}(W_{abs}^{Meq} = 0))$ ). With solid lines the linear fits to the data for the two discharge regimes has been shown. . . . .	134
5.13	Relative change of metastable $^3He$ atoms density with nuclear polarization $M$ during decay. . . . .	136
5.14	Comparison of $-\ln(T) \propto N_M$ values measured at $M = M_{eq}$ (red squares) and $M = 0$ (black squares) in "weak" (a) and "strong" (b) discharge regimes in function of the absorbed pump beam power $W_{abs}$ . . . . .	137

# List of Tables

2.1	Morse potential parameters for $a^3\Sigma_u^+$ and $e^3\Pi_g$ of $\text{He}_2$ . . . . .	14
3.1	Parameters of the simulated curves describing the Boyd-Kleinman factor $h$ versus $\sigma$ , for various $\xi$ values. . . . .	39
3.2	Compilation of the references with flux-grown PP-KTP applications to SHG and SFG providing the view on $d_{33}$ and $d_{eff}$ coefficients values for various wavelengths and crystal grating periods. $d_{33}$ are taken directly from references [TZL05,PBB <sup>+</sup> 01, ARM <sup>+</sup> 97,ZCG <sup>+</sup> 02], while in [JSW <sup>+</sup> 04] $d_{eff}$ is given. The rest of $d_{eff}$ were computed using the relation (3.7). . . . .	40
3.3	Computed values of focused beam waist, Boyd-Kleinman focusing factor $h$ and efficiency of SHG for the fundamental Gaussian beam with FWHM values corresponding to the measured elliptical beams horizontal and vertical FWHMs. $\eta_{SFG}$ values have been computed here for $d_{eff} = 9.5$ and $d_{eff}=7.5$ pm/V . . . . .	51
3.4	Results of the $\sqrt{P_b}$ fit performed to the experimental data of $T_{LD}$ and $T_{cr}$ matching curves. . . . .	61
4.1	The list and parameters of sealed optical cells made of Pyrex used in the experiment filled with helium under various pressure and isotopic content. . . . .	67
4.2	Full width at half maximum of <b>even</b> $N$ -numbered absorption lines profiles of $^3\text{He}_2$ at 8-267 mbar pressure range. For the 66.7 mbar two discharge excitation regimes has been studied - <i>weak</i> ( $w$ ) and <i>strong</i> ( $s$ ) (details further in the text). . . . .	78
4.3	Full width at half maximum of <b>odd</b> $N$ -numbered absorption lines profiles of $^3\text{He}_2$ at 8-267 mbar pressure range. For the 66.7 mbar two discharge excitation regimes has been studied - <i>weak</i> ( $w$ ) and <i>strong</i> ( $s$ ) (details further in the text). The error of the FWHM values for odd- $N$ transitions of 8 mbar $^3\text{He}$ cell are especially higher due to very low SNR of the profiles recordings - Fig. 4.6 (a) . . . . .	79
4.4	Full width at half maximum of $^4\text{He}_2$ absorption lines profiles of at 66.7 mbar pressure. Two discharge excitation regimes has been studied - <i>weak</i> ( $w$ ) and <i>strong</i> ( $s$ ) . . . . .	79
4.5	Values of the plasma absorbance ( $-\ln T$ ) for the observed molecular transitions for $^3\text{He}_2^*$ at different pressures between 8 to 266.7 mbar of isotopic pure cells. For 66.7 mbar two discharge regimes are considered of weak and strong rf excitation. The plasma condition inside the cells can be compared via 1083 nm absorbance values on $\text{C}_8$ atomic transition given in the first row of the absorbance values. NR - not recorded in the experiment. . . . .	86

4.6	Values of the plasma absorbance ( $-\ln T$ ) for the observed molecular transitions for $^4\text{He}_2^*$ at 66.7 mbar of isotopic pure cell. Two discharge regimes are considered of weak and strong rf excitation. The plasma condition inside the cell can be compared via 1083 nm absorbance values on $D_0$ atomic transition given in the first row of the absorbance values. . . . .	86
4.7	Molecular constants for $(^3\text{He}-^4\text{He})^*$ calculated with use of the mass scaling relations applied to known rotational constants for $^3\text{He}_2^*$ and $^4\text{He}_2^*$ isotopologues. $T_e + G(v = 0)$ is energy of so-called <i>band origin</i> . All the values are given in $\text{cm}^{-1}$ unit. . . . .	87
4.8	Position in wavelength scale of 11 absorption lines of $(^3\text{He}-^4\text{He})^*$ within expected tuning range of the blue laser. $\lambda_{calc}$ values are calculated using the molecular constants (Table 4.7), $\lambda_{exp}$ are experimentally determined positions of the lines, $\delta\lambda_{exp}$ are the uncertainties of line positions determination in voltage scale and its scaling to the wavelengths. Calculated values of the positions are in very good agreement (within 3rd decimal place) with given in [DGD77]. . . . .	90
4.9	Absorbance values for observed molecular transitions for $^3\text{He}_2^*$ , $^4\text{He}_2^*$ and $(^3\text{He}-^4\text{He})^*$ at 66.7 mbar of isotopic 1:1 mixture cell. . . . .	94
4.10	Compilation of the relative absorption lines amplitudes (with respect to the value for Q(2) transition) of $^3\text{He}_2^*$ for various gas pressures . . . . .	97
4.11	Compilation of the relative absorption lines amplitudes (with respect to the value for Q(3) transition) of $^4\text{He}_2^*$ . . . . .	99
4.12	Atomic and molecular evolution rate terms for creation and destruction processes in pure $^3\text{He}$ gas in the absence of optical pumping. . . . .	105
4.13	Compilation of parameters in the rate equations (4.8) and (4.9). (*) - $D_{mol}$ is obtained from published value for $^4\text{He}_2^*$ ( $361 \pm 34 \text{ cm}^2\text{Torr s}^{-1}$ , [GG70]) through the isotopic mass scaling: $D_i = D * \sqrt{M/M_i}$ . . . . .	106
5.1	Parameters characterizing the discharge plasma in MEOP experiment at 32 mbar of $^3\text{He}$ , 0.82 mT magnetic field in <i>weak</i> and <i>strong</i> regimes of excitation. . . . .	131
5.2	Results obtained from absorption measurements at $M=0$ and from polarization decay after MEOP (last line) . . . . .	131
A.1	Reference data on <i>a-e</i> transition spectrum for $^4\text{He}_2^*$ [BG71] . . . . .	141
A.2	Reference data on <i>a-e</i> transition spectrum for $^4\text{He}_2^*$ [DR50] . . . . .	142
A.3	Reference data on <i>a-e</i> transition spectrum for $^4\text{He}_2^*$ [DR50] . . . . .	143
C.1	Coefficients of the Sellmeier equation for the $n_z$ refractive index component reported in [FHH <sup>+</sup> 87, FASR99, KEOH01] . . . . .	149
C.2	Coefficients of the Sellmeier equation for the $n_z$ refractive index component reported in [FBP <sup>+</sup> 00, KT02, EA03] . . . . .	150
D.1	Molecular constants for $^4\text{He}_2^*$ and $^3\text{He}_2^*$ reported in [BG71] and [DR50] respectively. . . . .	152





# Abbreviations and used symbols

## Abbreviations

CM	Centre of the Mass
FWHM	Full Width at Half Maximum
IR	Infra Red
KTiOPO <sub>4</sub>	Potassium titanyl phosphate
LD	Laser Diode
LIA	Lock-In Amplifier
ME	Metastability Exchange
MEOP	Metastability Exchange Optical Pumping
MRI	Magnetic Resonance Imaging
NMR	Nuclear Magnetic Resonance
OP	Optical Pumping
PP-KTP	periodically polled KTiOPO <sub>4</sub>
QPM	Quasi Phase Matching
rf	radio frequency
RMS	Root Mean Square
SEOP	Spin Exchange Optical Pumping
SFG	Sum Frequency Generation
SHG	Second Harmonic Generation
SNR	Signal to Noise Ratio

## List of symbols

$Abs$	absorption rate
$A_{\sigma-}$	$\sigma-$ probe absorption signal
$A_{\sigma+}$	$\sigma+$ probe absorption signal
$a$	antisymmetric state
$a_1$	peak-to-peak amplitude of the first term in the square wave expansion in sine waves
$a_i$	relative population of $2^3S_1$ atomic state
$b_j$	relative population of $He(2^3P)$ atomic state
$B$	magnetic field (absolute value)
$B_e$	molecular rotational constant in harmonic oscillator and rigid rotor approximation

$B_v$	rotational constant in anharmonic oscillator and non-rigid rotor approximation related to the moment of inertia
$C_8, C_9$	designation of optical transitions of $^3\text{He}$
$D_{0-2}$	designation of optical transitions of $^4\text{He}$
$D_{at}$	diffusion coefficient for helium atom
$D_e$	depth of the interaction potential minimum
$D_e$	rotational constant of non-rigid rotator assuming no oscillation
$D_{mol}$	diffusion coefficient for helium molecule
$D$	Doppler width
$D_v$	rotational constant in anharmonic oscillator and non-rigid rotor approximation related to centrifugal force
$\vec{d}$	dipole momentum
$\hat{d}$	dipole moment operator
$\vec{d}_a, \vec{d}_a$	temporary dipole momenta
$\vec{d}_a^{ind}, \vec{d}_b^{ind}$	induced dipole momenta
$d_{eff}$	effective nonlinear coefficient
$\vec{E}$	electric field vector
$\vec{E}_a, \vec{E}_b$	electric field from temporary induced dipole momentum
$E_e$	electronic energy - the value at the bottom of the potential minimum
$E_{int}$	internal energy of the molecule related to vibrational and rotational motion
$E_{int}^{ab}$	potential energy of two induced dipole momenta interaction
$E_r$	energy of the rotational motion
$E_v$	energy of the vibrational motion
$F(\theta, \varphi) = F_{J,M}$	angular part of $\chi(R)$
$\mathbf{F}$	vector, quantum number of the total angular momentum of the molecule
$F_v(J)$	rotational energy term part
$f( \vec{R} )$	radial part of $\chi(R)$
$G(\nu)$	vibrational energy term part
$g$	third order derivative of oscillator potential at minimum position
$g_i, g_f$	degeneracy factor of $i$ and $f$ states
$h(\sigma, \xi)$	Boyd-Kleinman focusing factor
$\text{He}_2^*$	helium molecule in the metastable $a^3\Sigma_u^+$ state
$\text{He}(1^1S_0)$	helium atom in the ground state
$^4\text{He}_2^*$	homonuclear ( $^4\text{He}$ ) helium metastable molecule isotopologue
$^3\text{He}_2^*$	homonuclear ( $^3\text{He}$ ) helium metastable molecule isotopologue
$(^3\text{He}-^4\text{He})^*$	heteronuclear helium metastable molecule isotopologue
$\text{He}_a, \text{He}_b$	ground state helium atoms considered as two interacting induced dipoles
$I_1, I_2, I$	spin of the nucleus
$l$	crystal length
$I_{abs}$	incident light intensity weakened in absorption process
$I_{if}(\vec{r})$	intensity of the light at frequency tuned to the transition between initial and final states
$I_{inc}$	incident light intensity reaching the absorber

$\mathbf{J}, J$	total angular momentum vector, quantum number of molecule apart from nuclear spin
$k_1, k_2$	SFG fundamental wave vectors
$k_{av}$	arithmetic average of fundamentals $k_1$ and $k_2$ wave vectors
$k_b$	wave vector of generated harmonic
$I_1, I_2$	laser diodes feeding currents
$\mathbf{L}$	total electronic orbital angular momentum quantum number
$\hat{L}^2$	angular momentum operator
$L_{path}$	total length in cell traversed by probe beam
$M_1, M_2$	mass of two nuclei of interacting atoms
$M_{eq}$	steady state polarization
$M$	nuclear polarization of the ground atomic state $1^1S_0$
$m_F$	projection of the total atomic angular momentum quantum number
$M_L$	projection of total electronic orbital angular momentum quantum number on the internuclear axis
$\mathbf{N}, N$	total angular momentum vector, quantum number of molecule apart from electronic and nuclear spin
$N_g$	total number density of helium atoms in the cell
$N_M$	total number density of molecules
$n_1, n_2, n_b$	refraction indices for fundamentals and harmonic radiation
$n_M^i(\vec{r})$	number density of molecules in the initial state $i$
$n_m$	number density of helium atoms in metastable state $2^3S_1$
$\emptyset$	transmission measurement offset value
$OUT_nLIA$	output signal of the numerical lock-in amplifier
$P(z, t)$	induced electric polarization
$P$	gas pressure
$P_1, P_2$	power of fundamental radiation
$P_{av}$	arithmetic average of fundamentals radiation powers
$P_b$	power of generated harmonic
$Q(1-9), P(2-3), R(0)$	designations of molecular rotational transitions
$Q_{el}$	electronic partition function
$Q_{rot}$	rotation partition function
$Q_{vib}$	vibration partition function
$R$	distance from the dipole
$\mathbf{R}$	angular momentum of rotating nuclei
$\vec{R}_{CM}$	coordinates of the center of the mass
$R_e$	interatomic distance of the interaction potential minimum
$R^{RMS}$	lock-in amplifier output in RMS
$r$	ratio of probe absorption signals $r = \frac{A_{\sigma+}}{A_{\sigma-}}$
$\vec{r}_e$	electrons coordinates
$\vec{r}_n$	nucleus coordinates
$\mathbf{S}, S$	total electronic spin vector, quantum number
$S_{fi}$	line strength of $i - f$ transition
$S_{HL}$	Hönl-London coefficient
$S(\omega/2\pi, M)$	transition intensity (amplitude) as function of probe frequency $\omega/2\pi$ and polarization $M$

$S(v', v'')$	Franck-Condon factor for the transition between $v''$ and $v'$ vibrational sublevels
$s^i(n, \nu, N, p)$	distribution function within electronic, rotational and vibrational sublevels of certain parity $p$
$s$	symmetric state
$T, T$	vector, quantum number of the total nuclear spin, temperature
$T_{CR}$	crystal temperature
$T_e$	electronic energy term part
$T_{LD}$	laser diode temperature
$T_{pump}$	transmission coefficient of the pump light
$T_{rot}$	rotational temperature
$T(\nu, J)$	total energy term expressed in $[\text{cm}^{-1}]$
$T_{decay}$	decay time of polarisation without pumping light in presence of a plasma
$V(\vec{r}_e, \vec{r}_n)$	total potential energy of a dimmer
$V(R)$	potential of the nuclei interaction
$V_c$	volume of the pumping cell
$V_e(\vec{r}_n)$	electronic potential of the motionless nuclei electrostatic field
$V_n(\vec{r}_n)$	Coulomb internuclear interaction potential
$w(\omega - \omega_{fi})$	line profile function
$w_0$	waist of the focused beam
$W_{abs}$	absorbed pump light power
$w_G$	Gaussian half-width (FWHM) of the line profile
$w_L$	Lorentzian half-width (FWHM) of the line profile
$W_{las}$	power of the pump light
$w_V$	Voigt half-width (FWHM) of the line profile
$X, X_0$	matching tolerance parameter and its optimal value
$\alpha$	destruction rate in ionization collisions between atoms and molecules (Chapter 3)
	coefficient of linear expansion of the crystal material (Chapter 4)
$\alpha_e, \beta_e$	constants describing coupling strength between vibrational and rotational motions
$\beta_{at}$	destruction rate in ionization collisions (Penning) within atomic species
$\beta_{mol}$	destruction rate in ionization collisions (Penning) within molecular species
$\beta_n$	nuclear spin function
$1/\beta$	spin temperature
$\chi(R)$	wave function of the nuclei relative motion
$\chi^{(n)}$	$n$ -order expansion of electric susceptibility of the media
$\delta_m(T)$	temperature dependent rate constant of metastable molecule formation from the $2^3S_1$
$\delta_P(T)$	temperature dependent rate constant of metastable molecule formation from the $\text{He}(2^3P)$

$\eta$	nonlinear conversion efficiency (chapter III)
	quantum efficiency (chapter V)
$\eta_{C8}^D$	photon efficiency in Dehmelt OP regime on the $C_8$ transition
$\eta_{C8}^K$	photon efficiency in Kastler OP regime on the $C_8$ transition
$f_{\Gamma}$	function describing the change of ME contribution to polarisation decay $1^1S_0$ in absence of OP
$\gamma$	radiative decay rate of $He(2^3P)$ atomic state
$\Gamma_{decay}$	( $\equiv T_{decay}^{-1}$ ) decay rate of polarisation without pumping light in presence of a plasma
$\gamma_e$	metastability exchange collisions rate
$\Gamma_G$	intrinsic ground state relaxation rate
$\Gamma_{laser}$	additional OP/laser induced relaxation rate
$\Gamma_R$	total OP/laser enhanced relaxation rate
$\gamma_r^P$	relaxation rate in $He(2^3P)$ atomic state
$\gamma_r^S$	relaxation rate in $2^3S_1$ atomic state
$\Lambda$	modulus of the total electronic orbital angular momentum quantum number projection on the internuclear axis (Chapter 2)
	nonlinear crystal grating period (Chapter 3)
$\lambda_1, \lambda_2$	SFG fundamental wavelengths
$\lambda_{av}$	arithmetic average of fundamentals wavelengths
$\lambda_b$	wavelength of generated harmonic
$\mu$	reduced mass
$\Omega$	total electronic angular momentum of the molecule about the internu- clear axis
$\phi$	number related to the sublevel parity $p$
$\pi$	light polarization perpendicular to magnetic field
$\Psi(\vec{r}_e, \vec{r}_n)$	total wave function of electrons and nuclei of interacting atoms
$\Psi_e(\vec{r}_e; \vec{r}_n)$	electronic wave function part
$\Psi^i, \Psi^f$	initial and final states wave functions
$\Psi_n(\vec{r}_n)$	nuclear wave function part
$\rho$	square root of the isotopologues reduced masses ratio
$\Sigma$	total spin component about the internuclear dimer axis
$\sigma$	phase-matching parameter
$\sigma-$	left-handed circular light polarization parallel to magnetic field
$\sigma+$	right-handed circular light polarization parallel to magnetic field
$\sigma_{if}(\omega)$	frequency dependent cross section for $i$ to $f$ states transition
$\tau_{0.5}$	half-decay rate
$\tau_f$	lifetime of the excited state of $i - f$ transition
$\nu$	vibrational quantum number
$\omega_1, \omega_2$	fundamental frequencies in SFG process
$\omega_e$	harmonic oscillations frequency
$\omega_e x_e$	measure of the oscillator anharmonicity
$\omega_{fi}$	frequency of the transition between $i - f$ states
$\xi$	focusing parameter

# Chapter 1

## Introduction

Metastable molecules ( $\text{He}_2^*$ ) are ubiquitous in helium systems. They are produced by any excitation process that feeds in enough energy to create excited, ionic, or metastable atomic species (electric discharge, bombardment by charged particles, irradiation with ionizing radiation or intense laser pulses), provided that the density of ground state atoms is high enough to allow conversion by 3-body collisions. Extensive work has dealt with room temperature gas for basic studies of this unique dimer and of the complex processes involved in He plasmas, with a renewed interest driven by a variety of applications both at low and high pressures.

$\text{He}_2^*$  is the simplest molecule after the hydrogen dimer and its studies are interesting due to the possibility of direct testing of atom-atom interactions (in particular in the context of laser-cooled systems) and comparisons with theoretically computed molecular levels and structure (especially accurate for this few-electron system).

Apart from the gaseous phase at the room temperature  $\text{He}_2^*$  is observed also in dense gas as well as in liquid, droplets, and clusters at cryogenic temperatures (references in [TGN10]). In superfluid helium,  $\text{He}_2^*$  molecules have recently been used as probes of the fluid dynamics on microscopic length scales [GWC<sup>+</sup>09] due to the considerable line broadening induced by the surrounding medium.

Recently, molecules formed in helium radio frequency discharge plasma at pressures in the 1-300 mbar range have been suspected to play a significant role in the relaxation of the non-equilibrium nuclear polarization (hyperpolarization) of  $^3\text{He}$  achieved using the Metastability Exchange Optical Pumping (MEOP) method [NL85, Cou01, Bat11] - see also the beginning of chapter 5 for the details about the method. A quantitative answer to this hypothesis is of importance given the variety of applications for which hyperpolarized  $^3\text{He}$  is used, ranging from fundamental research to biomedicine, including the main ones [Bat11]: spin filters for polarizing neutrons, scattering targets for investigations of the structure of nucleons, investigations of nonlinear nuclear magnetic resonance (NMR) dynamics in hyperpolarized liquid  $^3\text{He}$ , magnetic resonance imaging (MRI) of the lung in humans and in animals with inhaled gas. This provides a strong motivation for improving the MEOP production efficiency of the largest amount with the highest gas polarization in the shortest time, through systematic investigation and for overcoming its limitations.

Studies on MEOP have been initiated in 1963 with the discovery of the method. It is a two stage process that results in non-equilibrium distribution of nuclear spin (spin 1/2) orientation of  $^3\text{He}$  ground state atoms. The three atomic states involved in the process are: the ground state

atoms  $1^1S_0$ , the metastable state  $He(2^3S)$  atoms and helium atoms in the second excited state  $2^3P$ . They are schematically drawn on the fig.1.1

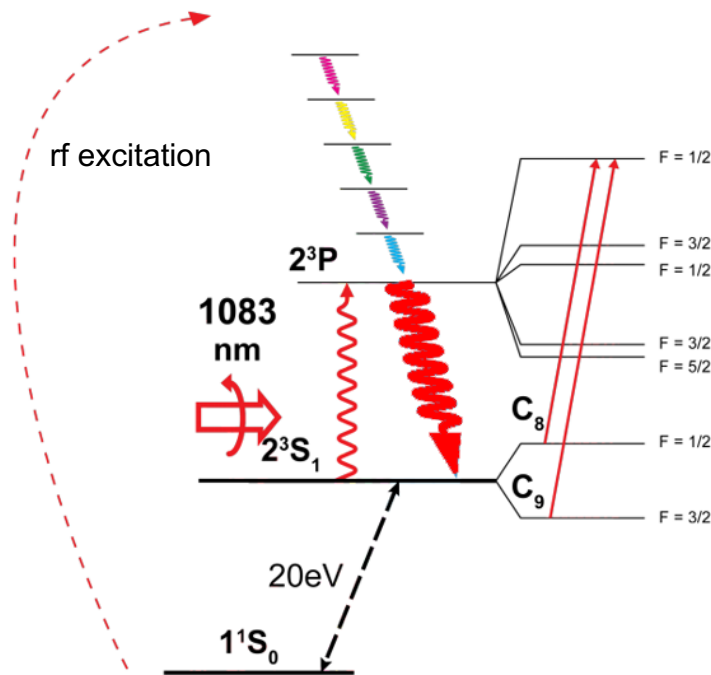


Figure 1.1: Schematic diagram of Metastability Exchange Optical Pumping process. Multi-color arrows represent radiative deexcitation cascade of high lying states populated by the rf excitation. Red arrows represent the 1083 nm transition and radiative deexcitation occurring between  $2^3S_1$  and  $2^3P$  states. Black dashed arrow represents the metastability exchange collision between  $2^3S_1$  and  $1^1S_0$  states. On the right side of the scheme, the  $C_8$  and  $C_9$  transitions between hyperfine sublevels of  $2^3S_1$  and  $2^3P$  states are presented

The hyperfine structure sublevels of the long-lived ( $10^3$ )  $2^3S_1$  state are populated through the radiative decay cascade of atoms being highly excited in collisions with electrons present in the discharge plasma sustained in the gas. The metastable state serves as a bottom state in the optical pumping process (OP) that is the first stage of the MEOP. The excited state in this OP scheme is the  $2^3P$ , coupled to the  $2^3S_1$  with optical transition at infra-red wavelength of 1083 nm. Orientation of the electronic angular momentum enforced by OP induces the orientation of spin of the nucleus due to strong entanglement between the electronic and the nuclear spin states in the  $2^3S_1$ . In the second stage of the MEOP the orientation of the nuclei is transferred to the ground  $1^1S_0$  state through the metastability exchange (ME) collisions. In this binary process the electronic excitation of the  $2^3S_1$  is overtaken by the colliding partner - the ground state atom, as well as the electron spins are exchanged. Contrary to the metastable excitation that is fully transferred from one atom to another, the nuclear orientation of both partners is conserved. It can be simply considered as the exchange of the nuclear spins, so that the output of the collision are the ground state atom with the nuclear spin with desired orientation and the metastable state atom with the nuclear orientation of the incident  $1^1S_0$  atom.

In spite of the development of new powerful laser sources at 1083 nm used for optical pumping, with adequate spectral characteristics [Tas00], no significant improvement in



achieved nuclear polarization values has been made. Differences between theoretically expected and experimentally measured polarizations and polarization build-up rates are observed [ASM<sup>+</sup>04, Abb05, Bat11] especially when the further increase of the pump laser power does not translate into higher steady-state polarization values. Detailed studies of this phenomenon have provided strong evidence of a relaxation process induced by the laser radiation used for the optical pumping process, that only depends on the amount of absorbed power by the metastable helium atoms. Currently there are two mechanisms under consideration that are suspected to play a key role in the laser enhanced relaxation: radiation trapping and relaxation by the helium metastable molecule. Their respective contributions remain to be quantitatively evaluated as a function of gas pressure, the leading process being potentially different at low (standard MEOP) and high (high field MEOP) gas pressure.

In the second process, the absorption of 1083 nm radiation is expected to increase the number of the metastable helium molecules formed through ternary collisions between one excited state atom and two ground state atoms  $\text{He}(1^1\text{S}_0)$ . The known rate constant for the reaction involving an excited atom in the  $2^3\text{P}$  state is about 100 times higher than that involving a metastable  $2^3\text{S}_1$  atom [EADL88]. The nuclear relaxation process itself has not yet been established but a scenario similar to that occurring for molecular ions ( $^3\text{He}_2^+$ ) might be considered. For instance, it has been proposed [Cou01] that during a collision between  $\text{He}^*_2$  and a polarized ground state atom the electronic excitation of the former can be transferred to the incoming ground state atom within the transient tri-atom molecule so that the polarized nucleus is "imprisoned" in the dimer while the unpolarized nucleus is carried away by the outgoing atom. The nuclear angular momentum of the freshly bounded polarized atom is expected to be quickly dissipated in numerous rotational molecular states due to spin-orbit coupling, which constitutes an efficient channel of relaxation.

A preliminary investigation on the helium metastable molecule in the plasma conditions used for MEOP has been performed with the use of emission spectroscopy method and laser induced fluorescence [Cou01] providing information about increased molecular density while 1083 nm light is absorbed. These spectroscopic emission studies, where the complex discharge kinetics preclude definitive interpretation of the time-resolved spectra, have not been carried out with simultaneous measurements of MEOP kinetics and molecular density.

In contrast, single-photon absorption is a sensitive technique for direct detection of  $\text{He}^*_2$  and absolute density measurements. To this aim, one needs a continuous-wave laser source providing radiation at one of the molecular transition wavelength.

The  $\text{He}^*_2$  molecular transitions frequently used in the literature are  $a^3\Sigma_u^+ (v = 0) - c^3\Sigma_g^+ (v = 0)$  (at 912-940 nm) and  $a^3\Sigma_u^+ (v = 0) - e^3\Pi_g (v = 0)$  (around 465 nm), the leading ones in terms of band strength in the whole range of the  $\text{He}_2$  spectrum [TKO<sup>+</sup>80]. However, to the best of the Author's knowledge, the latter is the only one for which the oscillator strength has been directly determined [NTSL94], allowing the calculation of absolute molecular density from the measured light transmittances. Apart from that, the  $\text{He}^*_2$  absorption spectrum at 465 nm offers a variety of absorption lines (P,Q,R branches) within a narrow wavelength range of about 2 nm [DR50, BG71, TKO<sup>+</sup>80], which corresponds to the typical tuning range of laser diodes. This makes the choice of this transition useful not only for observations of molecular density changes after proper line identification but also for performing detailed spectroscopy measurements. This has been the key motivation for obtaining laser source at 465 nm.

Developments of laser diodes at the wavelengths in the lower part of visible light spectrum resulted in various applications from home use - high density optical storage technologies

(e.g. Blu-ray, AOD - 405 nm) and high resolution laser printers through something more sophisticated as in medicine (laser-induced fluorescence of cancerous and precancerous cells in presence of blue laser light) or spectrophotometry in paper manufacturing to scientific use for atomic spectroscopy of chemical elements that have resonant lines in the blue/UV region including aluminum (396 nm), gallium (403 & 417 nm) and indium (450 nm). Unfortunately, at the time of the start of the present work, laser diodes at the wavelength of 465 nm were not available. Well-known methods for generation of short laser light wavelengths not available from simple laser diodes or other compact sources, are the non-linear processes of second harmonic generation (SHG) and sum frequency generation (SFG). The rapid development of the so-called quasi-phase matching techniques has conveniently allowed for the design of high quality non linear crystals tailored for optimal efficiency at various wavelengths. Suitable 930 nm laser diode for SHG were not available at the beginning of the Author's work. Therefore generation of 465 nm photon has been achieved through SFG process of two laser light beams at 923 nm and 937 nm in periodically poled crystal KTiOPO<sub>4</sub> (PP-KTP).

This PhD work concentrates on the development of the blue laser source and preliminary absorption measurements on the helium molecular species, with emphasis on the objective of simultaneous monitoring of molecular density and MEOP dynamics to determine the origin of the 1083 nm laser enhanced <sup>3</sup>He.

The manuscript is organized in the following way:

- Chapter II provides a basic introduction to molecular physics and spectroscopy focusing on the case of helium metastable dimer in the  $a^3\Sigma_u^+$  and  $e^3\Pi_g$  states. Detailed nomenclature is introduced, symmetries, coupling scheme of the angular momenta relevant in this case are discussed, leading to determination of the rotational lines that will be used in the experiment.
- Chapter III begins with a short introduction to the twin nonlinear processes of SHG and SFG, providing background for the discussion of up-conversion efficiency. Technical details about components and their arrangement in the final setup realization are described. This is followed by an experimental characterization of the performances: efficiency of 465 nm laser light generation, crystal and laser diodes phase matching tolerances, wavelength tuning range.
- Chapter IV is devoted to spectroscopic observations based on frequency scans of absorption line profiles. The experimental setup as well as the data acquisition scheme, the reduction and processing schemes are discussed. The presentation of the experimental results begins with a description of the observed complex line shapes. The position and amplitudes of the recorded absorption peaks are used for the registration of known <sup>3</sup>He<sub>2</sub><sup>\*</sup> and <sup>4</sup>He<sub>2</sub><sup>\*</sup> rotational lines and the calibration of the laser wavelength. The positions of the hetero-nuclear dimer (<sup>3</sup>He-<sup>4</sup>He)<sup>\*</sup> lines are computed using mass scaling and are confirmed experimentally. Preliminary investigations of the dynamics of He<sub>2</sub><sup>\*</sup> are presented and compared with atomic ones.
- Chapter V introduces the Metastable Exchange Optical Pumping method used to obtain high <sup>3</sup>He gas polarization, putting emphasis on the angular momentum budget of the atomic system, where the term responsible for laser-enhanced polarization loss explicitly appears. Conditions for MEOP at a few militeslas, for simultaneous nuclear polarization measurements (based on 1083 nm light absorption) and simultaneous monitoring of He<sub>2</sub><sup>\*</sup>

densities are described. After discussion of dedicated setup, data acquisition and analysis methods, the experimental results are presented. They include: characterization of the plasma conditions and steady-state nuclear polarization values, variations of laser-induced relaxation rates and molecular density with absorbed pump laser power. The molecular formation enhancement in presence of the OP light is studied both at steady-state and at null polarization values.



# Chapter 2

## The $\text{He}_2^*$ metastable molecule

Helium dimers, have been subjects of investigations since the first decades of the 20th century [Cur13]. However, the work has been mainly concentrated on the molecules that consist of the most common  $^4\text{He}$  isotope [Phe55, BG71] (natural abundance in Earth's atmosphere is 1 million higher than that of  $^3\text{He}$ ). The main source of available amount of lighter isotope, tritium decay being present in dismantled nuclear weapons, so investigations performed on molecular  $^3\text{He}$  begun after 1950 [DR50], resulting unfortunately in poor amount of references and spectroscopic data.

### 2.0.1 Binding between two He atoms

Helium molecule is an example of a dimer that consists of atoms belonging to the noble gases group. In this case completely filled electronic shells of the neutral atoms exclude formation of both covalent and ionic bonds but, still, existence of stable diatomic molecule is possible. The reason for that is presence of van der Waals interactions (vdW), resulting from the weak, long-distance, attractive electrostatic coupling between atomic permanent or transiently induced dipolar momenta. In the case of helium, ground state atom has an electronic cloud that has spherical symmetry. However, fluctuations give rise to finite time-dependent dipoles that provide same attractive contribution to the atom-atom interaction potential. As for other elements, the binding of the two He atoms depends on the existence of a net attractive potential as a result of the short-range strong repulsive interaction and the weak long-range vdW interaction. Composition of these two results in molecular potential curve describing the dependency of interaction on the interatomic distance. It can be purely repulsive or an attractive well, related to the reference energy being taken as the dissociation energy, can be present at the distance  $r_e$ .

Since 1928 the existence of the singlet bound state  $X^1\Sigma_g^+$  has been theoretically considered. The early calculations, in fair agreement with the more recent [WHD<sup>+</sup>10] (2010) modeling of the two ground state helium atom system interaction potential, indicated the shallow potential well of the  $D_e = 11$  K depth at the equilibrium interatomic distance  $r_e = 5.6 a_0$  (Bohr radius). In 1982 it has been reported [US82] that this potential well supports one and only one weakly (binding energy of 0.8 mK was provided) bounded state. This weakly bound state was observed experimentally [LMK<sup>+</sup>93] after electron impact ionization of a supersonic expansion of helium with translational temperature near 1 mK, as the binding energy had been estimated between 0.8 and 1.6 mK. This is in agreement with the recent (2009) theoretically determined value 1.3 mK [Gel09]. Such a low energy excludes presence of the ground state molecules at room

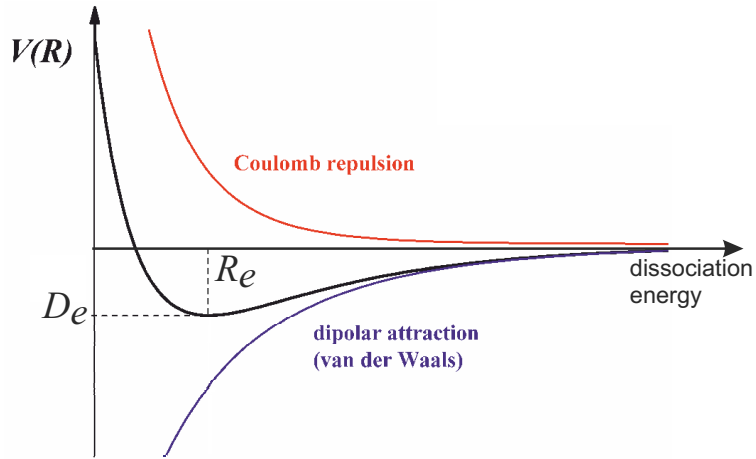
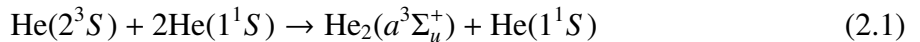


Figure 2.1: Potential curve of two interacting helium atoms. Red curve represents Coulomb repulsive interaction, blue - induced dipole attraction - van der Waals force. The addition of these interaction results in the characteristic shape of the potential (black curve) with well of  $D_e$  depth (in respect to the dissociation energy limit that is put = 0) at the  $r_e$  equilibrium bond (interatomic) distance.

temperature. In contrast to the  $X^1\Sigma_g^+$  state, a deep attractive potential exists for the interaction between a metastable helium atom and a ground state one. The metastable state atom can exist in either the singlet or the triplet state, so that  $A^1\Sigma_u^+$  and  $a^3\Sigma_u^+$  can be formed respectively (see the potential curves on Fig. 2.2). As it is clear from this figure also atoms in other excited states give with the ground state atoms a binding potentials, for instance the  $b^3\Pi_g$  molecular state formed by the  $2^3P$  and the ground state atoms. However, forbidden radiative transition to the ground atomic state from the triplet metastable atomic state, privileges this population over the atoms in the singlet metastable state and other highly excited states when the number densities are compared in the plasma conditions of this work. Thus, the higher temperature regime ( $\gg 1\text{mK}$ ) the  $a^3\Sigma_u^+$  is often considered as the lowest helium molecular state in fact being the first excited molecular state above the mentioned  $X^1\Sigma_g^+$ . The potential curve of the  $a$  state (marked with solid red line on the 2.2) with potential well (at  $1\text{\AA}$ ) depth is  $\sim 15700\text{ cm}^{-1}$  [Yar89], is result of interaction between one ground state He atom ( $1^1S_0$ ) and helium atom in the metastable state ( $2^3S_1$ ).

## 2.0.2 Formation rates for $\text{He}_2^*$

The association of these two atoms however requires presence of one additional ground state atom so that three body collision occurs.



This requirements is the result of presence of the repulsive barrier ( $484 \pm 48\text{ cm}^{-1}$ ) at intermediate nuclear separations ( $2.75 \pm 0.03\text{\AA}$ ) [KTZ<sup>+</sup>90, Yar89], as a result of the competition between the  $\text{He}_2^+(1\sigma_g^2 1\sigma_u)$  core attraction and  $\text{He}(1^1S) + \text{He}(2^3S)$  exchange repulsion.

The role of the third body can be explained on the basis of the simple dynamical model in which three-body collision is pictured as two binary collisions in rapid succession as presented

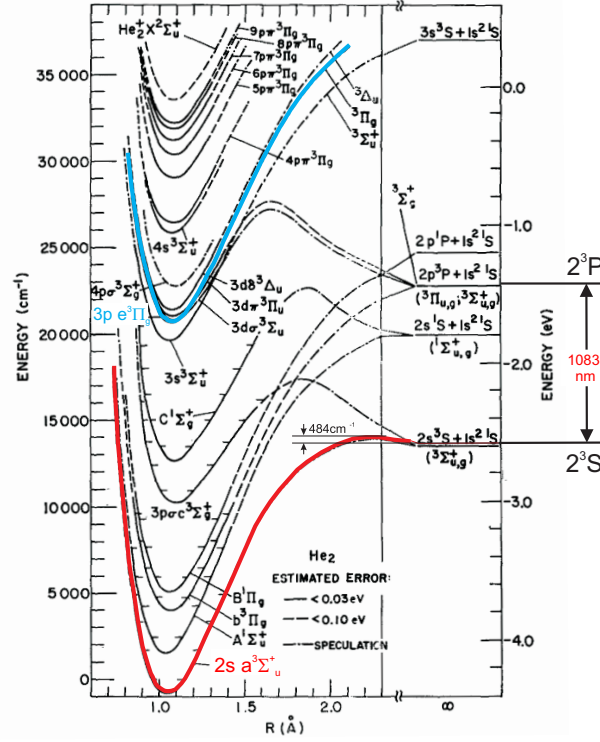


Figure 2.2: Potential curves for He<sub>2</sub> molecule [GB70]. Red - potential curve for  $a^3\Sigma_u^+$  state, blue - potential curve for  $e^3\Pi_g$  state. The potential curve of the ground state  $X^1\Sigma_g^+$  (18 eV below the  $a^3\Sigma_u^+$ ) has been omitted on the diagram and the energy of the first ( $v = 0, N = 0$ ) ro-vibrational level of  $a^3\Sigma_u^+$  state has been taken as 0 of the ordinate scale on the left; 0 of the right ordinate scale in electron volts is based on the lowest level in  $X^2\Sigma_u^+$  of He<sub>2</sub><sup>+</sup>. The transition and its wavelength value for the atomic  $2^3S - 2^3P$  transition has been marked on the right side.

by Köymen et al. [KTZ<sup>+</sup>90]. The temperature dependency of the rate constant  $\delta_m(T)$  for the formation of He<sub>2</sub> molecule has been measured for <sup>4</sup>He:

$$\delta_m(T) = T[8.7 \exp(-750/T) + 0.41 \exp(-200/T)] \times 10^{-36} \text{ cm}^6 \text{ s}^{-1} \quad (2.2)$$

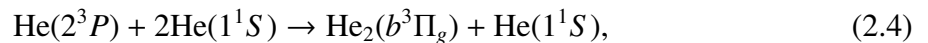
The temperature dependent rate constant  $\delta_m(T)$  is a coefficient in differential equation for temporal change of metastable helium atoms density  $n_m$  due to diffusion process ( $D_{at}$  - diffusion coefficient normalized to unit density) and associative ternary collisions with the ground state helium atoms (ground state atoms density  $N \propto P$ ,  $P$ -gas pressure):

$$\frac{\partial n_m}{\partial t} = D_{at} \nabla^2 n_m - \delta_m P^2 n_m \quad (2.3)$$

The product of  $\delta_m P^2$  is the frequency for destruction of  $2^3S$  atoms in three-body collision [KTZ<sup>+</sup>90, ZSB<sup>+</sup>93] - see also subsection 4.5.2.2 for reaction eq.(2.1)

The values of  $\delta_m(T)$  for <sup>3</sup>He isotope are measured to be  $\approx 33\%$  higher than given by eq.(2.2) due to increased thermal velocity of the lighter isotope. [KTZ<sup>+</sup>90]

Temperature dependent rate  $\delta_P(T)$  for molecule formation from  $2^3P$  state in reaction:



is given by:

$$\delta_P(T) = (2.5 + 267T^{-1}) \times 10^{-32} \text{cm}^6 \text{s}^{-1}, \quad (2.5)$$

because no repulsive potential barrier for the interaction between helium atoms in  $1^1\text{S}$  and  $2^3\text{P}$  states is existing in that case [ZSB<sup>+</sup>93].

The definition of  $\delta_P(T)$  rate coefficient is analogous as for  $\delta_m(T)$  but the differential equation similar to the eq. 2.3 concerns the change of the density of atoms in  $2^3\text{P}$  state ( $n_P$  instead of  $n_m$ ) and the diffusion process is described by the coefficient  $D_P$  (instead of  $D_{at}$ )

The ratio of rates for formation of metastable molecules given by (2.2) and (2.5) at room temperature (300K) is  $\delta_P(300\text{K})/\delta_m(300\text{K}) = \frac{3.4 \cdot 10^{-32}}{277 \cdot 10^{-34}} \approx 122$ , increased by two orders of magnitude. In this case the helium molecule in higher excited state  $b^3\Pi_g$  is formed that, however, de-excites to metastable state  $\text{He}_2(a^3\Sigma_u^+)$  [EADL88, RBBB88].

Hence, enhanced formation of metastable molecule is expected in presence of 1083 nm laser light, that resonantly promotes atoms from  $2^3\text{S}_1$  state to  $\text{He}(2^3\text{P})$  state during MEOP.

(inducing transition  $\text{He}(2^3\text{S}) \rightarrow \text{He}(2^3\text{P})$ ) and possibility of nuclear orientation of polarized helium atoms lose in collisions with molecular species gave an indication and motivation for investigations of relation between observed light-induced relaxation of atomic nuclear polarization and molecular formation dynamics.

## 2.1 Theoretical description of molecular dimer

Theoretical models describing pair of atoms associated in diatomic molecules has been already described in many literature sources thus only those issues that are needed for further understanding of the dissertation are presented.

Exact description of diatomic molecule in quantum mechanics comes down to solution of a many-body problem including interaction of two nuclei and  $N=4$  electrons. The Schrödinger equation (omitting the spin interactions between nuclei and electrons) has a following form:

$$\left( -\frac{\hbar^2}{2m} \sum_i \nabla_i^2 - \frac{\hbar^2}{2M_1} \nabla_1^2 - \frac{\hbar^2}{2M_2} \nabla_2^2 + V(\vec{r}_e, \vec{r}_n) \right) \Psi(\vec{r}_e, \vec{r}_n) = E \Psi(\vec{r}_e, \vec{r}_n), \quad (2.6)$$

$\nabla_i^2$  and  $\nabla_1^2, \nabla_2^2$  are Laplace operators corresponding to kinetic energy of electrons with mass  $m$  and each of nucleus having mass  $M_1$  and  $M_2$  forming the molecule. The total potential energy of a dimer  $V(\vec{r}_e, \vec{r}_n)$ , which graphical representations for  $\text{He}_2$  are given on 2.2, and the total wave function of electrons and nuclei  $\Psi(\vec{r}_e, \vec{r}_n)$  depend on electrons  $\vec{r}_e$  and nuclei  $\vec{r}_n$  spatial coordinates.

Exact solving of the equation (2.6) is not possible as its analytical solution does not exist. However, using certain assumptions, it can be simplified to the form that can be solved. Details of such procedures are well described in the literature, i.e. [Her50] thus only main steps will be shown leading to the final solutions. Born and Oppenheimer [BO27] assumed that the variation of internuclear distance (nuclei motion), which due to their mass is relatively slow in comparison with motion of light electrons, has a negligible influence on the latter. This allows separation of  $\Psi(\vec{r}_e, \vec{r}_n)$  into a product of electronic  $\Psi_e(\vec{r}_e; \vec{r}_n)$  and nuclear  $\Psi_n(\vec{r}_n)$  wave functions:

$$\Psi(\vec{r}_e, \vec{r}_n) = \Psi_e(\vec{r}_e; \vec{r}_n) \Psi_n(\vec{r}_n). \quad (2.7)$$



With this assumption the eq. (2.6) splits into two independent equations describing electrons movement in electrostatic field of motionless nuclei (2.8a) and nuclei motion (vibration and rotation) in effective potential  $V_n(\vec{r}_n) + V_e(\vec{r}_n)$  (2.8b)

$$\left( -\frac{\hbar^2}{2m} \sum_i \nabla_i^2 + V_e(\vec{r}_n) \right) \Psi_e(\vec{r}_e; \vec{r}_n) = E_{el} \Psi_e(\vec{r}_e; \vec{r}_n), \quad (2.8a)$$

$$\left( -\frac{\hbar^2}{2M_1} \nabla_1^2 - \frac{\hbar^2}{2M_2} \nabla_2^2 + V_n(\vec{r}_n) + V_e(\vec{r}_n) \right) \Psi_n(\vec{r}_n) = E \Psi_n(\vec{r}_n), \quad (2.8b)$$

$E_{el}$  and  $E$  are the electrons energy in the nuclei field and total energy of molecule respectively, while  $V_e$  and  $V_n$  are electronic and Coulomb internuclear interaction potentials. It has to be pointed out that in  $\Psi_e(\vec{r}_e; \vec{r}_n)$  the  $\vec{r}_n$  is not a variable but a parameter which is the consequence of variation of  $V_e$  with internuclear distance.

Solutions of eq.(2.8b) are of the special meaning in terms of interpretation of complex molecular absorption and emission spectra that exhibit the structure related to the relative movement of nuclei. However, symmetries of electronic wave functions  $\Psi_e$ , solutions of eq.(2.8a), decide about characteristics of the whole molecular state. Transformation of coordinate system in eq.(2.8b) into the center of the mass (CM) allows separation of relative nuclei motion from motion of the molecule as a whole. In the CM system  $R_{CM}$  and  $R$  coordinates appears which are describing position of the mass center and the intermolecular distance, as well as reduced mass  $\mu$  and total mass of nuclei  $M$ , so that (2.8b) takes form:

$$\left( -\frac{\hbar^2}{2M} \nabla_{R_{CM}}^2 - \frac{\hbar^2}{2\mu} \nabla_R^2 + V(\vec{R}) \right) \tilde{\Psi}_n(\vec{R}_{CM}, \vec{R}) = E \tilde{\Psi}_n(\vec{R}_{CM}, \vec{R}) \quad (2.9)$$

The wave function  $\tilde{\Psi}_n$  can be decomposed into the part describing the mass center motion  $\exp(i\vec{k}\vec{R}_{CM})$  and relative nuclear  $\chi(R)$  motion:

$$\tilde{\Psi}_n = \exp(i\vec{k}\vec{R}_{CM}) \chi(R), \quad (2.10)$$

with  $\vec{k}$  - wave vector describing the momentum of the molecule. Eigenvalues of eq.(2.9) are given by the sum of kinetic energy of the molecule and its internal energy  $E_{int}$ :

$$E = \frac{\hbar^2 k^2}{2M} + E_{int} \quad (2.11)$$

Considering only this part of (2.10) which depends on internuclear distance it is worth changing the Cartesian into spherical coordinate system as the potential  $V(\vec{R})$  depends only on relative nuclei positions. In this way wavefunction is factorized:  $\chi(\vec{R}) = f(|\vec{R}|)F(\theta, \varphi)$  and transformation of Laplace operator in (2.9) leads to

$$\left( -\frac{\hbar^2}{2\mu} \frac{d^2}{dR^2} - \frac{\hbar^2}{\mu} \frac{1}{R} \frac{d}{dR} + \frac{\hat{L}^2}{2\mu R^2} + V(R) \right) f(|\vec{R}|)F(\theta, \varphi) = E_{int} f(|\vec{R}|)F(\theta, \varphi), \quad (2.12)$$

where  $\hat{L}^2$  is a square of orbital angular momentum operator. Choosing the form of the angular part of the eigenfunction:  $F(\theta, \varphi) = F_{L,M}$  so that it is the eigenfunction of  $\hat{L}^2$ , fulfilling following eigenequations

$$\hat{L}^2 F_{L,M} = \hbar L(L+1) F_{L,M} \quad (2.13a)$$

and

$$\hat{L}_z F_{L,M} = \hbar M F_{L,M} \text{ , ,} \quad (2.13b)$$

quantization rules for orbital angular momentum quantum number  $L$  and its projection  $M$  on quantization  $z$  axis appears:

$$L = 0, 1, 2, \dots, \quad (2.14a)$$

$$-L \leq M \leq L, M \in \mathbb{Z}. \quad (2.14b)$$

Applying identity (2.13a) to (2.12) and assuming the term  $\frac{\hbar^2}{\mu} \frac{1}{R} \frac{d}{dR}$  is a small perturbation [HW98], thus it can be neglected, simplifying (2.12) to:

$$\left( -\frac{\hbar^2}{2\mu} \frac{d^2}{dR^2} + \frac{\hbar^2 L(L+1)}{2\mu R^2} + V(R) \right) f(|\vec{R}|) = E_{int} f(|\vec{R}|), \quad (2.15)$$

which does not contain any angular coordinate and describes only the radial part of the wave function  $\chi(\vec{R})$ . Its dependency on the value of quantum number  $L$  and  $M$  that has  $2L+1$  possible values leads to  $(2L+1)$ -fold degeneracy.

At this stage further solution of Schrödinger equation depends on choice of a function describing  $V(R)$  potential.

### 2.1.1 Approximations of $V(R)$ potential

The eigenproblem (2.15) represents the motion in a given potential, consists of terms responsible for centrifugal force and binding potential between the nuclei, which has to have the minimum if the bound state is considered. Application of approximation of a small oscillations about  $r_e$  leads to approximation of  $V(R)$  by expansion around  $r_e$  up to the second (harmonic oscillator) and the third (anharmonic oscillator) order of magnitude terms. Despite the model of a simple harmonic oscillator has no physical meaning in terms of proper description of diatomic molecule potential, simple results that can be obtained in this way can build up ones intuition for further understanding of more accurate, however more complicated, models.

**(a) Harmonic oscillator and rigid rotator** The expansion of  $V(R)$  up to the second order term is given by:

$$V(R) \approx V(r_e) + \frac{1}{2} k (R - r_e)^2, \quad (2.16)$$

where  $k$  is a second order derivative of the potential at  $R = r_e$  popularly known as a spring constant.

With this potential, assuming also small oscillations, where changes of  $R$  around  $r_e$  are much smaller than the equilibrium value, that  $R \approx r_e$  in the second term of (2.15), we obtain:

$$\left( -\frac{\hbar^2}{2\mu} \frac{d^2}{dR^2} + \frac{\hbar^2 J(J+1)}{2\mu r_e^2} + \frac{1}{2} k (R - r_e)^2 + V(r_e) \right) f(|\vec{R}|) = E_{int} f(|\vec{R}|), \quad (2.17)$$

Solution of (2.17) represents the internal energy of the molecule:

$$E_{int}(J, v) = V(r_e) + \hbar \omega_e \left( v + \frac{1}{2} \right) + B_e \left( J(J+1) \right). \quad (2.18)$$

Introduced rotational constant

$$B_e = \frac{\hbar^2}{2\mu r_e^2} \quad (2.19)$$

is related to the nuclear moment of inertia of the rotating molecule,  $\omega_e = \sqrt{\frac{k}{\mu}}$  is a frequency of harmonic oscillations which energy quantization is provided by a discrete values of vibrational quantum number  $\nu = 0, 1, 2, \dots$ . Components of eq.(2.18) can be interpreted as the electronic energy  $E_e$ , the energy of vibrational motion  $E_\nu$  and the rotational energy  $E_r$ , so that  $E_{int} = E_e + E_\nu + E_J$ .  $E_e$  is the value at the bottom of the potential minimum. In molecular spectroscopy energy is often expressed in the wavenumber unit [ $\text{cm}^{-1}$ ] term values  $T = E/hc$  and the total energy of molecule is given by:

$$T(\nu, J) = T_e + G(\nu) + F_\nu(J), \quad (2.20)$$

being the sum of electronic, vibrational and rotational terms. In the notation of the rotational term, by adding the subscript  $\nu$ , the parametric dependency of molecular rotational motion on vibrations has been emphasized, as it will be shown below, both can't be in fact considered separately. $\mu$

#### (b) Anharmonic oscillator and non-rigid rotator

To obtain more accurate and physical results further approximation of the potential  $V(R)$  has to be made by adding the third order expansion term in (2.16):

$$V(R) \approx V(r_e) + \frac{1}{2}k(R - r_e)^2 + \frac{1}{3}g(R - r_e)^3, \quad (2.21)$$

$g$  is the third order derivative of potential at  $R = r_e$ . Solution of (2.15) with anharmonic potential (2.21) provides equations for vibrational and rotational energy terms:

$$G(\nu) = \omega_e \left( \nu + \frac{1}{2} \right) - \omega_e x_e \left( \nu + \frac{1}{2} \right)^2 + \dots, \quad (2.22a)$$

$$F(J) = B_\nu J(J + 1) + D_\nu (J(J + 1))^2 + \dots. \quad (2.22b)$$

$\omega_e x_e$  is a constant which is a measure of the anharmonicity of the oscillator. Here, the rotational constants  $B_\nu$  and  $D_\nu$  are related to the moment of inertia and centrifugal force respectively. They are given by following expressions parametrically dependent on vibrational quantum number  $\nu$  and constants  $\alpha_e, \beta_e$  describing the coupling strength of vibrational and rotational motion:

$$B_\nu = B_e - \alpha_e \left( \nu + \frac{1}{2} \right) + \dots, \quad (2.23a)$$

$$D_\nu = D_e + \beta_e \left( \nu + \frac{1}{2} \right) + \dots. \quad (2.23b)$$

Rotational constant  $B_e$  was defined by (2.19) assuming the lack of oscillations. Under the same condition  $D_e$  is given by:

$$D_e = \frac{4B_e^3}{\omega_e^2}. \quad (2.24)$$

Morse potential parameter	$a^3\Sigma_u^+$	$e^3\Pi_g$
$r_e[\text{\AA}]$	1.045	1.075
$\beta[\text{\AA}^{-1}]$	2.129	2.031
$D_e\text{cm}^{-1}$	21400	21300

Table 2.1: Morse potential parameters for  $a^3\Sigma_u^+$  and  $e^3\Pi_g$  of  $\text{He}_2$

(c) **Morse potential** Very useful, especially in terms of the analysis of rotational structure of the molecular spectrum, is the Morse potential given by [Mor29]:

$$V(R) = D_e \exp^{-2\beta(R-r_e)} - 2D_e \exp^{-\beta(R-r_e)} \quad (2.25)$$

This representation correctly reproduces only the vicinity of the potential minimum (low  $v$  values) and exhibits nonphysical behavior for  $R = 0$  giving the finite value of repulsive potential. This work, however, considers the transition at around 465 nm which occurs between the states of which vibrational number is both equal 0 and Morse potential approximation can be applied by use of relations given below. It has to be remarked that  $D_e$  in (2.25) is **not** the rotational constant (2.24) but is the depth of the potential well at the minimum of internuclear distance  $R = r_e$  (see fig.2.1). The common designation of these quantities is well embedded in molecular terminology thus using proper remarks emphasizing each time the meaning of used  $D_e$  symbol seems to be less problematic than defining other designation to distinguish one from another. Moreover, the use of  $D_e$  as the rotational constant is predominant in this work. According to [CBB<sup>+</sup>78], Morse potential parameters values for the  $a^3\Sigma_u^+$  and  $e^3\Pi_g$  states relevant in this work are given in the table 2.1

Very useful expressions of Pekeris and Dunham related to Morse potential allow calculation of  $\alpha_e, \beta_e$  and therefore rotational constants  $B_v, D_v$  (required in eq.(2.22b)) on the basis of usually known  $B_e, \omega_e$  and  $\omega_e x_e$  for a given molecule. After Pekeris [Pek34]:

$$\alpha_e = \frac{6B_e}{\omega_e} \left( \sqrt{\omega_e x_e B_e} - B_e \right) \quad (2.26)$$

After Dunham [Dun32]

$$\beta_e = D_e \left( \frac{8\omega_e x_e}{\omega_e} - \frac{5\alpha_e}{B_e} - \frac{\alpha_e^2 \omega_e}{24B_e^3} \right) \quad (2.27)$$

These identities are useful when  $\alpha_e$  and  $\beta_e$  values are not reported in any experimental or theoretical reference (as is the case for helium-3 isotope), while the other molecular constants are usually known or can be obtained as discussed below.

#### (d) Isotopic scalings of molecular constants

Working with different isotopes of the same atom bound in the molecule, as it is the case in this work, and determining the levels structure requires the knowledge of the molecular constants for each of considered isotopic molecules. As the oscillation frequency  $\omega_e$  depends on the reduced mass  $\mu$  it is obvious that the isotopic change of the mass of one or both atoms affects the vibrational energy but also rotational energy, as the rotational constants are functions of reduced mass. After [Her50], indicating the quantities for isotopologue by superscript  $i$  and

defining  $\rho = \sqrt{\frac{\mu}{\mu'}}$ , the relations between isotopic molecular constants are given below:

for vibrational constants:

$$\omega_e^i = \rho \omega_e, \quad \omega_e^i x_e^i = \rho^2 \omega_e x_e \quad (2.28)$$

for rotational constants:

$$B_e^i = \rho^2 B_e, \quad \alpha_e^i = \rho^3 \alpha_e, \quad D_e^i = \rho^4 D_e, \quad \beta_e^i = \rho^5 \beta_e. \quad (2.29)$$

### 2.1.2 Electronic molecular states

Born-Oppenheimer approximation separates electronic and nuclear motion what results in two Schrödinger equations (2.8a) and (2.8b). Before, several potential approximations and resulting solutions for energy values were described for nuclear part, where the advantage of spherical symmetry of internuclear interaction was taken. In case of the electronic Schrödinger equation not the spherical but the axial symmetry of the field in which the electrons move complicates the problem of finding satisfactory approximation and numerical methods have to be engaged. This, however, won't be discussed here leaving the place for, more useful in terms of further analysis and discussion, description of the electronic states by the quantum numbers related to present angular momenta and their actual coupling. Also the parities of these states, deciding about the molecular spectra are discussed.

#### (a) Electron angular momenta in the molecules

One of the consequences of reduced symmetry (from spherical to axial when moving transfer separated atoms to diatomic molecule) is the change of the electrons constant of motion. For atoms the orbital angular momentum  $\mathbf{L}$  is the constant. In the axial symmetry of the molecule only the component of  $\mathbf{L}$  about the internuclear axis is a constant of the motion that takes values:

$$M_L = L, L - 1, L - 2, \dots, -L \quad (2.30)$$

The direction of motion of all electrons which decides about the sign of  $M_L$  has no influence on the energy value, thus a two-fold degeneracy of the states with equal  $|M_L|$  occurs, which is more appropriate value to classify the electronic states than  $L$ . The designation is introduced:

$$\Lambda = |M_L|. \quad (2.31)$$

The  $\Lambda$  as the modulus of the component of electronic orbital angular momentum vector  $\mathbf{L}$  can take  $L + 1$  different values ranging from 0 to  $L$ . For each of  $\Lambda \neq 0$  ( $\equiv |M_L| \neq 0$ ) two fold-degeneracy is present. Designation of the electronic states by the successive Greek letters:  $\Sigma, \Pi, \Delta, \Phi, \dots$  is related to the value of  $\Lambda = 0, 1, 2, 3, \dots$

In the same manner as in case of atoms, spins of individual electron results in total electronic spin vector  $\mathbf{S}$  and associated quantum number  $S$ , being half-integral or integral depending on the odd or even total number of electrons. The orbital motion of the electrons about the internuclear axis results in internal magnetic field along this axis. Thus, for  $\Pi, \Delta, \Phi, \dots$  states precession of  $\mathbf{S}$  occurs around the field direction so that the only constant is the total spin component about the axis of the dimer denoted by  $\Sigma$  (it should be not confused with the same symbol used for

$\Lambda = 0$  state designation). In contrast to  $\Lambda$ , spin component  $\Sigma$  can take both positive and negative values:  $\Sigma = S, S - 1, S - 2, \dots, -S$  (altogether  $(2S + 1)$  values) and is not defined when  $\Lambda = 0$ .

Molecular electronic state term symbols are usually denoted as follows:

$$n^{2S+1}\Lambda_{\Omega,g/u}^{+/-} \quad (2.32)$$

When  $\Lambda = 0$ ,  $\Omega$  is not defined, in other case it has  $(2S + 1)$  different values corresponding to different energies of the resulting molecular states.  $(2S + 1)$  value is called multiplicity of the state and is added as a left superscript in the , while the value of  $\Omega$  can be optionally added in the right subscript:

The symbol  $n$  in eq. (2.32) is substituted by the letter  $X$  for the ground state of the molecule and successive capital letters  $A, B, C, \dots$  for the excited states with the same multiplicity as the ground state. For excited states with other multiplicity  $(2S + 1)$  in the left superscript successive small letters are used  $a, b, c, \dots$ . The meaning of the symbols  $g$  or  $u$  and  $+$  or  $-$  is given in subsection 2.1.3 (a) as they reflect the state symmetry properties.

### (b) Molecular angular momentum coupling. Hund's case (b) and molecular energy levels scheme

Electronic angular momenta as well as angular momenta of the rotational motion of a dimer are actually coupled. So-called Hund's coupling cases refer to different possibilities of coupling between existing angular momenta, that depends on a given molecular state and determines good quantum numbers for the system description. There are five different coupling schemes denoted by successive letters (a)-(e). For explanation of other cases the Reader is referred to the popular handbooks treating about molecular systems (i.e. [Her50, BC03]) as in this dissertation the transition occurs between  $a^3\Sigma_u^+$  and  $e^3\Pi_g$  states of  $\text{He}_2$  that are, after [CBB<sup>+</sup>78, MC77], well described by coupling case (b), only this scheme will be discussed.

The Hund's coupling case (b) is valid for the states described by  $\Lambda = 0$ , when the electrons orbital angular momentum  $\mathbf{L}$  and spin  $\mathbf{S}$  are uncoupled or  $\Lambda \neq 0$ , but for such light molecules as  $\text{He}_2$ , the coupling between  $\mathbf{L}$  and  $\mathbf{S}$  is very weak. For the  $\Sigma$  state with  $\Lambda = 0$ , the  $\mathbf{L}$  is not coupled to the internuclear axis through electrostatic forces, this means that it does not precess about the axis. Therefore there is no magnetic field in molecule axis direction, hence no  $\mathbf{S}$  precession occurs about this axis. For the  $\Pi$  state, despite  $\Lambda = 1$  (precession of  $\mathbf{L}$  occurs), weak spin-orbit coupling prevents  $\mathbf{S}$  from the precession about the non-zero vector  $\mathbf{\Lambda}$  in the axis direction.

Vector coupling diagram is shown on the Fig.2.3

The corresponding to  $\mathbf{N}$  vector quantum number is:

$$N = \Lambda, \Lambda + 1, \Lambda + 2, \dots, \quad (2.33)$$

So as  $N$  can take all the integral values from 0 up. For  $\Lambda = 0$   $\mathbf{N}$  is identical with  $\mathbf{R}$  - perpendicular to internuclear axis.

Further  $\mathbf{N}$  adds to  $\mathbf{S}$  forming the total angular momentum  $\mathbf{J}$ . This indirect fine structure coupling between  $\mathbf{S}$  and  $\mathbf{N}$  results from a very slight magnetic moment in the direction of  $\mathbf{N}$  being a consequence of molecular rotation. For a given  $N$ , possible  $J$  values are given by:

$$J = (N + S), (N + S - 1), (N + S - 2), \dots, |N - S|, \quad (2.34)$$

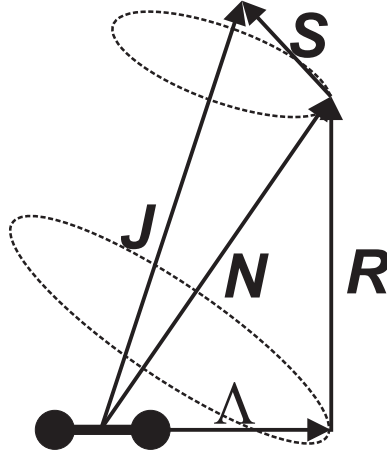


Figure 2.3: Hund's coupling (b). The component  $\Lambda$ , constant for electronic motion, resulting from  $\mathbf{L}$  precession about the internuclear axis, is coupled to the angular momentum of nuclear rotation  $\mathbf{R}$ , to form  $\mathbf{N}$ , that corresponds to the total angular momentum for a spin-less molecular system. The coupling on  $\mathbf{N}$  with  $\mathbf{S}$  provides the total angular momentum  $\mathbf{J}$  of the dimer.

so  $(2S + 1)$  components can be distinguished.

For  $\text{He}_2^*$  and  $(^3\text{He}-^4\text{He})^*$  molecules presence of non-zero nuclear spin  $\mathbf{I}$  has to be introduced into considerations. For two nuclei each with nuclear spin  $I_1$  and  $I_2$  the quantum number related to a total nuclear spin  $\mathbf{I}_T$  is given:

$$I_T = I_1 + I_2, I_1 + I_2 - 1, \dots, |I_1 - I_2|. \quad (2.35)$$

The total angular momentum of molecule including spin of the nuclei  $\mathbf{F}$  is resultant of  $\mathbf{J}$  and  $\mathbf{T}$ . Corresponding quantum number is then:

$$F = (J + T), (J + T - 1), \dots, |J - T|, \quad (2.36)$$

so each level described by  $J$  has  $(2T + 1)$  components.

Following abovementioned rules of angular momenta coupling and resulting values of quantum numbers that can be taken, the scheme of the rotational sublevels of the electronic states  $a^3\Sigma_u^+$  and  $e^3\Pi_g$  can be drawn as on Fig.2.4 and Fig.2.5. Not going into the details about meaning of "+" and "u" or "g" designations, that will be discussed later in the part of chapter dedicated to the states symmetry and transition rules, it is shown how abovementioned coupling scheme is reflected in the level structure. In  $^3\Sigma$  state for each value of quantum number  $N$  (except  $N = 0$ )  $J$  takes 3 values  $(N + 1), N, (N - 1)$ , as  $S = 1$  here. It has to be emphasized that the order of level position in terms of energy is not in order with increasing  $J$  value. Rotational level with  $J = N + 1$  (in the literature often labeled as  $F_1$ ; confusion with (2.36) should be avoided) is in between lower lying  $J = N$  ( $F_2$ ) and  $J = N - 1$  ( $F_3$ ). For the details about the splitting of  $N$ -sublevels into terms with different  $J$  values the Reader is sent to [Her50] p.223 where equations for energy terms depending on spin-spin and spin-orbit splitting constants  $\lambda$  and  $\gamma$  are given.

Looking at the rotational levels scheme of  $e^3\Pi_g$  state, the absence of  $N = 0$  is worth noting, which is a consequence of  $\Lambda = 1$  in (2.33). Non-zero  $\Lambda$  value results also in double splitting for each of  $J$ . In case of  $^3\Pi$  state the energy of rotational sublevels described by  $J$  for certain

$N$  increases with decreasing value of  $J$ . For the same reason as for  $\Sigma$  state the Reader is sent to [Her50] p.227 & 235 for detailed information about equation for energy terms taking into account splitting of sublevels described by common value of  $N$  as well as  $\Lambda$  doubling of levels described by single  $J$  number.

Resolving the absorption lines fine structure is not possible as the size of splitting is of the same order [LMV74, RBBB88] as combined Doppler and collisional absorption lines broadening  $B$  in conditions of experiments performed by the Author (several GHz). However its existence affects apparently the width and shape (distortion) of the lines. Ignoring the fine structure in further considerations, the Author decided to use simpler, than those to which the reference is given above in [Her50], formula for the rotational energy (given by (2.22b) in which  $J$  has to be replaced by  $N$  for rotational levels in Hund's case (b) ).



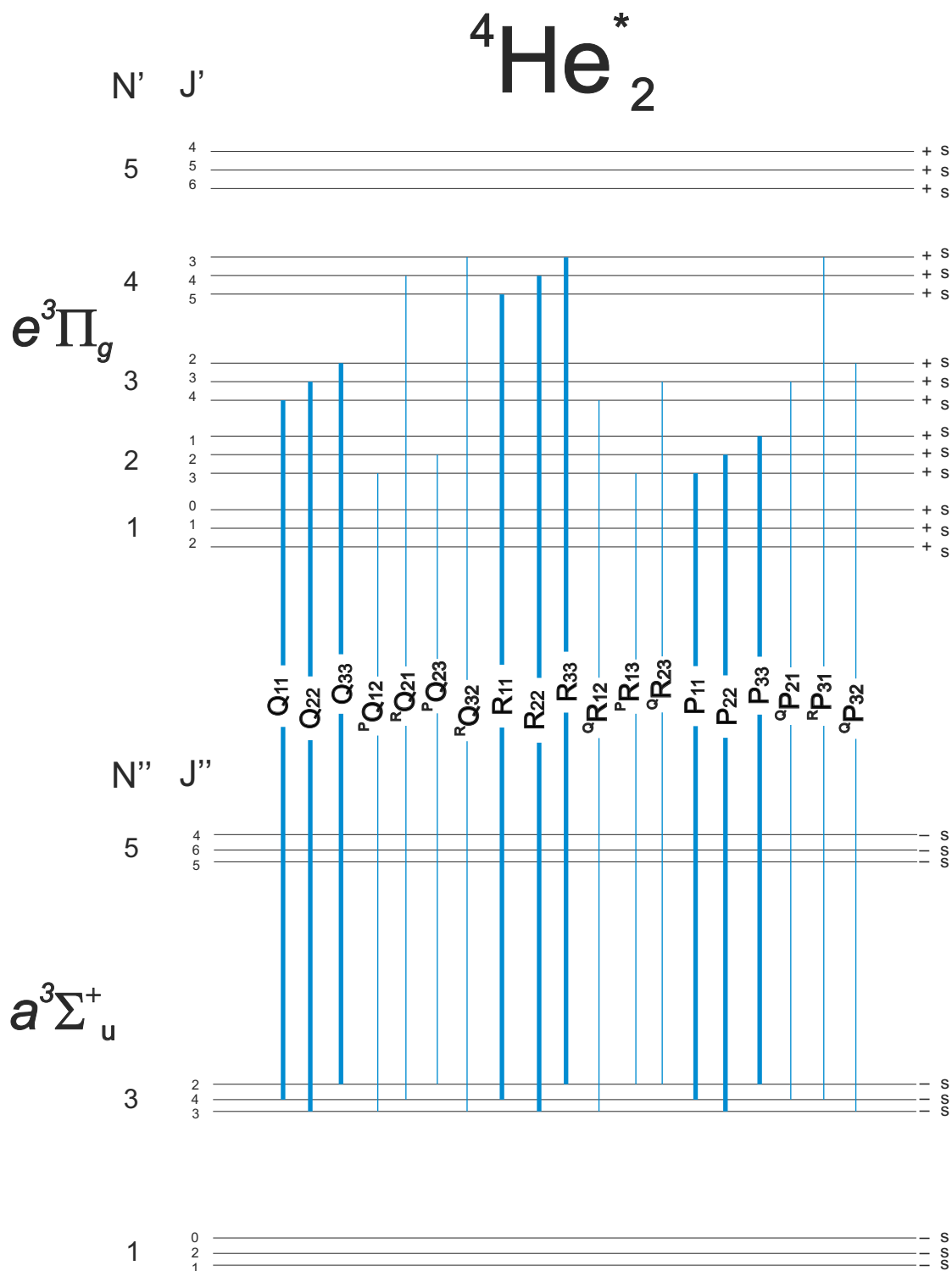


Figure 2.4: Scheme of rotational sublevels of  $a^3\Sigma_u^+$  and  $e^3\Pi_g$  states of  ${}^4\text{He}_2$ , being a consequence of discussed coupling scheme and wavefunction symmetry properties (paragraph 2.1.2 (b)). The possible transition (according to the rules explained in subsection 2.1.3(e)) from exemplary rotational sublevels and its fine structure are marked - the notation is explained in subsection 2.1.3(f). The absence of even numbered rotational levels for helium-4 isotope is characteristic.

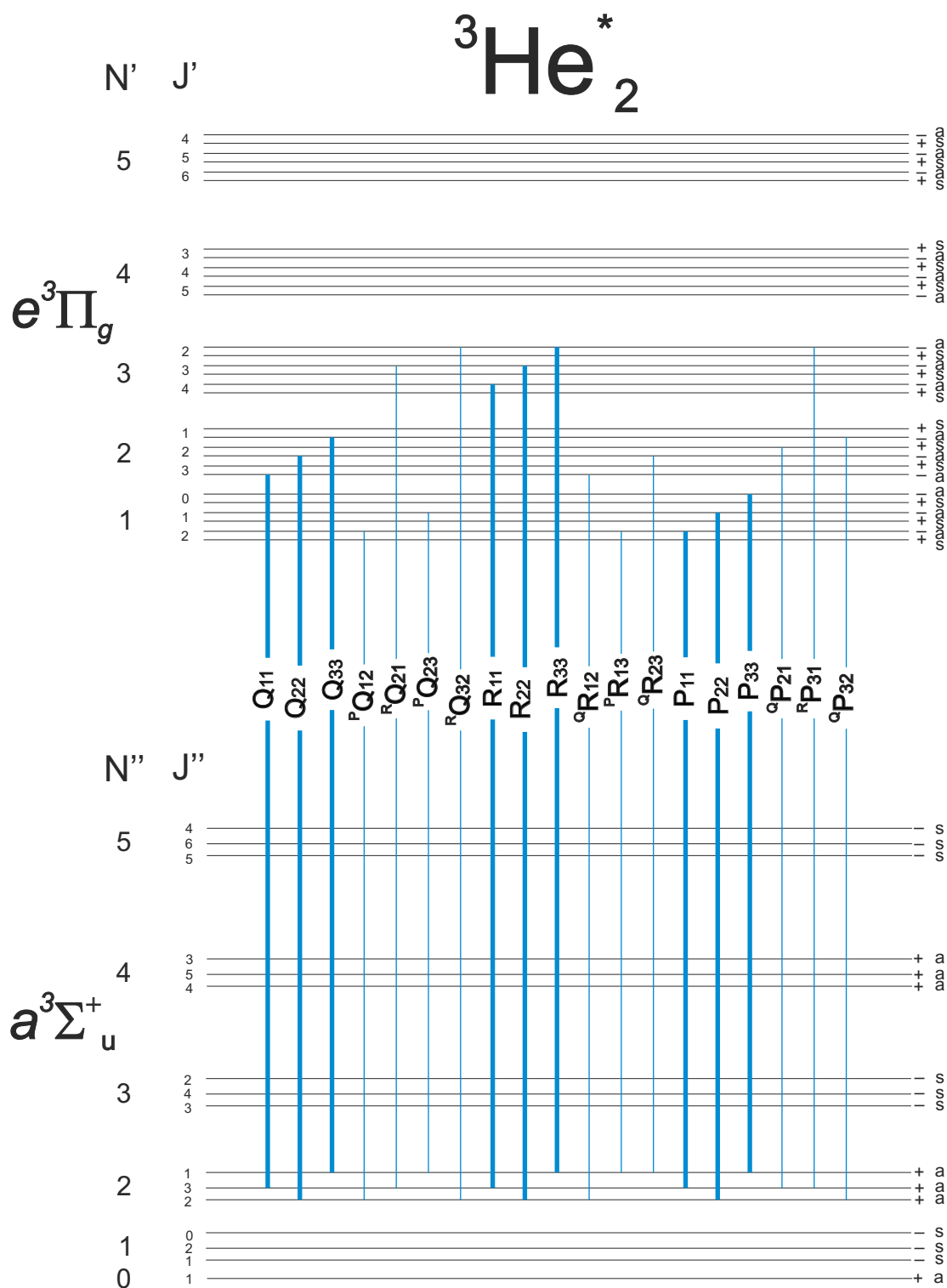


Figure 2.5: Scheme of rotational sublevels of  $a^3\Sigma_u^+$  and  $e^3\Pi_g$  states of  ${}^3\text{He}_2$ , being a consequence of discussed coupling scheme and wavefunction symmetry properties (paragraph 2.1.2 (b)). The possible transition (according to the rules explained in subsection 2.1.3(e)) from exemplary rotational sublevels and its fine structure are marked - the notation is explained in subsection 2.1.3(f).

### 2.1.3 Symmetries of the rotational levels and transition selection rules

For determination of which sublevels of the rotational structure of the  $a^3\Sigma_u^+$  and  $e^3\Pi_g$  states shown on Fig.2.4 are involved in dipolar transitions induced by the laser light or observed as emission lines, a transition rules has to be known, that are determined by the symmetry properties of molecules. So-called selection rules are the consequence of molecular wave function properties as well as dipolar momentum operator features. Thus, some general rules can be obtained independent of the angular momenta coupling schemes and those that holds only in certain Hund's cases. After describing relevant symmetries of rotational levels, their consequences in general transition rules and those valid only for case (b) are discussed.

**(a) Symmetry in respect to reflection at the origin** Looking at the Schrödinger equation (2.6) since del ( $\nabla$ ) operator (defined as a first order spatial derivative  $\frac{\partial}{\partial r_k}$  or explicitly  $\frac{\partial}{\partial x_k} + \frac{\partial}{\partial y_k} + \frac{\partial}{\partial z_k}$ , where  $k$  denotes particle considered) is raised to the second power, changing the sign of the system coordinates (all particles, i.e. electrons and nuclei) that is  $\vec{r}_e$  and  $\vec{r}_n \rightarrow -\vec{r}_e, -\vec{r}_n$  results in a new total eigenfunction. It has the same properties as  $\Psi$  in (2.6) but can differ in sign:  $\pm\Psi$ . The state described by the total wave function that is the solution of transformed Schrödinger equation and preserves the sign of  $\Psi$  is called *positive*, if it is contrary - *negative* state.

However, this general definition does not provide directly any information about connection between quantum numbers describing the structure of the molecule and states symmetry. To obtain this information it is worth looking at the total wave function distinguishing parts describing the electronic, the vibrational and the rotational contributions. It was partially made in eq. (2.7) at the beginning of the section 2.1, where separation of electronic  $\Psi_e(\vec{r}_e; \vec{r}_n)$  and nuclear  $\Psi_n(\vec{r}_n)$  parts were identified. The second - nuclear part depends only on nuclei coordinates and describes vibrational and rotational motion of the molecule. It is thus natural to look at the nuclear wave function as a resultant of two parts describing these, however mutually dependent, degrees of freedom [Her50]. That gives:

$$\Psi_n(\vec{r}_n) = \frac{1}{r} \Psi_v \Psi_r, \quad (2.37)$$

Explicit dependency of vibrational and rotational parts on nuclei spatial coordinates is not shown, however it is worth noting that the vibrational part depends only on the magnitude of the distance  $r$  between the nuclei and during inversion of the coordinates procedure it remains unaltered. On the other hand rotational part  $\Psi_r$  is described only by  $\vartheta, \varphi$  angles when spherical coordinate system is considered. In this system reflection of the rotator ( $\Lambda = 0$ ) at the origin is achieved by replacing  $\vartheta$  by  $\pi - \vartheta$  and  $\varphi$  by  $\pi + \varphi$ . It can be shown [Her50] that during such reflection at the origin  $\Psi_r$  remains unchanged for even values of rotational number  $N$  (those sublevels are *positive*) and change the sign to  $-\Psi_r$  for odd  $N$  values (*negative* sublevels). In the most interesting for the Author Hund's case (b)  $\mathbf{N}$  is coupled with electron spin  $\mathbf{S}$  resulting in  $\mathbf{J}$  so the question can be raised, why the symmetry of rotational eigenfunction depends on  $N$  value and not on the total number  $J$ . The answer lies in the fact that the function representing orientation of the electrons spins  $\beta_e$ , by which the total eigenfunction in eq.(2.7) should be multiplied (by now only electronic coordinate function  $\Psi$  was considered) is independent of an inversion. Thus, for one given value of  $N$  each of sublevels with different  $J$  resulting from (2.34) has the same *positive* or *negative* symmetry. In case of the state for which  $\Lambda \neq 0$  (i.e.  $\Pi$  state), as was mentioned 2.1.2(b)  $\Lambda$ -doubling occurs and for each  $J$  value one component is

positive and the other is negative. For each of  $J$  values the upper sublevel is positive for even  $N$  value and negative for odd  $N$ , while lower lying sublevel has the opposite sign.

Finally the symmetry properties of reflection at the origin of  $\Psi_e$  eigenfunction has to be considered, for the purpose of which inversion can be equivalently treated as combination of rotation of the molecule through  $180^\circ$  about an axis perpendicular to the internuclear axis and reflection at the plane perpendicular to this rotational axis and passing through the internuclear axis. The first operation does not alter  $\Psi_e$ , because it depends on coordinates of the electrons relative to the nuclei but the second transformation can change the sign of  $\Psi_e$ , so that the electronic state can have positive (designated as  $^+$  in the right superscript of molecular electronic state symbol i.e.  $\Sigma^+$ ) or negative ( $-$ ) symmetry.

In case of the  $\Sigma$  states the product of rotational  $\Psi_r$  and electronic  $\Psi_e$  eigenfunctions symmetries to the reflection at the origin gives the total symmetry of rotational level described by the quantum number  $N$ . Thus, for  $\Sigma^+$  even- $N$ -numbered rotational levels are positive and odd- $N$ -numbered are negative while for  $\Sigma^-$  state it is reversed even- $N$ -numbered are negative, odd- $N$ -numbered are positive.

One can also identify  $\Pi^+$  and  $\Pi^-$  states with the mentioned before symmetries for  $\Lambda \neq 0$  case (however it is not common in these states designation) as the upper of doubled  $J$  sublevels change their sign with  $N$  like  $\Sigma^+$  and the lower sublevels like  $\Sigma^-$ .

There is an additional symmetry for  $\Psi_e$  function when the dimers consisted of two nuclei with the same charge (isotopes, i.e.  $^3\text{He}_2$ ,  $^4\text{He}_2$  and  $^3\text{He}-^4\text{He}$ ) are considered. In this case the field in which electrons move has, in addition to the symmetry axis, a center of symmetry and the field remains unaltered when the nuclei are reflected at this center. Then, if reflection of only electrons coordinates at the origin is performed:  $\vec{r}_e \rightarrow -\vec{r}_e$  (before inversion at the origin of all the particles - electrons and nuclei - was considered) the state of which the electronic eigenfunction preserves the sign is called *even* (designated by subscript  $_g$ ), in opposite case is called *odd* state (designated by subscript  $_u$ ).

**(b) Nuclear spin symmetry** During the discussion about the symmetry of the molecular eigenfunction, the nuclear spin influence was omitted. If the two nuclei of the molecule are identical, each possessing the spin  $I_1 = I_2 = I$ , after their permutation the total molecular wavefunction  $\Psi$  can preserve (symmetry) or change its sign (antisymmetry). The former occurs for nuclei with integral and 0  $I$  values (bosons), while the latter case occurs for nuclei with  $I$  half-integral (fermions).

The presence of the nuclear spin requires introduction of the spin function  $\beta_n$  describing spatial state of two nuclei in (2.7). Function  $\beta_n$  can be either symmetric (ortho) or antisymmetric (para) in respect to the exchange of the nuclei. For a given  $I$ :

$$(I + 1)(2I + 1) \text{ is the number of symmetric} \quad (2.38a)$$

and

$$I(2I + 1) \text{ is the number of antisymmetric } \beta_n \text{ functions.} \quad (2.38b)$$

For  $I = 0$  spin there is only one symmetric  $\beta_n$  and for  $I = \frac{1}{2}$  there are 3 possible symmetric functions and only one antisymmetric  $\beta_n$ . This, on the other hand, has the consequence in

the rotational level occurrence to fulfill requirements of parity of total (including  $\beta_n$  and  $\beta_e$ ) molecular wavefunction  $\Psi(\vec{r}_e, \vec{r}_n, \beta_e, \beta_n)$  for bosons and fermions.

For bosons with  $I = 0$  symmetry of total wave function can be provided only if the rest of  $\Psi(\vec{r}_e, \vec{r}_n, \beta_e)$  without  $\beta_n$ , here symmetric, is also symmetric. Thus, antisymmetric rotational levels do not occur at all. For fermions with half-integral  $I$  value both symmetric and antisymmetric rotational levels are allowed, however, due to mentioned multiplicity of symmetric  $\beta_n$ , antisymmetric rotational levels occurs  $\frac{I+1}{I}$  times more frequent as the symmetric (for symmetric  $\beta_n$   $\Psi(\vec{r}_e, \vec{r}_n, \beta_e)$  has to be antisymmetric and reverse).

**(c) Nuclear spin influence on the electronic and the rotational wave functions symmetries** As the nuclei exchange can be alternatively performed as first the reflection of all the particles at the origin and then the reflection of only the electrons at the origin, the properties of homonuclear wave function transfers to the symmetry of electronic state and rotational levels which thus can be for bosons symmetric and for fermions antisymmetric in respect to the exchange of the nuclei. Taking into account the previous discussion about symmetries to the reflection at the origin for dimers with like nuclei it is straightforward that:

$$\text{for } \Sigma_g^+ N\text{-even states are symmetric} \equiv s, N\text{-odd states are antisymmetric} \equiv a \quad (2.39a)$$

$$\text{for } \Sigma_u^+ N\text{-even states are antisymmetric} \equiv a, N\text{-odd states are symmetric} \equiv s \quad (2.39b)$$

$$\text{for } \Sigma_g^- N\text{-even states are antisymmetric} \equiv a, N\text{-odd states are symmetric} \equiv s \quad (2.39c)$$

$$\text{for } \Sigma_u^- N\text{-even states are symmetric} \equiv s, N\text{-odd states are antisymmetric} \equiv a \quad (2.39d)$$

The same rules occurs for  $\Pi$  states where distinction between  $\Pi^+$  and  $\Pi^-$  is useful as then the similarity with  $\Sigma^{+/-}$  is easier to see.

**(d) Symmetries for helium isotope molecules** Knowing the symmetry properties of the total wave function in respect to the reflection at the origin and nuclei exchange as well as possible combinations of electronic states determined by these symmetries, the discussed rules can be applied in case of the  $a^3\Sigma_u^+$  and  $e^3\Pi_g$  states of  $^3\text{He}_2$  and  $^4\text{He}_2$  isotopes.

Since helium-4 atom has zero value of the nuclear spin the symmetry rules for homonuclear bosonic molecule are valid. Only the symmetric rotational levels exist which together with only symmetric  $\beta_n$ , gives the total wave function symmetric to the nuclei exchange. Thus, for the  $a^3\Sigma_u^+$  state only odd- $N$  numbered levels are possible and each even- $N$  numbered levels is missing. This results in absence of even-numbered lines in the rotational spectrum of this molecule.

Atoms of which  $^3\text{He}_2$  consists of have half-integral nuclear spin  $I = \frac{1}{2}$  so both symmetric and antisymmetric rotational levels occur as  $\beta_n$  can also be either symmetric or antisymmetric, however with different statistical weights. According to (2.38a) and (2.38b) there are 3 times more frequent symmetric functions  $\beta_n$  than antisymmetric. Simultaneously the total wave function for fermions has to be antisymmetric to the nuclei permutation, what results in three times more frequent rotational levels with even- $N$  value (antisymmetric) than with odd ones, when  $a^3\Sigma_u^+$  is considered. As it will be shown in [ref.experimental chapter] and was reported by [DR50] this symmetry properties results in the alternation of rotational spectra lines in ratio 3:1 between even numbered and odd numbered transitions.

For the heteronuclear dimer  $^3\text{He}-^4\text{He}$  the division of the rotational states into symmetric or antisymmetric ones disappears in respect to the nuclei exchange, as this operation leads to the configuration that is different from the initial one. In this case no missing rotational levels or any statistical weights of their occurring is expected.

**(e) Dipolar transition selection rules for helium dimer**

The first and general selection rule, valid for any atomic system, concerns the quantum number  $J$  of the total angular momentum:

$$\Delta J = 0, \pm 1 \text{ with the restriction } J = 0 \nrightarrow J = 0. \quad (2.40)$$

Selection rules of dipolar transition results from the properties of dipole moment operator which is the function of electrons coordinates  $\hat{d} = \sum e_i \hat{r}_i$  and therefore is antisymmetric to the reflection at the origin and at any plane through the internuclear axis. The matrix element of the dipole moment :

$$\int \Psi^{i*} \hat{d} \Psi^f dr_e \quad (2.41)$$

is non-zero only if the value under the integral is independent (i.e. does not change the sign) of any transformation of coordinates. This occurs when one of the total wave functions describing the  $i$  or  $f$  states between which the transition occurs is symmetric and the other is antisymmetric in respect to the reflection at the origin and at any plane through the internuclear axis. From this and previous discussion about the symmetries, transition rules results:

*the positive terms combine only with the negative and vice versa:*

$$+ \leftrightarrow -, \quad + \leftrightarrow +, \quad - \leftrightarrow - \quad (2.42)$$

*the even (g) electronic states combine only with the odd (u)*

$$g \leftrightarrow u, \quad g \leftrightarrow g, \quad u \leftrightarrow u \quad (2.43)$$

$\Sigma^+$  state cannot combine with  $\Sigma^-$ :

$$\Sigma^+ \leftrightarrow \Sigma^+, \quad \Sigma^- \leftrightarrow \Sigma^-, \quad \Sigma^+ \leftrightarrow \Sigma^-, \quad (2.44)$$

while both  $\Sigma^+$  and  $\Sigma^-$  combine with  $\Pi$  state.

For the states with defined quantum number  $\Lambda$  (valid for Hund's case (a) & (b) ) there is the selection rule:

$$\Lambda = 0, \pm 1 \quad (2.45)$$

Because the dipolar moment operator does not change its sign when the nuclei of homonuclear molecule possessing the spin are interchanged:

*only symmetric terms can combine with symmetric and antisymmetric only with antisymmetric*

$$s \leftrightarrow s, \quad a \leftrightarrow a, \quad s \leftrightarrow a \quad (2.46)$$

As for atoms, for Hund's case (b) where the resultant spin  $S$  is defined, the transition rule for corresponding quantum number is:

$$\Delta S = 0, \quad (2.47)$$

that connects only the states with equal multiplicities.

When both states between which possibility of transition occurrence is considered are within Hund's case (b), the following rule holds for the quantum number  $N$  of the total angular momentum apart from spin:

$$\Delta N = 0, \pm 1, \quad (2.48)$$

with restriction that:  $\Delta N = 0$  is forbidden for  $\Sigma \leftrightarrow \Sigma$  transitions.

On the value of  $\Delta N$  the designation of the transitions relies, so that: each transition with  $\Delta N = 0$  belongs to so called  $Q$  branch with  $\Delta N = -1$  to  $P$  branch and with  $\Delta N = 1$  to  $R$  branch. Additionally information about the value of  $N''$  (value of rotational quantum number  $N$  in the bottom state of the transition; for the top state it is marked as  $N'$ ) is given next to the designation of the branch:  $Q(N'')$ ,  $P(N'')$ ,  $R(N'')$ . This formalism of bottom '' and top ' levels of the transition designation extends also to the other quantum numbers describing the states as well as molecular rotational and vibrational constants (i.e.,  $B_e''$ ,  $B_e'$ ,  $\omega_e''x_e''$ ,  $\omega_e'x_e'$ ,  $\alpha_e'$  etc.).

#### (f) $a^3\Sigma_u^+ \rightarrow e^3\Pi_g$ transition details for $\text{He}_2$

The analysis of the Fig.2.4 and 2.5 together with the transition rules for helium molecule as described in paragraph 2.1.3 (e) leads to conclusion that each transition described by  $\Delta N$  value ( $P(N'')$ ,  $Q(N'')$ ,  $R(N'')$ ) has several components with different  $J''$  and  $J'$  combinations preserving the relation (2.34) and selection rule (2.40).<sup>1</sup> These are the fine structure of the line components and, as mentioned earlier 2.1.2(b), are beyond the resolving power of the experiment due to absorption line Doppler and collisional broadening. It is the same order as the fine structure splittings of the components and additional broadening and distortion of the lines is thus possible. As a consequence, all the transitions occurring from a common  $N''$  rotational level within one value of  $\Delta N$  will be treated as a single line without entering into its fine structure details. This approach will simplify the identification of the absorption lines by comparison with the only reference [DR50] for  $^3\text{He}_2$  as well as with [BG71] for  $^4\text{He}_2$  ( $\nu' (= 0) \rightarrow \nu'' (= 0)$ ) vibrational band transition of  $a^3\Sigma_u^+ - e^3\Pi_g$  on which the 465 nm laser wavelength calibration is based on. It will also give a possibility of using well known dependencies for the energies of the rotational levels eq.(2.22b) together with the proper statistics to obtain their population and correlate it with measured laser transmission values. Having that in mind for  $^4\text{He}_2$  only odd- $N''$  numbered transitions  $P$ ,  $Q$ ,  $R$  are expected in the  $a^3\Sigma_u^+ - e^3\Pi_g$  spectrum with the lack of  $P(1)$  due to absence of  $N' = 0$  rotational level in the  $e$  state. In case of  $^3\text{He}_2$  both even and odd  $N''$  numbered transitions are expected as well as  $R(0)$  transition. Due to statistics resulting from non-zero  $I = \frac{1}{2}$  nuclear spin of  $^3\text{He}$  atoms discussed in paragraph 2.1.3(b) there is 3:1 alternation of the spectral lines intensities (even- $N''$  to odd- $N''$  numbered lines). For the

<sup>1</sup>In case of resolved transition occurring from the fine structure  $J''$  sublevels the designation of the transitions is different. Instead of notation i.e.  $Q(N'')$  (meaning  $\Delta N(N'')$ ), the following is used:  $^{\Delta N}\Delta J_{F',F''}(N'')$ .  $\Delta N$  and  $\Delta J$  are substituted by respective  $P, Q, R$  letter and when  $\Delta N = \Delta J$  the letter corresponding to  $\Delta N$  is omitted in the superscript.  $F'$  and  $F''$  can take value of 1, 2 or 3 what means that  $J = N + 1$ ,  $J = N$ , or  $J = N - 1$  for the upper ' or the lower '' state respectively.

mixture helium molecule  $^3\text{He}$ - $^4\text{He}$  any absence or intensities alternation of the lines is expected as statistics for homonuclear molecule is not valid here anymore.

## 2.2 Intensities of the rotational lines of $a^3\Sigma_u^+$ (0)- $e^3\Pi_g$ (0) transition and molecular densities

The information about the molecular dynamics (formation, decay) can be obtained by quantitative measurements on the molecular spectrum, however the absolute density of the molecular species can be obtained only in the absorption techniques. Making use of the laser setup described in 3 the measurements of the laser light transmission through the absorber - helium molecules formed in the plasma - is possible. Assuming the linear regime of absorption (no dependency of absorption on electromagnetic wave intensity), according to eq. (B.5) the intensity  $I_{if}(\vec{r})$  change of the laser light propagating on the distance  $dz$  along the  $z$  axis through the absorber -  $n_M^i(\vec{r})$  - (number density) molecules in the initial  $i$  state of the transition to the  $f$  state is given by:

$$\frac{dI(\vec{r})}{dl} = -I_{if}(\vec{r})\sigma_{if}(\omega)n_M^i(\vec{r}), \quad (2.49)$$

where the dependency of the intensity change and number density on the spatial coordinates  $\vec{r}$  in the laser beam frame is given explicitly.  $\sigma_{if}$  is the cross section for the transition from the initial  $i$  to the final  $f$  state and depends on the transition frequency  $\omega_{fi}$ .

### (g) Distribution of molecules among rotational levels

Equation (2.49) gives an information about the population of only the initial state of the transition which, for a given wavelength of exciting light, is the number density of single rotational sublevel described by the  $N''$  number. In fact, the interesting value is the total number density  $N_M$  of molecules that are distributed along the laser beam path. Thus, it can be written that:

$$n_M^i = N_M s^i(n'', v'', N'', p), \quad (2.50)$$

where  $n'', v'', N'', p$  are the principal quantum number, vibrational and rotational quantum numbers as well as the parity of the initial transition sublevel respectively. For the case of  $\Sigma$  state in Hund's coupling (b), after [Tat67], the distribution function  $s^i(n'', v'', N'', p)$  is given by:

$$s^i(n'', v'', N'', p) = \frac{2\phi(2S'' + 1)(2N'' + 1) \exp\left[\frac{-hc}{kT}\left(T_e + G(v'') + F(N'')\right)\right]}{Q_{el}Q_{vib}Q_{rot}}, \quad (2.51)$$

where  $h, c, k, T$  are Planck constant, speed of light in vacuum, Boltzmann constant and the temperature. The vibrational  $G(v'')$  and rotational  $F(N'')$  energies are given by eq. (2.22a) and (2.22b) respectively.  $Q_{el}$ ,  $Q_{vib}$  and  $Q_{rot}$  are the electronic, vibration and rotation partition functions given by eq.(2.52a) -(2.52c):

$$Q_{el} = \sum_{\text{all states}} (2S'' + 1) \exp\left(-\frac{hc}{kT}T_e\right), \quad (2.52a)$$

$$Q_{vib} = \sum_{v=0}^{v_{max}} \exp\left(-\frac{hc}{kT}G(v'')\right), \quad (2.52b)$$



$$Q_{rot} = \frac{kT}{hcB_v} \text{ (for temperatures } > 0^\circ\text{C)}. \quad (2.52c)$$

The  $\phi$  parameter of eq.(2.51), that is resultant of a sublevel parity  $p$  is given by:

- for homonuclear molecules
  - with spinless nuclei molecules ( $^4\text{He}_2$ ):  $\phi = 1$
  - with odd-half-integral spin nuclei molecules ( $^3\text{He}_2$ ,  $I = \frac{1}{2}$ ):
 
$$\phi = \frac{I}{2I+1} = \frac{1}{4} \text{ in case of } s \text{ levels}$$

$$\phi = \frac{I+1}{2I+1} = \frac{3}{4} \text{ in case of } a \text{ levels.}$$
- for heteronuclear molecules:  $\phi = \frac{1}{2}$

According to [Tat67] the series given by eq. (2.52b) should be terminated at  $\nu_{max}$  which is the greatest integer value less than or equal to  $\nu = \frac{\omega_e}{2\omega_e x_e} - \frac{1}{2}$ .

#### (h) Absorption cross-section for $a^3\Sigma_u^+ - e^3\Pi_g$ transition for $^3\text{He}_2$ and $^4\text{He}_2$ molecules

Important in terms of absolute the  $N_M$  value determination from absorption measurements is the absorption cross-section  $\sigma_{if}(\omega)$  for the transition between rotational levels ( $i$  - initial, lower " - in case of absorption;  $f$  final, upper ' - in case of absorption) of considered electronic states. The angular transition frequency ( $\omega$ ) dependence of  $\sigma_{if}$  is explicit as well as hidden in the normalized absorption line profile function  $w(\omega - \omega_{fi})$  that contains the Doppler and collisional broadening contributions (discussed in details in Appendix B), where the relation between cross-section and the line strength  $S_{fi}$  is given by eq. (B.6):

$$\sigma_{if}(\omega) = \frac{1}{g_i} \frac{\pi\omega_{if}}{3\epsilon_0\hbar c} S_{fi} w(\omega - \omega_{fi}), \quad (2.53)$$

The degeneracy factor  $g$  that appears is, for the molecular state, given by:

$$g = (2 - \delta_{0,\Lambda})(2S + 1) \quad (2.54)$$

According to the relation (B.7)  $S_{fi} \propto |\int \Psi^f \hat{d} \Psi^i d\tau|^2$ . Taking into account the Born-Oppenheimer approximation which gave the eq. (2.7) and (2.37) the integral can be written as:

$$d_{fi} = \int \Psi_e'^* \frac{1}{r} \Psi_v'^* \Psi_r'^* \hat{d} \Psi_e'' \frac{1}{r} \Psi_v'' \Psi_r'' d\tau \quad (2.55)$$

After [Her50], division of the electric moment  $\hat{d}$  into the sum of parts depending on the electrons  $\hat{d}_e$  and depending on the nuclei  $\hat{d}_n$  can be performed. Separation of electrons' and nuclei spatial coordinates  $d\tau = d\tau_e r^2 \sin\vartheta dr d\vartheta d\varphi$ , where  $r$  is internuclear distance and  $d\tau_e$  is the volume of the space of the electronic coordinates, together with the orthogonality condition of the wave functions describing different electronic states  $\int \Psi_e' \Psi_e'' d\tau_e = 0$ , results in:

$$d_{fi} = \int \Psi_e'^* \hat{d}_e \Psi_e'' d\tau_e \int \Psi_v'^* \Psi_v'' dr \int \sin\vartheta \Psi_r'^* \Psi_r'' d\vartheta d\varphi \quad (2.56)$$

The first integral is so called electronic transition moment  $r_e$  which square is proportional to the electronic transition probability. The square of the second integral:  $|\int \Psi_v'^* \Psi_v'' dr|^2 \equiv S(v', v'')$  is the Franck-Condon factor, for which the following sum rule is valid:

$$\sum_{v'} S(v', v'') = \sum_{v''} S(v', v'') = 1 \quad (2.57)$$

The summation in the third integral of (2.56) is taken over the  $\vartheta$  and  $\varphi$  angles only, on which the rotational part of the wavefunction depends (sec.2.1.3(a)), that is described by rotational quantum numbers  $J$ . Thus, for a given  $i$  and  $f$  states, the set of  $J'', J'$  quantum numbers are given, and the integral takes the constant value. Its square is denoted as:  $\left| \int \sin \vartheta \Psi_r'^* \Psi_r'' d\vartheta d\varphi \right|^2 \equiv S_{HL}(J', J'')$

After [Tat67], in case of the molecule, the line strength  $S_{fi}$  of a single line is given by:

$$S = \frac{S_{HL}(J', J'') S(v', v'') r_e^2}{(2 - \delta_{0,\Lambda})(2S + 1)(2J + 1)} \quad (2.58)$$

$S_{HL}$  is the Hönl-London coefficient given for each of P,Q,R-form branches of  $^3\Pi$ (Hund case b)— $\Sigma$  transition in the Table 5 of [Sch64]. These coefficients are expressed in terms of the  $J''$  value of the fine structure levels, however, they can be given in terms of  $J'$  number of the excited state, using simple substitution from relations between  $J''$  and  $J'$  occurring for P, Q and R branches.

In the denominator of eq. (2.58)  $S$  and  $J$  are substituted by  $S'$  and  $J'$  or  $S''$  and  $J''$  when  $S_{HL}$  is expressed in terms of  $J'$  or  $J''$  respectively

The Hönl-London coefficients has to follow sum rules:

- for transitions having the same upper ( $J'$ ) or lower ( $J''$ ) levels the Hönl-London factors sum up to  $(2J' + 1)$  or  $(2J'' + 1)$  respectively
- sum of Hönl-London factors for all the branches in a band is  $(2 - \delta_{0,\Lambda})(2S + 1)(2J + 1)$  when the factors are expressed in terms of  $J$ , or  $(2 - \delta_{0,\Lambda})(2S + 1)(2N + 1)$  when they are expressed in terms of  $N$ .

Summing up the  $S_{HL}$  factors from [Sch64] for common  $J''$  values ( $J'' = N'' + 1$ ,  $J'' = N''$  or  $J'' = N'' - 1$ ) results in the value of  $\frac{1}{3}(2J'' + 1)$  that means - each Hönl-London factor given in the reference shall be multiplied by the factor of 3. Then, summing up  $S_{HL}$  of all possible branches P,Q,R of the band, value  $3(2J'' + 1)$  is achieved, what agrees with summing rule ( $S=1$  for the triplet states that are under consideration,  $\delta_{0,0} = 1$ ). Also the summing of coefficients expressed in terms of  $N''$  value leads to expected value of  $3(2N'' + 1)$ . For the case when no fine structure resolving of the spectral lines is considered, the Hönl-London factors can be arranged into the three groups corresponding to  $\Delta N = -1, 0$  or  $1$  values (P, Q, R branches in terms of  $N$  value change). Expressing the factors in terms of  $N''$  and summing all the factors in each group leads to the three Hönl-London coefficients for the  $P(N'')$ ,  $Q(N'')$  and  $R(N'')$  transitions:

$$\text{for } P \text{ branch: } S_{HL} = \frac{3}{2}(N'' - 1) \quad (2.59a)$$

$$\text{for } Q \text{ branch: } S_{HL} = \frac{3}{2}(2N'' + 1) \quad (2.59b)$$

$$\text{for } R \text{ branch: } S_{HL} = \frac{3}{2}(N'' + 2) \quad (2.59c)$$

The sum of abovegiven coefficients is equal to  $3(2N'' + 1)$  as it is at the same time the sum for all the transitions from common  $N''$  but also the sum of all the branches in the band. Using the Hönl-London coefficients expressed in terms of  $N''$ , the line strength  $S$  can be calculated for  $P(N'')$ ,  $Q(N'')$  and  $R(N'')$  transitions using formula (2.58) in which  $J$  is substituted by  $N''$ .

However, for completeness of  $S$  calculation, the value of product of  $r_e^2$  and  $S(v', v'')$ , named band strength, is needed. If the lifetime  $\tau_f$  of the excited rotational level  $f$  (described by certain  $N'$  and  $v'$  numbers) is known, its reciprocal can be decomposed into the sum of Einstein coefficients for spontaneous emission ( $A_{fi}$ ) from common  $f$  level to the possible lower state  $i$  (described by  $N''$  and  $v''$ ):

$$\sum_i A_{fi} = \frac{1}{\tau_{f(N', v')}} \quad (2.60)$$

Each of  $A_{fi}$  Einstein coefficients can be expressed in term of  $S_{fi}$  using relation:

$$A_{fi} = \frac{1}{g_f} \frac{2\omega_{fi}^3}{3h\epsilon_0 c^3} S_{fi} \quad (2.61)$$

After [MN94], approximation for every transition within one  $v' - v''$  band:  $\omega_{fi} \approx \omega_{v', v''}$  can be applied in equations: (B.6) and (2.61). The  $\omega_{v', v''}$  is the mean angular frequency of all the transitions within the band, normally substituted as a band origin (frequency corresponding to fictitious Q(0) transition of the band). With this approximation the (2.60) and (2.61) result in:

$$\frac{1}{\tau_{f(N', v')}} = \frac{1}{g_f} \frac{2}{3h\epsilon_0 c^3} \sum_{i(N'', v'')} \omega_{v', v''}^3 \frac{S_{HL}(N'_f, N''_i) S(v', v'') r_e^2}{(2 - \delta_{0, \Lambda'}) (2S' + 1) (2N' + 1)} \quad (2.62)$$

For all the transitions between rotational levels of upper and lower states within one single vibrational band, the value of  $S(v', v'') r_e^2$  is a constant. The sum of the  $S_{HL}(N'_f, N''_i)$  coefficients over  $i$  levels translates into the sum of Hönl-London coefficients for all possible transitions occurring from common  $N'$  level, which is, as before, the sum of the factors for all the possible branches in the band and equal to:  $(2 - \delta_{0, \Lambda'}) (2S' + 1) (2N' + 1)$ . As the consequence it can be written:

$$\frac{1}{\tau_{f(N', v')}} = \frac{1}{g_f} \frac{2}{3h\epsilon_0 c^3} r_e^2 \sum_{i(v'')} \omega_{v', v''}^3 S(v', v'') \quad (2.63)$$

According to the expression (2.63) all rotational levels within one vibrational level have the same radiative lifetime. This is in agreement with what is reported by [SPB82, GGMD76].

After [NTSL94] where the indication of the value of Franck-Condon for 0-0 band is given as  $S(0, 0) = 0.95$ , considering eq. (2.57), the de-excitation from  $e^3\Pi_g (v = 0)$  occurs almost totally to the lowest vibrational level of  $a^3\Sigma_u^+$ . Moreover, the transition energy of any other band  $0 - v'' \neq 0$  is lower than in case of 0-0 band, thus the associated angular frequencies  $\omega_{v', v'' \neq 0}$  are lower, what decreases, anyhow poor, contribution of  $S(v', v'' \neq 0)$  to the overall lifetime of  $e^3\Pi_g (v = 0)$ . This justifies the following approximation:

$$\frac{1}{\tau_{f(N', v'=0)}} \approx \frac{1}{g_f} \frac{2\omega_{0,0}^3}{3h\epsilon_0 c^3} r_e^2 S(0, 0) \quad (2.64)$$

The value of  $e^3\Pi_g (v = 0)$  lifetime is reported in [NTSL94] and amounts to:  $\tau_{v=0} = 67s$ . Using this value along with relations: (B.6), (2.58) and (2.64) as well as with appropriate

value of Hönl-London coefficients  $S_{HL}$ , allow calculation of the absorption cross-section  $\sigma_{if}$  essential for absolute molecular density calculation from absorption measurements. The reference [NTSL94] from which the radiative lifetime of  $e^3\Pi_g$  has been taken focuses also on the measurement of the lifetimes in the two other excited molecular  $d$  and  $f$  states. Their investigations are performed using both the absorption and emission methods. In the former case the transmission of the pulse dye laser is recorded after single pass through 1 m long cell filled with  $^4\text{He}$  gas at 3 bar excited with electron beam pulses in the room temperature conditions. The combination of the results obtained in absorption measurements as well as saturation (the transmission of the laser was measured in function of the laser intensity providing saturation curve) allowed proper choice of the absorption cross-section value and the density of metastable molecule values giving a best agreement with their experimental data when the differential rate equation for the transmitted laser intensity and molecular density were considered.

# Chapter 3

## Blue laser setup

Absorption studies on the helium metastable state performed on chosen transition  $a^3\Sigma_u^+(0) - e^3\Pi_g(0)$  requires the source of the laser radiation at the wavelength about 465 nm. The absorption measurements on the molecules to study their contribution to the laser enhanced relaxation, planned in parallel to the Metastability Exchange Optical Pumping process, does not require high laser powers that could perturb the helium plasma conditions. Values of order of tens or hundreds  $\mu\text{W}$  are sufficient for the absorption measurements with good SNR. Important characteristics of the required laser are its wavelength tuning range and spectral width so that the part of the spectrum containing several rotational components of  $a-e$  transition can be observed. According to [DR50, BG71] the tuning range of 2 nm is sufficient to observe several Q branch components as well as single R and P branch lines. Expected Doppler broadening for the helium molecule of about 3 GHz at the room temperature requires low spectral width of the laser source (several MHz) to allow good resolution of performed measurements. At the time of planning the investigation on the molecules in helium plasma in MEOP conditions such laser source was not commercially available. Well known nonlinear process of Second Harmonic Generation (SHG) gives the possibilities of obtaining laser beam of various wavelengths not available directly from the semiconductor laser sources, that recently are very popular due to their compactness and various spectral characteristics (e.g. narrow bandwidth, monomode emission). Generation of the laser light at 465 nm requires a laser diode working at the wavelength of 930 nm in infra-red (IR) range for SHG process to be performed and an appropriate nonlinear medium. Among the best commercially available efficient nonlinear medium providing wide phase-matching bandwidth are periodically poled  $\text{KTiOPO}_4$  (PP-KTP) crystals. They are often chosen for their properties such as high value of the effective nonlinear coefficient  $d_{eff}$ , operating around room temperature conditions at visible wavelengths, high flexibility of choice in the grating period suited to the targeted wavelength as well as good quality and reasonable price. Typical conversion efficiencies normalized to the crystal length  $l$  ( $\eta \equiv \frac{P_{out}}{lP_{in}^2}$ ) are on the order of 2.8 %  $\text{W}^{-1}\text{cm}^{-1}$  at 461 nm reported in [TZL05] for SHG and 2.2 %  $\text{W}^{-1}\text{cm}^{-1}$  at 492 nm given in [JSW<sup>+</sup>04] for Sum Frequency Generation (SFG). Thus one may expect expects second harmonic output power up to 300  $\mu\text{W}$  for input power  $P_{in} = 100 \text{ mW}$  in a 1 cm long crystal. According to what has been said before, this amount of power would be sufficient for the probe beam source. The setup had been designed and necessary components had been acquired before the Author has started to work on the project. At that time 930 nm emitting diode had not been available or later had shown up on the market providing only 40 mW of output power, while, for other laser diodes emitting in the vicinity of 930 nm (namely 923 nm

and 937 nm) 100 mW of maximum power each was specified. Hence, reaching desired 465 nm wavelength with 923 and 937 nm diodes could be achieved with SFG. The advantage of the both wavelength proximity (14 nm) is that the conditions here are very close to the SHG case and the same optics (suitable for this infra-red wavelength) can be used (crystal, mirrors), however the optical cavity design has to be planned so that these two beams will be overlapped before focusing into the small waist inside the nonlinear crystal. Similarity of SHG and SFG in this case facilitates the theoretical description of the latter process allowing easier comparison with obtained results. After the setup had been assembled by the Author, its rough performance and efficiency characterization, that was not the main goal in this work, has been performed. In this chapter the basics of up-conversion process theory is introduced providing background for estimation of efficiency and operating parameters tolerances. The construction details are then described emphasizing the original design of the laser cavity by Pierre-Jean Nacher, where a set of 3 prisms is used for beams overlapping. Comparison and discussion of experimental results and theoretical predictions of the laser operating parameters are given.

### 3.1 Second Harmonic Generation in PP-KTP

The nonlinear processes rely on the presence of higher than linear terms in the response of the media to the applied electric field  $E(z, t)$  associated with propagating electromagnetic waves. Induced electric polarization  $P(z, t)$  resulting from the spatial separation of the centers of positive and negative charges of the atoms is given by:

$$\mathcal{P}(z, t) = \epsilon_0 \chi^{(1)} E(z, t) + \epsilon_0 \chi^{(2)} [E(z, t)]^2 + \dots, \quad (3.1)$$

where  $\chi^{(n)}$  is the  $n$ -order expansion of electric susceptibility of the media,  $\epsilon_0$  is the permittivity of free space.

In general the field  $E(z, t)$  may be resultant of more than one electric field components related to different, propagating together in the same  $z$  direction, electromagnetic waves (called fundamentals) of frequency  $\omega_i$  and wave vector  $k_i$ , where  $i = 0, 1, 2, \dots$ , according to the number of monochromatic waves. For a single electromagnetic wave at frequency  $\omega_0$  interacting with a uniform nonlinear media, oscillation of  $\mathcal{P}(z, t)$  with doubled fundamental frequency - second harmonic:  $2 \cdot \omega_0$  occurs. Oscillating electric dipole is a source of the wave at the oscillation frequency - here at the second harmonic. To ensure that the generated second harmonic waves in all points along the nonlinear interaction path of the fundamental beam will add up constructively, certain phase relation has to be fulfilled, given by the equation:

$$\Delta k^{SHG} = k_b - 2k_0 = 0 \Rightarrow \Delta k^{SHG} = 2\pi \frac{n_b}{\lambda_b} - 2\pi \frac{2n_0}{\lambda_0} = 0, \quad (3.2)$$

where  $k_0$  and  $k_b$  are respectively the fundamental and generated harmonic wave vectors,  $n_b$  and  $n_0$  are proper refractive indexes in the nonlinear medium,  $\lambda_b$  and  $\lambda_0$  are proper wavelengths. The equation (3.2) is called phase-matching condition for SHG.

For the case of two electromagnetic waves, oscillation of  $\mathcal{P}(z, t)$  occurs with frequency being a resultant of several components: the second harmonics ( $2\omega_1$  and  $2\omega_2$ ), frequency sum ( $\omega_1 + \omega_2$ ) and frequency difference ( $\omega_1 - \omega_2$ ). A relation between the fundamental wave vectors  $k_1$ ,  $k_2$  and wave vector of generated harmonic  $k_b$ , called phase-matching condition for SFG (eq.(3.3)), has to be fulfilled to maximize the generation of sum-frequency component and prevent that of the components at other harmonic frequencies. In short, phase matching ensures that the wave at the frequency of interest (here, the sum of the two fundamental frequencies), locally generated in one section of the crystal, is in phase with the waves of the same frequency generated in the other crystal sections and adds up constructively with all of them. In the plane wave approximation, the phase-matching condition for SFG can be written as:

$$\Delta k^{SFG} = k_b - (k_1 + k_2) = 0 \quad (3.3)$$

Having the two fundamental wavelengths different only by about 14 nm, it is expected that the refractive indexes are nearly equal ( $n_1 \approx n_2$ , what is confirmed by the computations on the basis of Appendix C). We could set then both  $\lambda_1$  and  $\lambda_2$  as their common average value of  $\lambda_1 \approx \lambda_2 \approx \lambda_{av} = \frac{\lambda_1 + \lambda_2}{2}$ . The same with the refractive index value:  $n_1 \approx n_2 \approx n_{av} = \frac{n_1 + n_2}{2}$ .

Therefore, the equation (3.3) reduces to:

$$\Delta k^{SFG} \approx 2\pi \frac{n_b}{\lambda_b} - 2\pi \frac{2n_{av}}{\lambda_{av}} = k_b - 2k_{av} = 0 \quad (3.4)$$

We see then (identifying:  $\lambda_{av}$  as  $\lambda_0$ ,  $n_{av}$  by  $n_0$  and  $k_{av}$  by  $k_0$  from eq.(3.2)), that the properties of our laser setup components brings us to the approximation of the SFG process by the SHG well described in the literature. This approach should be sufficient for the rough estimation, analysis and evaluation of the experimental laser performance, that was not the main goal of this work, but had to be made to assure proper and fully controlled use of the laser device in further absorption measurements.

Both relations (3.3) and (3.4) are valid for *plane wave* approximation for the incident beams. For focused beams optimal phase-matching is obtained for  $\Delta k^{SFG} \neq 0$  as well as  $\Delta k^{SHG} \neq 0$  [BK68]. However, optimal wave vector differences  $\Delta k$  the corresponding final values are very small (see below - section 3.1.1). In practice, the phase-matching condition reduces to:  $2n_b - 2n_{av} = 0$  for the SHG.

### 3.1.1 Quasi-phase-matching

Fulfilling the phase-matching condition is problematic, as common nonlinear materials exhibit normal dispersion ( $n_b > n_1, n_2$ ). Some crystals, however, exhibit the birefringence along their crystallographic axes, that is, if the wave is polarized along one axis (i.e. *b*-axis) it travels slower than the wave which is polarized along other axis (i.e. *c*-axis). Thus, when the polarization of the fundamental wave is constrained to the "slow" axis *b*, and the polarization of second harmonic along the "fast" axis *c*, the phase velocity due to dispersion can be compensated for by the phase velocity difference due to birefringence. This is so called birefringence phase-matching and is sensitive not only to the fundamental wavelength but also on the crystal temperature and orientation in respect to the direction of waves propagation and polarization. So-called nonlinear coefficient  $d_{eff}$  is here a resultant of the nonlinear coefficients  $d_{ij}$  values related to the second order electric susceptibility tensor  $\chi^{(2)} \equiv \chi_{ijk}^{(2)}$  through equation  $2 \cdot d_{il} = \chi_{ijk}^{(2)}$  (index *l* is defined by a pair of indexes *jk*; indexes *ijk* refer to polarization directions of generated harmonic and fundamental waves respectively - see references [WPRN03, BK68] for further details). The form of  $d_{eff}$  dependency on  $d_{il}$  values results from the geometry of the interaction between nonlinear media and interacting fields, namely on chosen crystal material and its intrinsic symmetry properties as well as chosen polarization directions of these fields, providing generation of higher order harmonics. This method has several limitations among which there is insufficient birefringence of the crystal material to provide phase-matching at the wavelength of interest or the nonlinearity, expressed as a value of nonlinear coefficient  $d_{eff}$ , associated with this type of phase-matching is too low to be useful.

Very rapidly, people have realized that good results could be obtained using periodically poled crystal and achieving so-called quasi-phase-matching. It relies on the artificial structuring of the nonlinear material, so that the crystal is divided to  $N = \frac{l}{\Lambda}$  segments, called domains, in which the nonlinear coefficient, e.g. for PP-KTP  $d_{33}$  (that is related to second order electric susceptibility third-rank tensor  $d_{33} = \frac{1}{2}\chi_{333}^{(2)}$ ) alternately changes the sign - schematic drawing is given on the fig. 3.1. For PP-KTP the periodic modulation of  $d_{33}$  is usually chosen as its value is the highest of all the non-linear coefficients of KTP crystal, providing the highest nonlinear response of the media in this case.  $\Lambda$  is called the grating period (the length of the domain), *l* is the crystal length. Periodically change of  $d_{33}$  every distance of  $\Lambda/2$ , adapted to desired nonlinear process and wavelength of interest, prevents acquiring, by already generated and propagating in the material harmonic wave, more than  $\pi$  factor of the phase difference with locally generated harmonic. In this way amplitude of generated wave is accumulated along the



whole crystal length.

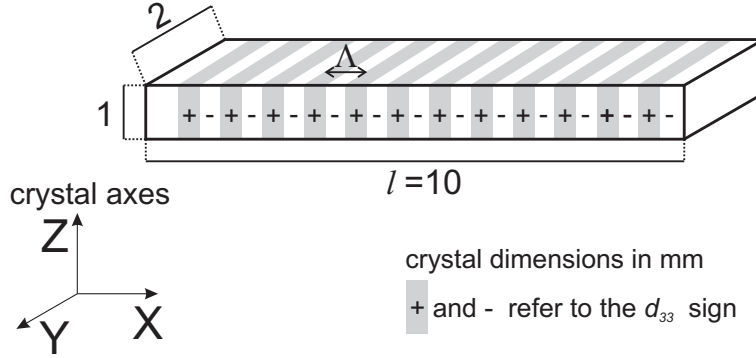


Figure 3.1: Schematic drawing of PP-KTP crystal. Periodical (with the period  $\Lambda$ ) change of the sign of the coefficient  $d_{33}$  has been indicated with white and gray stripes; the dimensions of the crystal are given in millimeters; crystal axes are marked according to the discussion in the text.

In this case the phase-matching condition given by the equation (3.4) must be replaced by so-called quasi-phase-matching (QPM) condition:

$$\frac{\Delta k_{QPM}^{SHG}}{2\pi} = \frac{n_b}{\lambda_b} - \frac{2n_{av}}{\lambda_{av}} - \frac{1}{\Lambda} = 0 \quad (3.5)$$

As stated before, the further consideration will base on the SHG theory and the eq.(3.5) can be rewritten in more convenient way in terms of  $\lambda_{av} \approx 2\lambda_b$  only:

$$\frac{\Delta k_{QPM}^{SHG}}{2\pi} = \frac{2(n_b - n_{av})}{\lambda_{av}} - \frac{1}{\Lambda} = 0 \quad (3.6)$$

From now on, the simpler notation  $\Delta k_{QPM}^{SHG} \equiv \Delta k_{QPM}$  will be used.

As the spatially modulated nonlinear coefficient is  $d_{33}$  here, in order to obtain nonlinear response on the second harmonic, the incident beam (in the experiment - the two beams) polarization direction has to be parallel to the Z-axis of the crystal. In this way, for SFG case, the highest available nonlinear coefficient can be used for both fundamental beams, what was not possible for birefringent phase matching case.

Of course, spatial periodicity of  $d_{33}$  coefficient along the beams path has to be taken into account when for example the efficiency of a non-linear conversion is to be considered. According to expectations there is an effective value of such non-linear coefficient for quasi-phase matching process and unfortunately is commonly noted as  $d_{eff}$ . This notation can be confusing with the  $d_{eff}$  values valid for birefringent phase matching, however few references (e.g. [WPRN03]) use other designation, namely  $d_{OPM}$ . Therefore in this work, also  $d_{eff}$  notation will be sustained allowing further results comparison with reference values without the need of additional comments.

For uniform periodic modulation the nonlinear coefficient value that has to be used is given by:

$$d_{eff} = \frac{2}{\pi} d_{33} \quad (3.7)$$

The fixed value of crystal's  $\Lambda$  determines the way in which the output second harmonic wavelength can be varied - through a change of the incident wavelength. However, crystal's temperature needs to be regulated to maintain the condition of quasi-phase-matching eq.(3.6). The relevant temperature dependency lies in the refractive indexes of the fundamental and second harmonic, namely its Z-axis component  $n^z$  as all the beams are polarized in one Z axis (see also fig.3.6, where z axis of the drawing has been chosen to be parallel with Z axis of the crystal). The values of  $n^z$  can be obtained for a given material and known wavelength as well as the material temperature (here the crystal temperature  $T_{cr}$ ) using Sellmeier's equation with coefficients proper for the certain material. Detailed equation as well as the parameters from [KT02] to [FBP<sup>+</sup>00] are given in the Appendix C. Using the averaged value of those obtained with equation parameters from references given, at 20°C :  $n_b^z(465 \text{ nm}) = 1.9172$  and  $n_{av}^z(930 \text{ nm}) = 1.8362$ . With  $\lambda_b = \frac{\lambda_{av}}{2} = 465 \text{ nm}$  and these refractive indexes, eq.(3.6) in the plane wave approximation provides rough grating period value in the way that:

$$\Lambda_{QPM} = \frac{\lambda_{av}}{2(n_b^z - n_{av}^z)} = 5.74 \mu m \quad (3.8)$$

This value is close to the specified for the crystal mounted in our experimental setup given in subsection 3.2.1.2. For the simplicity of notation, in further considerations it will be used as follows:  $n_b^z(T_{cr})=n_b$  for generated harmonic and  $n_{av}^z(T_{cr})=n_{av}$  for the fundamental wavelength.

### 3.1.2 Conversion efficiency

The estimation of the efficiency of SFG, in which two Gaussian laser beams with wavelengths  $\lambda_1 \approx \lambda_2$  and power  $P_1$  and  $P_2$  respectively are focused into the nonlinear crystal of length  $l$ , approximated by the SHG, could be performed using ready formula as given in [WPRN03,BK68]. In this way we assume, that the beams propagate along the same axis (are perfectly overlapped) as well as the focus and the waist size in the focal point are the same for both fundamental beams. However, one has to be aware that the direct substitution of average fundamental wavelength ( $\lambda_0 \rightarrow \lambda_{av}$ ) and refractive index values ( $n_0 \rightarrow n_{av}$ ) to the equation of the SHG efficiency will not bring correct value. If one would performed such calculation the result would be 4 times too low.

The definitions of the SHG and SFG efficiencies in terms of generated harmonic power  $P_b$  and fundamental ones  $P_0$  (for SHG) and  $P_1, P_2$  (for SFG) are as follows:

$$P_b = \eta_{SHG} \cdot P_0^2 \quad (3.9a)$$

$$P_b = \eta_{SFG} \cdot P_1 P_2 \quad (3.9b)$$

$P_0$  value present in the eq.(3.9a) is a total fundamental beam power. If we assume, what in fact reflects the experimental realization in this work, that  $P_1$  and  $P_2$  fundamental powers of SFG are equal and total fundamental radiation power is  $P_{tot} = P_1 + P_2$  in this case, then  $P_1 = P_2 = \frac{P_{tot}}{2}$ . If so defined  $P_1$  and  $P_2$  powers are substituted to the eq.(3.9b) one obtains:

$$\eta_{SFG} = \frac{4P_b}{P_{tot}^2} \quad (3.10)$$

For SHG approximation of SFG we can substitute  $P_{tot}^2$  by  $P_0$  as a total fundamental beam power. This leads to the relation:  $\eta_{SFG} = 4\eta_{SHG}$

Then, assuming that the two fundamentals and generated harmonic are propagating along the same crystallographic axis (no walk-off<sup>1</sup> angle between the beams) are focused in the middle of the crystal ( $l/2$ ) and are not absorbed inside the crystal, according to discussion above and the references [WPRN03, BK68], the SHG efficiency approximating the SFG process is given by:

$$\eta_{SFG} = \frac{P_b}{P_1 P_2} \approx 4\eta_{SHG} = 4 \frac{16\pi^2 d_{eff}^2}{\epsilon_0 c n_{av} n_b \lambda_{av}^3} l h(\sigma, \xi) \quad (3.11a)$$

$$h(\sigma, \xi) = \frac{1}{4\xi} \left| \int_{-\xi}^{\xi} \frac{\exp(i\sigma(\tau))}{(1 + i\tau)} d\tau \right|^2 \quad (3.11b)$$

In the equations above, the dimensionless parameters  $\xi, \sigma$  and function  $h(\xi, \sigma)$  are defined as follows:

- the  $h(\sigma, \xi)$  is called the *Boyd-Kleinman focusing factor* [BK68].
- $\sigma = -\frac{b\Delta k_{QPM}}{2}$ , called *phase mismatch* parameter
- $\xi = l/b = l\lambda_{av}/(2\pi n_{av} w_0^2)$ , where  $w_0$  is the waist of the focused incident beams (the radius for which the power reaches  $1/e^2$  of the peak value).  $\xi$  is called *focusing strength* parameter

It is also assumed that two incident Gaussian beams have the same value of confocal parameter ( $b = 2\pi n_{av} w_0^2 / \lambda_{av}$ ) and propagate along the same axis being spatially overlapped.

The parameters met in the equation (3.11b) appears in the considerations of the geometrical aspects of the nonlinear conversion process of SHG and SFG. The equation for the SHG efficiency (3.11a) together with definition of Boyd-Kleinman factor and  $\xi$  shows the dependency of  $\eta_{SFG}$  on a square of fundamentals beams waist  $w_0^2$ . That suggests the possibility of  $\eta_{SFG}$  increase more tightly confined the beam is made. This can be reached by focusing the beam inside the nonlinear crystal. However, stronger the beam confinement is, bigger the diffraction effect occurs, reducing the length on which the beam confinement is maintained.

According to [BK68] the maximum value that can be reached by Boyd-Kleinman focusing factor is  $h(\sigma_m, \xi_m) = 1.068$  for  $\xi_m = 2.84$  and  $\sigma_m = 0.576$ . The subscript  $m$  denotes optimized values  $\xi$  and  $\sigma$  providing maximum of the  $h(\sigma, \xi)$  function (phase-matching).

It can be shown straightforwardly, that the function of Boyd-Kleinman focusing factor in eq.(3.11b) is in fact real, with:

$$h(\sigma, \xi) = \frac{1}{\xi} \left| \int_0^{\xi} \frac{\cos(\sigma\tau) + \tau \sin(\sigma\tau)}{1 + \tau^2} d\tau \right|^2 \quad (3.12)$$

For the purpose of this work, a further step can be performed to remove the parametric bound of the integral thus obtaining the finite integral as follows:

$$h(\sigma, \xi) = \xi \left| \int_0^1 \frac{\cos(\sigma\xi u) + \xi u \sin(\sigma\xi u)}{1 + (\xi u)^2} du \right|^2 \quad (3.13)$$

---

<sup>1</sup>If the fundamental beams are not propagating in the crystallographic axis direction, the generated sum-frequency from the latter part of the crystal is spatially shifted in respect to the harmonic generated in the former part - this wave propagates at the angle  $\rho$  relative to the fundamentals and a parameter  $\beta \propto \rho$  appears then in  $h(\sigma, \xi, \beta)$  [BK68]. At the output, the generated beam has no longer Gaussian distribution. In this work, this is not the case, as fundamental beams propagate along one of the crystal axis - the walk-off angle is  $\rho = 0 = \beta$ .

Using the OriginLab Corporation Origin 8.0 SR6 version software and "Fitting Integral Function with parametric limit using NAG Library"<sup>2</sup> the simulation of integral  $h(\sigma, \xi)$  function is possible, to observe the change of the Boyd-Kleinman focusing factor with parameter  $\sigma$  at fixed value of  $\xi$ . In present work it was found useful to present simulation results of both  $h(\sigma, \xi)$  and  $\sqrt{h(\sigma, \xi)}$ , since the latter was used for the experimental fits (see section 3.3.3). The simulation for the  $\xi$  values from 1 to 5 has been shown on graph 3.2

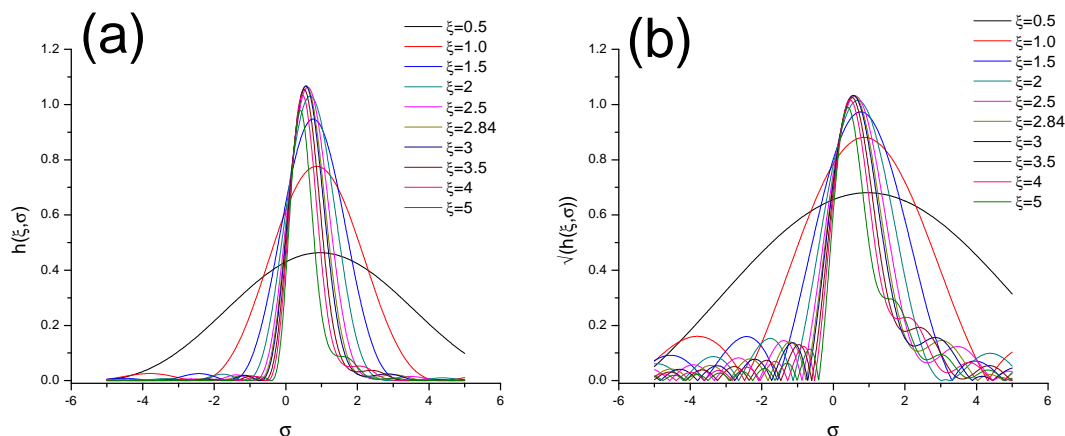


Figure 3.2: Simulated curves of Boyd-Kleinman focusing factor  $h(\sigma, \xi)$  (a) and its square root (b) versus  $\sigma$  for various parameter  $\xi$  values.

As it can be seen on fig.3.2 changing the focusing parameter  $\xi$  modifies both the maximal amplitude (see Fig. 3.4) and the halfwidth (Fig.3.5), as well the position ( $\sigma_m$ ) of the maximum (Fig.3.3). These values are listed in the Table 3.1.

In the loose focusing limit ( $\xi \rightarrow 0$ ) the integral in eq.(3.13) takes the value of  $\text{sinc}(\frac{\Delta k}{2}l)$  in agreement with the theory of SHG and SFG in the plane wave approximation [WPRN03]. More the fundamental beams are focused ( $\xi$  value increases), narrower the central maximum is and more side maximas on the both sides occurs in considered  $\sigma$  range. The amplitude of the side maximas for  $\sigma > 0$  becomes higher and those for  $\sigma < 0$  becomes lower with increased  $\xi$ . The position of the main maximum shifts also toward the lower  $\sigma$  values, what suggest that tight focusing requires a better phase-matching for SHG and SFG to be the most efficient. However, there is an optimal focusing value of  $\xi = \xi_m = 2.84$  above which the amplitude of maximum at  $\sigma_m$  of the function  $h(\sigma, \xi)$  decreases. The fact that the  $\sigma_m > 0$  implies that optimal phase-matching occurs for  $\Delta k > 0$  for focused beams, contrary for the  $\Delta k = 0$  for the plane waves approximation. Focused beam "can be thought of as containing plane waves having a range of propagation angles. Thus, when  $\Delta k > 0$ , phasematching of sum-frequency mixing processes involving these off-axis rays is possible, while this is not the case if  $\Delta k < 0$ " [WPRN03].

The values of  $\sigma = \sigma_m$  that provides the maximum of the  $h(\sigma, \xi)$  function for a given  $\xi$  within the investigated range are given on the Fig.3.3.

The values of maxima of the  $h(\sigma, \xi) = h(\sigma_m, \xi)$  curves presented on the graph 3.2 are plotted in function of the corresponding  $\xi$  values on the Fig.3.4 showing the maximum value of  $h(\sigma_m, \xi = \xi_m) = 1.068$  is reached for  $\xi = \xi_m = 2.84$  and  $\sigma_m = 0.576$ .

Figure 3.4 shows well known result of  $h(\xi, \sigma_m)$  optimization regarding the  $\xi$  value, as given for example on the fig. 2 of [BK68]. Existence of a single maximum of Boyd-Kleinman

<sup>2</sup>More info at the website <http://qhwiki.originlab.com>

$\xi$	$\sigma_m$	$h(\sigma_m, \xi)$	$\Delta\sigma_{1/2}$	FWHM [ $\Delta kl/2$ ]	$\eta_{SFG}^{d_{eff}=9.5\text{pm}} [W^{-1}]$	$\eta_{SFG}^{d_{eff}=7.5\text{pm}} [W^{-1}]$
0.5	0.956	0.2121	5.64	2.82	0.0161	0.0100
1	0.856	0.7761	2.93	2.93	0.0589	0.0367
1.5	0.766	0.9475	2.04	3.05	0.0719	0.0448
2	0.686	1.0303	1.59	3.17	0.0782	0.0487
2.5	0.616	1.0628	1.31	3.29	0.0806	0.0503
2.84	0.576	1.0677	1.18	3.36	0.0810	0.0505
3	0.556	1.0668	1.13	3.39	0.0809	0.0504
3.5	0.506	1.0546	1.00	3.49	0.0800	0.0499
4	0.465	1.0334	0.89	3.58	0.0784	0.0489
5	0.405	0.9790	0.75	3.74	0.0743	0.0463

Table 3.1: Parameters of the simulated curves describing the Boyd-Kleinman factor  $h$  versus  $\sigma$ , for various  $\xi$  values:  $\sigma_m$  - position of the maximum;  $h(\sigma_m, \xi)$  - maximum value;  $\Delta\sigma_{1/2}$  - fwhm. From these values we have computed the reduced wave vector mismatch [FWHM repeated in terms of  $\Delta kl/2$ ] and the expected conversion efficiency  $\eta_{SFG}$  assuming  $d_{eff} = 9.5\text{pm/V}$  or  $d_{eff} = 7.5\text{pm/V}$  being the limits of  $d_{eff}$  range given by the crystal manufacturer. The values are presented up to 4th decimal digit to show the difference between the values for respective  $\xi$  values.

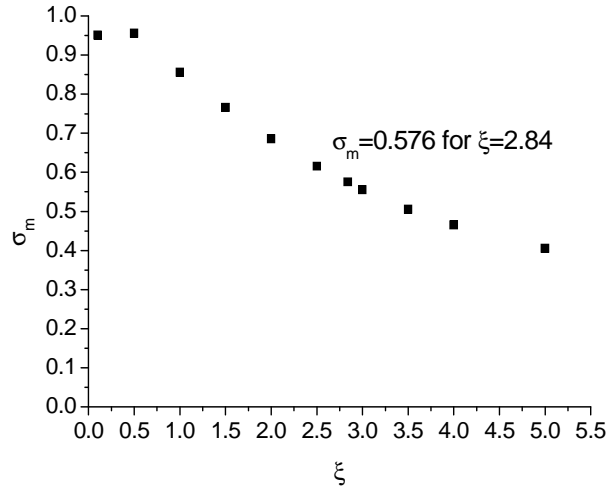


Figure 3.3: Change of the  $\sigma = \sigma_m$  in function of  $\xi$ .

focusing factor at  $\xi_m = 2.84$  is characteristic with a smooth and weak variation over a range of  $\xi$  values (eg. 2.5% from resonance for  $2.169 < \xi < 3.817$  that is equal to the waist  $w_0$  variation in the range  $19.3 < w_0 < 14.5\mu\text{m}$ ).

Having the values of  $\sigma_m = 0.576$  and  $\xi_m = 2.84$ , using the definitions of  $\xi$  and  $\sigma$  we obtain:

$$\frac{\Delta k_{QPM}}{2\pi} = -\frac{\sigma_m \xi}{\pi l} = 5.2 \times 10^{-5} \mu\text{m}^{-1} \ll \frac{1}{\Lambda}, \quad (3.14)$$

for  $\Lambda = 5.74\mu\text{m}$  determined before as well as the value specified by the crystal manufacturer  $\Lambda = 5.725\mu\text{m}$  (see subsection 3.2.1.2). It means that the quasi-phase-matching condition  $\Delta k_{QPM}$  can be legitimately reduced to the one for plane wave condition, namely  $\Delta k_{QPM} = 0$

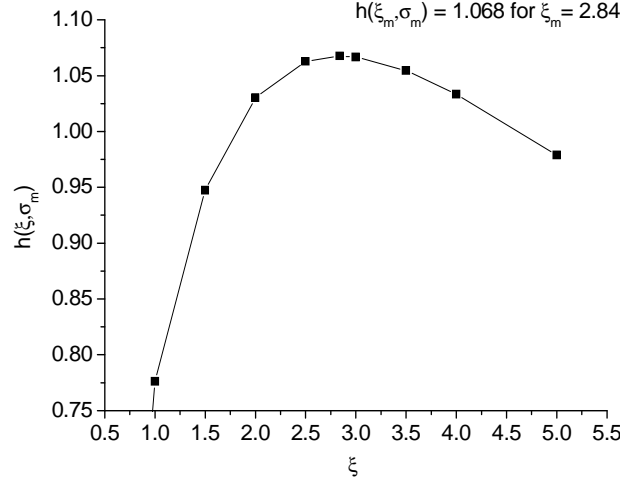


Figure 3.4: Optimization of Boyd-Kleinman focusing factor  $h(\sigma_m, \xi)$  in terms of  $\xi$  parameter

Reference	Process	$\Lambda[\mu m]$	$d_{33}[pm/V]$	$d_{eff}[pm/V]$	$\lambda_{generated}[nm]$
[JSW <sup>+</sup> 04]	SFG	6.99	15.7	10	492
[TZL05]	SHG	5.5	15	9.5	461
[PBB <sup>+</sup> 01]	SHG	-	16.9	10.8	>1500
[ARM <sup>+</sup> 97]	SHG	9	14.9	9.5	532
[ZCG <sup>+</sup> 02]	SHG	9.5	12.2	7.8	541

Table 3.2: Compilation of the references with flux-grown PP-KTP applications to SHG and SFG providing the view on  $d_{33}$  and  $d_{eff}$  coefficients values for various wavelengths and crystal grating periods.  $d_{33}$  are taken directly from references [TZL05, PBB<sup>+</sup>01, ARM<sup>+</sup>97, ZCG<sup>+</sup>02], while in [JSW<sup>+</sup>04]  $d_{eff}$  is given. The rest of  $d_{eff}$  were computed using the relation (3.7).

The values of FWHM of the main peak have been plotted, directly in  $\sigma$  units ( $\Delta\sigma_{1/2}$ ) as well as reduced wave vector mismatch  $\sigma\xi = \frac{\Delta k_{QPMl}}{2}$  in figures 3.5 (a) and (b).

Presented figures of the change in full width at half maximum FWHM shows the decrease with  $\xi$  until the limit of not focused beam is reached.

At this moment, every parameter of the equation(3.11a) is available to perform calculation of the expected efficiency, except of  $d_{eff}$ . Some typical values obtained from the literature are compiled in table 3.2.

The Raicol Crystals Ltd. company from which the crystal was bought, did not provide the  $d_{eff}$  value specific to our PP-KTP, mentioning only the range of values between 7.5 and 9.5 pm/V. Thus, the expected efficiency has been calculated for both of nonlinear coefficient. Speed of light as well as the vacuum permittivity are given in the table of constant at the end of the dissertation (section D),  $\lambda_1 = 923$  nm,  $\lambda_2 = 937$  nm and  $\lambda_b = 465$  nm are taken and  $n_b = 1.917 \pm 0.001$  being an average value of six refractive indexes obtained using Sellmeier equations and KTP parameters from various references presented in the Appendix C. For  $\lambda_1 = 923$  nm and  $\lambda_2 = 937$  nm the common refractive index value was taken equal to  $n_{av} = 1.836$  as the discrepancies between the values computed using several references were of the same order as the differences between refractive indexes for the two considered wavelengths within the same Sellmeiers equation reference parameters.

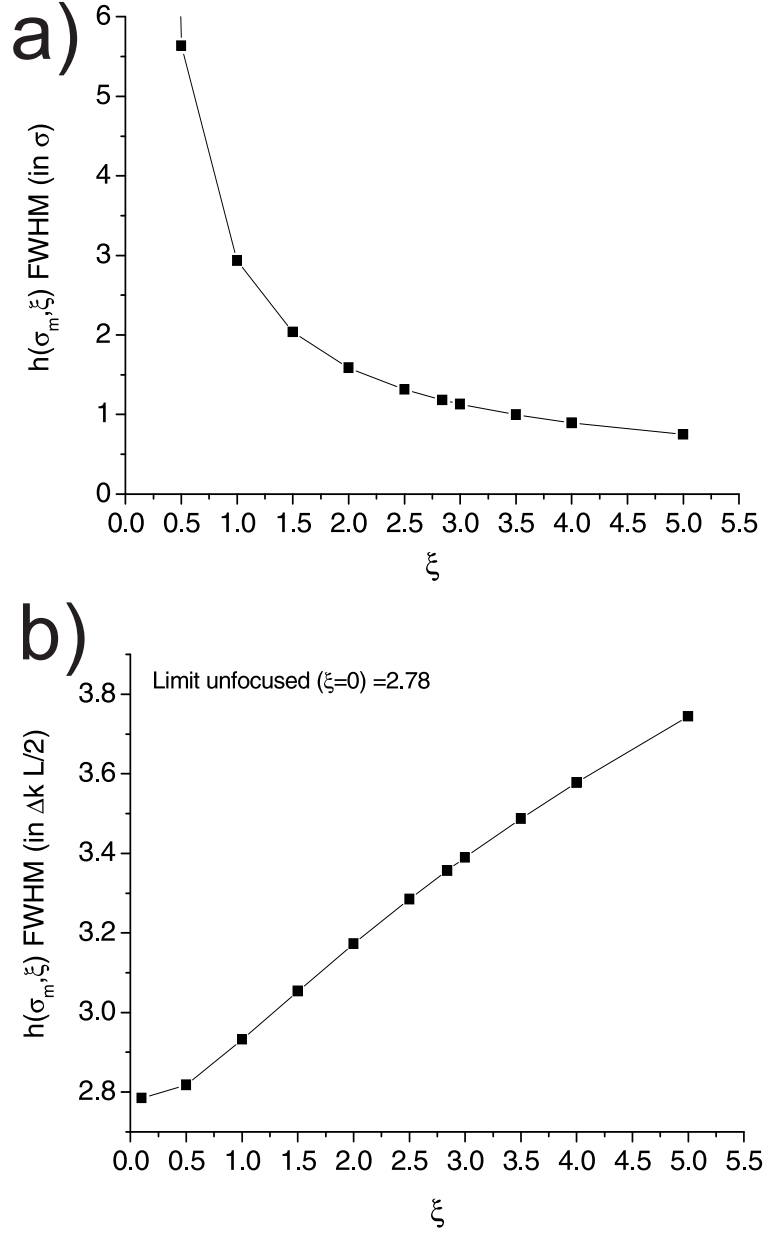


Figure 3.5: Change of the  $h(\sigma, \xi)$  function FWHM with  $\xi$  in (a)  $\sigma$  scale -  $\Delta\sigma_{1/2}$  as well as (b)  $\frac{\Delta k_{QPM} l}{2}$  scale. On the graph (b) the value FWHM value for no-focus ( $\xi = 0 \Rightarrow w_0 \rightarrow 0$ ) limit  $\Delta(\frac{\Delta k_{QPM} l}{2})_{1/2} = 2.78$

In the table 3.1 values of the efficiency  $\eta_{SG}$  are presented. The maximum value, for optimal focusing  $h(\sigma_m, \xi_m) = 1.068$  is about  $\eta_{SG}^{calc} = 8.10\%W^{-1}$  when the  $d_{eff} = 9.5$  pm/V is taken, whereas for  $d_{eff} = 7.5$  pm/V,  $\eta_{SG}^{calc} = 5.05\%W^{-1}$  is obtained.

### 3.1.3 Matching tolerances

If one wants to change the generated SHG wavelength by tuning the  $\lambda_{av}$  care should be taken for remaining at the quasi-phase-matching condition:  $\Delta k = \Delta k_{QPM}$  which has to remain constant not to have loss of generated power of the second harmonic. It has been already said that the refractive indexes of the crystal depend on its temperature, so it will be considered now how the quasi-phase-matching depends on the crystal temperature and how it is related to the change in  $\lambda_{av}$ . Let's consider

$$\frac{\Delta k}{2\pi} = \frac{\Delta k_0}{2\pi} - \frac{1}{\Lambda}, \quad (3.15)$$

where

$$\frac{\Delta k_0}{2\pi} = 2 \frac{1}{\lambda_{av}} (n_b(T_{cr}, \lambda_{av}/2) - n_{av}(T_{cr}, \lambda_{av})) \quad (3.16)$$

Matching for small variation of  $T_{cr}$  or  $\lambda_{av}$ , keeping  $\delta k$  equal to the optimal value  $\delta_{QPM}$ , leads to:

$$\frac{\partial}{\partial T_{cr}} \left[ l \left( \frac{\Delta k_0}{2\pi} - \frac{1}{\Lambda} \right) \right] dT_{cr} = - \frac{\partial}{\partial \lambda_{av}} \left[ l \left( \frac{\Delta k_0}{2\pi} - \frac{1}{\Lambda} \right) \right] d\lambda_{av} \quad (3.17)$$

Very straightforwardly, one has for the left hand side:

$$\frac{\partial}{\partial T_{cr}} \left( \frac{\Delta k l}{2\pi} \right) = \frac{\partial}{\partial T_{cr}} \left( \frac{\Delta k_0}{2\pi} - \frac{1}{\Lambda} \right) + l \frac{\partial}{\partial T_{cr}} \left( \frac{\Delta k_0}{2\pi} \right) - l \frac{\partial}{\partial T_{cr}} \left( \frac{1}{\Lambda} \right) = l \frac{\partial}{\partial T_{cr}} \left( \frac{\Delta k_0}{2\pi} \right) + \alpha l \frac{\Delta k_0}{2\pi} \quad (3.18)$$

where  $\alpha = l^{-1} \frac{\partial l}{\partial T_{cr}}$  is the coefficient of linear expansion. Since  $\frac{\partial l}{\partial T_{cr}} = \alpha l$  and  $\frac{\partial}{\partial T_{cr}} \left[ \frac{1}{\Lambda} \right] = -\frac{\alpha}{\Lambda}$  we write:

$$\frac{\partial}{\partial T_{cr}} \left( \frac{\Delta k l}{2\pi} \right) = 2 \frac{l}{\lambda_{av}} \left[ \left. \frac{\partial n}{\partial T_{cr}} \right|_{T_{cr}, \lambda_{av}/2} - \frac{\partial n}{\partial T_{cr}} \Big|_{T_{cr}, \lambda_{av}} \right] + 2\alpha \frac{l}{\lambda_{av}} \left( n_b(T_{cr}, \lambda_{av}/2) - n_{av}(T_{cr}, \lambda_{av}) \right) \quad (3.19)$$

Right hand side of eq.(3.17), for the wavelength derivative is equal to:

$$\begin{aligned} \frac{\partial}{\partial \lambda_{av}} \left( \frac{\Delta k l}{2\pi} \right) &= \frac{\partial}{\partial \lambda_{av}} \left( l \left( \frac{\Delta k_0}{2\pi} - \frac{1}{\Lambda} \right) \right) = \\ &= \frac{l}{\lambda_{av}} \left( \frac{\partial n}{\partial \lambda_{av}} \Big|_{T_{cr}, \lambda_{av}/2} - 2 \frac{\partial n}{\partial \lambda_{av}} \Big|_{T_{cr}, \lambda_{av}} \right) - \frac{2l}{\lambda_{av}^2} \left( n_b(T_{cr}, \lambda_{av}/2) - n_{av}(T_{cr}, \lambda_{av}) \right) = \\ &= 2 \frac{l}{\lambda_{av}} \left[ \frac{1}{2} \frac{\partial n}{\partial \lambda_{av}} \Big|_{T_{cr}, \lambda_{av}/2} - \frac{\partial n}{\partial \lambda_{av}} \Big|_{T_{cr}, \lambda_{av}} - \frac{1}{\lambda_{av}} (n_b(T_{cr}, \lambda_{av}/2) - n_{av}(T_{cr}, \lambda_{av})) \right] \end{aligned} \quad (3.20)$$



### (i) Matching line

If the eq.(3.17) is combined with equations (3.19) and (3.20),  $T_{cr}^{QPM(\lambda_{av})}$  satisfies:

$$\frac{dT_{cr}^{QPM(\lambda_{av})}}{d\lambda_{av}} = \frac{\frac{1}{2} \frac{\partial n}{\partial \lambda_{av}} \Big|_{T_{cr}, \lambda_{av}/2} - \frac{\partial n}{\partial \lambda_{av}} \Big|_{T_{cr}, \lambda_{av}} - \frac{1}{\lambda_{av}} (n_b(T_{cr}, \lambda_{av}/2) - n_{av}(T_{cr}, \lambda_{av}))}{\frac{\partial n}{\partial T_{cr}} \Big|_{T_{cr}, \lambda_{av}/2} - \frac{\partial n}{\partial T_{cr}} \Big|_{T_{cr}, \lambda_{av}} + 2\alpha \frac{1}{\lambda_{av}} (n_b(T_{cr}, \lambda_{av}/2) - n_{av}(T_{cr}, \lambda_{av}))} \quad (3.21)$$

This gives the slope of the matching line that describes the linear correlation between the optimal crystal temperature  $T_{cr}$  for a given incident wavelength  $\lambda_{av}$ .

### (j) Matching tolerances

Matching tolerances characterize the sensitivity of conversion efficiency  $\eta$  to any of the matching parameters  $X$ , i.e., the way efficiency decreases when  $X$  departs from its optimal value  $X_0$  while all other operating conditions remain fixed, in particular, focusing parameter  $\xi$  is fixed. They are commonly characterized by the corresponding acceptance bandwidth that corresponds to the FWHM of the response curve  $\eta(X)$ , i.e., the range  $\Delta X_{1/2}$  of parameter values  $X$  for which the conversion efficiency satisfies  $\eta(X) \geq \eta_0/2 = \eta(X_0)/2$ .

In the present work the conversion efficiency can be characterized by a temperature bandwidth associated to the control of crystal temperature  $T_{cr}$  and the spectral bandwidth associated to the average input wavelength  $\lambda_{av}$ , that can be varied either by the joint variation of  $\lambda_1$  and  $\lambda_2$  (controlled by the common temperature of the laser diodes (see subsection 3.2.1.1)) or their individual variations (controlled by the LD feeding currents).

Given the limited operating ranges of the LD and crystal, one can write to the first order:

$$\sigma(X) = \sigma(X_0) + \left[ \frac{\partial \sigma}{\partial X} \right]_{X_0} (X - X_0), \quad (3.22)$$

for any small variation of phase-matching parameter  $X$  around its value at optimal matching  $X_0$ , with  $\sigma(X_0) = \sigma_m(\xi)$ . The acceptance FWHM is then given by

$$\Delta X_{1/2} = \frac{\Delta \sigma_{1/2}(\xi)}{\left[ \frac{\partial \sigma}{\partial X} \right]_{X_0}} \quad (3.23)$$

where  $\Delta \sigma_{1/2}$  is the FWHM of the Boyd-Kleinman focusing factor  $h(\sigma, \xi)$ . The dependence of variation of  $\Delta \sigma_{1/2}$  with focusing parameter  $\xi$  is plotted in fig. 3.5 (a).

Using  $\left[ \frac{\partial \sigma}{\partial X} \right]_{X_0} = -\left( \frac{1}{2\xi} \right) \left[ \frac{\partial \Delta kl}{\partial X} \right]_{X_0}$ , according to the definition of  $\sigma$ , the expression of the acceptance bandwidths are given for:

- $X = T_{cr}$  (crystal matching):

$$\left[ \frac{\partial \sigma}{\partial T_{cr}} \right]_{T_{cr}^{(0)}} = -\frac{\pi}{\xi} \left[ \frac{\partial}{\partial T_{cr}} \frac{\Delta kl}{2\pi} \right]_{T_{cr}^{(0)}} \text{ with } T_{cr}^{(0)} \text{ being an optimal crystal temperature} \quad (3.24)$$

- $X = T_{LD}$  or  $X = I_{LD}$  (laser diodes  $\lambda_{av}$  matching by the temperature or the feeding current  $I_{LD}$  change):

$$\left[ \frac{\partial \sigma}{\partial T_{LD}} \right]_{T_{LD}^{(0)}} = \left[ \frac{\partial \sigma}{\partial \lambda_{av}} \right]_{\lambda_{av}^{(0)}} \left[ \frac{\partial \lambda_{av}}{\partial T_{LD}} \right]_{T_{LD}^{(0)}} \quad \text{or} \quad \left[ \frac{\partial \sigma}{\partial I_{LD}} \right]_{I_{LD}^{(0)}} = \left[ \frac{\partial \sigma}{\partial \lambda_{av}} \right]_{\lambda_{av}^{(0)}} \left[ \frac{\partial \lambda_{av}}{\partial I_{LD}} \right]_{I_{LD}^{(0)}}, \quad (3.25)$$

where:

$$\left[ \frac{\partial \sigma}{\partial \lambda_{av}} \right]_{\lambda_{av}^{(0)}} = -\frac{\pi}{\xi} \frac{\partial}{\partial \lambda_{av}} \left[ \frac{\Delta kl}{2\pi} \right]_{\lambda_{av}^{(0)}} \text{ according to the definition of } \sigma = -\frac{\Delta kl}{2\xi} = -\frac{\pi}{\xi} \left( \frac{\Delta kl}{2\pi} \right)$$

with  $T_{LD}^{(0)}$ ,  $I_{LD}^{(0)}$  and  $\lambda_{av}^{(0)}$  being the optimal laser diodes: temperature, feeding current and averaged fundametal wavelength respectively.

Derivatives of  $\frac{\Delta kl}{2\pi}$  over  $X = T_{cr}$  and  $\lambda_{av}$  - are readily obtained from equations (3.19) and (3.20).

These considerations are similar to derivations of tolerances and matching made as for example in [Ris96] and [FMJB92] carried out in the loose focusing limit where response to variations of matching parameters scales as  $\text{sinc}^2(\Delta kl/2)$ . Hence  $\text{FWHM}(\Delta kl/2)_{1/2} = 2 \cdot 0.4429 \cdot \pi = 2.783$ . To quantitatively account for the experimental tolerances fit or a priori knowledge of focusing parameter  $\xi$  needed as well as the slope of the  $\lambda_{av}$  change with either LDs temperature or LD current(s). Therefore, the expected values of the temperature tolerances are computed in the experimental part of this chapter, when required parameters are determined and they are compared with the FWHM values obtained directly from the phase-matching curves see subsection 3.3.3(b).

## 3.2 465 nm laser setup - description

The small difference in wavelength of about 14 nm between the incident light sources requires a more elaborate solution for beams' spatial overlapping before focusing in the center of the crystal, compared to other SFG setups, where wavelength difference between initial beams is around 200 nm [JSW<sup>+</sup>04, MSZ<sup>+</sup>08] and simple dichroic mirrors solve the problem. In this work, a set of 3 equilateral prisms was used. The dispersion results in the difference in beams deflection after the set, so that a spatial superposition of the beams is obtained before entering the non-linear crystal. The fundamentals passes the crystal once, contrary to the systems, where resonant cavity was arranged [MSZ<sup>+</sup>08]. Single pass configuration, however, limits the total conversion efficiency that can be achieved and thus the blue light output power but allowed build compact and robust construction, having sufficient output power and tunability to perform absorption measurements on He<sub>2</sub><sup>\*</sup>. In further subsections the components used to the realization of SFG setup are described in details with an emphasis on the main elements - the laser diodes and the nonlinear crystal. Detailed properties of other components such as mirrors (AM, M1-3, KM on the fig. 3.6), lenses (F1-2), and filter (LPF) are described together with the scheme of assembled blue laser device, so that the relation between their properties and function in the setup is easier to notice.

### 3.2.1 Laser setup components

#### 3.2.1.1 Laser diodes

The sources of the 923 nm (LD1) and 937 nm (LD2) beams are two DFB (Distributed Feed-back [GS03]) 100 mW, monomode laser diodes from Toptica Photonics AG. Both laser diode spectral linewidths are on the order of several MHz and nominal wavelengths at 25°C are 923.58 nm and 937.6 nm respectively. The wavelength tuning can be realized with the feeding current (from the lasing threshold values of 53 mA and 28 mA up to 180 mA and 150 mA respectively) or LD temperature change between 5 and 45 °C providing the access to specified wavelength tuning ranges: 922-925 nm and 936.3-938.7 nm respectively. Nominal variation of the wavelength with the temperature ( $d\lambda/dT$  [nm/K]) is 0.08 nm/K for LD1 and 0.06 nm/K for LD2. However, linear fit to the wavelength vs. laser diodes temperature dependency on (Fig.3.12), measured using Coherent WaveMate Wavelength Meter, gave the values of  $0.0578 \pm 0.0006$  nm/K and  $0.0552 \pm 0.0006$  nm/K respectively. The linear fit to the wavelength versus laser diodes feeding current  $I$  gave the values of  $d\lambda_1/dI_1 = 0.00448 \pm 0.00002$  nm/mA and  $d\lambda_2/dI_2 = 0.00607 \pm 0.00004$  nm/mA, as can be inferred from the slopes on the figures 3.8 and 3.7. The order of magnitude of the lambda-current coefficient than lambda-temperature, results in higher precision and better stability in the laser wavelength tuning across small  $\lambda$  ranges related to the absorption lines profiles.

Each diode is placed in a 9 mm inner diameter collimation tubes with optics ( $f = 4.5$  mm lens with AR coating). The collimated beams are of elliptical shapes with shorter axes of the emitted light in the horizontal plane, that is the direction of the emitted light linear polarization. The spatial profiles in the plane perpendicular to the direction of propagation were recorded using beam profiler. The camera of the profiler was placed after the 3<sup>rd</sup> prism (before the lens L1) - see fig. 3.6 - approximately on 140 cm of beam propagation path. The beams were well collimated, so the divergence has been neglected here. The profiles gave the full width at half maximum (FWHM) values in both horizontal ( $y$ ) ( $\text{FWHM}_h(923) = 1.2 \pm 0.1$

mm and  $\text{FWHM}_h(937) = 1.2 \pm 0.1$  mm) and vertical (z) ( $\text{FWHM}_v(923) = 1.5 \pm 0.1$  mm and  $\text{FWHM}_v(937) = 1.8 \pm 0.2$  mm) directions related to the coordinate system associated with the crystal (see the fig. 3.1). This shows that the beams have moderate ellipticity of about 25%.

Two collimating tubes were mounted in a common copper holder allowing simultaneous change of the laser diodes temperature using a thermoelectric cooler (TEC3-2.5 from Thorlabs) attached to the holder. In this way the emitted infra-red laser beam wavelengths can be changed. The copper holder due to a good material temperature conductivity, transfers the heat to the collimating tubes (made of aluminum) and thus to the laser diodes. The temperature of the copper holder is monitored using 10k $\Omega$  thermistor (TH10K from Thorlabs, material MS97) which accuracy is  $\pm 1^\circ\text{C}$  at  $25^\circ\text{C}$  and operating range from  $-50$  to  $150^\circ\text{C}$ . The resistance calibration with respect to the nominal value of  $R_{25} = 10\text{k}\Omega$  at  $25^\circ\text{C}$  is given by the equation:  $R/R_{25} = \exp(A + B/T + C/T^2 + D/T^3)$ , where temperature  $T$  is in Kelvin and the parameters  $A, B, C, D$  are provided by the manufacturer. The value of thermistor temperature-dependent resistance is used as a feedback signal for the homemade thermocontroller device that feeds the thermoelectric cooler with the current. The direction of the current flow and its value decides about the temperature of the cooler.

### 3.2.1.2 Nonlinear PP-KTP crystal

A flux-grown PP-KTP (periodically poled  $\text{KTiOPO}_4$ ) crystal (Raicol Crystals Ltd.) has been chosen as the nonlinear medium for SFG of 465 nm. The crystal used in the experiment is 10 mm in (X-axis) long and 1x2 mm (ZxY axes) in cross-section. The effective nonlinear coefficient  $d_{eff}$  for the Z-axis of the crystal (direction of the 1 mm long edge, optical axis of the crystal) has been specified between 7.5-9.5 pm/V. The crystal has no anti-reflection coating.

The crystal, mounted in a copper holder is temperature regulated (between  $25$  and  $50^\circ\text{C}$ ) using the same elements as in case of the laser diodes (thermoelectric cooler TEC3-2.5, thermistor TH10K serving the feedback for separate thermocontroller device). Thermal control allows fulfilling the quasi-phase-matching condition (eq.(3.6)) when the IR laser diodes wavelength is changed and thus generated sum frequency wavelength is tuned. The phasematching curve for a given wavelength is shown later on fig. 3.16(a). The grating value at the room temperature ( $25^\circ\text{C}$ ) has been specified by the manufacturer to be  $\Lambda = 5.725\mu\text{m}$ .

### 3.2.2 Setup for SFG - construction scheme

According to the demands of SFG technique discussed in section 3.1 the incident infra-red beams need to be spatially overlapped providing simultaneous interaction of two electric fields on the same volume of nonlinear crystal. It was also explained that beams focusing in the center of the crystal increases the nonlinear conversion efficiency. Relying on these two conditions, the laser diodes and the crystal together with various optical elements as prisms, mirrors and filters (detailed description further in the text) are arranged as shown on the fig.3.6.

The silver coated right angle prism mirror (AM, Thorlabs MRA10-P01,  $\sim 99\%$  of reflectivity at 930 nm) together with the broadband dielectric mirror (M1, Thorlabs BB05-E03,  $>99\%$  reflectivity at 930 nm) are used to decrease the distance between the two parallel beams to approximately 0.5 cm and tilt the 937 nm beam by the angle of about  $0.2^\circ$ . Thus, after 75-cm long propagation, being reflected by the broadband dielectric mirrors (M2) and (M2) (of the same type as M3), two beams are entering the first of the three dispersive prisms at the angle

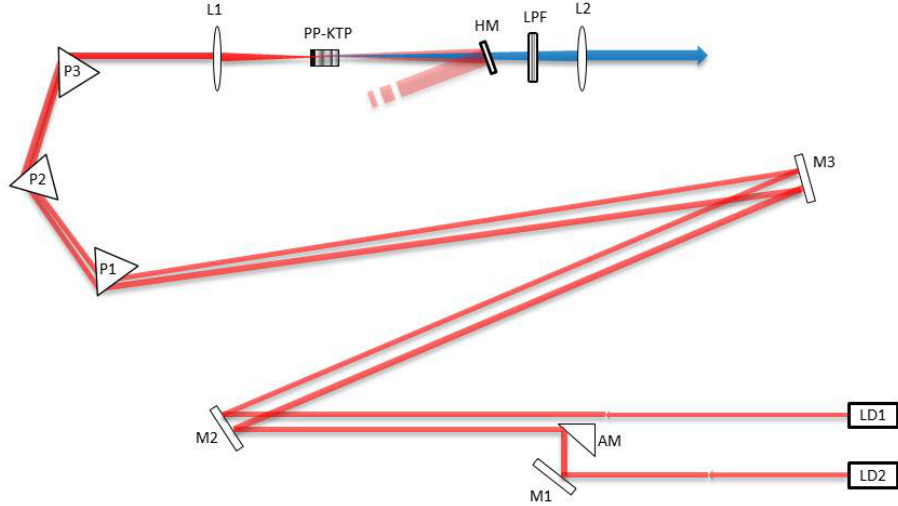


Figure 3.6: Laser set-up. LD1, 2: LD at 923.58, 937.6 nm; M: mirror; AM: angle mirror; P: prism; L: lens; HM: hot mirror; LPF: low pass filter. HM and LPF both filter out the 465 nm radiation. Detailed description in the text.

of minimum deviation, still with  $0.2^\circ$  angular difference. The prisms (P1-3, Thorlabs PS851, apex angle  $60^\circ$ ) are made of SF11 glass for which the difference in refractive indexes for 923 and 937 nm light results in the different values of minimum angle of deviation for those wavelengths. Angular difference between the beams changes by  $0.064^\circ$  after passing a single prism, so passing through the combination of three prisms allows removing the angular difference of  $0.2^\circ$  existing at the input of the set. As a consequence overlapped infra-red laser beams enter the PP-KTP crystal. They are focused by a lens with anti-reflection coating (F1) into the middle of the crystal. The crystal, mounted in the copper holder, is oriented in the way that the short (Z-axis) 1 mm edge is in the horizontal plane and the crystal input facet is perpendicular to the oncoming overlapped beams. In this way the polarization of the infra-red beams (also in horizontal plane) is in the direction of crystal Z-axis, what allows using the nonlinear coefficient  $d_{33}$ .

The fine position of the crystal around the lens focal point can be regulated with the use of XYZ-axis-translation stage to which the copper holder with the crystal is attached. At the output of the crystal, the two IR beams and generated sum-frequency are present. As the only 465 nm beam is relevant for this work, the fundamentals are removed: first more than 90% is reflected from the hot mirror (HM, Thorlabs FM01). Second, a several  $\mu\text{W}$  (measured 1-2  $\mu\text{W}$  of IR fraction when blue light power was measured) is transmitted through the low pass-filter (LPF, Thorlabs FGB37). The transmission coefficients for the hot mirror and for the low pass filter determined experimentally for 465 nm wavelength are  $T^{HM} = 0.85$  and  $T^{LPF} = 0.86$  respectively. The outgoing, diverging beam is collimated by the anti-reflection coated lens (F2). All the setup elements, placed on the aluminum raster breadboard  $30 \times 45 \text{ cm}^2$ , are protected with an aluminum cover with the hole for the outgoing blue beam and a movable beam stopper. There are 6 BNC connectors attached to the aluminum cover: for laser diodes power supply as well as lasers and crystal temperature control and monitoring.

### 3.2.3 Laser output wavelength tuning

A change of laser diodes temperature results in the change of emitted infra-red laser beams wavelengths and thus the wavelength of generated harmonic according to eq.(3.6), but has no impact on the delivered laser power. The crystal temperature has just to be changed to maintain the quasi-phase-matching condition. In contrast, when the blue wavelength is tuned by changing the feeding current of one or both the laser diodes, the incident power(s) hence, the output power varies. For the need of the experiment the voltage control of the feeding current was used for small frequency scans, where smooth, monotonous linear current vs. wavelength change was obtained with good reproducibility of the wavelength sweep.

For the purpose of identification of absorption line and calibration of the laser setup wavelength based on their known positions, as well as for accurate recording of the line profiles both laser wavelength tuning methods were used. First, rough position of the absorption line center was found with the laser diodes temperature tuning and crystal matching. For the fixed temperature settings, the recording of the absorption line profile was made with the 937 nm laser diode current change driven by the external voltage varied linearly.

The laser diodes feeding current change with the value of external voltage applied to the current controller is shown on the fig. 3.7. Advantage of using the voltage current control for 937 nm laser diode is visible in comparison to 923 nm, as the slope is about 1.5 times higher for the former one. So that the wider current range is available for this diode with the same range of driving voltage. It was avoided not to exceed 165-170 mA current for each diode not to shorten their lifetimes using the currents well above the operating values specified by the manufacturer - 150 mA and 180 mA for 937 nm and 923 nm laser diodes respectively.

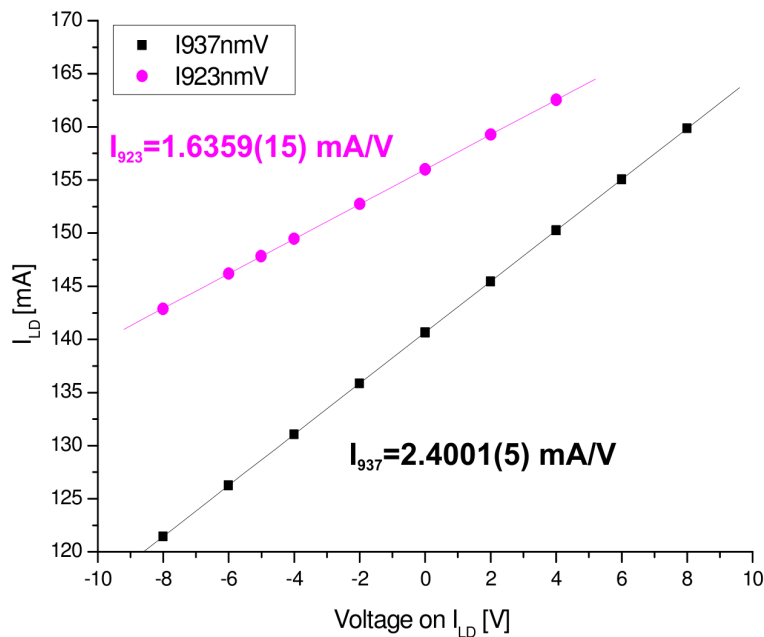


Figure 3.7: Change of the laser diodes feeding current value with external voltage applied to the power supply controller

The measured change of the infra-red emitted wavelengths within the same voltage range as before has been shown together with the fitted slopes of the linear dependency -fig. 3.8. 2

times higher value of the slope  $\frac{d\lambda_{937}}{dV}$  over  $\frac{d\lambda_{923}}{dV}$  suggested the choice of 937 nm diode to be tuned with the external voltage.

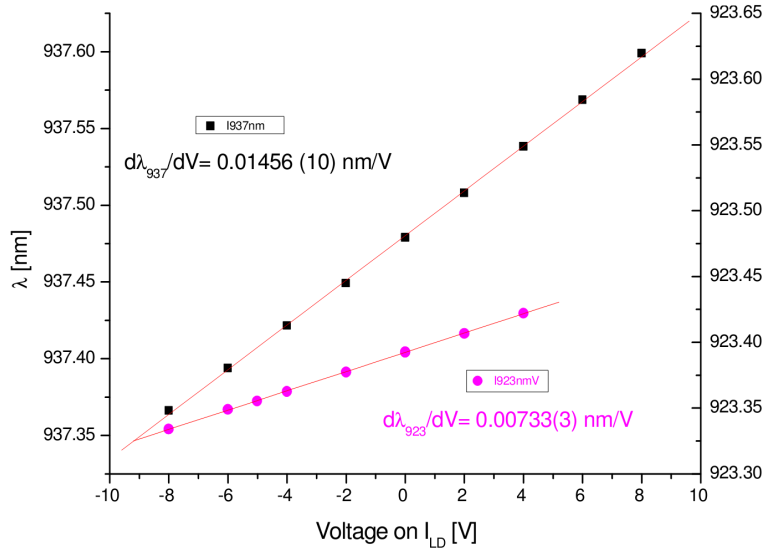


Figure 3.8: Infra red laser diodes wavelength tuning with the external voltage driven feeding current.

Frequency scans performed using the laser diodes temperature fine regulation also with the driving voltage control resulted in hysteresis (when the temperature driving voltage was on positive and negative slope) both in the recorded line position and the shape. This problem may be caused by too high thermal inertia of the holding copper construction of the laser diodes that was thermally stabilized by thermoelectric element as well as the response time of the thermistor and the feedback loop of the thermocontroller (For more details about the methodology of the absorption lines profiles measurement the Reader is sent to subsection 4.1.3).

### 3.3 Laser performance - experimental results

During the work with the assembled laser system its parameters such as fundamental and generated harmonic beams spatial profiles has been measured with the movable diaphragm and the power meter. Later, the beam profiler device has become available so that precise measurements could be made and their results were presented in subsection, when the beam profiles dimensions were described (subsection 3.2.1). These numbers are used also for the estimation of the fundamental beams ellipticity influence on the achieved SFG process efficiency. Also, during all the work, the knowledge about the wavelength of generated blue harmonic was based on registered positions of  $\text{He}_2^*$  absorption lines met in the literature. As it was with the beam profiles, here also the wavelength meter became available later allowing quantitative assessment of parameters inferred earlier.

#### 3.3.1 Output power and efficiency

For the laser setup described in subsection 3.2.1 and 3.2.2 the maximum power value generated at 465 nm measured (superscript  $m$ ) after the hot mirror and low-pass filter is  $P_b^m = 175 \pm 1 \mu\text{W}$  while the input power of the IR light from the laser diodes are  $P_{923}^m = 75.4 \pm 0.1 \text{ mW}$  and  $P_{937}^m = 80.4 \pm 0.1 \text{ mW}$  for 923 nm and 937 nm respectively. The fundamental beams power values were measured after the 3rd prism, thus before they reached the collimating lens and the input window of the crystal. The uncertainties here are the power measurement precision on used power meter range. It has been determined experimentally, that there is a fraction of about 1-2  $\mu\text{W}$  of the IR light that is not filtered out by the hot mirror and low pass filter and reaches the photodiode during the blue light power measurements. If the losses of the power of 465 nm beam on the output crystal window, low-pass filter and the hot mirror are taken into account (see subsection 3.2.2 for the transmission coefficient values), the value of generated sum frequency at the end of the crystal is equal to:  $P_b = 266 \pm 9 \mu\text{W}$ . For the fundamentals, the powers that are involved in the nonlinear interaction are lower than measured due to reflection losses at the input window of the crystal, so that  $P_1 = 68.8 \pm 0.1 \text{ mW}$  and  $P_2 = 73.4 \pm \text{mW}$ . Transmission coefficients ( $T^C$ ) through the crystal windows, for the beams propagation perpendicular to the surface, have been computed from relation  $T^C = 1 - \frac{(1-n)^2}{(1+n)^2}$ , substituting  $n$  by the refractive indexes  $n_{av}$  and  $n_b$  for IR and blue light, respectively.

The value of efficiency, according to the equation (3.9b), is equal:

$$\eta_{SFG} = (5.3 \pm 0.2) \% W^{-1}, \text{ for our 1 cm long crystal.} \quad (3.26)$$

The influence of remaining IR power on the efficiency value stays within the error bar. Experimental value is higher than the value of SFG efficiency  $2.2 \% W^{-1} \text{cm}^{-1}$  at 492 nm reported by [JSW<sup>+</sup>04]. If one wants to compare the SFG efficiency with the values reported for SHG process, factor of 4 has to be taken into account, so that  $4\eta_{SHG}$  is relevant for such comparison. In this way value of 11.2% corresponding to SHG efficiency of  $2.8 \% W^{-1} \text{cm}^{-1}$  at 461 nm reported in [TZL05] is almost twice higher than the efficiency obtained in this work. Our value for 1 cm crystal fits well within the range change it of  $5.1\text{-}8.1 \% W^{-1}$  estimated in the section 3.1.2 and is closer to the value for the lower  $d_{eff}$  value of the crystal. However, in the mentioned estimations the assumption of the most optimal focusing has been made ( $\xi = 2.84$ ). Knowing the FWHM's of the fundamental beams (see subsection 3.2.1.1) it is possible to compute the  $\xi$  value for our setup but one has to remember that the spatial profiles shown the moderate



	FWHM [mm]	$w_0$ [μm]	$\xi$	$h[\xi, \sigma_m]$	$\eta_{SG}^{d_{eff}=9.5}$ [%W <sup>-1</sup> ]	$\eta_{SG}^{d_{eff}=7.5}$ [%W <sup>-1</sup> ]
	1.2	21.8	1.70	0.989	7.5	4.7
	1.5	17.4	2.65	1.066	8.1	5.0
	1.8	14.5	3.82	1.041	7.9	4.9
Average	$1.50 \pm 0.17$	$17.9 \pm 2.1$	$2.73 \pm 0.61$	$1.032 \pm 0.039$	$7.8 \pm 0.2$	$4.9 \pm 0.1$

Table 3.3: Computed values of focused beam waist, Boyd-Kleinman focusing factor  $h$  and efficiency of SHG for the fundamental Gaussian beam with FWHM values corresponding to the measured elliptical beams horizontal and vertical FWHMs.  $\eta_{SG}$  values have been computed here for  $d_{eff} = 9.5$  and  $d_{eff}=7.5$  pm/V

ellipticity of the beams. This results in 3 different (horizontal dimensions are equal for 923 nm and 938 nm laser diodes,  $FWHM_h=1.2$  mm) values of the FWHM, that are: 1.2 mm, 1.5 mm and 1.8 mm. In this situation one could perform computations of Boyd-Kleinman focusing factor  $h$  for the elliptical beam where (staying within SHG approximation) two  $\xi$  values for horizontal and vertical directions would have to be considered. This of course would complicate the computations of the  $h$  function values that was performed earlier. From the other hand, having a large discrepancy in the  $d_{eff}$  value from 7.5-9.5 pm/V, that sets the absolute value of 1% of uncertainty range for possible  $\eta_{SG}$  values, one wouldn't gain on the  $\eta_{SG}$  accuracy estimation through  $h$  computation for the elliptical beam. However, not to avoid completely the problem of beams ellipticity, simplified approach is made. The function  $h(\xi, \sigma)$  is simulated (staying within single Gaussian-circular beam approximation) for the  $\xi$  values that results from three given beams dimensions. This will give at least an order of magnitude of the changes in estimated efficiency values caused by the moderate ellipticity. Recalling the definition of  $\xi$ :  $\xi = l\lambda_{av}/(2\pi n_{av}w_0^2)$  one needs the waist  $w_0$  value that, depends on the lens focal length (lens L1 before the crystal:  $f=75$  mm) and the FWHM of the beam. From the Gaussian optics, for the beam focused by the lens with focal length  $f$ , we obtain the minimum beam radius ( $w_0$ ) at the lens focal point:

$$w_0 = \sqrt{2 \ln 2} \frac{\lambda_{av} f}{\pi FWHM} \quad (3.27)$$

FWHM of the beam is measured at the lens position.

In the table 3.3 the results of computations are presented for each of FWHM and the average values are given at the bottom. Efficiency  $\eta_{SG}$  was computed for  $d_{eff} = 9.5$  pm/V as well as for  $d_{eff} = 7.5$  pm/V.

In the limits of the error bars the experimental value of the efficiency agrees well with an average for the lower  $d_{eff}$  value shown in the table. The SHG is the most efficient here for the 1.5 mm FWHM and the lowest value of the estimated  $\eta_{SG}$  occurs for the horizontal elliptical beams  $FWHM_h=1.2$  mm - the relative difference between the highest and lowest  $\eta_{SG}$  exceeds 7%. On the other hand, for the relative difference in  $\eta_{SG}$  between the value for the largest FWHM of 1.8 mm and is for FWHM=1.5 mm is about 2%. It shows that the averaged efficiency value (that estimates the experimental value obtained in true SFG process of elliptical beams) is under a stronger influence lower value of input - it confirms the simulation result shown earlier on the fig.3.4 where the decrease of  $h(\xi, \sigma_m)$  for the lower  $\xi$  values is stronger than for higher  $\xi$  values.

The experimentally determined efficiency value allows calculation  $d_{eff}^{(exp)}$  - experimental values of effective nonlinear coefficients for our PP-KTP crystal.

$$d_{eff}^{(exp)} = \sqrt{\frac{\eta_{SFG} \epsilon_0 c n_{av} n_b \lambda_{av}^3}{64 \pi^2 l h(\sigma, \xi)}} = 7.7 \pm 0.2 \text{ pm/V} \quad (3.28)$$

The value of  $h(\xi = 3, \sigma_m) = 1.067$  has been taken here, as the experimental value  $\xi = 3$  is obtained in the analysis of matching tolerances performed in the subsection 3.3.3. The  $d_{eff}^{(exp)}$  fits well within the range specified by the crystal manufacturer and commonly met values in the literature.

### 3.3.2 Tuning range and matching conditions

#### 3.3.2.1 Laser wavelength calibration

The precise absolute wavelength calibration of the temperature settings of the laser diodes and the crystal relies on the recorded positions of the molecular absorption lines. The positions in wavelength scale are known for both  $^3\text{He}_2^*$  [DR50] and  $^4\text{He}_2^*$  [DR50, BG71]. Within the operating temperature range of the laser diodes and the crystal 10 absorption lines of  $^3\text{He}_2^*$  (Q(1)-Q(8), P(2) and R(0)) and 6 of  $^4\text{He}_2^*$  (Q(1)-Q(9), P(3)) are present. Comparison of the line splittings in reference data and recorded positions, confirmed by characteristic line intensities distribution for  $^3\text{He}_2^*$ , allows identification of the experimental transitions in registered spectrum (see fig. 4.21).

For the purpose of the blue laser wavelength calibration the observed absorption line positions has to be determined in terms of the laser setup control settings that allows the emitted wavelength change. These are the laser diodes temperature and voltage of the 937 nm laser diode control. For consistency the temperature change equivalence of current change has to be known resulting in the same effect on the wavelength.

To obtain such relation following experiment was performed: the laser settings (temperature for set value of laser diode current) was tuned to the position of the top peak of one rotational transition (Q(2)). Later the 937 nm laser diode current was being lowered in several steps, each time correcting the temperature of the laser diodes to remain the maximum value of the signal - top peak value of the chosen line. As a result, correspondence between  $\Delta I_{937}$  and  $\Delta T_{LD}$  resulting in the same value of the wavelength change was determined to be:  $\Delta I_{937} = 19.5 \cdot \Delta T_{LD}$ . The negative slope of measured dependency shown on the fig. 3.9 can be confusing when it is compared with the positive value of the  $\frac{\Delta I_{937}}{\Delta T_{LD}}$ , however it has to be mentioned, that this is a conditional dependency of current and temperature change assuring the tuning to the maximum of the absorption line. The decrease of the current changes the wavelength, which has to be corrected (the same absolute value of wavelength change but with a different sign) by the increase of the temperature to maintain the maximum absorption signal on the top of the line. It means that the increase of the current is equivalent in terms of the effect on the wavelength (with coefficient of the positive sign) to the increase of the temperature, similarly with the decrease of the current and the decrease of temperature.

Obtained values of the line positions of  $^4\text{He}_2^*$  isotope (Q(1), Q(3), Q(5), Q(7), Q(9), R(0) and P(2)) and  $^3\text{He}_2^*$  (Q(1-8), R(0) and P(2)) from the profiles recorded in isotopic pure  $^3\text{He}$  and  $^4\text{He}$  cells of 67 mbar pressure expressed in terms of the laser diodes temperature were added to the

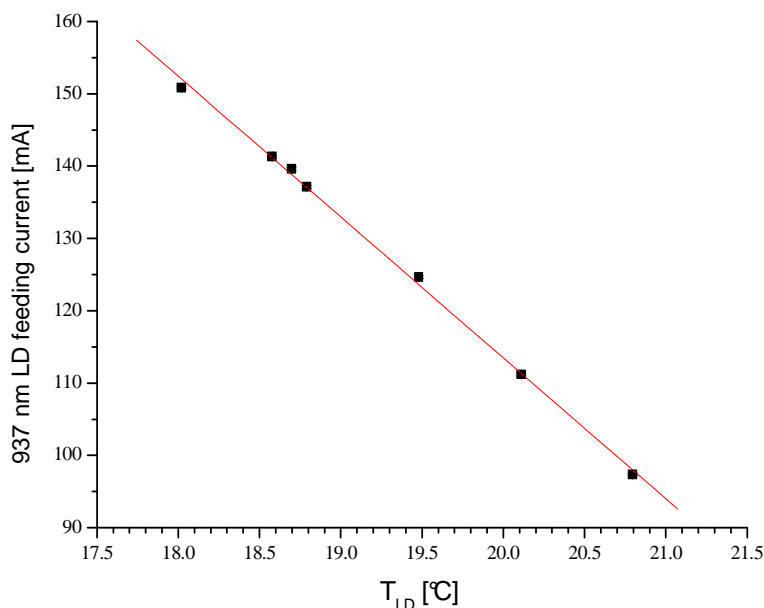


Figure 3.9: Settings of the 937 nm laser diode current providing compensation of  $\lambda_b$  wavelength change with variation of the  $T_{LD}$ . Value of the fitted linear function slope:  $\frac{dI_{937}}{dT_{LD}} = -19.5 \text{ mA/}^\circ\text{C}$

temperature values of laser diodes measured with the thermistor, for which the voltage scans were performed. These temperature values together with the wavelength values of the observed absorption lines were put on the graph providing absolute wavelength calibration of the blue laser setup, shown on the fig.3.10. The choice of 67 mbar pressure cells was conditioned by good SNR for the absorption lines of both isotopologues, less broaden than for higher (i.e. 128 mbar) pressure values - more accurate line position determination, as well as availability equal pressure isotopic pure cells.

The relation between laser diodes temperature and the reported line positions, on which basis the laser calibration relies, is shown on the graph 3.10.

The linear fit ( $\lambda = a * T_{LD} + b$ ) to the points presented on the fig. 3.10 (red curve) provides the parameters of LD temperature (in  $^\circ\text{C}$ ) - wavelength absolute calibration:  $a = 0.0281 \pm 0.0005 \text{ nm/}^\circ\text{C}$ ,  $b = 464.66 \pm 0.02 \text{ nm}$ . The result has been confirmed with the measurement performed with use of the wavelength meter device.

For the wavelength change through the voltage  $V$  controlled 937 nm laser diode feeding current regulation,  $\frac{d\lambda}{dV}|_{\text{current}}$  coefficient could be determined and compared to direct measurement by wavelength meter. For this purpose the presence of well separated multiple (2 or 3) absorption lines within peak to peak voltage amplitude value of 20 V ( $\pm 10$  V) was used for several different laser diodes temperatures. There is non-linear trend present on the figure 3.11 presenting dependency between the wavelength and laser diodes temperature. In range of  $T_{LD} = 16\text{--}21$   $^\circ\text{C}$  several sets of peaks are present, especially those of isotopic pure isotopologues of the molecule (Q(1)-Q(5)). Within this range of temperature the averaged value of wavelength-voltage coefficient is equal:  $\frac{d\lambda}{dV} = (3.5 \pm 0.3) \cdot 10^{-3} \text{ nmV}^{-1}$ . If the values at the lowest and the highest temperatures of about 1.5 and 48  $^\circ\text{C}$  are taken into consideration, the deviation of the coefficient increases to  $\pm 0.6 \cdot 10^{-3} \text{ nmV}^{-1}$ . Most of the investigations in this work, however, have been made avoiding these extremal temperature values to prevent the laser diodes from its damage as explained in the next subsection.

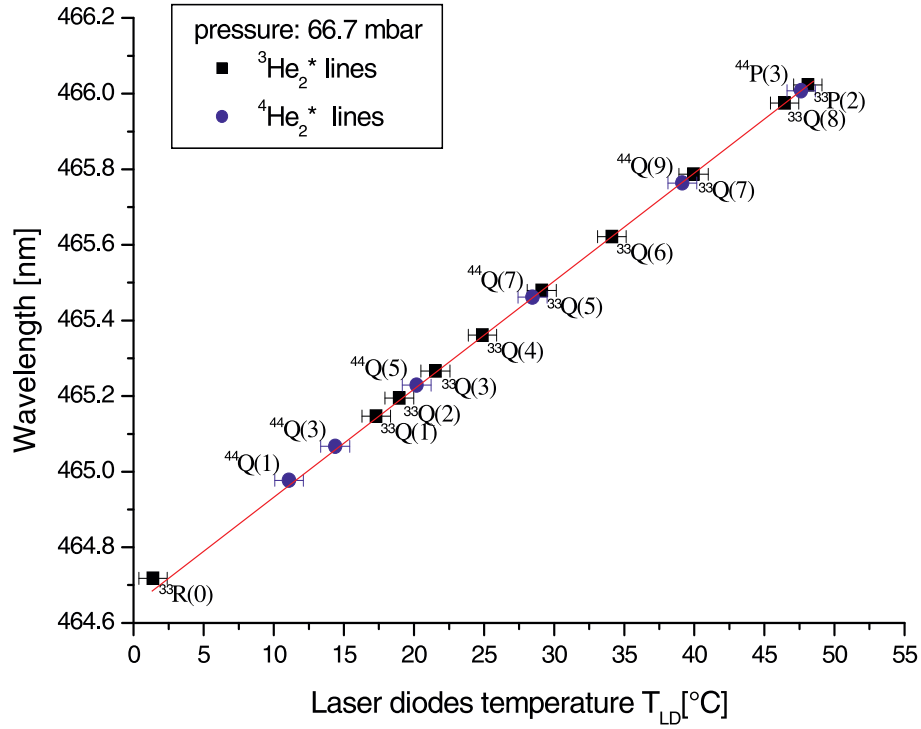


Figure 3.10: The relation between the wavelength of absorption line maximum [DR50, BG71] and corresponding laser diodes temperature. Black squares represent the lines recorded for  $^3\text{He}_2^*$ , blue circles - lines recorded for  $^4\text{He}_2^*$  in 67 mbar pressure isotopic mixture cell. Designation of identified molecular transitions are given next to the points. The red line represents the linear fit, used as - the calibration curve. The error bars on the points for temperature values come from the accuracy of the line maximum position determination (including error caused by hysteresis effect) and the accuracy of the temperature measurement with the thermistor ( $\pm 1^\circ\text{C}$ ).

### 3.3.2.2 Matching conditions

The wavelength operating range of the infra-red laser diodes is available mainly through the diodes temperature regulation. The main constraint on the available range of the infra red beams is the operating conditions. In the laboratory conditions it is difficult to go lower than about  $10^\circ\text{C}$  where, depending on humidity, the water vapor condensates on the lens (without blowing dry air to avoid short circuit and damage). Overheating the diodes is not recommended as it contributes to their lifetime shortening. The wavelengths generated by each of the diodes in the  $10\text{-}40^\circ\text{C}$  temperature range has been measured with the wavelength meter and presented on the graph 3.12. Both wavelength-temperature dependencies are linear with similar slopes:  $\frac{d\lambda_1}{dT_{LD}} = 0.05784(62) \text{ nm/mA}$  and  $\frac{d\lambda_2}{dT_{LD}} = 0.05515(56) \text{ nm/mA}$  within the respective ranges of  $922.93\text{-}924.47 \text{ nm}$  and  $937.03\text{-}938.49 \text{ nm}$ . The result is in agreement with the manufacturer's diodes specification sheet.

Similar constraint apply to the crystal temperature. The main concern being irreversible damage to the crystal in case of overheating is given.

Within the both laser diodes and crystal operating ranges the pairs of  $T_{LD}$  and  $T_{cr}$  values ensuring the quasi-phase-matching condition fulfilled when the laser was tuned to 8  $^3\text{He}_2^*$  lines (R(0), Q(1)-Q(6) and P(2)) have been shown on the Fig.3.13.

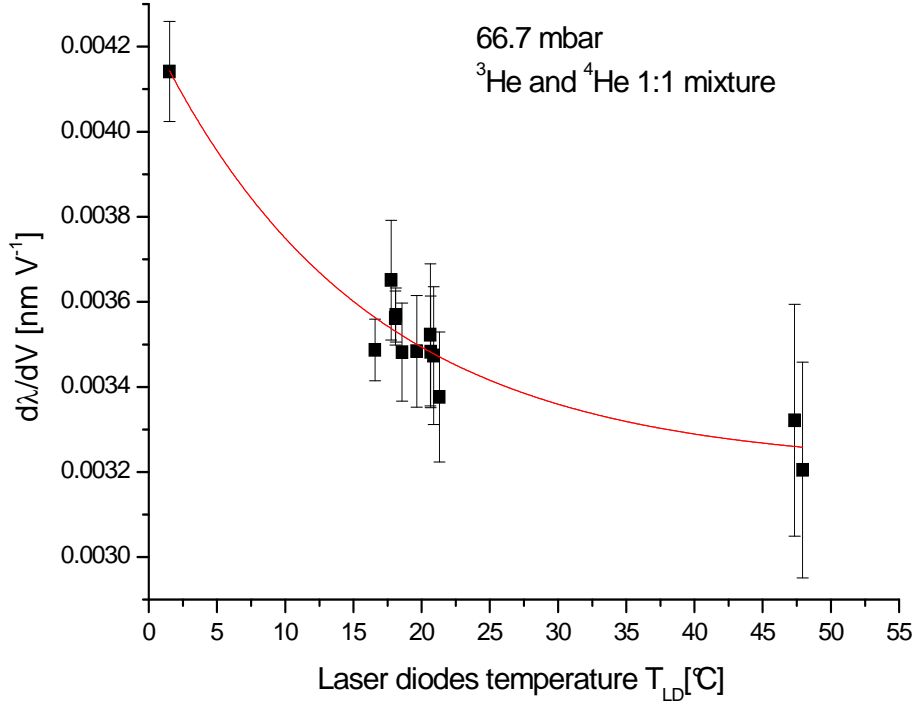


Figure 3.11: Evolution of the wavelength-to-driving voltage for control of LD current coefficient  $\frac{d\lambda}{dV}$  in the laser diodes temperature tuning range. The coefficient values are based on the splittings of 2-3 absorption lines registered in the same frequency scan. The decrease for the  $T_{LD}$  increase is visible, however there are not enough data points to understand a phenomenological fit of the exponential function given on the graph. Errors are the resultant of the accuracy of absorption lines maxima position determination.

Using the wavelength calibration (fig.3.10) the variation of the matching temperature  $T_{cr}$  as a function of the emitted blue wavelength  $\lambda_b$  was obtained.

For the SHG process the phase-matching depends only on the  $\lambda_{av}$  and the difference in the refractive indexes for the fundamental and generated wavelength according to the definition given by eq. (3.6). Knowing, from the linear function fits (Fig.3.12), the relations between  $T_{LD}$  and each of infra-red wavelengths  $\lambda_1$  and  $\lambda_2$  are set, so that the  $\lambda_{av}$  is known. From the other hand, the relation between the crystal and the laser diodes temperatures that provide the matching conditions also has been set (fig.3.13) so that  $\lambda_{av}$  is known as a function of  $T_{cr}$  as well as  $\lambda_b$  relation to  $T_{cr}$  was obtained (fig. 3.14). The refractive indexes (Appendix C) can be calculated for  $\lambda_{av}$  and  $\lambda_b$  for known crystal temperatures. Thus, the plot of the values of  $\frac{\Delta k_{QPM}}{2\pi}$  in function of  $\lambda_{av}$  has been made on the fig. 3.15. The nominal phase mismatch value is right in the middle (excluding the most extending values based on [FBP<sup>+</sup>00] - Boulanger00 reference) of the range constituted by the scattered values resulting from differences in Sellmeiers equation coefficient.

Figure 3.15 shows that estimated value of phase mismatch  $\frac{\Delta k_{QPM}}{2\pi}$  using the focusing parameter  $\xi$  from the subsection 3.3.3 is in line with expectations from the calculations performed based on the crystal and laser diodes temperatures hence the wavelengths, especially given the scatter,  $\pm 0.001$ , in  $\frac{\Delta k_{QPM}}{2\pi}$  value due to the discrepancies in Sellmeier's coefficients met in the references [KT02, FHH<sup>+</sup>87, FASR99, FBP<sup>+</sup>00, KEOH01, EA03]. Author, however, does not

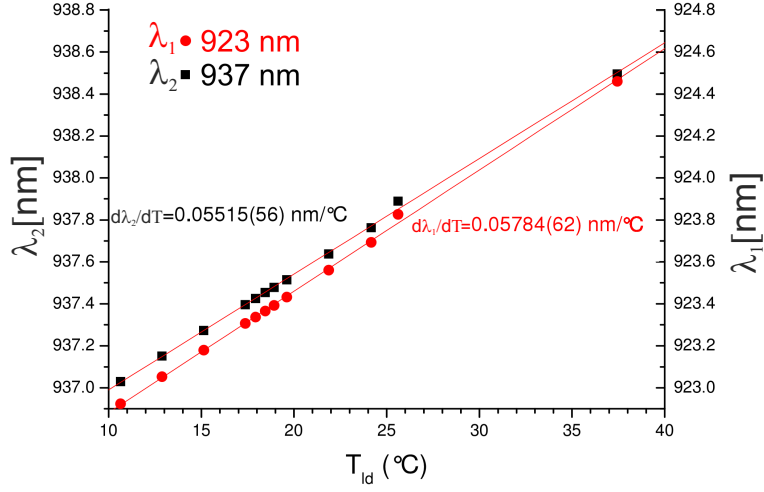


Figure 3.12: Infra-red laser diodes wavelength tuning within  $T_{LD}$  10-40°C range.

conclude about the reliability of these references in terms of the closest agreement with his result, as it has been obtained under approximation of SFG by SHG process as well as other approximations, discussed earlier, related to the PP-KTP crystal properties and geometry of the interaction with the light, were made (i.e. lack of exact  $d_{eff}$  value, no light absorption, focus in the center of the crystal etc.). The main goal here was checking the consistency of the matching relations between the crystal temperature and infra-red wavelength (for the ranges explored during further experiments on the molecular helium) with the experimental results shown in the subsection 3.3.3 .

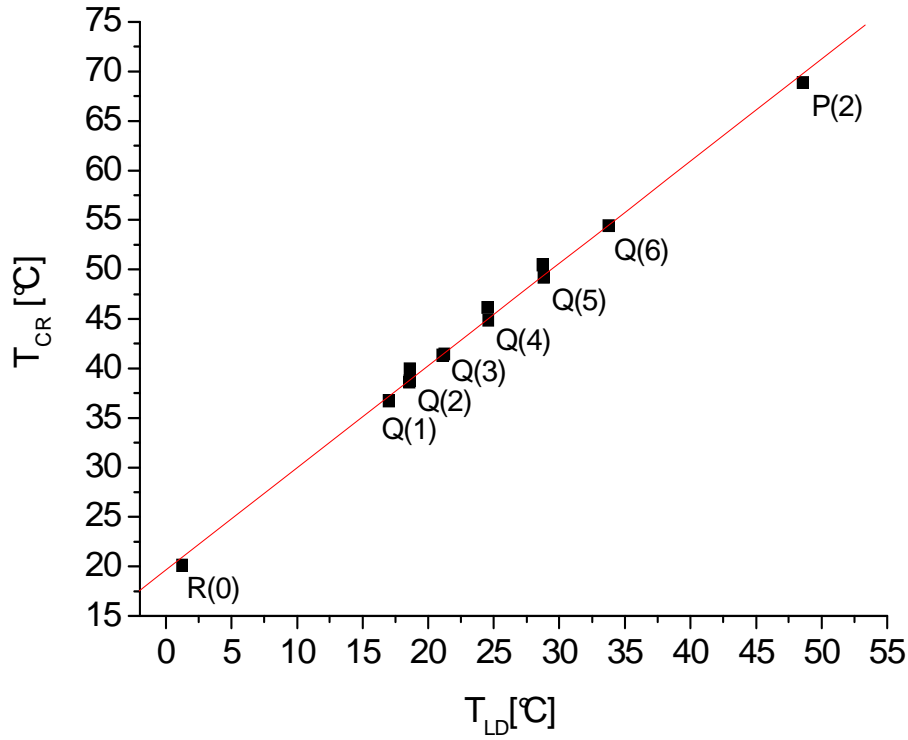


Figure 3.13: Crystal matching temperature and laser diodes temperature matching points fulfilling quasi-phase-matching conditions within available operating range. The parameters of the linear fit allows to write the functional dependency between both temperatures as follows:  $T_{cr} = 19.7(5) + 1.03(2) * T_{LD}$

#### (a) The slope of the matching line experimental determination

The equation for the matching line eq.(3.21) puts a strict constraint on the values of the experimental parameters  $T_{cr}$  and  $T_{LD}$  for which matching is actually achieved . They must satisfy:

$$\left. \frac{dT_{cr}}{dT_{LD}} \right|_{QPM} = \left. \frac{dT_{cr}}{d\lambda_{av}} \right|_{QPM} \frac{d\lambda_{av}}{dT_{LD}} \quad (3.29)$$

, where  $\left. \frac{dT_{cr}}{d\lambda_{av}} \right|_{QPM}$  is given by eq.(3.21).

The experimental value of the derivative  $\frac{d\lambda_{av}}{dT_{LD}}$  is obtained from the measurements of the infrared wavelengths  $\lambda_1$  and  $\lambda_2$  with the high resolution spectrometer (Fig.3.12):  $\frac{d\lambda_{av}}{dT_{LD}} = 0.05650(59)$  nm/°C.

The expected value of the coefficient  $\left. \frac{dT_{cr}}{d\lambda_{av}} \right|_{QPM}$  is obtained from the known values of the KTP bulk properties using equation (3.17), as follows:

$$\left. \frac{dT_{cr}}{d\lambda_{av}} \right|_{QPM} = \frac{-\frac{\partial}{\partial \lambda_{av}} \left[ \frac{\Delta k l}{2\pi} \right]}{\frac{\partial}{\partial T_{cr}} \frac{\Delta k l}{2\pi}}$$

The temperature derivative  $\frac{\partial}{\partial T_{cr}} \frac{\Delta k l}{2\pi}$  is given by eq.(3.19). Its first term on the right side of

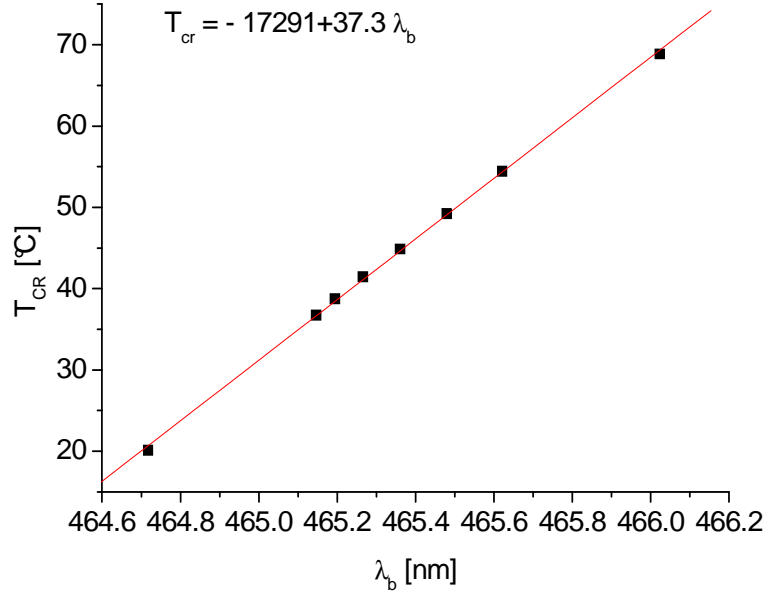


Figure 3.14: Crystal matching temperature versus output blue wavelength -  $\lambda_b$

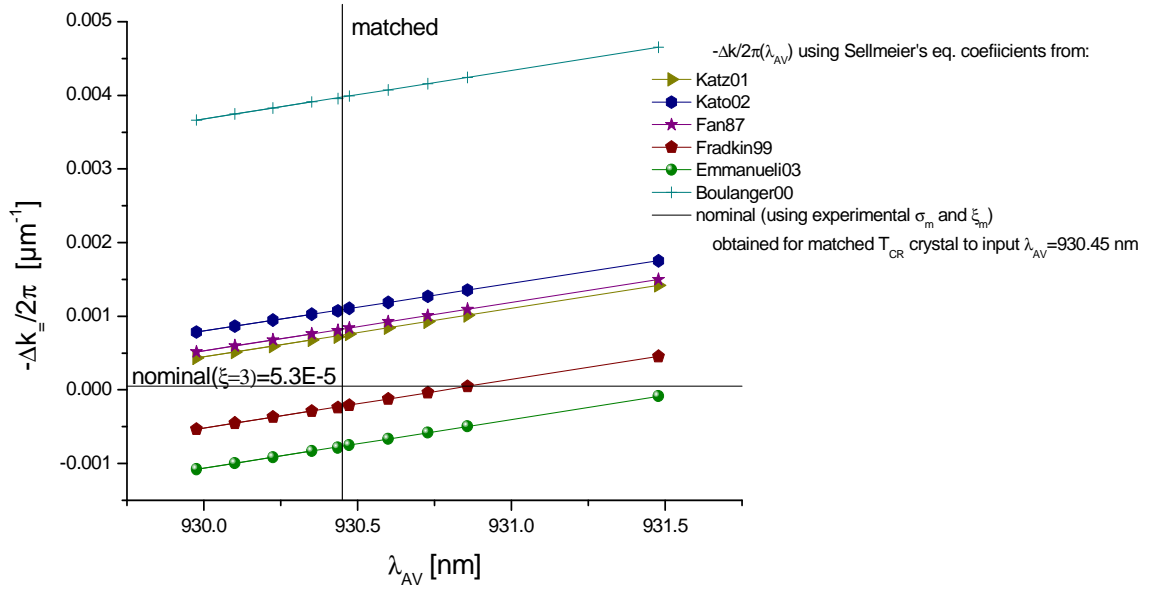


Figure 3.15: Computed  $\Delta k$  (phase-matched wavevectors difference) for fundamental beam wavelength in 930-931.5 nm range. Several data sets are obtained according to the different values of KTP Sellmeier's coefficients met in the literature. The computations are compared to the nominal value of  $\Delta k = 5.3 \cdot 10^{-5}$  for  $\xi=3$ .

equation equal:

$$2 \frac{l}{\lambda_{av}} \left[ \left. \frac{\partial n}{\partial T_{cr}} \right|_{T_{cr}, \lambda_{av}/2} - \left. \frac{\partial n}{\partial T_{cr}} \right|_{T_{cr}, \lambda_{av}} \right] = 2.15 \cdot 10^4 \left( \left. \frac{\partial n}{\partial T_{cr}} \right|_{T_{cr}, \lambda_{av}/2} - \left. \frac{\partial n}{\partial T_{cr}} \right|_{T_{cr}, \lambda_{av}} \right) \approx$$

$$\approx 2.15 \cdot 10^4 \cdot 1.6 \cdot 10^{-5} = 0.344^\circ \text{C}^{-1}$$



The last term, equal to  $\frac{2\alpha l}{\lambda_{av}}$  is negligible given  $\alpha = 0.6 - 11 \cdot 10^{-6} \text{ }^\circ\text{C}^{-1}$  [BV89],  $n(465\text{nm}) - n(930\text{nm}) = 0.08$  and  $\frac{2l}{\lambda_{av}=2.1510^4}$ , which gives a value in the  $(1 - 19) \cdot 10^{-3} \text{ }^\circ\text{C}^{-1}$  range.

Therefore, the value of the derivative is:

$$\frac{\partial}{\partial T_{cr}} \frac{\Delta kl}{2\pi} = 0.344^\circ\text{C}^{-1}. \quad (3.30)$$

The wavelength derivative  $\frac{\partial}{\partial \lambda_{av}} \left( \frac{\Delta kl}{2\pi} \right) = \frac{\partial}{\partial \lambda_{av}} \left( l \left( \frac{\Delta k_0}{2\pi} - \frac{1}{\Lambda} \right) \right)$  is given by eq.(3.20)

With:  $\left( \frac{\partial n}{\partial \lambda} \right) = -0.548 \mu\text{m}^{-1}$  for  $\lambda = 465 \text{ nm}$  and  $\frac{\partial n}{\partial \lambda} = -0.055 \mu\text{m}^{-1}$  for  $\lambda = 930 \text{ nm}$

as well as  $\frac{1}{\lambda_{av}} (n_b(T_{cr}, \lambda_{av}/2) - n_{av}(T_{cr}, \lambda_{av})) = \frac{1}{2} \frac{\Delta k_0}{2\pi} \approx \frac{1}{2\Lambda} = 9.96 \cdot 10^{-2} \mu\text{m}^{-1}$ .

the derivative  $\frac{\partial}{\partial \lambda_{av}} \left( \frac{\Delta kl}{2\pi} \right)$  is thus equal to:

$$\frac{\partial}{\partial \lambda_{av}} \left( \frac{\Delta kl}{2\pi} \right) = 2 \cdot 1.075 \cdot 10^4 \cdot (-0.319 \mu\text{m}^{-1}) = -6.85 \cdot 10^3 \mu\text{m}^{-1}$$

Finally, over the small tuning range of the laser, the matching line is a straight line with slope:  $\frac{dT_{cr}}{dT_{LD}} = - \left( \frac{-6.8510^3 \mu\text{m}^{-1}}{0.344^\circ\text{C}^{-1}} \right) * 0.0565 \cdot 10^{-3} \text{ nm}/^\circ\text{C} = 1.12$

This is in agreement within 6% with the experimental value 1.03 value (see fig.3.13).

### 3.3.3 Matching tolerances in the experiment

Important in terms of using the blue laser beam for the absorption measurements, especially for obtaining the full absorption line profiles, is the dependency of the output power on the laser diodes temperature tuning. The change of the fundamental wavelengths brings laser out of the optimal phase-matching condition unless the crystal temperature follows that change. Therefore, the output power in terms of regulated laser diodes temperature was measured with the crystal temperature set constant and the result is shown on the fig.3.16(b). Similarly the change of the output power in terms of regulated crystal temperature was measured while the laser temperature was constant - result on the fig.3.16(a). These dependencies are so-called phase-matching curves, as the generated harmonic power is shown versus the variables related to the phase-matching condition -  $T_{LD}$  and  $T_{cr}$ . Both dependencies have the same character - there is strong single maximum around the optimal phase-matching and a small side maximum - at lower and higher temperatures for the first and the second dependency respectively. The presence of the side maximum is well predicted by the Boyd-Kleinman focusing factor function  $h(\sigma, \xi)$  (see eq.(3.11b) and figure 3.2). The fact, that in the power vs  $T_{LD}$  the side maximum is on the left side of the strong one while it is reverse for power vs  $T_{cr}$  results from the sign difference in the derivative of phase mismatch  $\Delta k$  over  $T_{cr}$  and  $\lambda_{av}$  ( $\lambda_{av}$  is related to the  $T_{LD}$  of course and  $\frac{\lambda_{av}}{dT_{LD}} > 0$  - see fig.3.12).

The acceptance bandwidth (strong maximum full half-width) of  $\Delta T_{LD} = 2.7 \pm 0.4 \text{ }^\circ\text{C}$  for laser diode tuning and  $\Delta T_{cr} = 2.9 \pm 0.4 \text{ }^\circ\text{C}$ .

These figures 3.16(a) and 3.16 (b) are the experimental realization of the simulation curves presented in the section 3.1.2 - fig.3.2. Instead of the general phase mismatch parameter  $\sigma$  we

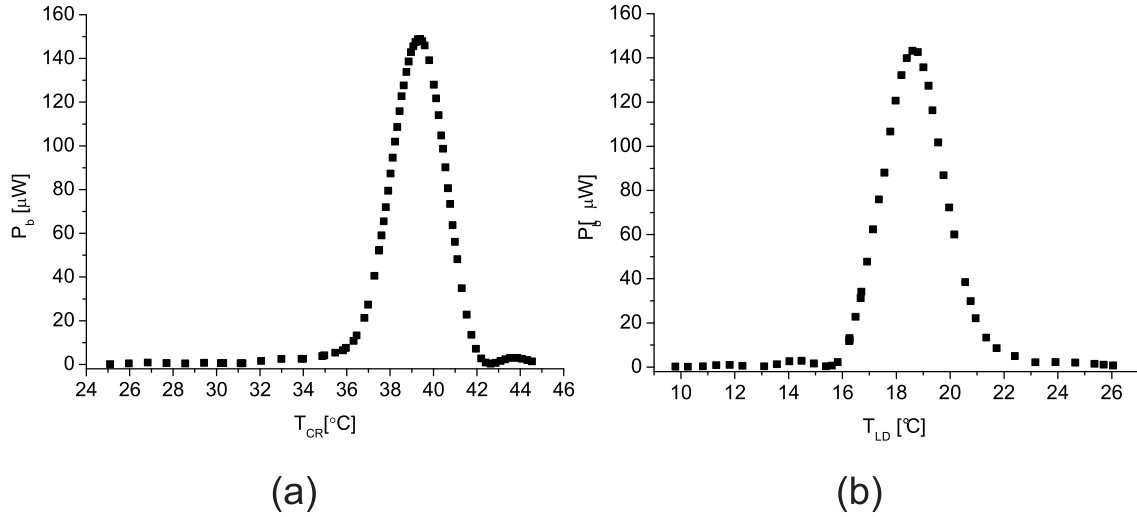


Figure 3.16: The phase-matching curves for the crystal (a) and laser diodes (b). (a) The  $T_{LD} = \text{const.} = 19^\circ\text{C}$  setting the  $\lambda_b = 465.1946\text{nm}$  (wavelength of Q(2) line of  $^3\text{He}_2^*$ ). (b)  $T_{cr} = \text{const.} = 39^\circ\text{C}$ .

have here the experimental matching parameters  $T_{cr}$  and  $T_{LD}$ , according to the relation eq.(3.22) and its discussion.

Therefore, writing eq. (3.11a) as  $P_b = Ah(\sigma, \xi)$  and expressing the  $\sigma$  parameter in the eq. (3.13) by the experimental matching parameters,  $X = T_{cr}$  or  $X = T_{LD}$ , according to eq. (3.22), one obtains:

$$P_b = A * \left| \int_0^1 \frac{\cos\left(\xi u(\sigma(X_0) + \left(\frac{\partial\sigma}{\partial X}\right)_{X_0}(X - X_0))\right) + \xi u \sin\left(\xi u(\sigma(X_0) + \left(\frac{\partial\sigma}{\partial X}\right)_{X_0}(X - X_0))\right)}{(1 + \xi u)^2} du \right|^2 \quad (3.31)$$

with  $X_0 = T_{LD}^{(0)}$   $X_0 = T_{cr}^{(0)}$  being the temperature values for optimal phase-matching when laser diode or crystal temperature is considered as a matching parameter.

To extract the parameters of the equation (3.31) such as  $A, \xi, \sigma(X_0)$  and  $\frac{\partial\sigma}{\partial X}\bigg|_{X_0}$ , one can perform the direct fit to the experimental data given on the figures 3.16 (a) and (b). However, as considered in the subsection 3.1.2, it is worth considering fitting function being the square root of the harmonic power  $P_b$ , as it is then more sensitive to the side lobes of the dependency.

The fitted curves of  $\sqrt{P_b}$  function are presented on the graphs 3.18 for laser diodes matching and 3.17 for crystal temperature matching. Output parameters of the fit are presented in the table 3.4.

The fitted value  $\xi = 3.0 \pm 0.07$  is close to the optimal value  $\xi_m = 2.84$ . This yields a phase-matched value of the Boyd function (obtained for  $\sigma_m = 0.556$ ) equal to  $h(\sigma_m, \xi_m) = 1.067 \pm 0.001$  versus 1.06767 - the value predicted for the most optimal case. The very good agreement within the error bar between the two values has been achieved.

The focusing parameter  $\xi = \frac{\lambda_{av} l}{2\pi n_{av} w_0^2}$  provides a measure of the fundamental beam waist inside the crystal,

$$w_0 = \sqrt{\left(\frac{l\lambda_{av}}{2\pi n_{av}\xi}\right)} = 16.4 \pm 0.2\mu\text{m}, \quad (3.32)$$

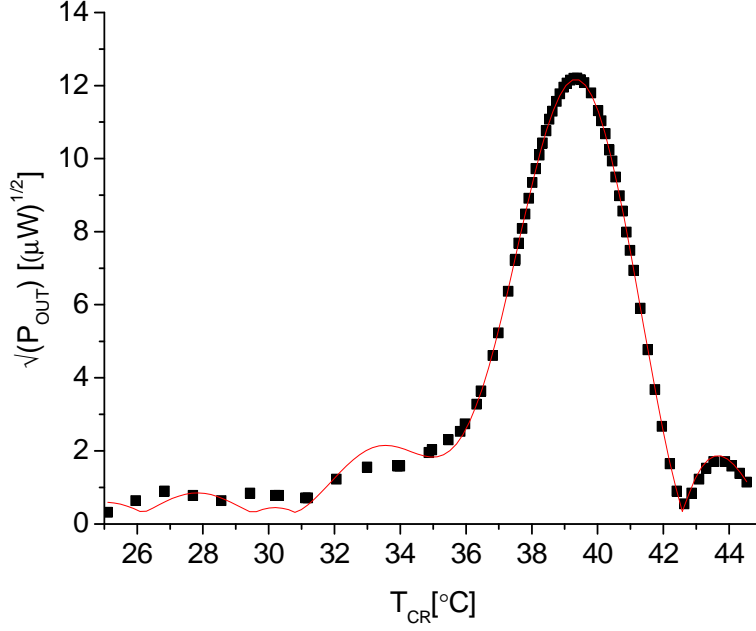


Figure 3.17:  $\sqrt{P_b}$  dependency on crystal temperature ( $T_{cr}$ ) as a matching parameter. The data are the same as presented on the  $P_b$  vs  $T_{cr}$  graph on the fig. 3.16 (a). Red curve represents fit function according to the eq.(3.31)

Fit parameter	$X = T_{LD}$	$X = T_{cr}$
$A[\mu W]$	$126 \pm 3$	$132 \pm 1$
$\xi$	$2.93 \pm 0.09$	$3.06 \pm 0.05$
$\sigma(X_0)$	$0.59 \pm 0.03$	$0.528 \pm 0.005$
$\frac{\partial \sigma}{\partial X} _{X_0} [^{\circ}C^{-1}]$	$0.42 \pm 0.01$	$-0.385 \pm 0.005$

Table 3.4: Results of the  $\sqrt{P_b}$  fit performed to the experimental data of  $T_{LD}$  and  $T_{cr}$  matching curves.

assuming perfect beam collimation without the divergence. Obtained value of the waist is close to the optimal value in our case ( $w_0 = 16.85 \mu m$  for our wavelength and  $\xi=2.84$ ) as well as in well agreement with the average resulting from different fundamental beams FWHMs - see table 3.3.

$\xi = 3.0$  also yields  $\sigma_m = 0.5556$ , what agrees with averaged fit parameter  $\sigma_0 \geq 0.568 \pm 0.04$  as well as  $\Delta\sigma_{1/2} = 1.1299$  used below for tolerance checks based on known PP-KTP dispersion and laser diodes features.

#### (b) Further results - consistency check of the $\sqrt{P_b}$ fits

The fit of experimental data for tolerance curves provides the value of  $\xi$  on which basis the phase-matching tolerance in terms of  $T_{LD}$  and  $T_{cr}$  can be calculated according to eq. (3.23) The  $\xi$  value determines the value of  $\Delta\sigma_{1/2}(\xi)$  (according to the table 3.1 and fig.3.5(a)) as well as allows computation of  $[\frac{\partial \sigma}{\partial X}]|_{X_0}$  when  $X = T_{LD}$  or  $X = T_{cr}$  according to the equations (3.25) or (3.24) respectively. The necessary values of  $\frac{\partial}{\partial T_{cr}} \frac{\Delta k l}{2\pi}$  and  $\frac{\partial}{\partial \lambda_{av}} \frac{\Delta k l}{2\pi}$  has been already computed in

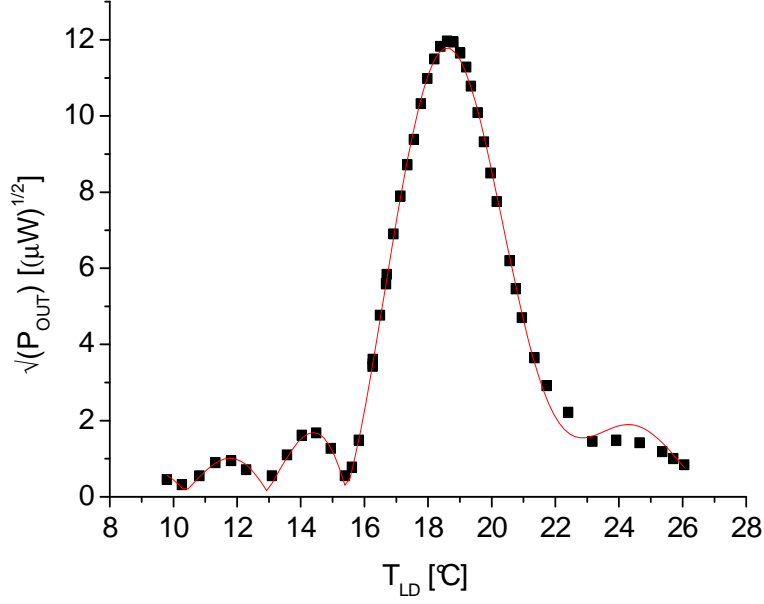


Figure 3.18:  $\sqrt{P_b}$  dependency on laser diode temperature ( $T_{LD}$ ) as a matching parameter. The data are the same as presented on the  $P_b$  vs  $T_{LD}$  graph on the fig. 3.16 (b). Red curve represents fit function according to the eq.(3.31)

subsection 3.3.2.2(a)

So that:

- For  $X = T_{cr}$

$$\text{Experimental } \Delta T_{cr} = \Delta\sigma(\xi = 3) \cdot \left[ \frac{\partial\sigma}{\partial T_{cr}} \right]^{-1} = \Delta\sigma(\xi = 3) \cdot \frac{\xi}{\pi} \left[ \frac{\partial}{\partial T_{cr}} \frac{\Delta kl}{2\pi} \right]^{-1} = 1.13 \cdot \frac{3}{\pi} \frac{1}{0.344} = 3.14^\circ\text{C}$$

It is in well agreement (within 6.6%) with the experimental value obtained from the phase-matching curve given on the fig.3.16(a).

- For  $X = T_{LD}$

$$\Delta T_{LD} = \Delta\sigma(\xi = 3) \cdot \left[ \frac{\partial\sigma}{\partial T_{LD}} \right]^{-1} = \Delta\sigma(\xi = 3) \cdot \left[ \frac{\pi}{\xi} \frac{\partial\lambda_{av}}{\partial T_{LD}} \frac{\partial}{\partial\lambda_{av}} \left[ \frac{\Delta kl}{2\pi} \right] \right]^{-1} = 1.13 \cdot \left[ \frac{\pi}{3} \cdot 0.0565 \cdot 6.85 \right]^{-1} = 2.79^\circ\text{C}$$

It is in good agreement (within 3.3%) with the experimental value obtained from the phase-matching curve given on the fig.3.16(b)

### 3.4 Summary and conclusions

The laser setup based on the Sum Frequency Generation Process has been built and characterized in terms of its efficiency and working parameters. It covers the wavelength range of 464.7 to 466.1 nm, where the lines of the  $a^3\Sigma_u^+$  (0)-  $e^3\Pi_g$  (0) transition for molecular helium are reported [DR50,BG71,DGD77] for three isotopologues:  $^4\text{He}_2^*$ ,  $^3\text{He}_2^*$  and  $(^3\text{He}-^4\text{He})^*$ . The tuning

range is sufficient for observation of the main rotational transitions of the dimer. Achieved conversion efficiency  $\eta_{SFG} = 5.3 \pm 0.2\%W^{-1}$  of the SFG process, within the estimated error bars, reaches the optimum value determined from the theory of nonlinear conversion. Also the analysis of the phase-matching tolerances is well confirmed by the experimental results, altogether legitimating several approximations that were made.

One especially important is that SFG process has been approximated by the SHG approach. The  $d_{eff}$  is not well defined value for our PP-KTP crystal resulting in the more than 1% uncertainty of the  $\eta_{SFG}$  estimation and the beams ellipticity has been considered in a simplified manner. Beside that, assumption of lack of the beams absorption inside the crystal, null walk-off angle and fundamentals beam focus position in the middle of the crystal has been made when Boyd-Kleinman focusing factor was introduced, what causes the  $\eta_{SFG}$  overestimation. In overall, having satisfactory agreement between the expectations and the result, performed analysis seems to be correct and sufficient for the laser performance evaluation before a further absorption experiments are made. Emitted power around  $200 \mu W$  is more than sufficient to perform absorption measurement on molecular helium species with good SNR. However, it could be increased by introducing several cavity modifications, e.g. multiple pass of the fundamental beams through the crystal achieved inside the resonator cavity. Additionally laser control, currently 100% manual, can be automatized, especially if it comes to the matching of the crystal temperature to the change of fundamental wavelength (change of the laser diodes temperature). One could also think about extending the wavelength tuning range, for example by cooling down the laser diodes less than  $0^{\circ}C$ , providing the air blowing onto the lenses not to allow the water vapor condensation. Going into higher temperature regimes one has to remember about the diodes life shortening then. Overall the performed calculations and expectations stay in agreement with experimental measurements results and fitting procedure. Behavior is in line with expectations for single-pass SHG in PP-KTP, for quasi-optimal optical configuration.



## Chapter 4

# Absorption measurements on helium molecule - experimental results

In this chapter the results of absorption measurements performed on helium molecules in metastable  $a^3\Sigma_u^+$  state of  $^3\text{He}_2^*$ ,  $^4\text{He}_2^*$  as well as  $(^3\text{He}-^4\text{He})^*$  are presented with use of the 465 nm laser described in chapter 3. The measurements were performed in sealed pyrex cells usually used for MEOP tests, filled with the gas (isotopic pure or mixture) at different pressures ranging from 8 to 267 mbar. The series of experiments was begun with absorption lines profiles recording from which their position in terms of laser diodes temperature settings was inferred, thus allowing the blue laser wavelength calibration. Using the mass scaling laws for vibrational and rotational constants between molecular isotopologues, heteronuclear dimer lines wavelength positions were calculated and confirmed by the experiment as well as by [DGD77]. The intensities of the absorption lines were used for rotational temperature determination according to eq. (2.51).

### 4.1 Experimental setup

The experimental configuration is a simple transmission measurement scheme. The the probe laser beam coming out from the blue laser setup (chapter 3) is transmitted twice through the absorber - plasma inside the OP cell (fig.4.1).

The blue beam passes the cell volume twice along its length at small angle with respect to the cylindrical symmetry axis of the cell. The beam is reflected by the MB mirrors - suitable for the visible wavelengths and its power is being measured by the photodiode (PDB) chosen for its sensitivity in the blue region (Silicon photodiode BPW 34, 0.15 A/W @465 nm). Double pass of the beam through the rf plasma filling the cell volume provides increased absorption signal in comparison to single pass, while elongating the beam path after the second pass in the cell by reflection on two MB mirrors reduces the amount of a stray light - fluorescent light from the discharge plasma entering PDB. As a complementary measurements the transmission of the IR probe beam through the same OP cell and plasma conditions can be investigated by simply putting the MIR - metallic mirrors of good reflectivity at 1083 nm in front of MB mirrors. The IR probe beam, delivered to the optical table by the fiber is send to the OP cell on similar path as in case of the blue light, and its power is measured by the photodiode PDIR suitable for this wavelength. The presence of the IR beam was mainly used for comparison between the absorption rates between atoms and molecules in the same pressure and plasma conditions, as

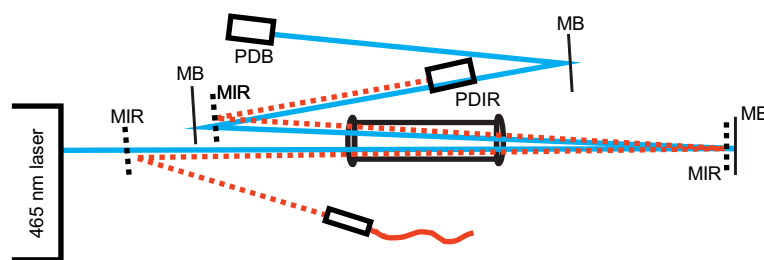


Figure 4.1: Optical setup scheme for absorption measurements on molecules (with use of 465 nm laser) and atoms (with use of 1083 nm laser). The measurements on both species has to be performed independently as it is required to put the optical elements suitable for 1083 nm (red dashed line - IR beam path, black dashed lines - MIR metallic mirrors and PDIR - photodiode for infra-red wavelength) on the way of blue beam (solid blue line - beam path, solid black line - MB - mirrors and PDB - photodiode for visible wavelengths).

well as to compare the dynamics of the density decay of both species when the rf excitation is turned off.

Depending on the purpose of the experiment - molecular absorption measurements with blue laser frequency scans or investigations on the density decay times two different experiment schemes can be distinguished and will be described in following subsections.

#### 4.1.1 Cell and rf discharge

Absorption measurements on the molecules with use of the blue laser beam were performed in a sealed cells, made of Pyrex, filled with helium under various pressures of isotopic pure  $^3\text{He}$ ,  $^4\text{He}$  or 1:1 mixture. The table 4.1 presents the details about the size and filling pressure (in mbar) , filling temperature (in  $^{\circ}\text{C}$ ) and the gas density (in amagats). Each of the cell was so called bone-shaped, meaning that the both ends of the cylindrical tube (15 mm inner and 18 outer diameter for each cell), where the optical windows are welded, expand to about 25 mm diameter corresponding to round windows size.

Before the gas cells were filled with helium at desired isotopic content and pressure a careful cleaning procedure of a glass is performed. The cell is rinsed with ethanol, baked out for several days under vacuum conditions (about  $10^{-8}$  mbar). After that strong rf-discharges in helium are applied with several gas changes until only spectral lines of helium are observed in the plasma fluorescence [Bat11].  $^4\text{He}$  is used for the cleaning discharges for cells filled with  $^4\text{He}$  or isotopic mixtures.  $^3\text{He}$  is used for cells filled with  $^3\text{He}$  and in which the final isotopic purity is important.

The radiofrequency voltage required for helium plasma generation was delivered to the optical cells through circular electrodes, wired around on the outer surface of the cylinder, alternately in respect to the applied voltage sign with about 1 cm spacing. Radiofrequency output signal (frequency around 2 MHz) from the generator was amplified by a 20 W amplifier and applied on the electrodes through a voltage transformer. Discharge amplitude modulation of the rf power (around 70 Hz) could be used as an internal setting of the voltage generator.



Isotopic content	Designation	Filling pressure [mbar]	Filling temperature[°C]	Gas density [amagat] $\times 10^{-2}$	Cylinder length [mm]
$^3\text{He}$	8 mbar	8.219	25	0.74	116.5
	66.7 mbar	66.77	24.6	6.05	112.6
	128 mbar	128.43	27.6	11.51	114.2
	267 mbar	267.2	20.4	24.54	112.1
$^4\text{He}$	66.7 mbar $^4\text{He}$	66.86	24	6.07	112.5
$^3\text{He}$ and $^4\text{He}$ 1:1 mixture	66.7 mbar mixture	66.84	23.2	6.08	112.5

Table 4.1: The list and parameters of sealed optical cells made of Pyrex used in the experiment filled with helium under various pressure and isotopic content. Filling pressures and temperatures are given allowing gas density computation. Each cell is so-called bone-shaped with: cylindrical tube external diameter 18 mm (internal 15 mm) with expanding diameter at both ends of about 25 mm- diameter of optical window of 2 mm thickness. The cylinder length values given in the table is the internal length.

#### 4.1.2 Laser frequency scans. Acquisition scheme

The acquisition and setup control scheme for the realization of frequency scan absorption measurements with use of the 465 nm laser setup is presented on the fig.4.2.

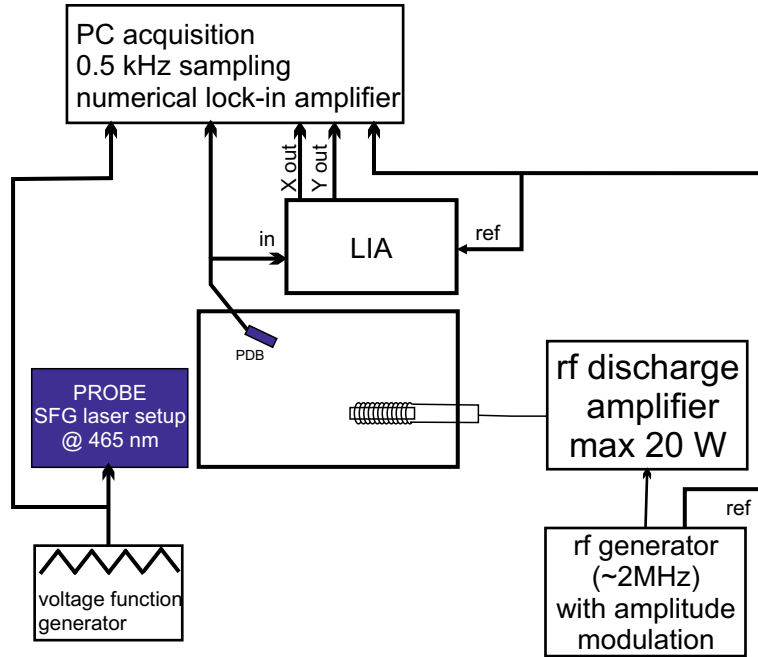


Figure 4.2: Scheme of the acquisition setup for the absorption frequency scans using voltage (triangle course of the  $V(t)$  function) control of 937 nm laser diode current supply being a component of the blue laser setup.

The transmitted power of blue laser beam through the OP cell is measured by the photo-diode PDB and the output signal is sent to the input of the lock-in amplifier (LIA) as well as

the PC USB acquisition card (Data Translation DT9816). Lock-in detection has been applied together with the rf voltage discharge excitation amplitude modulation, so that the distinction between plasma response to the laser absorption and power fluctuations of the light source can be performed increasing the SNR. 100% of square or partial (up to about 20%) sine amplitude modulation at frequency of a few tens Hz was provided by the voltage generator of which TTL modulation reference signal was sent to the lock-in amplifier and to the PC acquisition card. The rf voltage was then amplified by 20 W power amplifier and sent to the tuned rf transformer circuit and then to the wire electrodes wound on the OP cell with alternating polarity. The output signals from X and Y (in-phase and quadrature components) channels are sent to the PC acquisition card. The wavelength emitted by the blue laser setup was controlled by the voltage function generator delivering periodical triangle signal to the 937 nm laser diode power supply causing the linear response in the feeding current of the diode, thus allowing emitted infra red wavelength change what results in change of blue laser wavelength as well. The triangle signal has been recorded during the frequency scan measurements.

### 4.1.3 Frequency scans recordings procedure

The blue laser frequency scans were performed to obtain full absorption line profiles for the these He<sub>2</sub><sup>\*</sup> isotopologues transitions that are available within the laser tuning range. In case of the homonuclear molecules single line profiles scans were performed, while for the heteronuclear isotopologue triplets and even quartets of the absorption lines were present on the single scan. The main restriction in the frequency range value that could be reached in a single scan lies in the departure from the phase matching condition as well as in the drop of the 937 nm lasing power when the feeding current value is being lowered - increase of the current above the maximum specified by the manufacturer also had to be avoided. In fact, the scans within the wavelength range of about 0.07 nm can be performed corresponding to  $\pm 10$  V peak-to-peak amplitude of triangle voltage signal. Usually, however, the voltage amplitude  $\pm 5$  and  $\pm 10$  V were used, depending on the presence of multiple neighboring lines within about 0.07 nm range (helium isotopic mixture cell) or intention of recording full single line profile with long recording of the baseline level for accurate peak height and shape determination. The frequency of the triangle voltage was set to 0.001 Hz and 0.0005 Hz for short ( $\pm 5$  V) and long ( $\pm 10$  V) scans of which the duration was set to 12.5 and 25 minutes providing equal speed of the voltage driven current change of the laser diode. The acquisition was performed with the sampling frequency 500 pts/s.

Before each laser frequency scan of the single line profile the blue laser was roughly tuned (by the change of the laser diodes and crystal temperature) to the maximum of the chosen absorption line with help of the lock-in amplifier present in the acquisition scheme. In case of the scans of the multiple neighboring lines the blue laser wavelength was roughly set in between the two extreme lines positions. During the frequency scan the laser diodes temperatures as well as crystal's were not changed. As it has been shown on the fig. 3.11 (subsection 3.3.2.1) the linear wavelength change in function of the voltage changes the slope with the laser diodes temperature, what has been taken into account when the transformation between internal voltage scan scale to more appropriate in further considerations GHz or nm units has been performed.

#### 4.1.4 Measurements of the density decay times

To compare the atomic and molecular dynamics the laser transmission change recordings after the source of the rf excitation is turned off has been performed. In this experiments the laser had to be constantly tuned to the maximum of chosen absorption line - for the helium atoms the infra-red laser was tuned to the  $C_8$  transition for  $^3\text{He}^*$  and  $D_0$  for  $^4\text{He}^*$  (see fig.4.3). In the mixture cell measurements on the atoms, the  $C_{6-7}$  line had to be chosen because both  $C_8$  and  $C_9$  overlaps with  $D_{1-2}$  lines (see Fig.5.2).

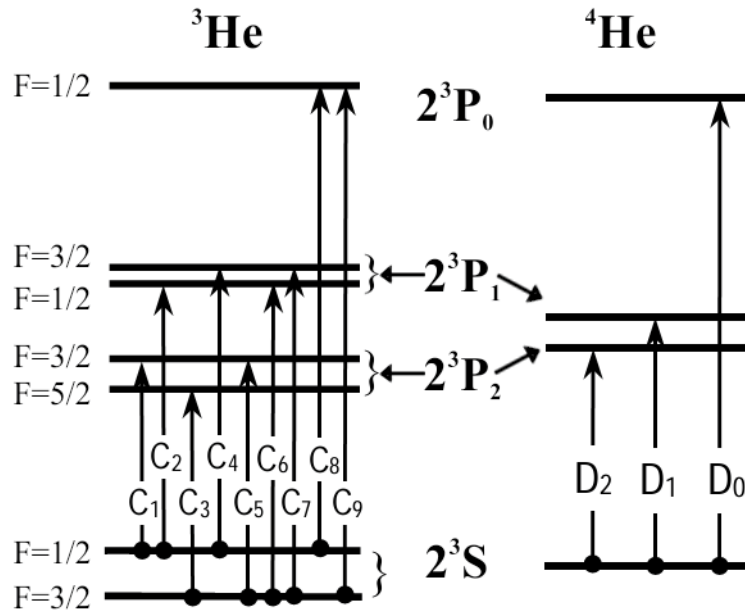


Figure 4.3: Diagram of  $2^3S_1$  and  $2^3P$  states of  $^3\text{He}$  and  $^4\text{He}$  with possible optical transitions signed as  $C_1$  to  $C_9$  and  $D_0$  to  $D_2$  respectively [NL85]. The examples of the absorption spectrum corresponding to these diagrams is given on the fig.5.2

For the molecules, depending on the isotopologue:  $^3\text{He}_2^*$  - Q(2),  $^4\text{He}_2^*$  - Q(3),  $(^3\text{He}-^4\text{He})^*$  - Q(3) - as those lines provide the highest SNR of all in the available spectra parts for each isotopologue. The tuning of the blue laser wavelength to the line maximum was performed relying on the lock-in displayed demodulated signal of absorption. Basically the setup configuration shown on the fig.4.1 has been used and the output voltages of the photodiodes were sent directly to the oscilloscope device providing on-line observation of the transmission signal. 100% square amplitude modulation of the discharge plasma was applied at the frequency between 10-50 Hz (depending on the pressure and species under investigation 10-20 Hz for molecules and more for atoms). The TTL signal of the modulation has been used as a trigger signal for the oscilloscope. The frequency of modulation has been chosen to provide switching off the discharge for the time sufficient for recovery of full laser transmission value when there is no absorption due to lack of absorbing molecular or atomic species. The oscilloscope device allowed using up to 512 recorded signals (each resulting from single modulation period) averaging what was necessary due to observed microphonic noise on the laser intensity occurring from time to time. The recordings provided direct values of the laser transmitted power through the helium cell in both situations of discharges *on* (beginning of the decay recording) and for discharges *off* (asymptotic value at the end of the decay curve). This allows absorption rates

calculation during all the decay and thus the transmission value  $T$  that is convenient value in further considerations as the  $-\ln(T)$  is directly proportional to the absorber density.

## 4.2 Data processing and data reduction

Basic spectroscopy measurements performed on the helium molecule between its metastable  $a^3\Sigma_u^+$  and  $e^3\Pi_g$  states including three isotopologues  $^3\text{He}_2^*$ ,  $^4\text{He}_2^*$  and  $(^3\text{He}-^4\text{He})^*$  relies mostly on the transition lines absorption profiles available in the wavelength tuning range of the blue laser setup (chapter 3). The rough determination of the line positions, their number in considered range as well as relative amplitudes was based on the reading of the absorption signal on the hardware lock-in amplifier display. For isotopic pure ( $^3\text{He}$  and  $^4\text{He}$ ) helium cells it allowed to assign the molecular transitions within the rotational structures of both states to the observed lines, by comparison of the splittings between them and the relative heights (characteristic intensity alternation with 1:3 ratio for  $^3\text{He}_2^*$ , absence of even-N numbered lines for  $^4\text{He}_2^*$ ) with reference data of [DR50, GB70]. The  $(^3\text{He}-^4\text{He})^*$  line positions, both in the wavelength scale and then the laser parameters settings, were first determined in the calculations using the mass scaling rules for the molecular constants and then experimentally confirmed in the frequency scans in 1:1  $^3\text{He}:^4\text{He}$  helium mixture cell.

Accurate determination of the line positions in terms of the laser work-settings (also used to the blue laser setup absolute wavelength calibration), line shapes and the absorption rates has been made by performing and analyzing the frequency scans of the full absorption line profiles. They were performed by the blue laser light transmission measurement for continuously changed wavelength in the vicinity of earlier determined rough line position. This section describes the way that the recorded data from frequency scans has been processed and parameters as line position and absorption were extracted. Apart from the molecular absorption lines profiles the decay times of the molecular and atomic species densities have been investigated, however the data processing here was reduced to only averaging of the discharge *off* signal period at the end of the decay curve when no absorption was expected and asymptotic value was reached, so that the time-change in the transmission  $T$  values could be determined. Then the values of  $-\ln(T)$  has been calculated and plotted as a function of time, reflecting directly time evolution of the atomic and molecular densities.

### 4.2.1 Processing of the recorded data files in numerical lock-in software

Recorded during the 465 nm laser frequency scans data files were processed in the numerical lock-in software written by P.-J. Nacher to demodulate the transmission signal directly from the PDB photodiode. The program was also used in case of signals demodulation of MEOP measurements recordings and its detailed description is given in the subsection 5.4.3.1 as well as in [Bat11]. The data recorded by the acquisition program contain also the X and Y (in-phase and quadrature) outputs of the hardware lock-in amplifier. However, it was found to be more convenient to use the numerical demodulation due to possible repeated choice of lock-in settings as time constant and phase. The only difference lock-in output files in comparison with the MEOP recordings is the generic content of the program, that here are:

- time scale of the experiment

- 937 nm laser diode current driving voltage triangle function
- magnitude (R) of the demodulated signal divided by the averaged transmitted signal of the blue beam
- in-phase (X) component of the demodulated signal divided by the averaged transmitted signal of the blue beam
- quadrature (Y) component of the demodulated signal divided by the averaged transmitted signal of the blue beam

The choice of using the demodulated signal magnitude R or in-phase X component for further analysis has to be made. Provided that the phase value is correctly chosen so that the quadrature (Y) component remains equal to 0 during all the frequency scan, both R and X data are nearly equal, except the cases where the SNR reaches low values and low signal amplitudes are biased as a result of the Rician noise (see [Bat11]).

Having calculated the in-phase and quadrature components together with the magnitude of the signal becomes important when processed photodiode voltage contains contributions other than just the targeted transmitted power. As only the phase amplitude is pure additive quantity it allows to properly remove them.

Making the ratios of magnitude, in-phase and quadrature of the transmission signals to the averaged transmitted signals for each of the beams allows reducing effects of laser intensity fluctuations and of optical thickness of the gas on measured absorptions [CMN<sup>+</sup>02, Bat11]. These ratio for magnitude (and in-phase component if the phase is properly set) is proportional to the absorbing species density provided that the rf discharge modulation depth do not exceed about 20% of peak-to-peak discharge voltage variation amplitude [Cou01].

It is important from a practical point of view, that the mentioned signals delivered in the output files of used numerical lock-in software are pure peak amplitudes of sinusoidal oscillation due to the discharge modulation, contrary to the hardware lock-ins that provide RMS (root mean square) values ( $R^{RMS}$ ) at their output ( $1/\sqrt{2}$  of the peak value in case of sinusoidal change). Furthermore, all the signals included in the output files are corrected for any DC offset in the input data acquired directly from the photodiodes, so that the values of magnitudes ( $\sqrt{2}R^{RMS}$ ) divided by the time-averaged transmission signal ( $\langle PD \rangle$ ) corrected for the DC offset ( $S_{\emptyset}$ ) can be written as:

$$OUT_nLIA = \frac{\sqrt{2}R^{RMS}}{\langle PD \rangle - S_{\emptyset}} \quad (4.1)$$

An example of demodulated signal, proportional to the absorbancem as a function of the recording time is shown fig.4.4 together with the variation of the voltage function applied to the 937 nm laser diode current supply.

Comparing the position of the lines during one recording that included 1.5 of voltage course period it is shown that the hysteresis of the line maximum position is present. Value of the difference between positions for the negative and positive slope is approximately constant - independent of the considered transition line or the isotopologue and varies between 0.15-0.17 V. The examples of the line position determination are shown and discussed in the next subsection 4.2.2. There is also a small difference of about 0.04 V in position of the lines recorded with the same slope. This values were taken into account when the errors of the

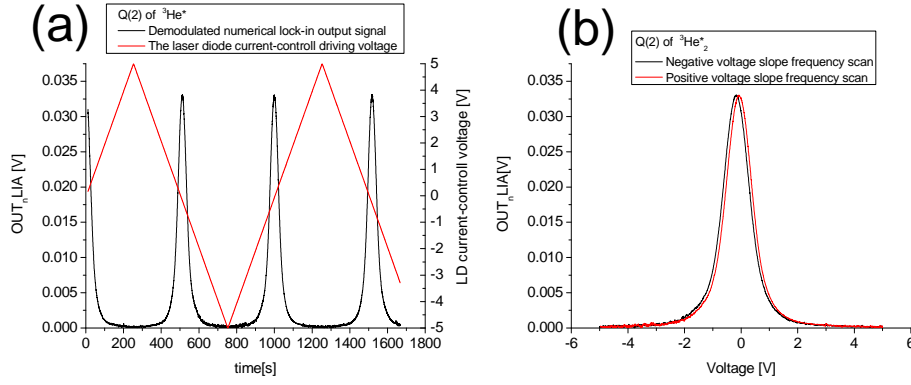


Figure 4.4: (a) Demodulated signal for transmitted blue laser (black solid curve) with laser diode current control triangle voltage (red dashed curve) in function of the recording time. The record last 1.5 period of the voltage triangular function allowing comparison of the line profiles and positions reproducibility with the negative (solid black) and positive (solid red) voltage slope (b).

positions of the line were being determined. To increase the reproducibility and to standardize the analysis procedure, only the line profiles recorded within negative slope of the voltage change were taken into account in further considerations, except for the determination of the line position to the blue laser calibration purposes, where the average of the values on negative and positive slopes were taken as the final value. Simultaneous recording of the transmission signal and the current-control voltage allowed simple scaling of the line profiles in terms of the voltage value on abscissa.

#### 4.2.2 Absorption line profile position determination

Accurate determination of the position of recorded absorption lines in voltage scale and then expressing in the temperature was needed to calibrate the laser setup settings of laser diodes temperature with respect to the line positions in the wavelength scale reported in [DR50,BG71]. For the purposes of the laser calibration the data from scans of 66.7 mbar isotopic pure  $^3\text{He}$  and  $^4\text{He}$  cells were chosen providing high SNR of the observed lines as well as moderate line pressure broadening - the choice is a compromise between the signal magnitude and accuracy of position determination due to the broadening effect.

In this pressure conditions, due to comparable effects of Doppler and collisional broadening effects, separately being described by the Gaussian and Lorentzian line shape functions, the line profile has to be considered as their convolution - Voigt profile. If the observed line profiles would correspond to the single transitions between  $a^3\Sigma_u^+$  and  $e^3\Pi_g$ , then the line position and amplitude would be reduced to Voigt function fit to the experimental data. However, as it is presented in the section 4.3, the line profiles uncover the underlying structure being more (odd-N numbered transitions) or less (even-N numbered transitions) distorted from the expected Voigt shape. Thus, in these conditions the fit of such function is assumed to be flawed with the systematic error, especially for odd-N numbered lines. On the other hand it is known, that the top part of the Voigt profile is mostly influenced by the Gaussian component while the bottom of the line by the Lorentzian. Relying on this property, the Gaussian function fit was performed to the top peak part from about 2/3 of amplitude maximum. In this way - from the

difference between position from Voigt and Gaussian function fits, the additional error value was determined for the recorded line position that, in fact, was taken from the Voigt fit.

Summarizing, in the value of the total error for the position value, the hysteresis value takes into account, the small discrepancy between profiles within chosen voltage change slope as well as the difference in positions resulting from the Voigt and Gaussian fits. While the first two mentioned are approximately independent of the recorded line transition and isotopologue, the last varies due to mentioned line underlying structure and distortion - for even-N numbered and N=1 line amounts to about 0.01 V and 0.14 V for odd-N numbered lines.

Apart from the position of the absorption line determination, the Gauss function fits to the values above 2/3 of the amplitude were performed to obtain accurate value of the amplitude assuming that the baseline level is 0, what leads to an relative error less than 5% in each case, mostly less than 1% of the amplitude value. The relative amplitudes are used later for rotational temperature determination, where the underlying line structure has been neglected and it is assumed the lines correspond to the single transitions between the rotational sublevels described by the rotational numbers N of the states involved in the transition.

### 4.2.3 Absorbance and demodulated signal relations

Presented on the fig.4.4 line profiles ordinate axis is a raw data from the numerical lock-in output file. This signal should be of course transformed to the quantity directly related to the absorber density - molecular density  $N_M$ . According to the B this quantity is absorbance being  $a - \ln T \propto N_M$ , where  $T$  is a transmission coefficient defined as:

$$T = \frac{S_{trans} - S_{\emptyset}}{S_{inc} - S_{\emptyset}}, \quad (4.2)$$

where  $S_{inc}$  and  $S_{trans}$  are measured photodiode signals corresponding respectively to the maximum of transmitted power (no absorption - incident laser power before interaction with plasma) and incident beam power weakened through the absorption process in plasma.  $S_{\emptyset}$  is the DC offset photodiode signal.

It has been written earlier, that the value of numerical lock-in magnitude R divided by the average input signal corrected for the offset value is the amplitude modulation depth - value directly proportional to the absorbance [TBNT11, Cou01], what can be written as:

$$-\ln T \propto \frac{S_{inc} - S_{trans}}{\langle PD \rangle - S_{\emptyset}} \quad (4.3)$$

Proportionality factor depends on the function shape of the amplitude modulation used in the frequency scan experiment - 100% square or partial sine.

In next two paragraphs the extracting of information about the absorbance value is described for 100% and partial sine modulations.

#### 4.2.3.1 100% square modulation

**(a) Absorption determination from hardware lock-in output signal** In the square function 100% amplitude modulation scheme, the discharge is periodically switched *off* and *on* - the maximum (no absorption) and the minimum (steady-state absorption). The time-course of the measured transmitted signal for this modulation has the form of a square wave with peak-to-peak amplitude  $a_1$  equal to  $(S_{inc} - S_{trans})$ . The hardware lock-in amplifier provides  $R^{RMS}$

value of the signal. For a square-wave modulation  $R_{RMS} = \frac{2}{\pi} \frac{a_1}{\sqrt{2}}$ . Therefore, for a 100% amplitude modulation, the absorbance can be determined from the lock-in output signal using the equation:

$$-\ln T = \frac{\pi}{2} \frac{\sqrt{2} \cdot R^{RMS}}{\langle PD \rangle - S_{\emptyset}} = \frac{\pi}{2} \cdot OUT_nLIA \quad (4.4)$$

#### 4.2.3.2 Partial sine amplitude modulation

With the partial (small < 10%) amplitude sine modulation the relation between the lock-in output  $R^{RMS}$  (or  $a_i = \sqrt{2} \cdot R^{RMS}$ ) value and  $(S_{inc} - S_{abs})$  is not usually known qualitatively (it is not approximately  $\frac{\pi}{2}$  anymore as for 100% square modulation). This is in spite of the fact that, even the rf voltage amplitude modulation can be quantitatively defined, the plasma response and thus variation of the absorbing species - metastable atom or molecules, does not necessarily exhibit the same level of modulation as the driving voltage. This was not an issue for 100% square modulation, where the discharge are just toggled between steady-state and off values. For the partial modulation, there is unknown prefactor ( $\equiv \varepsilon$ ) associated to the actual modulation depth of the absorbers density and the absorbance reads:

$$-\ln T = \frac{\varepsilon \sqrt{2} \cdot R^{RMS}}{\langle PD \rangle - S_{\emptyset}} \quad (4.5)$$

Any attempts to compute the  $\varepsilon$  cannot provide enough precise values. An empirical way to determine the value of  $\varepsilon$  factor for discharge modulation rate and a given set of rf excitation conditions (frequency, amplitude) at given gas pressure is measure the absolute value of the absorbance for 100% square modulation with the probe laser tuned to the transition frequency and then switch to sine modulation, with the laser tuned at the same frequency. For a small enough amplitude of modulation the average metastable atoms number density is approximately constant and equal to the previous steady-state value during the "discharge on" half period, and  $\varepsilon$  can be deduced from the comparison of the two displayed RMS values. For each pressure cell, the discharge intensity and sine modulation amplitude the determination of the  $\varepsilon$  factor has been performed in each series of the frequency scans. Once determined for certain discharge conditions, this value of  $\varepsilon$  factor can be used to determine the peak amplitude absorption for the laser tuned to other transitions.

### 4.3 Absorption lines shape

The absorption lines profiles presented in this section have been recorded using voltage control of the laser diode 937 nm feeding current after rough positioning of the laser wavelength on the line center using the laser diodes temperature controller. On all the figures presenting the absorption lines shapes the abscissa scale named as "frequency" is actually a detuning of the laser frequency from the value when no voltage is applied to the 937 nm laser diode current controller.

Absorption line profiles obtained in the recordings can be distinguished in terms of the value of  $N$  rotational number. The distortion of the lineshape (which for the single transition is expected to be described by Voigt function) corresponding to odd- $N$  numbered transitions is visually greater than in case of even- $N$  numbered transitions, as it is compared on the Fig. 4.5.



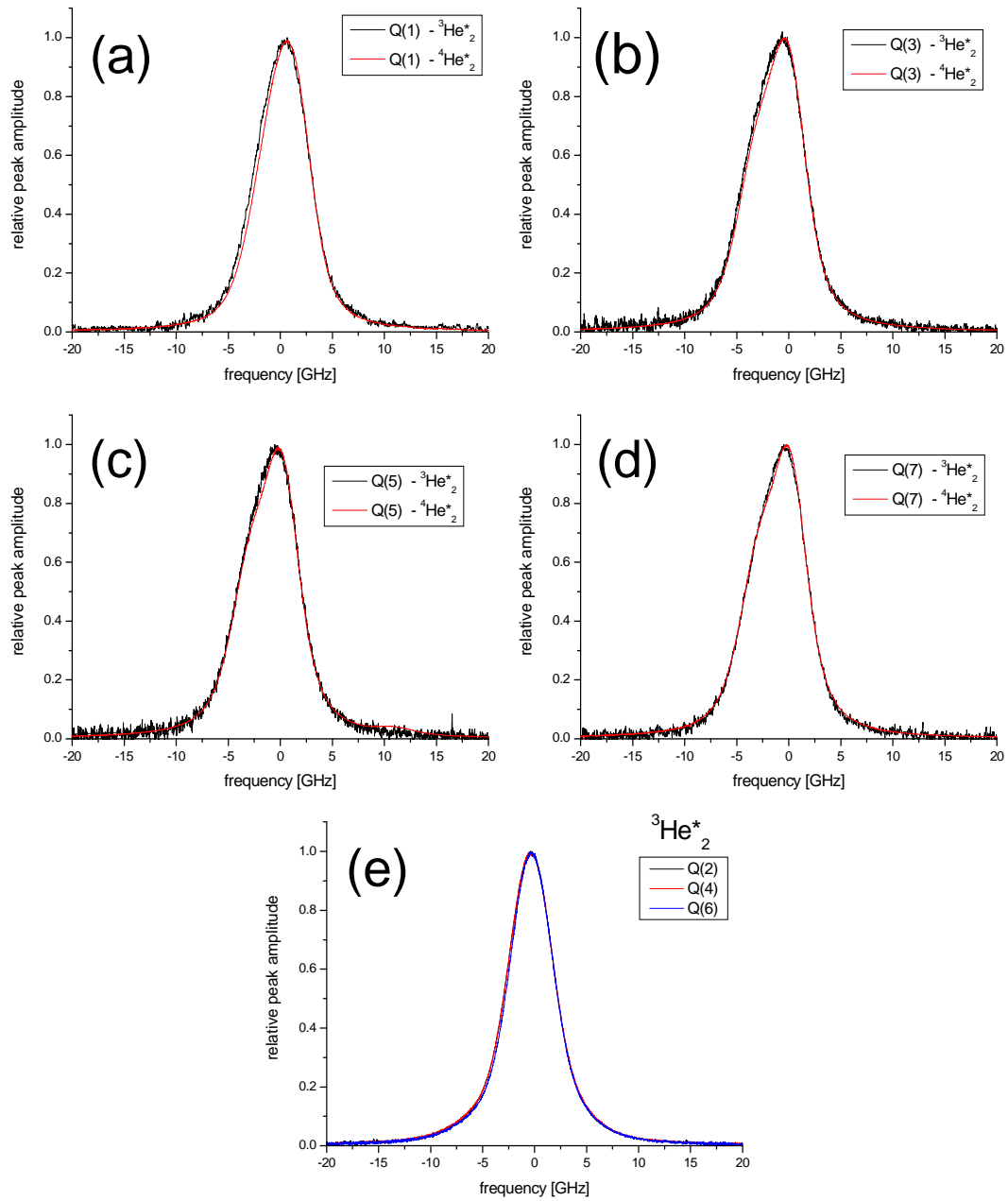


Figure 4.5: Comparison of the molecular absorption lineshapes of Q branch of two isotopologues  $^3\text{He}_2^*$  and  $^4\text{He}_2^*$  (pure gas cells, 66.7 mbar). Graphs (a)-(d) present pairs of the lines with the same odd-N value. Graph (e) shows the even-N numbered lines of  $^3\text{He}_2^*$ . The SNR of the odd-N numbered Q lines of  $^3\text{He}_2^*$  is lower than of the  $^4\text{He}_2^*$  due to 1:3 statistical ratio of the line intensities.

The motivation of choice of the 66.7 mbar pressure for lineshapes investigations discussion is a compromise between increase of the molecular absorption with the pressure and collisional broadening that tends to shade the details of the line structure. Recordings of the line profiles performed for the pure  $^3\text{He}$  gas at 8 mbar (Fig.4.6(a)) with low SNR bring no additional information except that the odd-N numbered lines are distorted in the same way - here any difference in the top peak part can't be distinguish due to the noise, as well as determination of any difference in peaks FWHM is not possible - they seems to be equal within the data points scatter. Here, even the Q(1) tends to be distorted as higher odd-N numbered Q-lines. On the other hand, line profile scans in the high pressure pure  $^3\text{He}$  cells as 128 (Fig.4.6(b)) and 266 mbar (Fig.4.6(c)) do not allow to observe characteristic distortion due to the pressure broadening effect. However, here still the Q(1) is outstanding from other odd-N numbered lines as it was the case for 66.7 mbar cell both in pure  $^3\text{He}$  and  $^4\text{He}$  cells.

On the frequency scan of line Q(5) of  $^4\text{He}_2^*$  (Fig.4.5) there is additional line present at longer wavelength from the Q(5) position. This line was identified as R(5) of the (1-1) vibrational band. Another example of such close-lying lines is the P(2) of  $^3\text{He}_2^*$  (considered (0-0) band) with R(2) of (1-1) band, however, here the lines are on the same wavelength positions (see reference data [DR50]) thus no resolving is possible.

The only difference between odd-N numbered lines for  $N>1$  of both  $^3\text{He}_2^*$  and  $^4\text{He}_2^*$  is broader top part (above about 0.7 of the relative amplitude) of the lines for the former molecule. The only exception in the line profile shapes for odd-N numbered transitions is the line for  $N=1$ . For both  $^4\text{He}_2^*$  and  $^3\text{He}_2^*$  it is the line that exhibits distortion in a lesser degree and is rather similar to the even-N numbered  $^3\text{He}_2^*$  lines, however still, the Q(1) line is broader than the Q(2). what is shown on the fig.4.7.

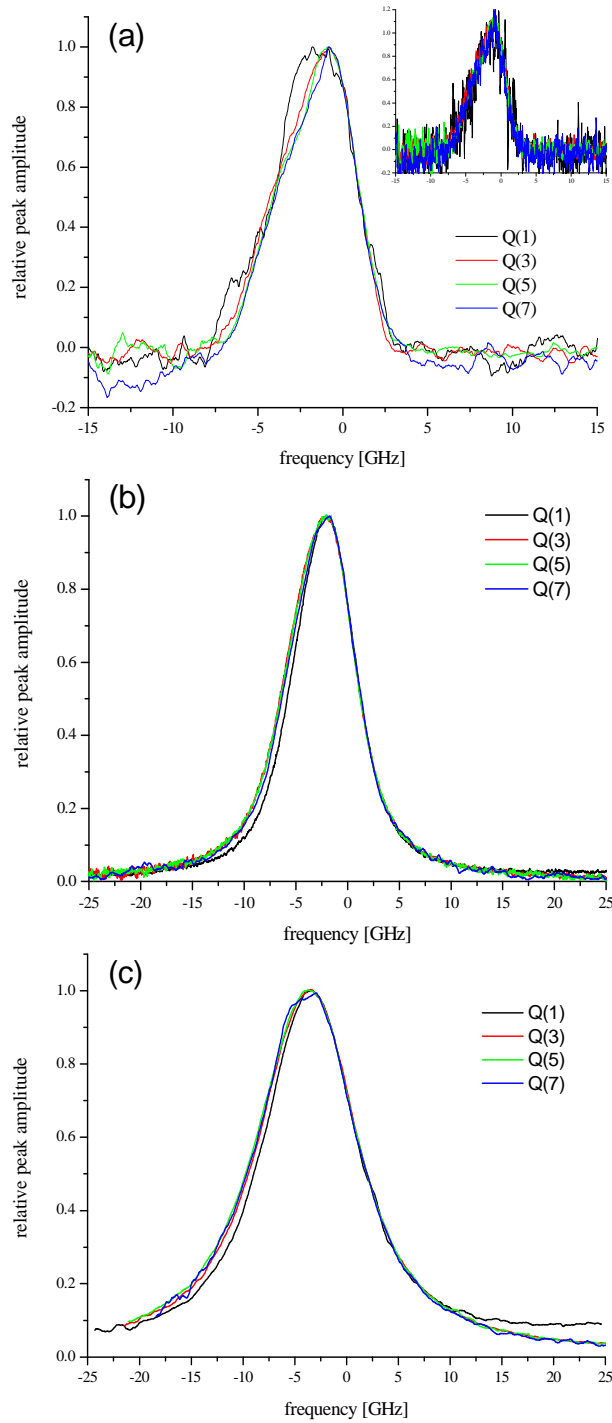


Figure 4.6: Odd-N numbered Q-branch transitions lineshapes change with the gas pressure. 8 - (a), 128 - (b) and 266.7 - (c) mbar pure  $^3\text{He}$  pressure cells. Due to low SNR (graph (a)) or high pressure broadening effect (graphs (b) and (c)) these profiles are not suitable for the analysis of the complex lineshapes of odd-N numbered lines clearly distinguishable at 67.6 mbar. The noise on the curves of the graph (a) was averaged - for visualization of the noise magnitude non-averaged curves are shown in the inset.

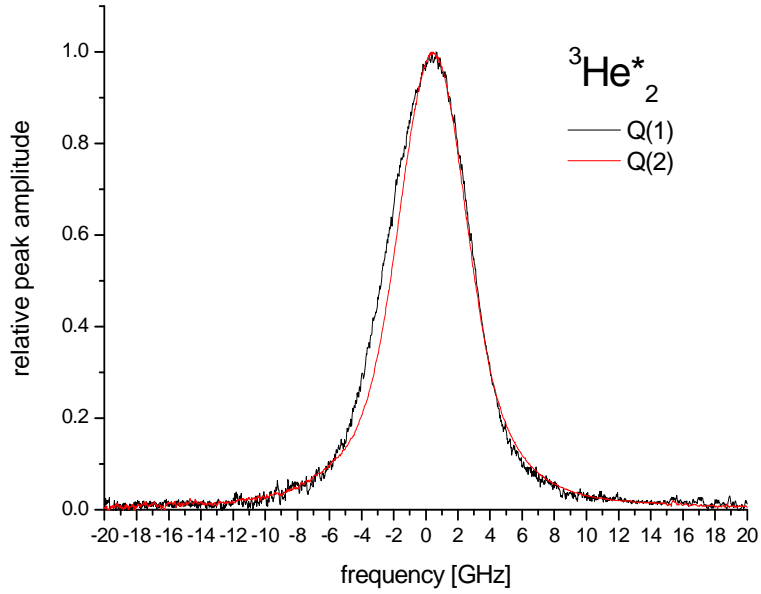


Figure 4.7: Line profiles comparison for Q(1) and Q(2) lines. The less distorted line from the odd-N numbered group is still broader than even-N numbered lines.

For more quantitative comparison it is useful to look at the full width at half maximum (FWHM) values of absorption profiles presented in the tables 4.2, 4.3 and 4.4.

	Line designation	FWHM [GHz]				
		8 mbar	66.7 mbar		128 mbar	267 mbar
			<i>w</i>	<i>s</i>		
$^3\text{He}_2^*$	Q(2)	$3.95 \pm 0.04$	$5.26 \pm 0.05$	$5.11 \pm 0.05$	$6.67 \pm 0.05$	$10.59 \pm 0.05$
	Q(4)	$4.14 \pm 0.05$	$5.24 \pm 0.03$	$5.13 \pm 0.05$	$6.97 \pm 0.04$	$11.27 \pm 0.05$
	Q(6)	$3.95 \pm 0.05$	$5.11 \pm 0.04$	$5.04 \pm 0.06$	$6.74 \pm 0.07$	$11.23 \pm 0.05$
	Q(8)	$4.00 \pm 0.47$	$4.96 \pm 0.17$	$5.06 \pm 0.04$	$6.60 \pm 0.11$	$10.94 \pm 0.29$
	P(2)		$4.86 \pm 0.05$		$6.54 \pm 0.15$	$10.17 \pm 0.11$
	R(0)		$5.62 \pm 0.06$	$5.58 \pm 0.05$		

Table 4.2: Full width at half maximum of **even**  $N$ -numbered absorption lines profiles of  $^3\text{He}_2$  at 8-267 mbar pressure range. For the 66.7 mbar two discharge excitation regimes has been studied - *weak* ( $w$ ) and *strong* ( $s$ ) (details further in the text).

In both cases of even and odd- $N$  numbered transitions of  $^3\text{He}$  at various pressures the FWHM values clearly changing within one pressure value - the differences are significant (even 10 times higher than the error bars). Values for odd- $N$  numbered transitions are systematically higher about 0.5-1.5 GHz than those for even- $N$  transitions within one pressure. The fact of varying FWHM values within one pressure (with constant temperature  $\approx 300\text{K}$  value) even for the less distorted from expected Voigt shape line profiles allows to suspect, that here also the complex line structure is present - for single transition lines one would expect the constant value of FWHM within one pressure conditions. Comparison of the results obtained for different strengths of discharge excitation within single pressure of 66.7 mbar both for  $^3\text{He}$  and  $^4\text{He}$  cells shows the reproducibility of the measurements.

	Line designation	FWHM [GHz]				
		8 mbar	66.7 mbar		128 mbar	267 mbar
			<i>w</i>	<i>s</i>		
$^3\text{He}_2^*$	Q(1)	4.56 $\pm$ 5.58	5.90 $\pm$ 0.05	5.81 $\pm$ 0.28	7.16 $\pm$ 0.05	10.71 $\pm$ 0.35
	Q(3)	5.24 $\pm$ 0.56	6.40 $\pm$ 0.03	6.32 $\pm$ 0.09	7.85 $\pm$ 0.05	11.41 $\pm$ 0.10
	Q(5)	5.19 $\pm$ 0.44	6.30 $\pm$ 0.07	6.24 $\pm$ 0.09	7.73 $\pm$ 0.04	11.79 $\pm$ 0.07
	Q(7)	4.46 $\pm$ 2.05	6.20 $\pm$ 0.07	6.22 $\pm$ 0.04	7.55 $\pm$ 0.04	11.51 $\pm$ 0.27

Table 4.3: Full width at half maximum of **odd**  $N$ -numbered absorption lines profiles of  $^3\text{He}_2$  at 8-267 mbar pressure range. For the 66.7 mbar two discharge excitation regimes has been studied - *weak* ( $w$ ) and *strong* ( $s$ ) (details further in the text). The error of the FWHM values for odd- $N$  transitions of 8 mbar  $^3\text{He}$  cell are especially higher due to very low SNR of the profiles recordings - Fig. 4.6 (a)

	Line designation	66.7 mbar of $^4\text{He}$	
		<i>w</i>	<i>s</i>
		FWHM [GHz]	
$^4\text{He}_2^*$	Q(1)	5.60 $\pm$ 0.05	5.64 $\pm$ 0.05
	Q(3)	6.28 $\pm$ 0.05	6.30 $\pm$ 0.05
	Q(5)	6.27 $\pm$ 0.05	6.22 $\pm$ 0.05
	Q(7)	6.19 $\pm$ 0.05	6.21 $\pm$ 0.04
	Q(9)	6.06 $\pm$ 0.16	6.15 $\pm$ 0.04

Table 4.4: Full width at half maximum of  $^4\text{He}_2$  absorption lines profiles of at 66.7 mbar pressure. Two discharge excitation regimes has been studied - *weak* ( $w$ ) and *strong* ( $s$ )

Using the formula of [OL77] relating Voigt profile half width with the Lorentzian and Gaussian convoluted profiles half widths  $w_L$  and  $w_G$ :

$$w_V = 0.5346 * w_L + \sqrt{0.2166 * w_L^2 + w_G^2} \quad (4.6)$$

inverting the dependency to have  $w_L(w_V)$ , assuming the room temperature plasma conditions ( $w_G=3.26$  GHz, at 300 K for  $^3\text{He}_2^*$  according to the eq.(B.15b) in Appendix B) in the experiments,  $w_L$  pressure dependency can be obtained as shown on the Fig.4.8.

The slope value obtained with the linear fit on the fig.4.8 is equal to  $32.5 \pm 0.5$  MHz/mbar. From such considerations one usually concludes about the pressure broadening of the line. Here, such interpretation of obtained value is very delicate and Author avoids it, as the line profiles from which the linewidths were obtained, are distorted and the reason for this, presence of several lines within observed profile, is not confirmed. However, the obtained value is close to the values met in case of helium-4 atomic lines pressure broadening, for example: 33.1 MHz/mbar for components of  $2^3\text{P} - 3^3\text{S}_1$  transition at 706.5 nm of  $^4\text{He}$  reported in [SN90]; or about 20 MHz/mbar for the  $2^3\text{S}_1 - 2^3\text{P}$  transition at 1083 nm met in [BTL85].

The intercept value at null pressure (no pressure broadening) on the Fig.4.8 indicates 0.85 GHz of natural line width for the helium dimer. According to [NTSL94] the lifetime of the molecular excited  $e^3\Pi_g$  that is populated due to 465 nm radiation absorption is about 67 ns that results in the natural broadening of the line of order 15 MHz - more than order of magnitude

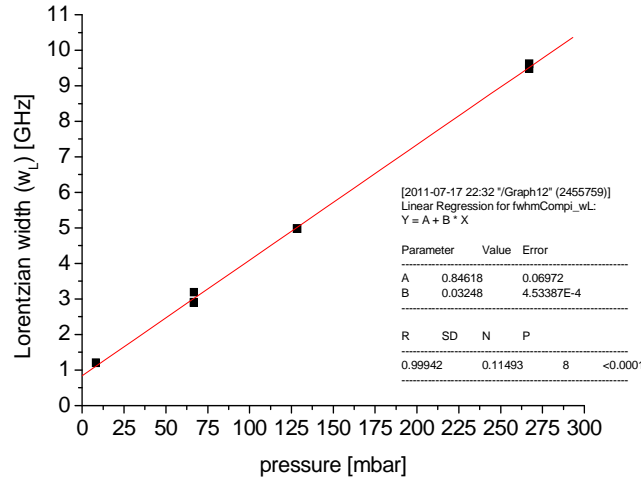


Figure 4.8: Lorentzian half width of Voigt profiles for Q(2) transition absorption lines at 8.66, 66.7, 128 and 267 mbar pressure of  $^3\text{He}$ . Linear fit to the experimental points has been performed providing the slope value  $32.5 \pm 0.5$  [MHz/mbar] and intercept  $0.85 \pm 0.07$  GHz. Natural width inferred from the radiative lifetime of  $e^3\Pi_g$  state given in [NTSL94] is about 15 MHz.

less than the value obtained here. This may indicate that none of observed absorption lines corresponds to a single transition

It was obvious from the beginning that the odd- $N$  numbered lines profiles possesses an underlying structure, indicating that the observed profile does not correspond to a single transition but is the resultant of several absorption lines associated with respective transitions within fine or hyperfine structure of rotational sublevels, as it can be concluded from the similarity of the line profiles with those reported in [HNB95].

According to [LMV74, LW78, KB90] the two farthest fine structure sublevels within one rotational level of  $a^3\Sigma_u^+$  state are separated by 2.2 to 1.2 GHz - decreasing with increasing  $N$  value from  $N=1$  to  $N=9$ . This is of order of magnitude of the observed line half-widths and their variation (several GHz) so could explain their not symmetrical shape due to overlapping of fine structure components - each of them separately broadened by pressure and collisional effects. Splittings of the fine structure sublevels of  $e^3\Pi_g$  are, for the Author's knowledge, not presented in any reference as well as parameters necessary for their calculation.

The presence of the underlying line structure can be also found with the line profile fitting procedure with the Voigt function in Origin 7.5 data analysis software. Obtained residual data between the experimental points and fitted curve, exhibits regular, across the investigated pressure range, maxima of residual data on the left line slope - Fig.4.9 to Fig.4.12.

This residual data behavior is an indication of the discrepancy between expected Voigt profile and the recorded one which is the resultant of several close lying absorption lines.

The reason of the fact why the even- $N$  numbered of  $^3\text{He}_2^*$  lines look differently from the odd- $N$  numbered in terms of the fine structure is hard to explain, as, for the Author's knowledge, the values of spin-spin  $\lambda$  and spin-rotation  $\gamma$  fine structure coefficients are not known for this isotope. Furthermore, these coefficients for the  $^4\text{He}_2^*$  are given only for the  $a^3\Sigma_u^+$  [HNB95]. The lack of the coefficients in the excited  $e^3\Pi_g$  state doesn't allow to conclude about the reason for the difference in the lineshapes of odd- $N$  and even- $N$  numbered lines. One should exclude the hyperfine structure influence on the basis of similarity of the odd- $N$  numbered

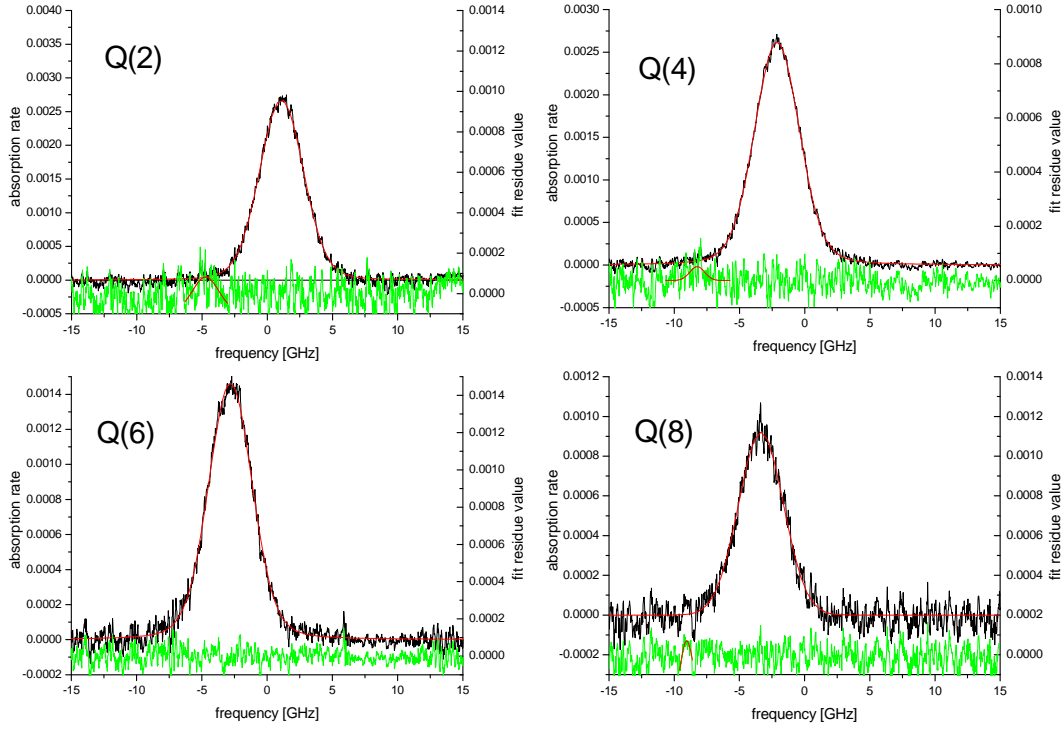


Figure 4.9: Even-N numbered Q branch line profiles for 8 mbar pure  $^3\text{He}$  cell. The curve described by the Voigt function was fit to each profile showing regular residue maxima at negative frequencies.

lines of both isotopologues. Using the coefficients  $\lambda$  and  $\gamma$  of the  $^4\text{He}_2$  in calculations of the  $^3\text{He}_2^*$  fine structure sublevels' separation doesn't bring the answer about the shape difference. The changes of the sublevels' separations are monotonous through  $N=1,2,3,\dots,9$  without any significant variation for even-N values, that could result in decrease of line distortion seen for odd-N numbers. Thus, the reason lies in the fine structure of the levels of the excited state or other effect corresponding to the isotopic difference. Unfortunately only the two lines of heteronuclear dimer ( $^3\text{He}-^4\text{He}$ )\* of Q branch with  $N=2$  and  $N=3$  are well resolved from the spectra of other isotopologues thus their shape can be compared with isotopic pure molecules. The P(2) and Q(4) lines, however separated from their neighbors, experience the influence of their wings, what makes the conclusions about such detailed discrepancy of the profiles doubtful.

The line profile of odd-N numbered line of heteronuclear dimer (Fig.4.13) does not exhibit such strong distortion as in case of two other isotopologues, however, the analysis of residual data of the Voigt fit still shows the maximum on the left side of the peak slope. Presented line distortion due to its internal structure raise the question of possibility of using top peak value of absorption over the cell length for helium molecule in metastable state number density determination. The reference given in the paragraph (h) of subsection 2.2 providing the value of the rotational levels lifetime does not mention any internal structure of the line. Thus, no cross-section values can be calculated for the transition occurring within the structures of rotational levels of  $a$  and  $e$  states involved in the N numbered transition. Moreover, the individual lines amplitudes are not resolved within this structure. On the other hand, the discrepancy (residue) of presented even-N numbered line profiles with the fitted Voigt profiles is about 1%

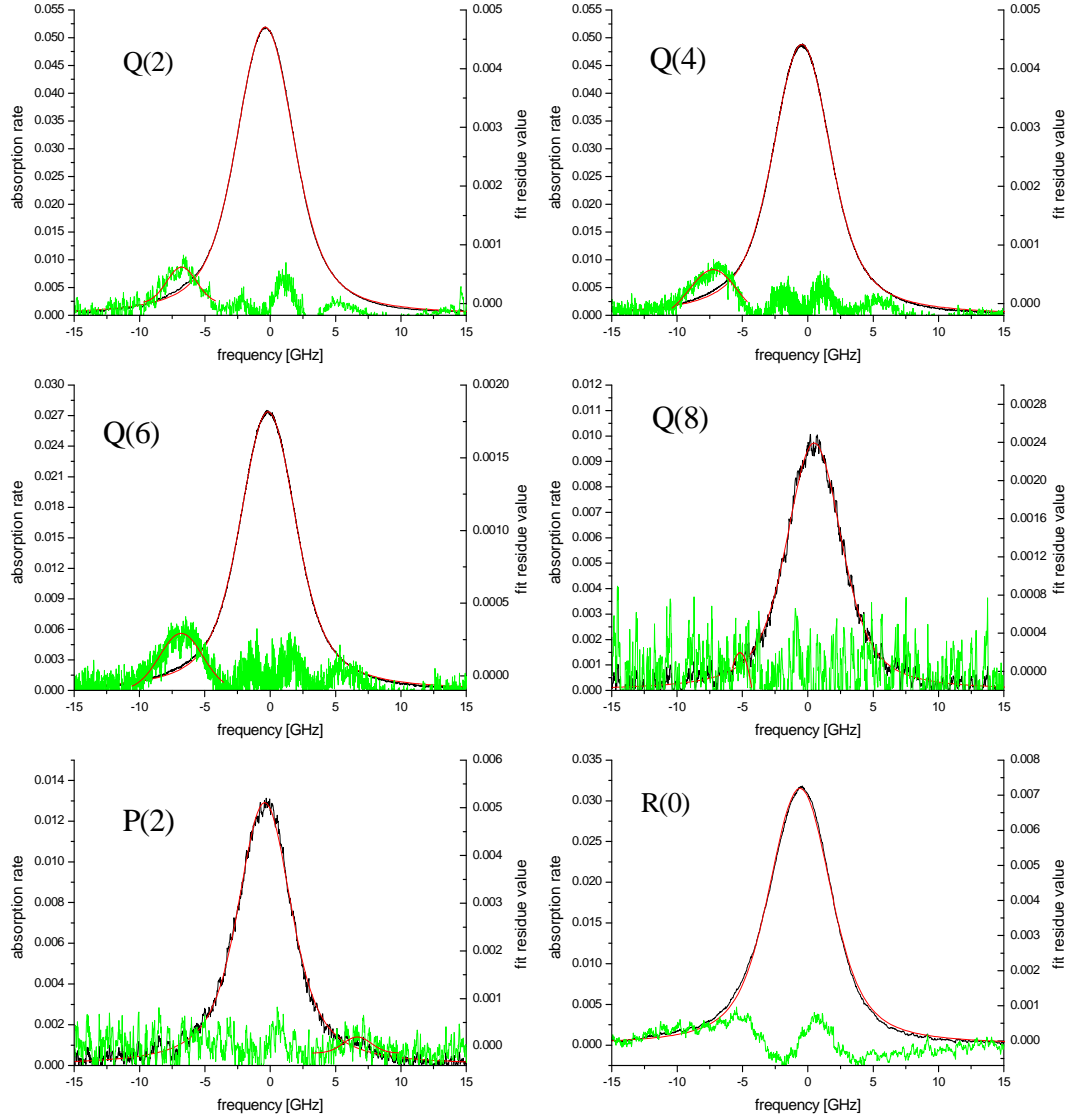


Figure 4.10: Even-N numbered Q branch line profiles for 66.7 mbar pure  $^3\text{He}$  cell. The curve described by the Voigt function was fit to each profile showing regular residue maxima at negative frequencies. The last two graphs present the profile of P(2) and R(0) lines. For the former line small Voigt fit residue maximum at positive frequency is present, whereas in the latter line profile any explicit maximum can be distinguished.



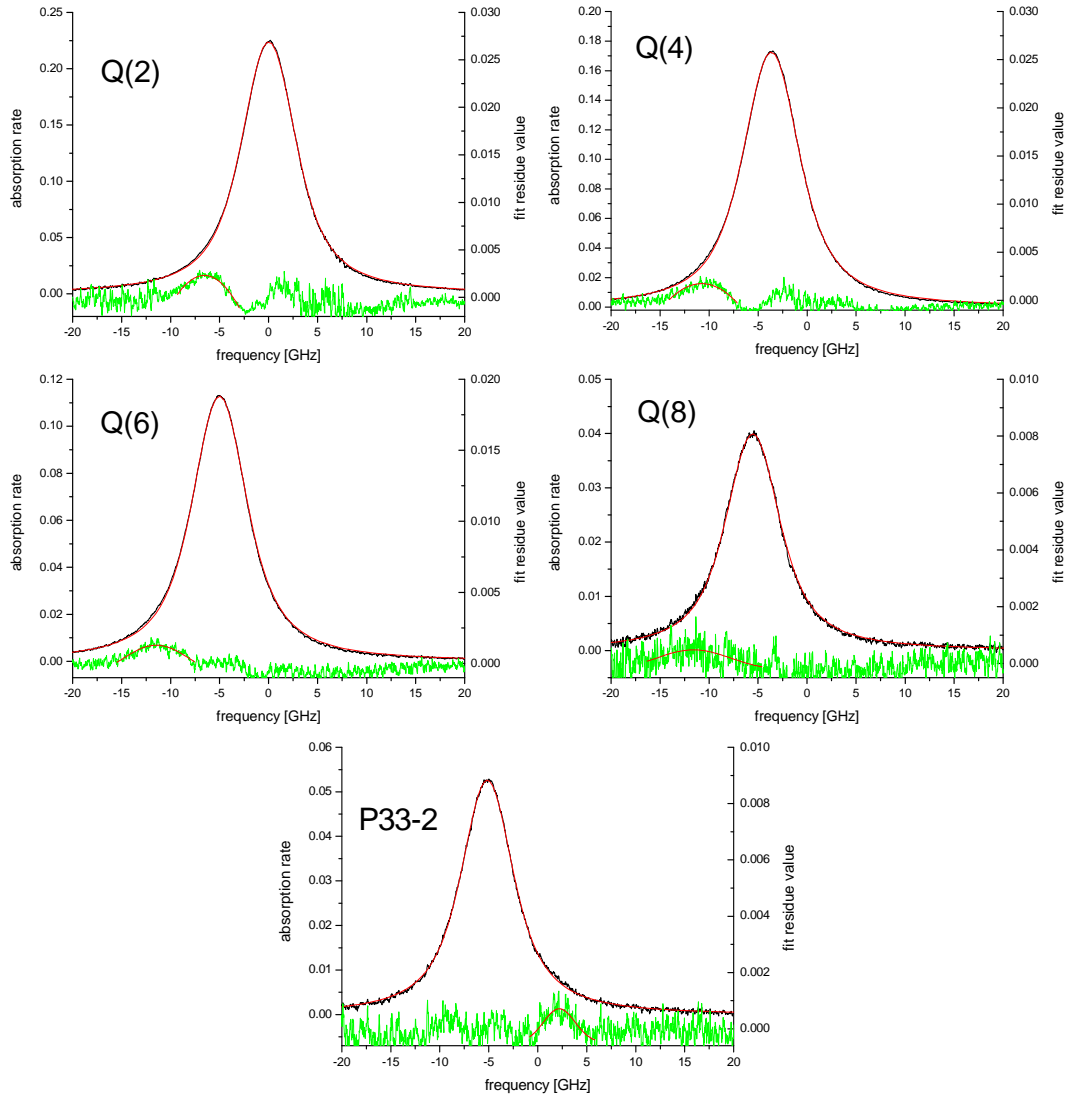


Figure 4.11: Even-N numbered Q branch line profiles for 128 mbar pure  $^3\text{He}$  cell. The curve described by the Voigt function was fit to each profile showing regular residue maxima at negative frequencies. The last graph presents the profile of P(2) line. Small fit residue maximum can be distinguished for positive frequency, as in case of data for 66.7 mbar.

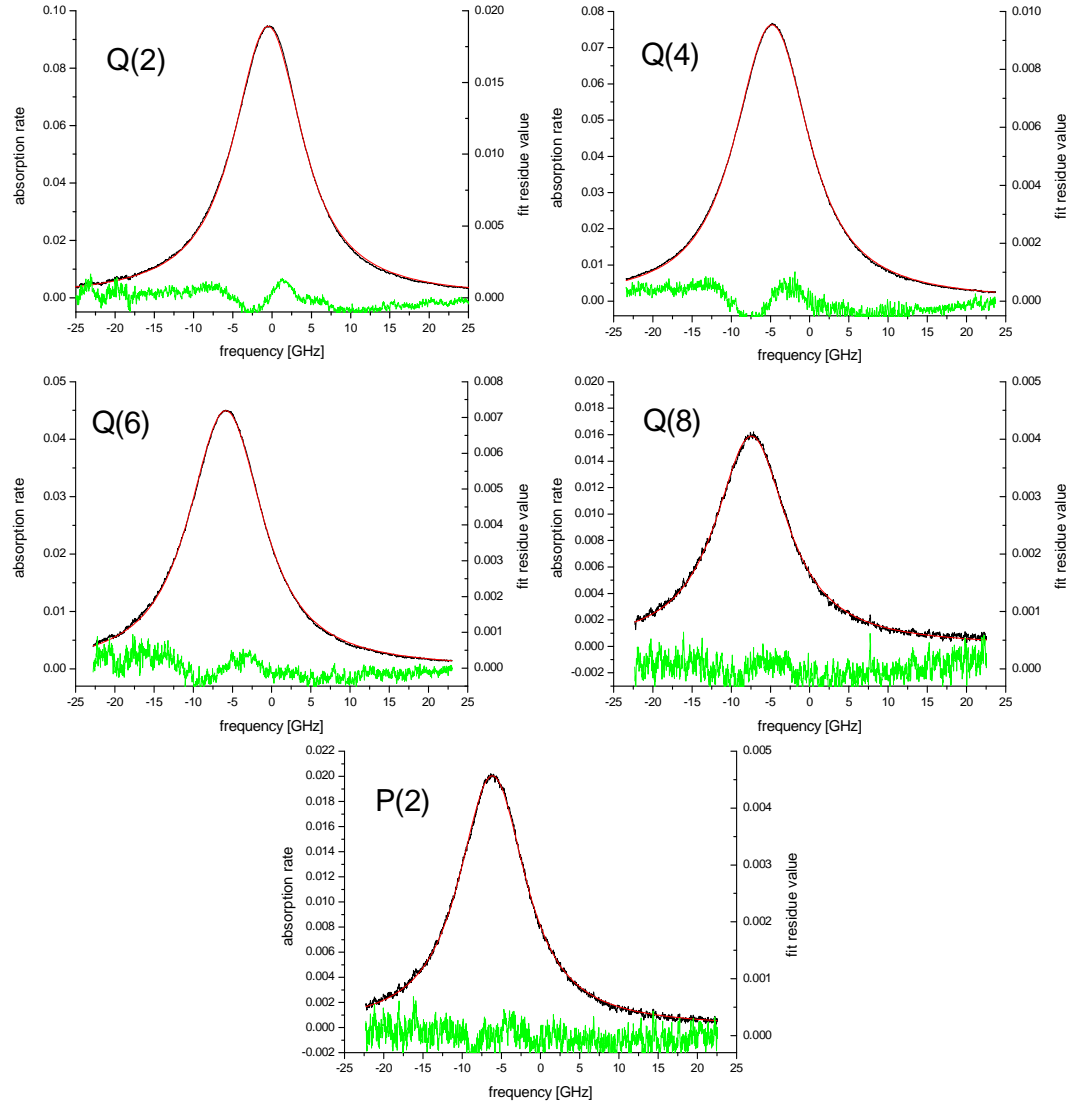


Figure 4.12: Even-N numbered Q branch line profiles for 266 mbar pure  $^3\text{He}$  cell. The curve described by the Voigt function was fit to each profile, however, in case of this pressure characteristic maxima of the fit residues seen at lower pressures are not observed.

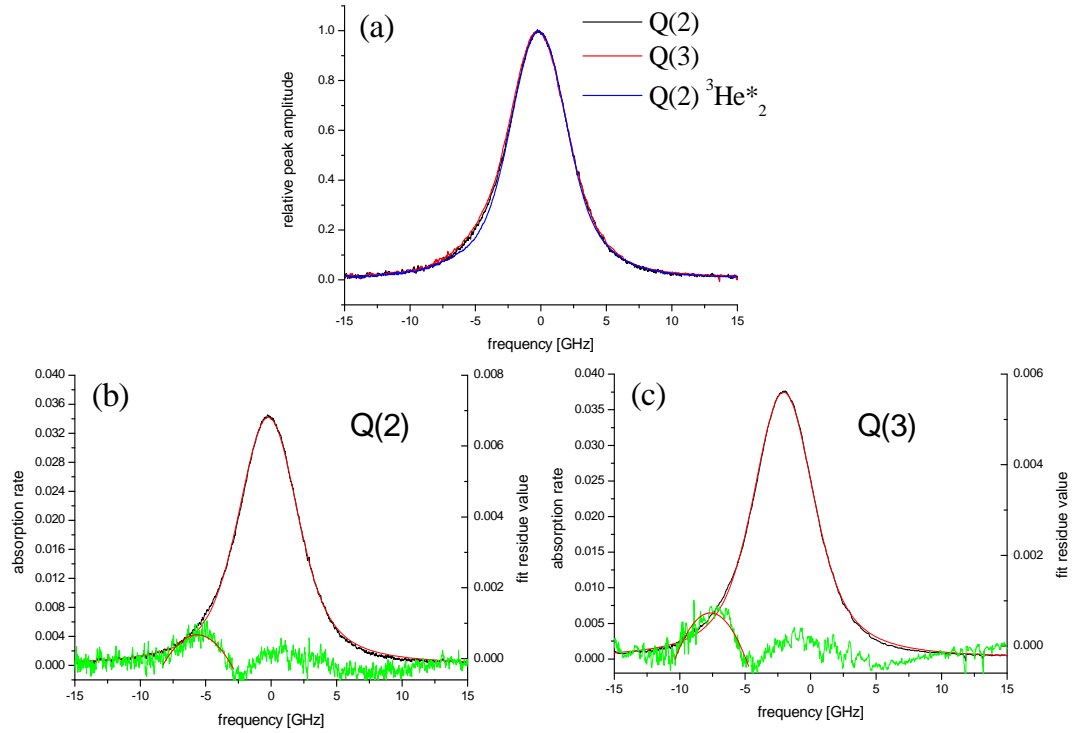


Figure 4.13: Lineshapes comparison between the only well-resolved lines of  $(^3\text{He}-^4\text{He})^*$  and Q(2) line of  $^3\text{He}_2^*$ . Mixture lines, although one odd-N numbered and the second even-N numbered are of the same shape (compare with the difference of even-N and odd-N numbered lines for  $^3\text{He}_2^*$ ), similar to the "not-distorted" even-N numbered line (i.e. Q(2)) of  $^3\text{He}_2^*$  isotopoogue. Small broadening, in comparison with Q(2) of  $^3\text{He}_2^*$ , is present on the negative frequency wings for Q(2) and Q(3) lines of the heteronuclear dimer, what is confirmed in the existence of fit residue maxima relatively (as compared to the line height) higher than for Q(2) lines

of the top peak value and possibly the strongest line components are lying close enough for the assumption of single transition between rotational levels occurring is valid, as it is in the references reporting about the lines positions [DR50, BG71] and excited electronic states' rotational levels lifetimes [NTSL94]. Under this assumption the recorded line profiles and their amplitudes allow obtaining the absolute values of metastable molecule densities. Decision of the Author is to use only even-N numbered lines for such calculations, because of, as it was discussed, negligible distortion due to internal line structure. Presence of the line structure pose the difficulties in their linewidth analysis. For the case of single line corresponding to a single transition the linewidth is a resultant of several process discussed in paragraph (a) of the appendix B - Doppler and pressure broadening. Here, several lines are present within the single profile, thus resolving the Gaussian and Lorentzian widths is impossible, as the profile given can't be described by single Voigt function.

The accurate values of the absorption rate measured for presented molecular transitions for both  $^3\text{He}_2^*$  and  $^4\text{He}_2^*$  are presented in the tables 4.5 and 4.6 respectively. For the 66.7 mbar two discharge regimes are considered weak and strong. Those two regimes differs in the rf discharge excitation amplitude. The best indication of the discharge conditions is the 1083 nm laser absorption on the atomic transitions and thus the metastable atom density  $n_m$ . It increases

with the strength of excitation reflecting the change in plasma properties more reliably than any of the voltage generator amplitude or the sent/reflected power amplifier displayed values. Thus, the absorption values on the  $C_8$  and  $D_0$  transitions has been given in the tables for  $^3\text{He}$  and  $^4\text{He}$  respectively.

	Line designation	$-\ln T \cdot 10^{-2}$				
		66.7 mbar		8 mbar	128 mbar	266.7 mbar
		weak discharge	strong discharge			
$^3\text{He}_2^*$	$C_8$	149	208	177	33.5	8.1
	$n_m[\text{cm}^{-3}]\times 10^{11}$	2.76	3.85	3.28	0.62	0.15
	Q(1)	1.2	2.9	0.03	2.6	1.9
	Q(2)	5.2	13.6	0.16	14.8	10.4
	Q(3)	1.6	4.0	0.04	2.8	2.2
	Q(4)	5.0	12.5	0.14	7.7	6.7
	Q(5)	1.1	2.8	0.03	1.8	1.4
	Q(6)	2.8	6.8	0.08	2.9	3.2
	Q(7)	0.5	1.2	0.007	0.35	0.4
	Q(8)	1.0	2.4	0.015	0.98	0.7
	P(2)	1.3	3.0	0.03	1.1	0.8
	R(0)	3.2	7.6	NR	NR	NR

Table 4.5: Values of the plasma absorbance ( $-\ln T$ ) for the observed molecular transitions for  $^3\text{He}_2^*$  at different pressures between 8 to 266.7 mbar of isotopic pure cells. For 66.7 mbar two discharge regimes are considered of weak and strong rf excitation. The plasma condition inside the cells can be compared via 1083 nm absorbance values on  $C_8$  atomic transition given in the first row of the absorbance values. NR - not recorded in the experiment.

	Line designation	$-\ln T \cdot 10^{-2}$	
		66.7 mbar, $^4\text{He}$	
		weak discharge	strong discharge
$^4\text{He}_2^*$	$D_0$	30.1	230
	$n_m \times 10^{11} [\text{cm}^{-3}]$	$0.22 \pm 0.02$	$1.70 \pm 0.02$
	Q(1)	3.0	10.6
	Q(3)	4.4	15.5
	Q(5)	3.6	12.2
	Q(7)	1.9	6.8
	Q(9)	0.8	2.6
	P(3)	1.5	5.5

Table 4.6: Values of the plasma absorbance ( $-\ln T$ ) for the observed molecular transitions for  $^4\text{He}_2^*$  at 66.7 mbar of isotopic pure cell. Two discharge regimes are considered of weak and strong rf excitation. The plasma condition inside the cell can be compared via 1083 nm absorbance values on  $D_0$  atomic transition given in the first row of the absorbance values.

## 4.4 Position of absorption lines

Reference data of [DR50] and [BG71] provide the positions of the Q,P and R branches of rotational spectrum corresponding to the transitions occurring between rotational levels of  $a^3\Sigma_u^+$  and  $e^3\Pi_g$  states. Any structure of the observed lines was not mentioned by the authors of the references. In the previous section the shapes of the profiles were discussed, that are different for even- and odd-N numbered lines. The fact of bigger or smaller line distortion due to its internal structure implies the contribution to the error value of position determination beside the error induced by hysteresis of voltage current sweep, reproducibility of line profile recording and statistical accuracy of the fit for position determination.

### 4.4.1 Isotopic mixture cell - recordings of multiple lines

Independent recordings performed in isotopic pure cells that provided the wavelength calibration of the blue laser, show that there are close lying absorption lines of both isotopologues within laser diodes temperature/wavelength acceptance bandwidth for certain crystal temperature (according to a matching curve on 3.16(b))  $^3\text{He}_2^* - ^4\text{He}_2^*$  : Q(2)-Q(5), Q(3)-Q(5), Q(5)-Q(7), Q(7)-Q(9), Q(8)-P(3), P(2)-P(3).

Moreover, when the cell is filled with 1:1 proportion of both isotopes, there are expected also the absorption lines of the heteronuclear dimer ( $^3\text{He}-^4\text{He}$ )\* that, according to the mass scaling rules for the isotopes, are shifted with respect to their isotopologues' equivalents. For the heteronuclear dimer, due to the lack of the symmetry of the nuclei interchange, the overall symmetry properties results in presence of both even- and odd-N numbered lines (as for  $^3\text{He}_2^*$ ), with no line amplitude alternation. Due to presence of the line of the heteronuclear dimers, there are only three pairs of 6 mentioned before  $^3\text{He}_2^* - ^4\text{He}_2^*$  close lying doublets in which the homonuclear molecule lines are well resolved - see Fig. 4.14. In other cases one of the line in the pair is overlapped with the line of ( $^3\text{He}-^4\text{He}$ )\* - Fig.4.15. On both figures peaks are designated with proper letter for the rotational branch and the isotopic composition in the superscript (e.g.  $^{44}$  for  $^4\text{He}_2^*$ ,  $^{34}$  for ( $^3\text{He}-^4\text{He}$ )\* )

Using the mentioned mass scaling rules for molecular constants equations:(2.28), (2.29) and reference values of the constants for isotopic pure isotopologues from [DR50, BG71] (see Appendix D), the constants are determined for the ( $^3\text{He}-^4\text{He}$ )\* (presented in table 4.7) and so the wavelengths of the rotational transitions Q(1-9), R(0), P(2) are calculated using eq.(2.20) together with the dependencies given in subsections 2.1.1 (b) and (c). The results of the calculations are presented in the table 4.8, together with the experimental results.

	$a^3\Sigma_u^+$	$e^3\Pi_g$
$B_0$	8.82	8.34
$D_0 \cdot 10^4$	7.49	7.02
$\omega_e$	1951.85	1856.69
$\omega_e x_e$	44.95	40.55
$T_e + G(\nu = 0)$	21503.37	

Table 4.7: Molecular constants for ( $^3\text{He}-^4\text{He}$ )\* calculated with use of the mass scaling relations applied to known rotational constants for  $^3\text{He}_2^*$  and  $^4\text{He}_2^*$  isotopologues.  $T_e + G(\nu = 0)$  is energy of so-called *band origin*. All the values are given in  $\text{cm}^{-1}$  unit.

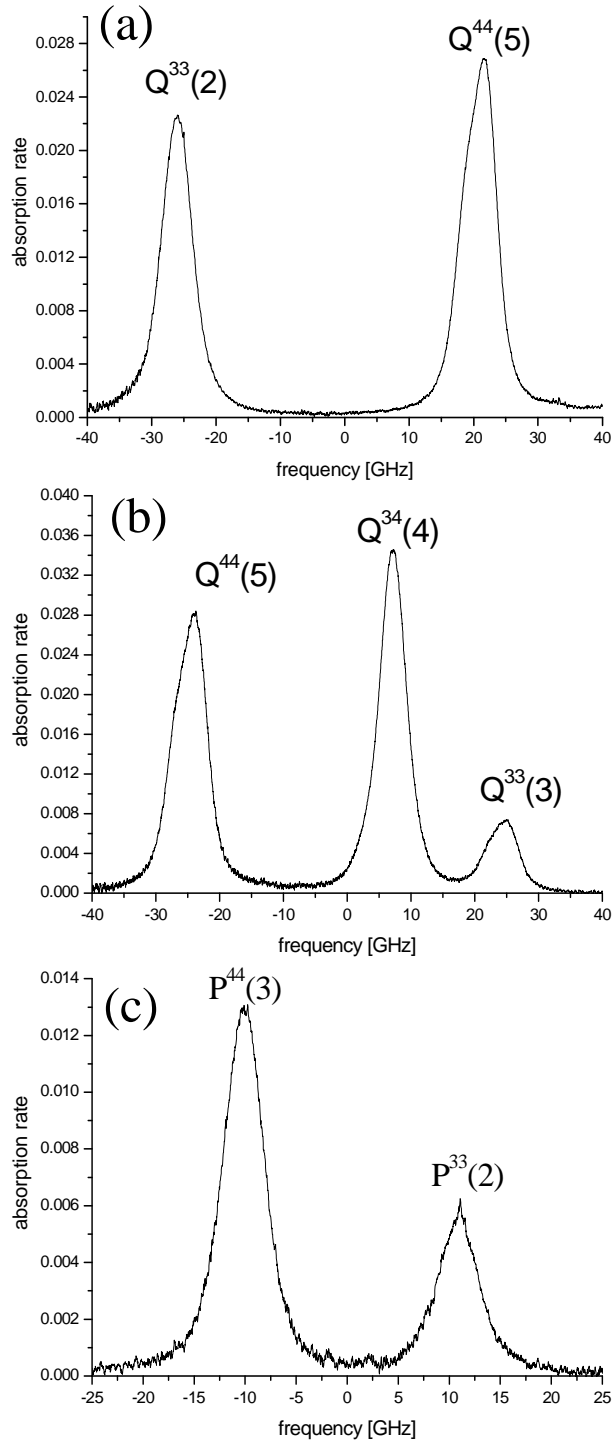


Figure 4.14: Three frequency scans including more than one molecular line (a) doublet of  $^3\text{He}_2^*$  and  $^4\text{He}_2^*$  lines Q(2) and Q(5), respectively noted  $^{33}\text{Q}(2)$  and  $^{44}\text{Q}(5)$ ; (b) triplet consisting of  $^3\text{He}_2^*$ ,  $^4\text{He}_2^*$  and  $(^3\text{He}-^4\text{He})^*$  lines; (c) doublet of P(3) and P(2)  $^4\text{He}_2^*$  and  $^3\text{He}_2^*$  isotopologues.

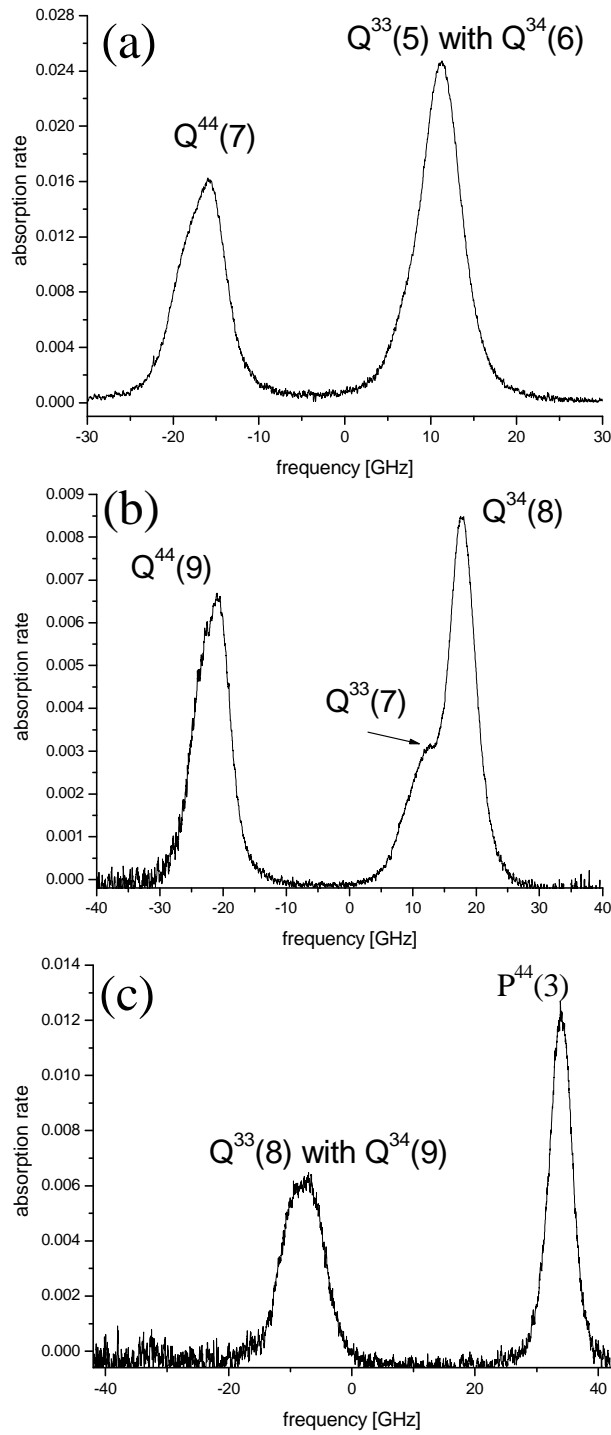


Figure 4.15: Frequency scans of close lying  $^3\text{He}_2^*$  and  $^4\text{He}_2^*$  molecular lines for which one is overlapping with an absorption line of the hetero nuclear isotopologue ( $^3\text{He}-^4\text{He}$ ) $^*$ .

	Line designation	$\lambda_{calc}$ [nm]	$\lambda_{exp}$ [nm]	$\delta\lambda_{exp}$ [nm]	$\lambda_{ref}$ [DGD77]
$(^3\text{He}-^4\text{He})^*$	Q(1)	465.064	-	-	465.064
	Q(2)	465.106	465.106	0.001	465.106
	Q(3)	465.169	465.169	0.001	465.169
	Q(4)	465.252	465.253	0.002	465.253
	Q(5)	465.357	465.365	0.003	465.357
	Q(6)	465.482	-	-	465.482
	Q(7)	465.629	465.627	0.002	465.628
	Q(8)	465.795	465.794	0.002	465.794
	Q(9)	465.982	-	-	465.980
	P(2)	465.828	465.838	0.003	465.832
	R(0)	464.682	-	-	464.683

Table 4.8: Position in wavelength scale of 11 absorption lines of  $(^3\text{He}-^4\text{He})^*$  within expected tuning range of the blue laser.  $\lambda_{calc}$  values are calculated using the molecular constants (Table 4.7),  $\lambda_{exp}$  are experimentally determined positions of the lines,  $\delta\lambda_{exp}$  are the uncertainties of line positions determination in voltage scale and its scaling to the wavelengths. Calculated values of the positions are in very good agreement (within 3rd decimal place) with given in [DGD77].

The positions of Q(3) and Q(4) lines of  $(^3\text{He}-^4\text{He})^*$ , the only well resolved from two close lying (close enough to be able to scan together) isotopologues' neighboring lines, were determined from the frequency scans where three absorption lines were present - one line of heteronuclear dimer and two lines of pure  $^3\text{He}$  and  $^4\text{He}$  isotopologues. Q(3) of the heteronuclear dimer in the vicinity of the isotopologues lines is shown on the Fig.4.16, while Q(4) was presented on the Fig.4.14 (b). This gave the local value of  $\frac{d\lambda}{dV}$  and the position of heteronuclear dimer line was determined with better accuracy (0.002 nm).

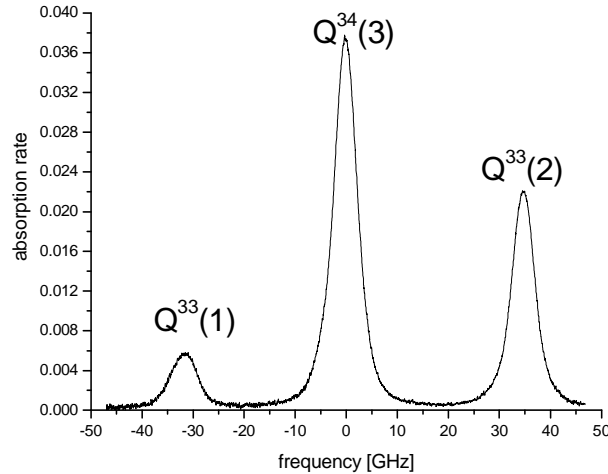


Figure 4.16: Frequency scan for which well resolved absorption lines of  $^3\text{He}_2^*$ ,  $^4\text{He}_2^*$  and  $(^3\text{He}-^4\text{He})^*$  are present.

Other local values of wavelength-voltage coefficient were determined using the frequency scans of line pairs (i.e. Fig.4.17) on which the Q(1)-Q(5) lines of isotopic pure isotopologues were present (due to different combinations multiple values within this range are given - see



fig.3.11). These values are equal within their uncertainties, thus weighted average was determined  $((3.52 \pm 0.01) \cdot 10^{-3} \text{ nmV}^{-1})$ , which can be used for voltage-wavelength scaling in the positions range between Q(1) and Q(5) of  $^3\text{He}_2^*$ .

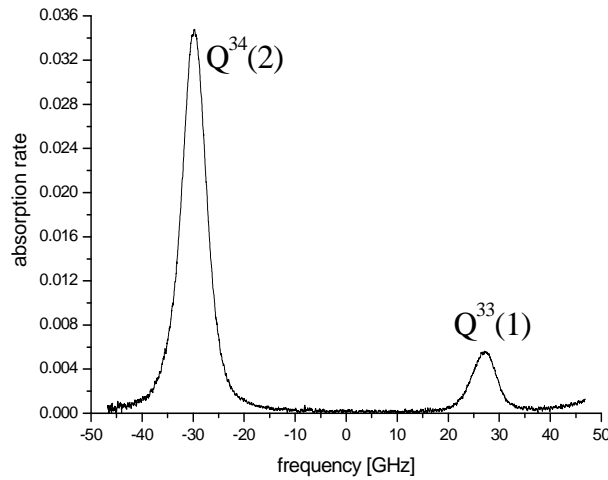


Figure 4.17: Example of the frequency scan containing only two absorption lines, the registered  $^{33}\text{Q}(1)$  (Q(1) of  $^3\text{He}_2^*$ ) and one of the hetero nuclear dimer. Line position for  $(^3\text{He}-^4\text{He})^*$  is computed assuming the value of  $\frac{d\lambda}{dV}$  to be known from the frequency scan of another triplet including also  $^{33}\text{Q}(1)$  of  $^3\text{He}_2^*$  -shown in Fig.4.16.

The coefficient  $\frac{d\lambda}{dV}$  was also determined from the common scan of P(3) and P(2) lines of  $^4\text{He}_2^*$  and  $^3\text{He}_2^*$  Fig.4.14 (c) respectively.

Lines of  $(^3\text{He}-^4\text{He})^*$  such as Q(1) (Fig.4.18), Q(6),Q(9) (Fig. 4.15 (a) and (c)) are completely overlapped with the lines of isotopologues, thus their precise position could not be determined.

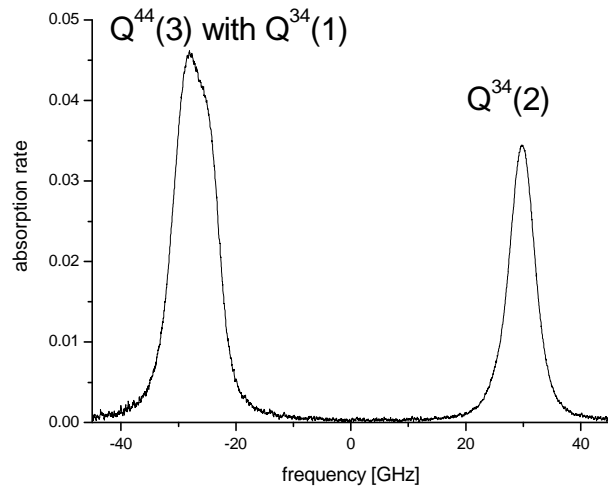


Figure 4.18: Frequency scan of unresolved triplet - two absorption lines of the  $(^3\text{He}-^4\text{He})^*$  molecule and one of  $^4\text{He}_2^*$  overlapped with  $^{34}\text{Q}(2)$

The line Q(2) was recorded on the single scan together with Q(1) of  $^3\text{He}_2^*$  (Fig.4.17), thus, with the same value of  $\frac{d\lambda}{dV}$  as for Q(3) and Q(4) lines of  $(^3\text{He}-^4\text{He})^*$ , the exact position could

be determined from the experiment. The heteronuclear dimer lines Q(5), Q(7) (Fig.4.19(a) and (b)) and Q(8) (Fig.4.15(b)) are partially overlapped with isotopologue's neighbors on the frequency scans where two lines are present.

For those lines one should be aware of increased error in position (shift) due to the influence of the signal of the partner. Q(8) line is partially overlapped with Q(7) of  $^3\text{He}_2^*$ , however there is Q(9) of  $^4\text{He}_2^*$  on the scan that allows Q(8) scaling of position in the wavelength. In case of determination of  $(^3\text{He}-^4\text{He})^*$  Q(5) line partially overlapped with  $^3\text{He}_2^*$  Q(4) also the value of  $\frac{d\lambda}{dV} = 0.00352$  was used.

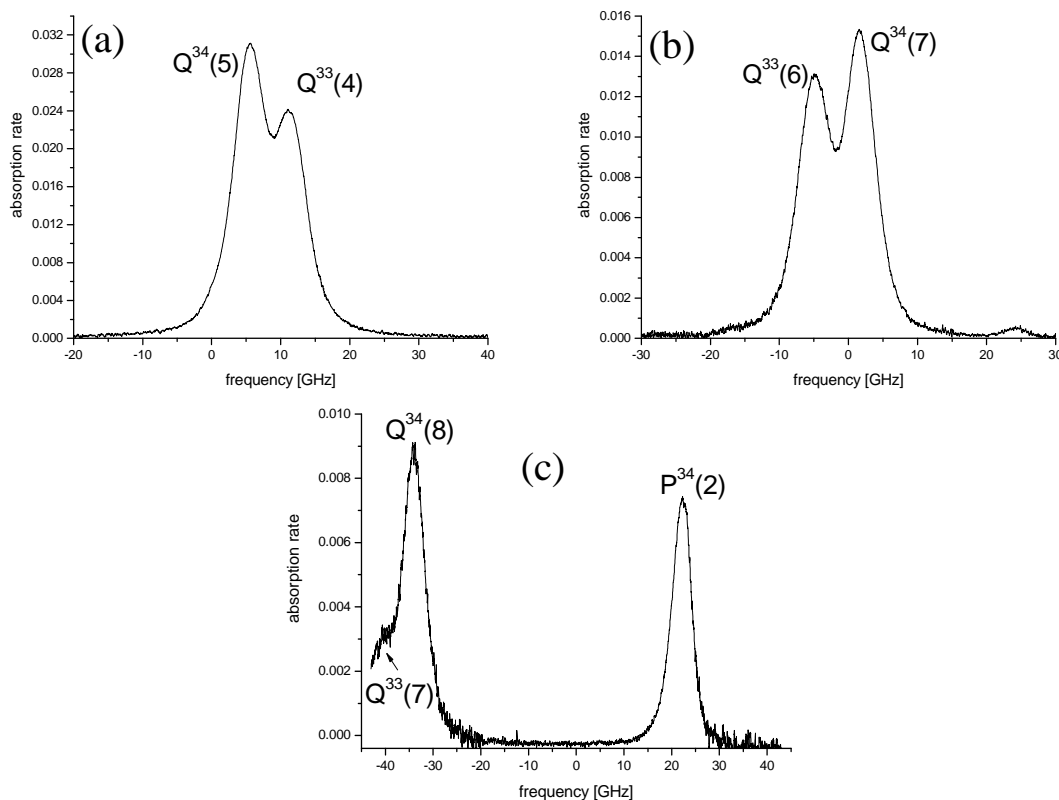


Figure 4.19: Frequency scans of partially overlapped absorption lines doublets for  $^3\text{He}_2^*$  and  $(^3\text{He}-^4\text{He})^*$ . Graph (c) can be compared with Fig.4.15(b) where the same complex of  $Q^{34}(8)$  and  $Q^{33}(7)$  is shown, however, here the range of higher frequency is presented containing the  $P^{34}(2)$  absorption line.

For Q(7) and Q(8) lines the wavelength-voltage coefficient is in between the values obtained for Q(3), Q(4) and for P(3) ( $^4\text{He}_2^*$ ), P(2) ( $^3\text{He}_2^*$ ) (value placed on the fig.3.11). Thus, the positions of Q(7) and Q(8) were determined using both values of  $\frac{d\lambda}{dV}$ . As the results the average of positions values was taken together with the averaged errors. P(2) line was recorded on a single frequency scan with Q(8) (Fig.4.19(c)) for which the wavelength position is also determined here. The error of Q(8) wavelength position determination adds up to the value uncertainty for P(2) line. No information about  $\frac{d\lambda}{dV}$  in the vicinity of R(0) line results in the lack of wavelength position scaling for this line, despite of the fact, that it is present with R(0) line of  $^3\text{He}_2^*$  on single frequency scan - Fig.4.20. However, using  $(^3\text{He}-^4\text{He})^*$  wavelength data [DGD77], the value of  $\frac{d\lambda}{dV}$  shown on the fig. 3.11 was determined.

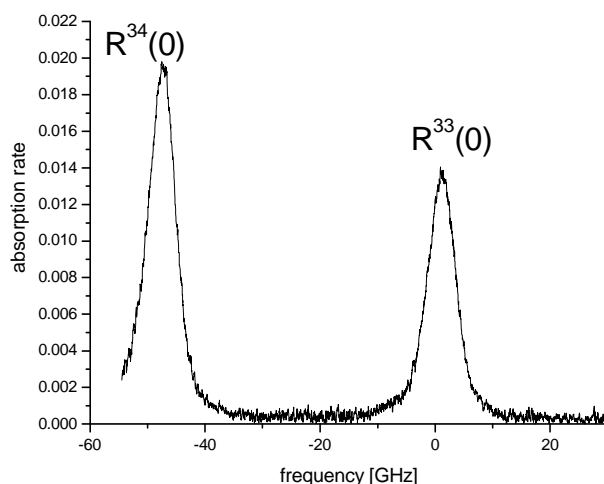


Figure 4.20: Frequency scans of the R(0) lines doublet of  $^3\text{He}_2^*$  and  $(^3\text{He}-^4\text{He})^*$  ( $^{33}\text{R}(0)$  and  $^{34}\text{R}(0)$ ).

After the time when the calculation had been made and experimental confirmation of obtained results was performed, the reference [DGD77] was found staying in good agreement with Author's calculations (within 3rd decimal place - the order of accuracy of the data presented in [DGD77] and in the sources of the rotational constants for  $^3\text{He}_2^*$  and  $^4\text{He}_2^*$ , as well as given molecular constants error). The mentioned reference was found much later the calculations and the measurements were made and serves as a check of calculations correctness, especially with the peak positions that are not available experimentally due to the lines overlapping.

The accurate values of the absorption rate measured for presented molecular transitions of three helium molecule isotopologues are presented in the table 4.9. Here as well the two discharge regimes - weak and strong are considered. In the table the overlapping of respective lines has been explicitly given mentioning which line is partially or totally overlapped with the isotopologue's neighbor.

Line designation	$-\ln T \cdot 10^{-2}$					
	66.7 mbar 1:1 $^3\text{He}:$ $^4\text{He}$ mixture					
	weak discharges			strong discharges		
$D_0$	NR			200		
	$^3\text{He}_2^*$	$^4\text{He}_2^*$	$(^3\text{He}-^4\text{He})^*$	$^3\text{He}_2^*$	$^4\text{He}_2^*$	$(^3\text{He}-^4\text{He})^*$
Q(1)	0.10	0.39	o Q <sup>44</sup> (3)	0.55	2.28	o Q <sup>44</sup> (3)
Q(2)	0.38	—	0.76	2.23	—	3.48
Q(3)	0.12	o Q <sup>34</sup> (1)	0.69	0.74	o Q <sup>34</sup> (1)	3.71
Q(4)	po Q <sup>34</sup> (5)	—	0.58	po Q <sup>34</sup> (5)	—	3.52
Q(5)	o Q <sup>34</sup> (6)	0.39	po Q <sup>33</sup> (4)	o Q <sup>34</sup> (6)	3.15	po Q <sup>33</sup> (4)
Q(6)	po Q <sup>34</sup> (7)	—	o Q <sup>33</sup> (5)	po Q <sup>34</sup> (7)	—	o Q <sup>33</sup> (5)
Q(7)	o Q <sup>34</sup> (8)	0.23	po Q <sup>33</sup> (6)	o Q <sup>34</sup> (8)	1.61	po Q <sup>33</sup> (6)
Q(8)	o Q <sup>34</sup> (9)	—	o Q <sup>33</sup> (7)	o Q <sup>34</sup> (9)	—	o Q <sup>33</sup> (7)
Q(9)	NA	0.10	o Q <sup>33</sup> (8)	NA	0.66	o Q <sup>33</sup> (8)
P(2)	NR	—	0.15	0.58	—	0.73
P(3)	NA	NR	NA	NA	1.299	NA
R(0)	NR	—	NR	1.37	NA	1.96

Table 4.9: Absorbance values for observed molecular transitions for  $^3\text{He}_2^*$ ,  $^4\text{He}_2^*$  and  $(^3\text{He}-^4\text{He})^*$  at 66.7 mbar of isotopic 1:1 mixture cell. Two discharge regimes are considered (weak and strong rf excitations). Some molecular absorption lines are totally (o) or partially (po) overlapped with close lying lines of other isotopologue. Some lines are not available for detection (NA) due to limited blue laser tuning range. There are lines for which the profiles have not been recorded (NR) and absorbances have not been measured

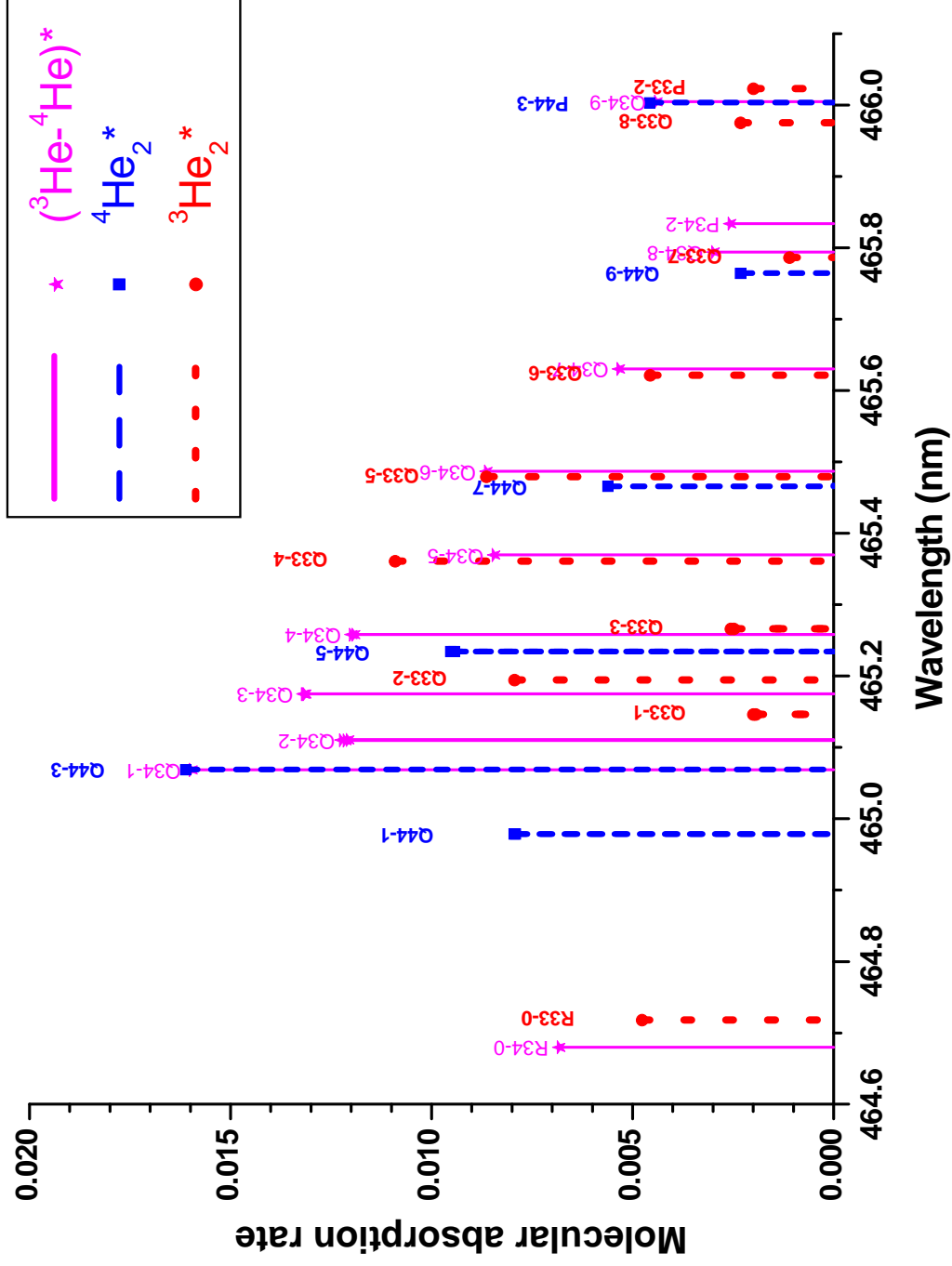


Figure 4.21: Positions of all the helium molecule isotopologues  $^3\text{He}^*\text{He}_2$ ,  $^4\text{He}^*\text{He}_2$  and  $(^3\text{He}-^4\text{He})^*$  absorption lines observed using the  $a^3\Sigma_u^+(0) - e^3\Pi_g(0)$  transition around 465 nm. Overlapping of the lines indicated using the information in the Table 4.9

## 4.5 Intensities of absorption lines

### 4.5.1 Rotational temperature determination from relative absorption rates

Apart from the numerical factors of the line oscillator strength (discussed in subsection 2.2), the Doppler and pressure broadening values  $\omega_G$  and  $\omega_L$  required in the spectral term of the cross-section (see (B.6),(B.16)) and besides the light transmission value when the frequency is tuned to the chosen transition ( $\omega_{if}$ ), the gas rotational temperature  $T$  (that appears in eq.(2.51)) is needed for absolute molecular density  $N_M$  determination. This temperature is commonly standing as  $T_{rot}$ .

For the determination of  $T_{rot}$  value the knowledge of relative line intensities within one pressure cell and discharge condition is sufficient. In case of such ratios, several factors present in the cross-sections  $\sigma_{fi}$  and line strengths  $s^i$  definitions simplify, as the electronic and vibrational terms are common here, as well as total electronic spin value and  $\Lambda$  quantum number are the same in every rotational sublevel of the  $a^3\Sigma_u^+$  state. If  $T_1$  and  $T_2$  stand for the transmission values for the laser beam tuned to transitions occurring from  $N_1''$  and  $N_2''$  rotational sublevels, the ratio of absorbances can be expressed as:

$$\frac{\ln T_1}{\ln T_2} = \frac{\phi_1 S_{HL}(N_1', N_1'')}{\phi_2 S_{HL}(N_1', N_2'')} \exp\left(-\frac{hc}{kT_{rot}}(F(N_1'') - F(N_2''))\right) \quad (4.7)$$

As before (subsection 2.2)  $S_{HL}(N', N'')$  is the Hönl-London coefficient adequate to considered branch (P,Q or R);  $\phi$  is a parameter depending on the parity of the sublevel ( $a, s$  for like nuclei). All these parameters are known and were discussed in mentioned subsection. Their values are given explicitly in the Tables 4.10 and 4.11 for observed transitions together with their relative peak amplitudes in respect to Q(2) and Q(3) transitions for  $^3\text{He}_2^*$  and  $^4\text{He}_2^*$  molecules respectively for investigated pressures of 8, 66.7, 128 and 266.7 mbar. The values of rotational energies of the  $N''$  sublevels have been calculated using the eq. (2.22b) applying the rotational constants met in [DR50] and [BG71] for  $^3\text{He}_2^*$  and  $^4\text{He}_2^*$  respectively. These constants have been determined assuming that the observed lines correspond to single transition within the rotational sublevels structure of  $a^3\Sigma_u^+$  and  $e^3\Pi_g$  states. However, as discussed in the section 4.3 this is not the case, as clear evidence of the line structure is presented in the absorption line frequency scans. This leads to the lower accuracy in determined molecular constant values in [DR50, BG71] that has been applied here. This uncertainty on rotational constants and later on the rotational energies and then fit of linear function to extract the  $T_{rot}$  value is hard to estimate and won't be performed here, however one has to take it into account when the results will be compared and unexplained discrepancies would be met.

Line designation	$N''$	$F(N'')$ [cm <sup>-1</sup> ]	$S_{HL}(N', N'')$	$\phi$	Relative (to Q(2)) $OUT_nLIA$				
					8	66.7 w	66.7 s	128	266.7
<sup>3</sup> He <sub>2</sub> *	Q1	20.09	$\frac{3}{2}(2 \cdot N'' + 1)$	4.5	0.25	0.22	0.24	0.25	0.23
	Q2	60.24		7.5	0.75	1.00	1.00	1.00	1.00
	Q3	120.41		10.5	0.25	0.32	0.31	0.34	0.30
	Q4	200.53		13.5	0.75	0.97	0.94	0.77	0.81
	Q5	300.5		16.5	0.25	0.19	0.22	0.22	0.23
	Q6	420.21		19.5	0.75	0.54	0.53	0.50	0.48
	Q7	559.52		22.5	0.25	0.09	0.10	0.10	0.10
	Q8	718.25		25.5	0.75	0.23	0.19	0.18	0.17
	P2	60.24	$\frac{3}{2}(N'' - 1)$	1.5	0.75	NR	0.25	0.23	0.21
	R0	0	$\frac{3}{2}(N'' + 1)$	3	0.75	NR	0.61	0.56	NR
	<b>T<sub>rot</sub> [K]</b>				<b>331±9</b>	<b>313±8</b>	<b>320±6</b>	<b>314±13</b>	<b>318±8</b>
	Discharge amplitude modulation function type				SIN	SQ	SIN	SIN	SIN
	Absorbance on Q(2) transition [ $\cdot 10^{-2}$ ]				0.24	5.20	12.25	12.42	9.67
	$\epsilon$ factor (see eq.4.5)				1.56	NC	10.41	12.28	7.08

Table 4.10: Compilation of the relative absorption lines amplitudes (with respect to the value for Q(2) transition) of <sup>3</sup>He<sub>2</sub>\* for various gas pressures. These data have been used for the  $T_{rot}$  determination (see fig.4.22) using the relation (4.7) and results are indicated in bold characters. Error values  $\delta T_{rot}$  results from the statistical error on line intensities determination used for the linear fit. The absolute values of absorbances measured on the Q(2) transition are recalled in the last row before the end (see Table 4.5). For the sine modulation, the modulation depth factor  $\epsilon$  (see subsection 4.2.3.2) is indicated. Abbreviations:  $n_m$  - density of atoms in 2<sup>3</sup>S<sub>1</sub> state,  $w$  - weak discharges excitation,  $s$  - strong discharge excitation, SIN, SQ - partial sinusoidal and 100% square amplitude modulation, NR- not recorded, NC- not considered for 100% square modulation

If the  $T_2$  is fixed to be the transmission for one chosen line (i.e. Q(2) for  $^3\text{He}_2^*$ ) and  $T_1$  is going through all the transmission values obtained for all the other lines within the pressure cell, isotope and discharge conditions, the dependency of the absorbances ratios on the rotational energy differences  $\Delta F = F(N_1'') - F(N_2'')$  can be set - it is linear when the natural logarithm of the absorbances ratio is taken and the ratios of  $\phi$  and Hönl-London factors are calculated. Fitting the linear function, the slope is obtained, that, through the velocity of the light  $c$ , Planck's  $h$  and Boltzmann  $k$  constants leads to the value of  $T_{rot}$ . On the figure 4.22, the performed fits for  $T_{rot}$  determination for different pressures of  $^3\text{He}$  are shown, and the obtained values of the temperature are given in the Table 4.10. The intensity of P(2) line of  $^3\text{He}_2^*$  was not taken into account in the linear fit, as is overlapped with the R(2) line of (1-1) vibrational band.

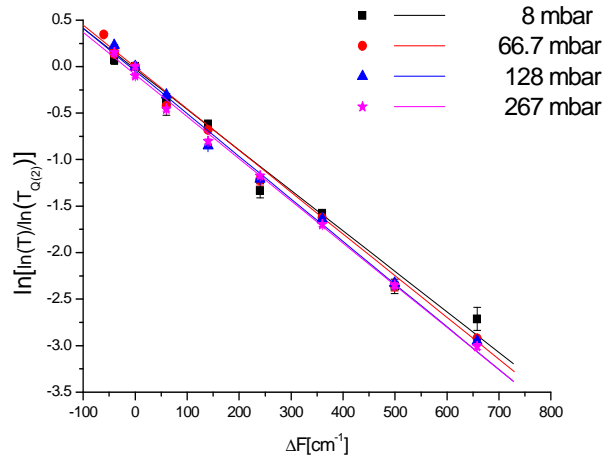


Figure 4.22: Comparison of the linear fits to the  $\ln\left(\ln T / \ln T_{Q(2)}\right)$  on  $\Delta F = F(N) - F(2)$  dependency (under the natural logarithm - the relative blue light transmission ratio for chosen transition from N rotational sublevel);  $T_{Q(2)}$  is the transmission of the blue laser beam tuned to Q(2) dependency on rotational sublevels energy difference  $\Delta F = F(N) - F(2)$  in 8, 66.7, 128 and 266 mbar pure  $^3\text{He}$  cell. From the slope value the rotational temperature  $T_{rot}$  has been determined (see the text and the Table 4.10)

Across the considered pressure range no significant (beyond the error values) change of rotational temperature value is observed. The only exception is the data for 8 mbar pressure, where increased value is noticed. however, it is not clear if this is the effect of the pressure change on  $T_{rot}$  (not observed for example between 67 and 266 mbar) or the low SNR for the frequency scans at this lowest pressure, affecting the line intensities values and thus their ratios. Besides the value for 8 mbar, the average  $T_{rot} = 318 \pm 4\text{K}$  was determined. This value is higher than the gas temperature of about 300 K inferred from the atomic helium-3 Gaussian linewidth component.

It is difficult to state about the difference in  $T_{rot}$  temperature between the two discharge regimes within the same pressure cell. For both isotopologues  $^3\text{He}_2^*$  and  $^4\text{He}_2^*$  the differences in rotational temperature for weak and strong discharge excitation are within the error bars of both  $T_{rot}$  values (see Table 4.10 and 4.11), however the tendency of a slight increase by 7 and 2 K respectively in the temperature with increase of the excitation amplitude would be in agreement with the expectations - it could be felt that the cell heats up more for the stronger discharges.



	Line designation	$N''$	$F(N'')$ [cm <sup>-1</sup> ]	$S_{HL}(N', N'')$		$\phi$	Relative (to Q(3))	
							$OUT_nLIA$	
							66.7 [mbar]	
							weak	strong
<sup>4</sup> He <sub>2</sub> *	Q1	1	15.17	$\frac{3}{2}(2 \cdot N'' + 1)$	4.5	1	0.69	0.66
	Q3	3	90.97		10.5		1.00	1.00
	Q5	5	227.12		16.5		0.82	0.82
	Q7	7	423.16		22.5		0.43	0.46
	Q9	9	678.40		28.5		0.18	0.18
	P3	3	90.97	$\frac{3}{2}(N'' - 1)$	3		0.35	0.37
	<b><math>T_{rot}</math> [K]</b>						<b>306±5</b>	<b>308±6</b>
	Discharge amplitude modulation function type						SQ	SIN
	Absorbance on Q(3) transition [ $\cdot 10^{-2}$ ]						4.44	15.35
	X factor						NC	8.84

Table 4.11: Compilation of the relative absorption lines amplitudes (with respect to the value for Q(3) transition) of <sup>4</sup>He<sub>2</sub>\*. These data have been used for the  $T_{rot}$  determination (see fig.4.23) using the relation (4.7) and results are indicated in bold characters. Error values  $\delta T_{rot}$  results from the error on line intensities determination used for the linear fit. The absolute values of absorbances measured on the Q(2) transition are recalled in the last row before the end (see Table 4.6). For the sine modulation, the modulation depth factor  $\varepsilon$  (see subsection 4.2.3.2) is indicated. Abbreviations: SIN, SQ partial sinusoidal and 100% square amplitude modulation, NC not considered for 100% square modulation

The change of  $T_{rot}$  with different isotope was investigated for two 66.7 mbar cells filled with <sup>3</sup>He and <sup>4</sup>He as well as in 67 mbar mixture cell only for <sup>4</sup>He (see comment further in the text) - Fig.4.23.

In case of the cell filled with 67 mbar 1:1 helium isotopic mixture the reliable determination of the  $T_{rot}$  for the (<sup>3</sup>He-<sup>4</sup>He)\* as well as <sup>3</sup>He<sub>2</sub>\* was not possible due to insufficient number of well resolved lines. Partially overlapped lines could not be used, as their measured intensity would not correspond to the population of the  $N''$  sublevel and thus would give the transmission ratio not reflecting the rotational temperature distribution. According to the fig.4.24, for (<sup>3</sup>He-<sup>4</sup>He)\* 5 lines were available, however, corresponding to the transition occurring from the neighboring rotational sublevels. Thus, the small range of  $\Delta F$  values (-60 to 120 cm<sup>-1</sup>) allow obtaining  $T_{rot} = 284 \pm 7K$  that could not be trusted, especially when in similar case of <sup>3</sup>He<sub>2</sub>\* , the fit to only three available points within  $\Delta F$  (-40 to 60 cm<sup>-1</sup>) gave unreasonable value of  $T_{rot} = 236 \pm 8K$ , much below the results obtained earlier for the same pressure and similar discharge conditions. However, the spectral lines for <sup>4</sup>He<sub>2</sub>\* , except Q(3) do not coincide with any of other isotopologue's, and determination of rotational temperature confirmed previously obtained values ( $T_{rot} = 299 \pm 13K$ ).

Obtained results of the rotational temperature  $T_{rot}$  are close to the temperature of the gas ( $T_{gas} = 300 K$ ) inferred from the Doppler width of helium-3 atomic lines doublet C<sub>8</sub> and C<sub>9</sub>. Similar experimental conditions has been met in [SBG<sup>+</sup>85] where <sup>4</sup>He<sub>2</sub>\* has been investigated in the pressure range of 2 to 160 mbar. Authors report about two coexisting thermal ensembles up to  $N'' = 9$  and for  $N'' > 9$  for which two different temperatures has been determined: about

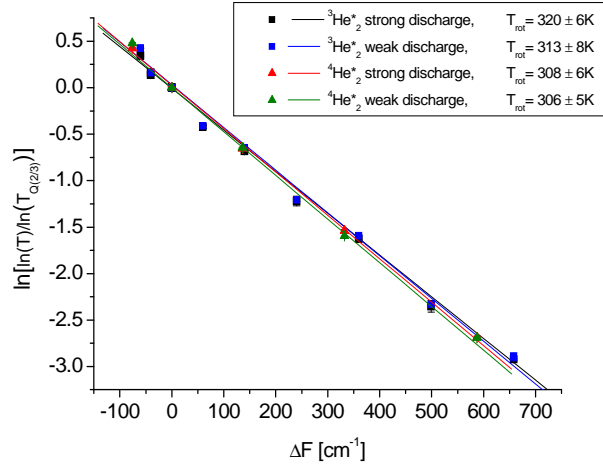


Figure 4.23: Comparison of the rotational temperatures between two isotopologues  $^3\text{He}_2^*$  and  $^4\text{He}_2^*$  at the pressure of 66.7 mbar. Investigations were performed in two separate isotopic pure cells for two discharge regimes - weak and strong in each case. Change in the slope value indicates the change in  $T_{rot}$ . Lower the slope value, lower the  $T_{rot}$  temperature - for the weak discharges  $T_{rot}$  is lower than for strong discharge regime in case of both isotopologues. Temperatures are higher for  $^3\text{He}_2^*$  than for  $^4\text{He}_2^*$ .

300K and 2000 K respectively. According to their division, in this work only low temperature ensemble is available for the investigations and fair agreement has been obtained in comparison with reported value that is given as approximated one without the error value. Higher rotational sublevels are out of the laser source range and can't be investigated nor compared with this reference. Also reference [DR50] mention about change in the slope of the linear fit for rotational temperature determination, however much stronger discharge excitation has been used and therefore temperatures ranging between 580 to 820 K are reported.

#### 4.5.2 Dynamics of helium molecule

Measurements of the transmission using continuous wave laser source as it is the case of 465 nm laser setup allows following molecular dynamics, that is the decay process of their density when the discharge plasma fades after the applied alternate voltage is stopped. At the beginning, before the discharge is being switched off the processes of formation and destruction of molecular species are in balance, so the steady state is set, the density of metastable molecule is constant. When the discharges are turned off, the decay of metastable atoms density results in simultaneous decrease of the three body collisions being the source of the molecules in  $a^3\Sigma_u^+$  state. Predominance of the destruction processes results in progressive decrease of their density. This behavior can be observed by the laser transmission changes observation that reflects the metastable molecules density variations. By the comparison between the decay processes of metastable atoms and molecules, the proper terms in differential equations describing the dynamics of both related species can be identified and characterized quantitatively. As it will be shown those decays are not simply exponential what is a consequence of variety of occurring processes of the destruction and domination of one over the others. Also the gas pressure change has its consequences in the shape of the decay curve giving information about the importance of the destruction terms related to this intensive parameter.

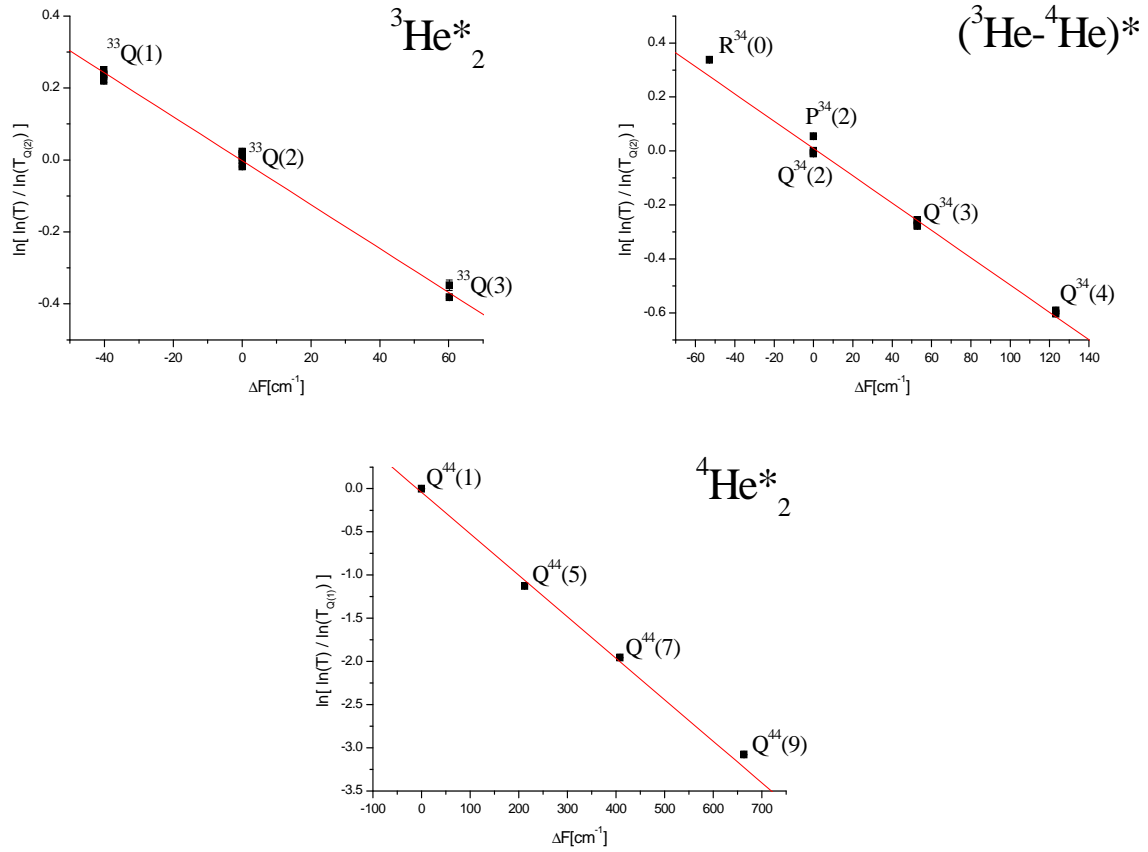


Figure 4.24: Comparison of the linear fits to the  $\ln(\ln T / \ln T_{Q(2)})$  on  $\Delta F = F(N) - F(2)$  dependency for three helium molecular isotopologues present in 1:1  ${}^3\text{He}$  and  ${}^4\text{He}$  isotopic mixture gas at 66.7 mbar pressure. The lines of  ${}^3\text{He}^*_2$  and  $({}^3\text{He}-{}^4\text{He})^*$  spectrum suitable for the analysis (well separated lines from the others present in the overall spectrum for three isotopologues) are covering a small range of  $\Delta F$  values so that reliable linear fits for  $T_{rot}$  determination in these cases are not possible, contrary to the  ${}^4\text{He}^*_2$  molecule. Only in case of the  ${}^4\text{He}^*_2$  present in the mixture, determined  $T_{rot}$  agrees with the one resulting from the measurements in isotopic pure cells.

#### 4.5.2.1 Molecular and atomic density decay curves

The recordings of the transmission decays were performed in four different gas pressure between 8 and 266 mbar of  ${}^3\text{He}$  gas as well as for isotopic pure  ${}^3\text{He}$ ,  ${}^4\text{He}$  and mixture at 66.7 mbar when no optical pumping is performed (neglecting formation from  $\text{He}(2^3\text{P})$ ).

Figures 4.25 shows the absorbance value decay curves (proportional to the atomic and molecular densities decrease) being a result of measurements described in subsection 4.1.4. The dynamics for both atomic and molecular species are shown. The non-exponential character of the decays of both atomic and molecular densities is clearly visible on the plots in the ln scale, where simple exponential dependency should result in the linear change in time.

Comparing the decay curves for the atoms and molecules for pressure range between 8 - 266 mbar on Fig.4.25(a)-(d), one can see the difference not only in the decay times between both species, but also that the character of this process is different.

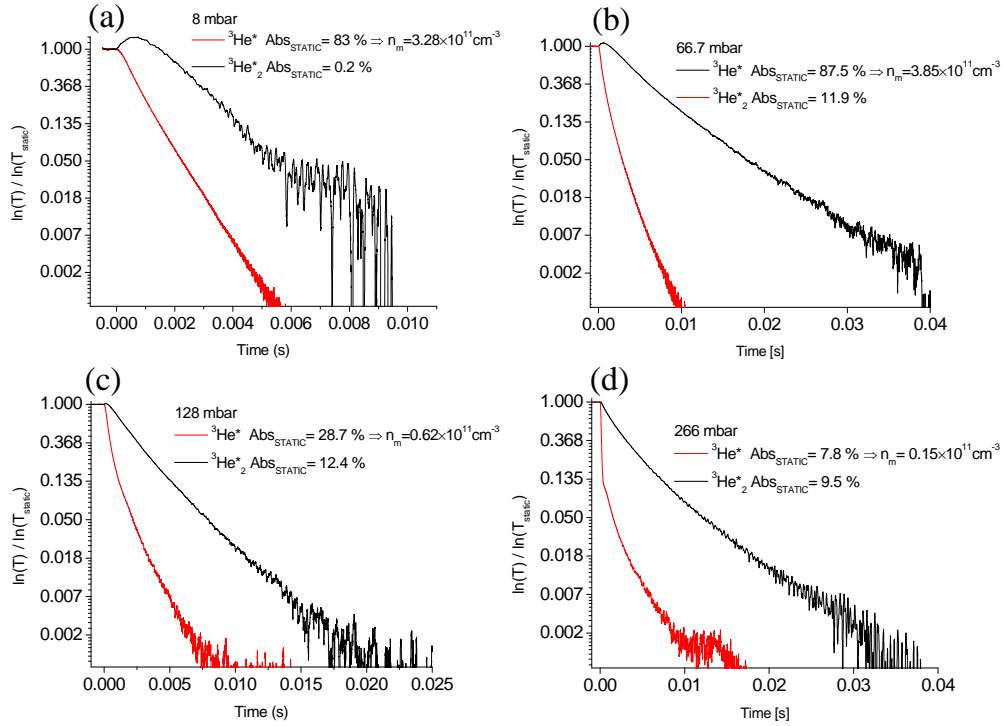


Figure 4.25: Time decay curves of atomic (red lines) and molecular (black lines) relative to the steady state densities values (plasma discharges are switched off at Time=0 on the graphs), as the ratios of obtained absorbances  $\ln(T)/\ln(T_{static})$  in pure  $^3\text{He}$  cells at: (a) 8 mbar, (b) 66.7 mbar, (c) 128 mbar, (d) 267 mbar. The semi-log graphs (a)-(d) emphasize the non-exponential character of both atomic and molecular densities decays.

For the atoms, the half-life time  $\tau_{0.5}$  (time after which the absorber density reaches the half of the initial value - before the plasma discharge is being switched off) decreases with the pressure increase - Fig.4.26(a). There is no such tendency in the half-life times for the molecules - Fig.4.26(b). In case of the molecules, just after the discharge is being turned off, there is an increase of  $-\ln(T)$  value at early times ( 0.1-0.7 ms) for 128 - 8 mbar respectively. The effect decreases with pressure - Fig.4.26(c), starting at the increase of 38% in respect to the static value for 8 mbar ending at almost no increase ( 0.1%) after discharge turning off at 266 mbar. Such effect does not occur for the atoms, however for the latter the decay at the highest considered pressure is worth noting. Up to about 0.3 ms the decay is much rapid then for the later times - the effect is increased when going from lower to higher pressure indicating that there are different leading processes of metastable atoms density decay at considered time periods. The fact, that both - the increase of the molecular density and the change of the atomic decay slope occurs at common time scale of gives an indication of a relation between the decrease of metastable atoms number and increase of molecular density.

The difference is also visible when comparing the molecular decays between three isotopologues. The increase of the  $-\ln(T)$  signal at early times ( 0.4 ms) is the lowest for the  $^3\text{He}_2^*$  and rises with the mass of the molecule, so as the half-decay time.

In contrast to the molecular species, the comparison of the atomic  $^4\text{He}$  and  $^3\text{He}$  decay curves does not exhibit any qualitative or quantitative difference - Fig.4.28.

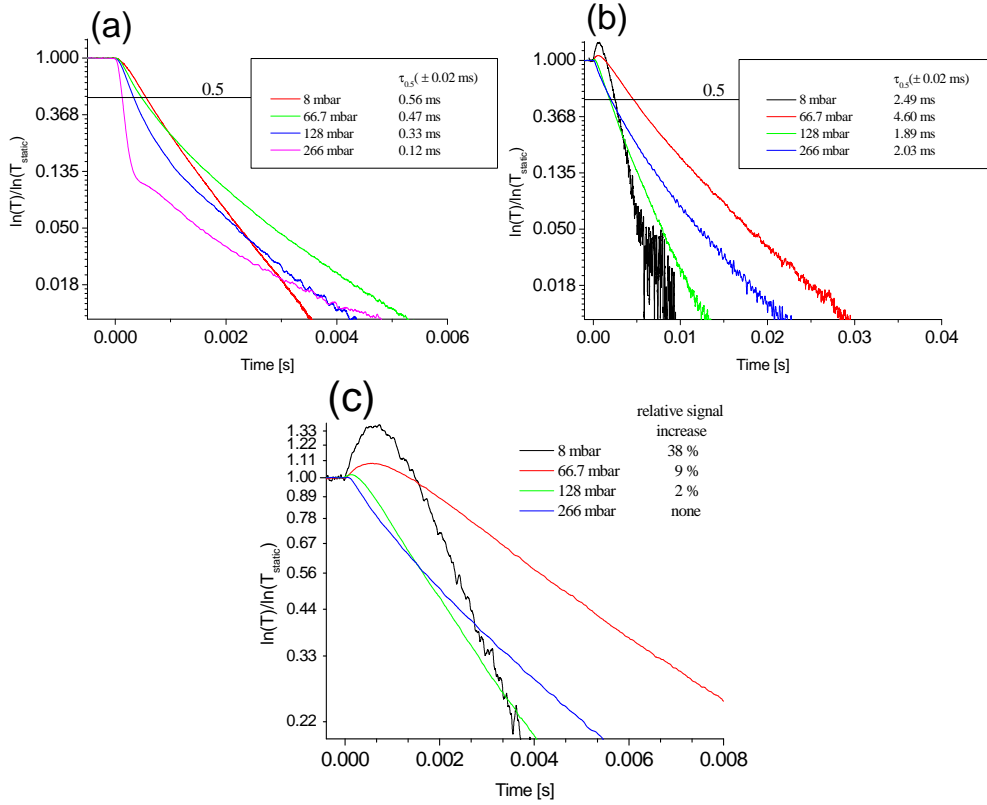


Figure 4.26: Impact of gas pressure on the atomic (a) and molecular (b) densities time evolutions. The half-life times  $\tau_{0.5}$  are pasted on the graphs for each pressure (the  $y=0.5$  line is plotted as a guide for the eye). The early part of the time decay is blown-up in the graph (c) with linear scale to show the significant increase in molecular density with respect to the steady-state value observed shortly after switching off the discharges. The percentage values of signal increase are given for each pressure.

#### 4.5.2.2 Atomic and molecular coupled rate equations

As the molecular species formation relies on the three-body collision between the excited state atom and two ground state atoms, one expects that the rate equation of formation and destruction of molecular and atomic species to be coupled. As the processes driving the both atomic and molecular species population changes  $\frac{\partial n_m}{\partial t}$  and  $\frac{\partial N_M}{\partial t}$  are common it is useful to mention them together allowing straightforward comparison as well as emphasizing the coupling terms in which both populations occur simultaneously. Following collisional processes have to be considered [DMCL76]:

- formation of the metastable molecules in 3-body collision between metastable state atoms and ground state atoms:  $\text{He}(2^3S) + 2\text{He}(1^1S) \rightarrow \text{He}_2(a^3\Sigma_u^+) + \text{He}(1^1S)$
- Ionization collisions within only atomic or only molecular species:  
for atoms:  $\text{He}(2^3S) + \text{He}(2^3S) \rightarrow \text{He}^+ + \text{He} + e + 15.0 \text{ eV}$   
and  $\text{He}(2^3S) + \text{He}(2^3S) \rightarrow \text{He}_2^+ + e + 17.4$   
for molecules:  $\text{He}_2(a^3\Sigma_u^+) + \text{He}_2(a^3\Sigma_u^+) \rightarrow \text{He}^+ + 3\text{He} + e + 11.3 \text{ eV}$   
and  $\text{He}_2(a^3\Sigma_u^+) + \text{He}_2(a^3\Sigma_u^+) \rightarrow \text{He}_2^+ + 2\text{He} + e + 13.7 \text{ eV}$

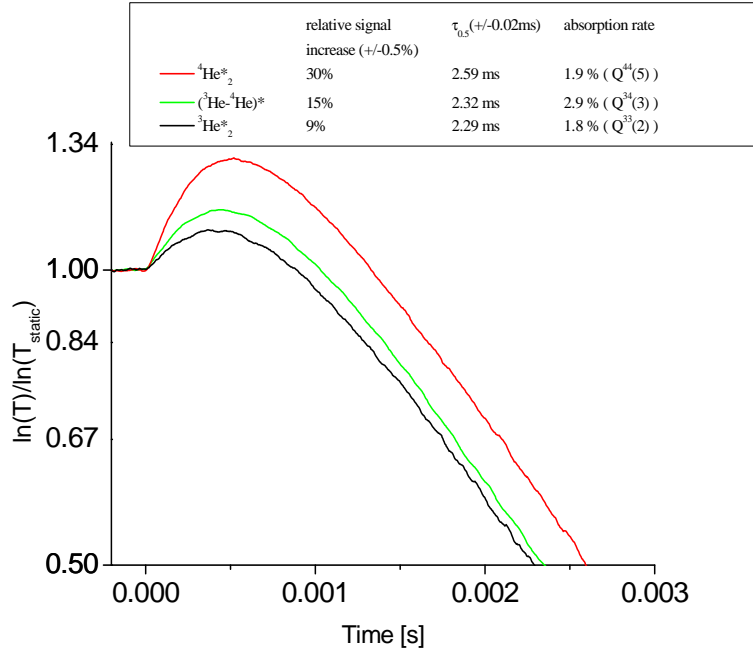


Figure 4.27: Comparison of the decay curves for three isotopologues of  $\text{He}_2^*$ . Relative increase of the molecular density is given on the graph as well as half-life times and steady-state molecular absorption rates. They both increase with the mass of the molecule what could be addressed to the inverse proportionality of the diffusion coefficient  $D_{mol}$  (appearing in the eq.(4.9)) on the molecular mass.

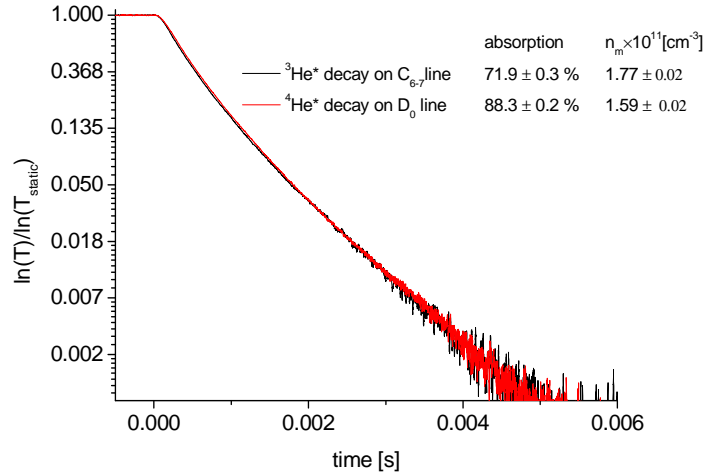
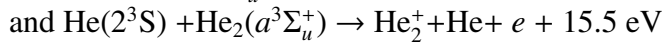
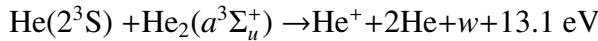


Figure 4.28: Comparison of the time evolutions of atomic  $^3\text{He}$  and  $^4\text{He}$  densities in the 1:1 isotopic mixture cell at 66.7 mbar. Absorption values measured on  $C_{6-7}$  and  $D_0$  transitions and corresponding  $n_m$  densities are given on the figure.

Process	Contribution to the rate equation	
	$\frac{\partial n_m}{\partial t}$ for He( $2^3S$ )	$\frac{\partial N_M}{\partial t}$ for He $_2(a^3\Sigma_u^+)$
Diffusion term - atoms and molecules freely diffuse due to their densities gradients. It is assumed that the densities are null at the cell wall surface.	$-D_{at}\nabla^2 n_m$ $D_{at}$ - diffusion coefficient for helium atom	$-D_{mol}\nabla^2 N_M$ $D_{mol}$ - diffusion coefficient for helium molecule
Conversion of metastable $2^3S_1$ atoms into molecules in 3 body collisions - presence of ground state atoms impose the pressure dependency of $P^2$	$-\delta_m P^2 n_m$ $\delta_m$ - creation rate coefficient from the $2^3S_1$ state (see section 2.0.1)	$+\delta_m P^2 n_m$
Ionization collisions within one species - Penning collisions with the destruction rate coefficients $\beta_{at}$ and $\beta_{mol}$ for atoms and molecules respectively.	$-\beta_{at} n_m^2$	$-\beta_{mol} N_M^2$
Ionization collisions between the two considered species with common destruction rate coefficient $\beta_{at-mol}$	$-\beta_{at-mol} n_m N_M$	
Direct creation by rf-driven excitation processes [e.g. electron-ion recombination]	$+creation_{n_m}$	$+creation_{N_M}$

Table 4.12: Atomic and molecular evolution rate terms for creation and destruction processes in pure  $^3\text{He}$  gas in the absence of optical pumping.

- Ionization collisions between metastable atoms and molecules:



Making use of the terms presented in the Table 4.12 global evolution equations can be written (according to [Cou01], preserving the notation) for both metastable species as follows:

$$\frac{\partial n_m}{\partial t} = -D_{at}\nabla^2 n_m - \delta_m P^2 n_m - \beta_{at} n_m^2 - \frac{1}{2}\beta_{at-mol} n_m N_M + creation_{n_m} \quad (4.8)$$

$$\frac{\partial N_M}{\partial t} = -D_{mol}\nabla^2 N_M + \delta_m P^2 n_m - \beta_{mol} N_M^2 - \frac{1}{2}\beta_{at-mol} n_m N_M + creation_{N_M} \quad (4.9)$$

Required parameters standing next to the rate equations terms of the Table 4.12 has been found in the literature and are compiled in the Table 4.13.

Presented equations refers to the situation when no laser enhanced molecular formation takes place - no OP pump beam present. In this conditions the term  $\pm\delta_P^2 n_P P^2$  related to the formation from He( $2^3P$ ) has been neglected in both equations.

Parameter name	Rate equations parameter value	
	$^3\text{He}^*$	$^3\text{He}^*_2$
Diffusion coefficient [ $\text{cm}^2\text{Torr s}^{-1}$ ]	$D_{at} = (554 \pm 30)^{[\text{FLW68}]}$	$D_{mol} = (416 \pm 39)^{(*)}$
$\delta_m [\text{Torr}^{-2}\text{s}^{-1}]$	$(0.16 \pm 0.04)^{[\text{EADL88}]}$	
$\beta \times 10^{-9} [\text{cm}^3\text{s}^{-1}]$	$\beta_{at} = (1.5 \pm 0.3)^{[\text{DMCL76}]}$	$\beta_{mol} = (1.5 \pm 0.5)^{[\text{DMCL76}]}$
$\beta_{at-mol} \times 10^{-9} [\text{cm}^3\text{s}^{-1}]$	$(2.5 \pm 1.5)^{[\text{DMCL76}]}$	
$creation_{n_m} [\text{at}\cdot\text{cm}^{-3}\text{s}^{-1}]$	$10^{13}$	

Table 4.13: Compilation of parameters in the rate equations (4.8) and (4.9).

(\*) -  $D_{mol}$  is obtained from published value for  $^4\text{He}^*_2$  ( $361 \pm 34 \text{ cm}^2\text{Torr s}^{-1}$ , [GG70]) through the isotopic mass scaling:  $D_i = D * \sqrt{M/M_i}$

Preliminary numerical analysis, that is in progress, of these atomic and molecular coupled equation rates, that only include molecular creation through 3-body collisions, destruction by Penning collisions, diffusion and quenching, show that the main features of observed time evolution behavior of both species can be qualitatively reproduced, including:

- the increase of  $N_M$  above the steady-state equilibrium value at early times, the difference of the increase magnitude between three isotopologues and disappearance of the effect with the pressure increase
- differences in the life times between isotopologues
- identical time evolution for metastable  $^3\text{He}$  and  $^4\text{He}$  in the gas mixture
- correct orders of magnitude for molecular densities and time scales of evolution when the available rate coefficients are combined with the experimentally measured  $n_m$  values. Suitable time scales for evolution are obtained using the published coefficient rates for "reasonably" guessed molecular densities. Further work is needed to check whether the existing and/or some complementary body of experimental data can be used to reliably infer  $n_M$  values (and validate the cross-section values from [NTSL94]) and qualitatively confirm/constrain the rate coefficients (that are not so well known).

## 4.6 Summary and conclusions

Absorption measurements performed on the metastable helium molecules  $\text{He}_2^*$  were an introduction to the dedicated measurements in the condition of the metastability exchange optical pumping that are the matter of the following chapter. Simple transmission spectroscopy allowed identification of the  $a^3\Sigma_u^+ - e^3\Pi_g$  transition lines within the wavelength tuning range of the blue laser setup (see chapter 3). These measurements were in fact the basis of the laser wavelength calibration at the initial stage of its performance characterization, relying on the spectroscopic references for  $^3\text{He}_2^*$  [DR50] and  $^4\text{He}_2^*$  [DR50, BG71]. This was further confirmed by the measurements using the wavelength meter device. In this way, the mentioned references of molecular helium emission spectroscopy data were confirmed here by the absorption spectroscopy technique. Relying on the published molecular constants for heteronuclear isotopologues, the positions of the first eleven ( $^3\text{He}$ - $^4\text{He}$ ) $^*$  isotopologue lines were computed



using the mass scaling laws and confirmed with the measurements, and later by the reference data ([DGD77]). The good agreement proved the correctness of computations performed on the basis of the theory presented in chapter 2.

The continuous fine tuning of the laser wavelength allowed molecular lines absorption profiles recording. This revealed a complex structure of the observed profiles, not reported elsewhere for the  $a^3\Sigma_u^+ - e^3\Pi_g$  transition, . Graphical analysis and comparison with the available reference for different  $\text{He}_2^*$  transition (  $a^3\Sigma_u^+ - c^3\Sigma_g^+$  ) allows to suspect that every observed profile of chosen rotational transition consists of several components that are lines corresponding to transitions between fine structure sublevels of the involved lower and upper rotational levels. The lack of the fine structure parameters in the  $e^3\Pi_g$  state at the time of the PhD project did not allow to fully qualitatively and quantitatively explain the observed profiles shapes in terms of mentioned structure. It is therefore an indication that further measurements could be performed, for example using Doppler free spectroscopy methods (e.g. saturation spectroscopy with two counter propagating beams weak and strong), to resolve the complex profiles structure and to determine the unknown coefficients. As has been presented, measurements at low gas pressures do not provide any additional information as the SNR drops significantly and the line profiles shape issues (e.g. differences between odd- and even-N numbered transitions, difference between the lineshape of Q(1) and the higher odd-N numbered transitions within a single isotopologue spectrum) seen even at higher pressure, get lost in the noise. From another point of view the fact that the complex line structure is not resolved but appears as a single line and is treated in such manner in numerous references given in this work, justifies in this work the use of reported parameters values such as rotational constants, oscillator strengths and lifetimes. They were in fact determined from spectroscopic data where the structure remained hidden within single line profiles. Although the components of the observed profiles are so close to each other that their resultant resembles a single transition line profile, the absolute density value of metastable molecules inferred from the measured absorbance cannot be precise, when dependencies worked up in the case of a transition between rotational levels without taking sub-structure into account are used. As it is shown in the next chapter, in the case of an investigation on a possible relationship between the enhancement in molecular formation due to the presence of a 1083 nm pumping light during the MEOP and the laser enhanced relaxation, the relative change in the molecular density is important. Staying tuned with a laser to a chosen rotational transition the relative change (for example in respect to some steady-state plasma condition) of the molecular density depends only on the ratio of measured absorbances, while all factors related to the chosen transition (e.g. parameters related to the statistics, oscillator strengths) cancel out. To conclude, the determination of the absolute molecular density value would be desired, but not necessarily needed to achieve the aim of this work.



# Chapter 5

## Investigations on Metastability Exchange Optical Pumping dynamics with blue laser

The Metastability Exchange Optical Pumping (MEOP) is well developed method of polarized  $^3\text{He}$  gas production for the variety of applications such as polarized targets in nuclear physics experiments, cold neutron spin filters and magnetic resonance imaging (MRI) of human respiratory system air spaces. The MEOP is an alternative method of obtaining the polarized helium-3 to Spin Exchange Optical Pumping (SEOP). For the details about the second method the Reader is sent to [WH97] . In this work the former method of polarization has undergone investigations with use of the laser setup working at 465 nm for helium molecule detection (see chapter 3) serving complementary information to the model of MEOP developed by both cooperating scientific groups since 1985 [NL85, CMN<sup>+</sup>02, BNT11]. Presented in this work details of the MEOP model are limited to the minimum providing the background of the main target of these investigations which is the expected influence of molecular helium species on the polarization loss induced by optical pumping light at 1083 nm. For more detailed description of the model the Reader is sent to the references mentioned.

### 5.1 Basics of MEOP

Metastability Exchange Optical Pumping is a two stage process that results in non-equilibrium distribution of nuclear spin (spin 1/2) orientation of  $^3\text{He}$  atoms. During the process three states are involved that are: ground state atoms  $1^1\text{S}_0$  of which the nuclear polarization is of the main interest, the metastable state  $\text{He}(2^3\text{S})$  atoms and helium atoms in the second excited state  $2^3\text{P}$  .

The 6 hyperfine structure sublevels ( $a_i, i = 1, \dots, 6$ ) of the long-lived  $2^3\text{S}_1$  state ( $8 \cdot 10^3$  s compared to  $10^{-7}$  s of natural lifetime of  $2^3\text{P}$  ) are being populated through the radiative decay cascade of highly excited atoms present in the discharge plasma sustained in the gas - see the scheme on the fig.5.1 given also before in the manuscript introduction - Chapter 1. This metastable state serves as a bottom state in the optical pumping process (OP) that is the first stage of the MEOP. The excited state in this OP scheme is the  $2^3\text{P}$  , which 18 hyperfine structure sublevels ( $b_j, j = 1, \dots, 18$ ), is coupled to the  $2^3\text{S}_1$  with optical transition at infra-red wavelength of 1083 nm. Orientation of the electronic angular momentum enforced by OP induces the orientation of spin of the nucleus due to existence of strong entanglement between both electronic and nuclear spin state in the  $2^3\text{S}_1$  . In the second stage of MEOP the orientation of the nuclei is transferred to the ground  $1^1\text{S}_0$  state through the metastability exchange (ME)

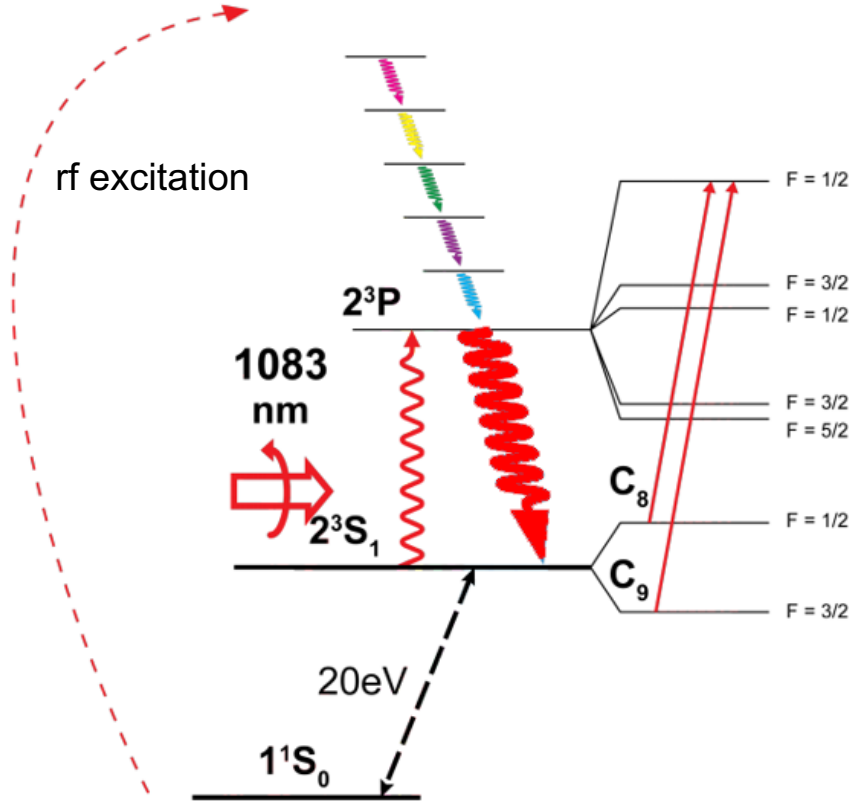


Figure 5.1: Schematic diagram of Metastability Exchange Optical Pumping process. Multi-color arrows represent radiative deexcitation cascade of high lying states populated by the rf excitation. Red arrows represent the 1083 nm transition and radiative deexcitation occurring between  $2^3S_1$  and  $2^3P$  states. Black dashed arrow represents the metastability exchange collision between  $2^3S_1$  and  $1^1S_0$  states. On the right side of the scheme, the  $C_8$  and  $C_9$  transitions between hyperfine sublevels of  $2^3S_1$  and  $2^3P$  states are presented.

collisions. In this binary process the electronic excitation of the  $2^3S_1$  is overtaken by the colliding partner - the ground state atom, as well as the electron spins are exchanged (this is the only non-zero electronic angular momentum in both states). Contrary to the metastable excitation that is fully (without any change of describing quantum number) transferred from one atom to another, the nuclear orientation of both partners is conserved. It can be simply considered as the exchange of the nuclear spins, so that the output of the collision are the ground state atom with the nuclear spin with desired orientation and the metastable state atom with the nuclear orientation of the incident  $1^1S_0$  atom.

The MEOP was originally performed in so-called "standard" conditions of low helium gas pressure of several mbar and magnetic fields of several mT and in this pressure and field regime has been mainly developed. However, the application requirements of the polarized gas at higher pressures at about 1 bar, enforced the development of gas compression methods characterized by low polarization losses during this mechanical procedure. Alternatively the MEOP at high (several tens or hundredths mbar, reducing or even avoiding the compression) helium-3 pressures was proposed and successively and efficiently performed at much higher ( $10^2 - 10^3$

times) magnetic field exclusively. The details about the electronic states involved in the MEOP process as well as the possible optical transitions used in optical pumping stage are well described in [NL85, CMN<sup>+</sup>02] and their notation has been applied in this work.

Both populations coupled by the ME collisions follow the Boltzmann-like distribution of angular momentum ( $\exp(\beta)$ ), provided that no OP is performed and relaxation has negligible influence on the populations. This distribution is driven completely by the spin temperature ( $1/\beta$ ) of the ground state  $1^1S_0$ , which number density  $N_g$  is about 6 orders of magnitude higher than  $n_m$  of the  $2^3S_1$  state. The spin temperature depends on the nuclear polarization  $M$  of the ground state, defined as the difference between amount of atoms for which nuclei  $m_I = 1/2$  and  $m_I = -1/2$  normalized by the total number of the atoms in the gas ( $M = \frac{N_{1/2} - N_{-1/2}}{N_{1/2} + N_{-1/2}}$ ), by the relation

$$\exp(\beta) = (1 + M)/(1 - M) \quad (5.1)$$

Independently of the magnetic field the knowledge of the polarization  $M$  and therefore spin temperature allows obtaining the relative  $a_i$  ( $\sum_{i=1}^6 a_i = 1$ ) populations of chosen metastable state sublevel characterised by the projection of total atomic angular momentum  $m_F$ :

$$a_i = \frac{e^{\beta m_F}}{e^{-3\beta/2} + 2e^{-\beta/2} + 2e^{\beta/2} + e^{3\beta/2}} \quad (5.2)$$

Optical pumping, performed with use of the circularly polarized light at 1083 nm, affects the distribution of metastable state atoms within its 6 sublevels and consequently, through the collisional ME coupling with the ground state, the value of  $M$  is being changed. Of course during only the OP process the spin distribution is not valid, as the sublevels addressed by the laser, depending on chosen transition  $C_8$  or  $C_9$  (see Fig.5.2), are efficiently depleted, however, if only the pumping light is off, the system returns to the Boltzmann distribution with spin temperature determined by the increased value of  $M$ . At each of the MEOP stages as well as for already polarized gas there are relaxation processes that tends to restore the equilibrium conditions where  $M$  is close to 0 (low thermal polarization of order  $10^{-9}$  at 1 atm and field 1 mT to  $10^{-6}$  at 1.5 T still remains). When the discharge plasma is exposed to the pumping laser beam, relaxation is competing with the OP, that depopulates certain sublevels of  $2^3S_1$  creating unbalanced nuclear orientation in one direction that is transfered to the ground state atoms in ME collisions occurring at the pressure dependent rate  $\gamma_e/p = 3.75 \times 10^7 \text{ s}^{-1}/\text{mbar}$  [DRLL71].

The  $2^3S_1$ ,  $2^3P$  and  $1^1S_0$  states populations development is driven by the two stages of the MEOP and so called relaxation in the metastable and  $2^3P$  state that is the aim of these states to equalize their sublevels population as it is the case for equilibrium  $M=0$ . The relaxation in the metastable state is rather slow compared to the  $2^3P$  state. The collisions in which the  $2^3S_1$  atoms are involved in can couple the populations only through the spin exchange and the relaxation is associated for instance with de-excitation of the atom and re-excitation in the plasma, providing the relaxation rate  $\gamma_r^S$  value depending on pressure, cell dimension, gas purity, of order  $10^3 \text{ s}^{-1}$ . The loss of metastable excitation takes place usually during its collision with the cell wall what is a result of the atoms diffusion and provides a lower bound for the rate. The relaxation in the  $2^3P$  state is much faster due to possible  $J$  changing collisions occurring at the pressure dependent rate  $\gamma_r^P = 0.32 \times 10^7 \text{ s}^{-1}/\text{mbar}$  [Bat11]. This means a significant transfer between populations of the state sublevels during its radiative lifetime  $\tau$  ( $\equiv 1/\gamma \sim 10^{-7} \text{ s}$ ) Detailed equations of the  $2^3S_1$  and  $2^3P$  states evolution when relaxation, OP and ME processes are taken into account are given in [BNT11] for certain velocity class with  $v_z$  projection along

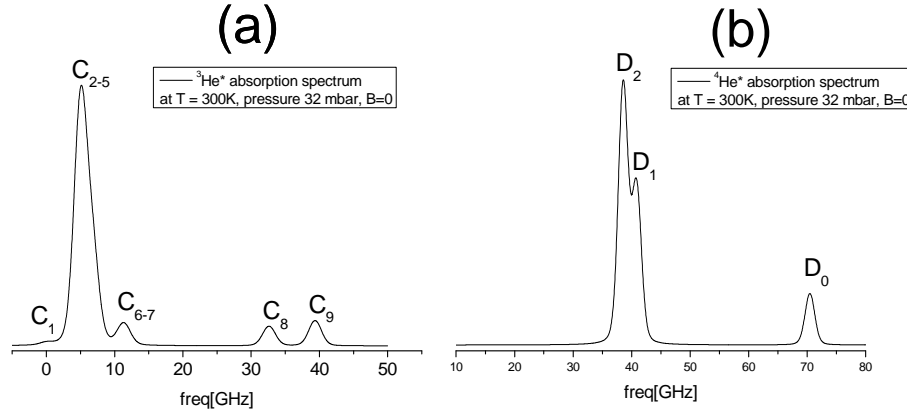


Figure 5.2: Calculated absorption spectra of  $^3\text{He}^*$  (a) and  $^4\text{He}^*$  (b) at 300 K, pressure 32 mbar and null magnetic field  $B$ . Doppler and pressure broadening effects has been taken into account. The lines designation is given according to well established nomenclature [NL85]. Notice the frequency scale and overlapping of  $C_8$  and  $C_9$  lines with  $D_2$  and  $D_1$  if absorption spectroscopy in isotopic mixture gas is performed.

OP beam. This velocity dependence is introduced by the OP process due to presence of the Doppler shifts and a given laser beam spectral profile. Characterization of OP influence on the electronic and nuclear orientations and on the light absorption by the gas can be performed by numerical calculations of the populations in  $2^3\text{S}_1$  and  $2^3\text{P}$  states from the rates equation, under following assumptions. Due to complexity induced by presence of various velocity classes and coupling of their populations by velocity-changing and ME collisions, the model of two broad classes has been proposed: strongly pumped atoms in the center of Maxwell velocity distribution and weakly pumped atoms in the wings of the distribution. This attempt has been confirmed to give reliable quantitative results. The evolution, described by the rate values  $\gamma_e$  and  $\gamma$ , of the two states involved in the OP is about 6 orders of magnitude faster than the ground state nuclear polarization time evolution. This justifies the method of solving the  $2^3\text{S}_1$  and  $2^3\text{P}$  rate equations adiabatically, what means fixing all the values together with  $M$  as a constant. The solutions providing also an information about changes of OP laser beam absorption due to different from non-equilibrium spin-temperature populations distribution. The absorption is decreasing with the  $M$  as well as incident laser power increase.

## 5.2 Achievements in MEOP in standard and non-standard conditions

The MEOP method, originally developed in the low field and low pressure conditions has been recently extensively investigated with the purpose of working out theoretical model as well as to finding optimal operation conditions such as gas pressure, magnetic field strength, radio frequency discharge intensity, power as well as spectral and spatial transverse profile of the pumping laser beam. The work was done in the sealed cells containing pure helium-3 gas or helium-3 and helium-4 mixture, prepared, cleaned and filled according to well-tried procedures. Analogous investigations were performed at high magnetic fields (from 0.1 T up to 4.7 T) and pressures up to 266 mbar. Satisfactory results were then obtained with open cells with gas

flow during the MEOP process, in a dedicated gas polarizer setup, that produces the polarized gas ready to use in various applications. The first high-field MEOP polarizer has been under construction and testing during this work (see reference [Col11]).

The results of the systematic investigations on MEOP lead to several conclusions about the process efficiency in various conditions briefly recalled here:

- Steady-state polarization  $M_{eq}$  decays with the increased gas pressure. At low magnetic field polarizations up to  $M_{eq} = 0.8$  are obtained at about 1 mbar gas pressure and to less than 0.1 at 32 mbar [ASM<sup>+</sup>04]. This effect has first been attributed to the increased rate of auto-ionizing Penning collisions at high pressure [SR70], that shortens the metastable state atom lifetime and limits its density in the plasma. Another reason proposed for the observed decrease of  $M_{eq}$  with pressure is the enhanced formation of helium metastable molecules  $\text{He}_2^*$  due to the increased likelihood of three-body collisions. The polarized metastable and ground state atoms associated in a molecule can loose their orientation of their nuclear angular momenta, due to coupling of the nucleus spin and orbital angular momenta, in one of the rotational molecular states. The results presented in [Nik10] clearly shows the inhibition of the influence of relaxation processes on achieved  $M_{eq}$  values for high ( $>10$  mbar) pressure cells at high magnetic field of 1.5-4.7 T, where high values of  $M_{eq}$  achieved, i.e. 0.75 for 32 mbar at 2T and 0.25 for 266 mbar at 4.7 T.
- The time required to reach the steady state polarization (so-called build-up time  $\equiv t_b$ , polarization dependent -  $t_b(M)$ ) increases with the gas pressure and with the magnetic field. Improvement (shortening) in the  $t_b$  value can be obtained increasing an absorbed power of the pump laser. However, the increase of  $M_{eq}$  with absorbed laser power is lower than predicted by the model, suggesting additional relaxation channel enhanced by the presence of the pumping light. More details about the manifestation of such relaxation is discussed in following subsection 5.3 where angular momentum budget during the MEOP is presented and compared with the results of previous investigations.

### 5.3 MEOP angular momentum budget and laser induced relaxation

The effect of OP and ME on the built up of ground state nuclear polarization can be investigated also considering the angular momentum budget in the system, where angular momentum deposited by the photon in the atomic variables of metastable state flows through the ME collisions to the ground state and the mechanism is affected by the relaxation of the angular momentum in both states [Bat11, BNT11]. The stored in the  $1^1\text{S}_0$  and  $2^3\text{S}_1$  states angular momentum (the two terms on the left side of eq.(5.3)) can be expressed as a difference between deposited angular momentum in the OP process (first term on the right) and amount that has been lost due to relaxation process occurring in these states (the second and the third term on the right):

$$\frac{dM}{dt} = 2\eta \left( \frac{W_{abs}}{N_g V_c \hbar \omega_{ij}} \right) - M \Gamma_R \quad (5.3)$$

$W_{abs}$  is absorbed pump laser power;  $\omega_{ij}$  is the angular frequency of OP transition;  $\Gamma_R$  is total polarization loss rate (see also eq.(5.4));  $V_c$  is the optical pumping cell volume filled with

the gas. In the absence of relaxation the number of ground state flipped nuclei is given by  $(N_g V_c / 2) dM/dt|_{ME}$  that can be expressed as the product of the quantity  $\eta$  called photon efficiency (PE) defined as the number of polarized nuclei per absorbed photon, and number of absorbed photons per unit time  $W_{abs}/\hbar\omega_{ij}$ .

Within the total relaxation rate  $\Gamma_R$  two components can be distinguished:  $\Gamma_g$  - decay rate corresponding to relaxation processes directly acting on atoms in the ground state and the term related to the relaxation of the ground state polarization from the ME collisions. The latter results from the relaxation process occurring in the  $2^3S_1$  state, that tends to equalize the  $a_i$  populations, induces a flow of angular momentum from the polarized ground state atoms so that the  $2^3S_1$  state that drives their distribution to spin temperature. Introducing a M-dependent coefficient  $f_T$  that asymptotically reaches 1 at very low M, contribution to relaxation can be written as:

$$\Gamma_R = \Gamma_g + f_T \frac{11}{3} \frac{n_m}{N_g} \gamma_r^S \quad (5.4)$$

The photon efficiency depends on several parameters of the actually performed MEOP experiment. In all situations it depends on the magnetic field. If the OP transition addresses a single sublevel in Zeeman structure of  $2^3S_1$  state  $\eta$  is independent of the pumping light intensity and nuclear polarization, is the case for  $C_8$  transition, contrary to  $C_9$ , where two metastable state sublevels are depopulated by OP. The PE for  $C_8$  line  $\eta_{C8}$ , depends on the relative values of the radiative decay ( $\gamma$ ) and collisional mixing ( $\gamma_r^P$ ) rates and varies with gas pressure as:

$$\eta_{C8} = \frac{\gamma \eta_{C8}^K + \gamma_r^P \eta_{C8}^D}{\gamma + \gamma_r^P}, \quad (5.5)$$

where  $\eta_{C8}^K = 0.896$  is evaluated for the low-pressure OP where negligible redistribution in  $2^3P$  state occurs, i.e.  $\gamma_r^P \ll \gamma$  (so called Kastler regime), and  $\eta_{C8}^D = 0.5$  is evaluated in opposite limit of full redistribution at high pressures so that  $\gamma_r^P \gg \gamma$  (Dehmelt regime of OP). In the experimental conditions of the experiment performed here the pressure of 32 mbar inside the optical pumping cell brings us to the Dehmelt regime and  $\eta = 0.5$  that has been used in further calculations.

Thus, from the measurement of pumping light transmission at  $M_{eq}$  (the deposited by OP angular momentum is totally balanced by the loss terms at steady-state) value of total relaxation rate  $\Gamma_R$  can be obtained from eq. (5.3):

$$\Gamma_R M^{eq} = 2\eta \frac{W_{abs}^{M=M^{eq}}}{N_g \hbar \omega_{ij}} \quad (5.6)$$

The studies of the MEOP dynamics, in addition to the monitoring of evolution of polarization during the OP include observations of polarization change after the pumping light is turned off (measurement of decay rate  $\Gamma_{decay}$ ). In the absence of OP,  $\Gamma_R = \Gamma_{decay}$ . In the presence of OP as reported in [BNT11, ASM<sup>+</sup>04, AST<sup>+</sup>05, Abb05],  $\Gamma_R$  is higher than  $\Gamma_{decay}$  and the difference between these two values depends on absorbed pump laser power. As reported in [Bat11], for low-field MEOP in the 0.6-2.6 mbar pressure range, the  $\Gamma_R$  value increases linearly with increasing absorbed laser power, with a slope independent of gas pressure, and asymptotically reaches  $\Gamma_{decay}$  at very low absorbed power. At high enough absorbed power (above  $10^{-4} \text{ W}\cdot\text{cm}^{-3}$  that is absorbed power per pumping cell volume), independently of the transition,  $\Gamma_R$  can reach



the value more than 2 orders of magnitude higher than  $\Gamma_{decay}$ . The effect is present also in the non-standard conditions of elevated pressure and magnetic field. The difference between two relaxation rates is an indication of existence of an additional relaxation process during the OP stage, whose contribution has not been included in the above-described angular momentum budget, and can be introduced by an extra, laser-induced loss rate  $\Gamma_{laser}$  equal to:

$$\Gamma_{laser} = \Gamma_R - \Gamma_{decay}. \quad (5.7)$$

Therefore, the steady-state value of nuclear polarization  $M_{eq}$  is lower than expected from OP and ME processes only. As discussed in section 2.0.1 formation rate of helium metastable molecules increases about 100 times when we compare the association from the  $2^3P$  and from  $2^3S_1$  states, coupled with the transition at 1083 nm induced by the OP light. Creation of the molecule can affect the MEOP process in two ways: involving two atoms in formation process, one of the metastable state and the second ground state, reduces the amount of the species that participate in the optical pumping; by collisions occurring between the molecule and polarized ground state atoms that may exchange its electronic excitation with the ground state atom within the helium dimer, so that the ground state atom outgoing from the collision is unpolarized, while spin polarization of the bounded atom is being dissipated in numerous rotational states of the molecule due to spin-orbit coupling.

## 5.4 Description of MEOP experiment with blue light transmission measurement on molecular helium

Studies on the possible contribution of increased molecular formation in presence of OP radiation to the laser-enhanced relaxation  $\Gamma_{laser}$  have been performed including a recording of the 465 nm probe laser power transmitted through the OP cell in the measurements of standard MEOP dynamics. Hence direct comparison between increase of the atomic nuclear angular momentum loss rate and of molecular species density can be made as a function of the absorbed OP light power. This requires a modification of the standard MEOP setup (basically consisting of the OP pumping cell, pump laser beam and probe laser beam transmitted through the cell - together with necessary optical elements, homogeneous magnetic field in the cell volume and a source of the rf discharge excitation - see e.g.. [BNT11]) to let a blue probe laser beam propagates also through the OP cell. The final design of such a system depends, of course, on the conditions in which the MEOP is performed. In this work, the low magnetic field and moderate pressure (32 mbar) conditions impose the optical polarization measurement technique described in [TBNT11] and the main issues are discussed in the subsection 5.4.1.2. The section is devoted to the experimental setup description involving optical arrangement and data acquisition technique. Experimental time charts are described allowing extraction of the parameters included in the equations describing the angular momentum budget (i.e. pump laser transmission at  $M=0$  and  $M_{eq}$ ) as well as calculation of the atomic and molecular densities at different stages of the process. Later, the data reduction and data processing methods used to obtain quantitative information about parameters describing the MEOP process (such as  $M_{eq}$ ,  $\Gamma_{decay}$ ,  $\Gamma_R$  and  $\Gamma_{laser}$ ) are discussed. On the basis of obtained values, the relations of the parameters characterizing the MEOP and atomic species with the molecular density change are shown and discussed.

## 5.4.1 Design of the MEOP experimental setup

### 5.4.1.1 General constraints

Basically few conditions must be fulfilled to perform MEOP:

- presence of the magnetic field in the volume of optical pumping cell filled with  $^3\text{He}$  gas (the cell with optical quality windows minimizing the transmitted laser beam distortion; cell rather of long cylindrical shape increasing the optical path). The homogeneity of the field in this volume is important as strong field gradients would result in shortening of the nuclear polarization relaxation time. Efficient optical pumping occurs at low pressure (a few mbar) and low magnetic field induction (a few mT). Efficient polarization of the gas at the pressure of tens or hundreds of mbar is possible but requires magnetic field much stronger - of order 1 T - not considered in this work.
- presence of discharge plasma that allows populating the  $2^3\text{S}_1$  state
- presence of the 1083 nm circularly polarized light that induces the transition between hyperfine sublevels of  $2^3\text{S}_1$  and  $\text{He}(2^3\text{P})$  states so that non-equilibrium distribution of the metastable atoms is created and transferred to the  $1^1\text{S}_0$  state in the metastability exchange collisions.

The investigations of the dynamics of the MEOP and relaxation processes requires measurement of the instantaneous value of the polarization.

In general there are 3 methods of nuclear polarization measurement in the  $1^1\text{S}_0$  state: nuclear magnetic resonance (NMR) technique - direct method, optical polarimetry of the light emitted by the atoms that are spontaneously decaying radiatively from the various excited states induced by the rf discharge - indirect method and optical absorption of 1083 nm light, that relies on the determination of the relative populations of  $2^3\text{S}_1$  state - also an indirect method.

In this work, the last method has been employed for its accuracy and the fact that gives an absolute polarization values - does not require any calibration and can be used in arbitrary pressure and magnetic field [TBNT11].

### 5.4.1.2 Nuclear polarization measurement method choice - pros and cons

The choice of the most suitable method of nuclear polarization has to be made taking into account the MEOP conditions. Due to expected pressure dependency of correlations between atomic and molecular dynamics (three body collisions responsible for their formation) the wide range of pressure is to be investigated - from a few to a few hundreds of mbar - what excludes the polarimetry method valid up to 5 mbar. On the other hand, the NMR method is difficult to perform during the polarization build-up when discharge excitation is present due to the rf noise generation in the pick-up coils. Looking at this main issues it points out that the most suitable method of polarization measurements is the absorption technique that does not require any calibration and provides good sensitivity in the all range of pressures and magnetic fields.

Among the absorption technique two schemes taking advantage of linearly polarized probe beam at 1083 nm are considered:

- probe laser propagating at the right angle in respect to the magnetic field B direction and, in case of used OP cells, transversally to the cylindrical part. The information about the M

value is inferred from the ratio of two different sublevels populations what in fact can be expressed as the ratio ( $r_{\perp} = A_{\pi}/A_{\sigma}$ ) of the absorption signals of two linear polarizations  $\pi$  - parallel to B and  $\sigma$  - perpendicular to B that are probing these two sublevels. This constraints the choice of the probing line transition for MEOP in pure  $^3\text{He}$  to  $C_9$  as for  $C_8$  the  $\pi$  and  $\sigma$  polarizations probes the same sublevels. This method is advantageous in terms of insensitivity to OP light, however its main drawbacks are low sensitivity at small polarizations and weak absorption values as the optical path through along the diameter of the cylindrical cell is short.

- probe laser propagating parallel to B and along the cell length. The M value is inferred using the ratio  $r_{\parallel} = A_{\sigma+}/A_{\sigma-}$  of absorption signals of two circular polarizations of opposite helicity  $\sigma+$  and  $\sigma-$  for which the linear polarization of the probe beam can be decomposed. In this case, for  $^3\text{He}$  MEOP use of both  $C_8$  and  $C_9$  transitions as a probes is possible, however, mentioned in the transverse method difficulties with  $C_9$  are still valid here, not present when the  $C_8$  is chosen.

Important issue of the both methods is that the absorption of the different polarization beam component are measured simultaneously at exactly the same position in the plasma volume. In the MEOP however, the magnetic field B is present in the cell volume causing the frequency splitting of the transition components for different polarization that in null field conditions overlapping in terms of the frequency transition. In this work, the low field MEOP is performed, where, according to [Bat11], the splittings at  $B = 0.82$  mT (the magnetic field in the experiment) are negligible in comparison with the Doppler width of absorption profiles at room ( $T=300$  K) temperature of the experiments. Thus, the idea of the probe beam frequency fixing to the line position at  $B=0$  and measurement of both polarization components absorption remains valid.

Comparing both schemes and desired experimental conditions the choice of Author is toward the longitudinal configuration. In this case, the longer optical path of the probe beam along the cell length instead of the path along the radius (transverse) increases the SNR of absorption measurements. Moreover, the longitudinal configuration (beam passes through the optical quality windows) does not require any optical geometry corrections of the probe beam contrary to the case of the transverse path where beam's wavefront is being distorted passing the curved surfaces of the cylinder walls [TBNT11]. As the experiment of MEOP in low field are performed for the elevated pressure of a few tens of mbar, the expected polarization value in that pressure range is  $<20\%$  [Abb05]. According to [TBNT11], where details about absorption method of polarization are given, the sensitivity of the transverse method is low below that M value. At this point the longitudinal probe scheme is advantageous. The details about the measurement principle is given for example in [CMN<sup>+</sup>02]. The main issue is to simultaneously measure the absorption signals of both light polarization components in the same probed plasma volumes at arbitrary period of MEOP process or during the decay (with the rf discharge still applied) preceded with the measurement of these quantities at  $M=0$  ( $A^{M=0}$ ) before the OP is performed. In such case, according to (5.2) one obtains:

$$e^{\beta} = \frac{A_{\sigma-}^{M=0} A_{\sigma+}}{A_{\sigma+}^{M=0} A_{\sigma-}}, \quad (5.8)$$

from what the M value is obtained.

### 5.4.1.3 Blue laser in MEOP setup

For the realization of the purpose of this work the observation of molecular density change when MEOP experiment is performed is needed. The laser setup generating 465 nm was developed allowing the metastable molecular species  $\text{He}_2(a^3\Sigma_u^+)$  excitation to the  $e^3\Pi_g$  state. In comparison with the previously used methods based on laser induced fluorescence [Cou01] the single-photon absorption technique allows direct detection of  $\text{He}_2^*$  as well as absolute and time resolved density measurements. The beam has to probe the same plasma distribution profile (characterized by the radial symmetry due to cylindrical cell shape together with collinearity of magnetic field and cell axes) in the cell as the infra red probe to assure the proportionality between observed changes for both atomic and molecular species. Thus, the path of the blue beam is also chosen to be in longitudinal configuration.

### 5.4.2 MEOP experimental setup - realization

The arrangement of the optical elements of the Metastability Exchange Optical Pumping setup with simultaneous molecular absorption measurements is shown on the Fig.5.3. The setup was placed on the aluminum threaded board 120 cm long and 30 cm wide so that the geometrical realization of the scheme of simultaneous transmission of 3 laser beams (infra-red pump and probe beam as well as blue laser light) is possible. The main constraint here is the optical pumping cell (the same used in the molecular spectroscopy measurements - see section 4.1) shape and size, imposing the low incident angles (with respect to the cell axis) of the IR and blue beams entering the cell. This required using long beam paths to fit into the cell geometry and not to shade the co-existing beams with the optical elements such as mirrors, cubes and the analyzer setup. Also these elements, that interacts with magnetic field - contains magnetic elements - especially photodiodes has to be far away from the OP cell position not to introduce magnetic field inhomogeneities that speeds up nuclear relaxation processes. The whole optical setup stands on the 14 cm high supports matching the cell axis height to the axis position of the magnetic field generated by the system of 6 square coils. The square coils (42x42 cm) are placed one after the other with the centers of symmetry on a common axis. The coils are divided into 3 pairs in which the same current flows (but the number of the wire turns changes between the pairs). The coils of the outer pair are 80 cm distant setting the dimension of the coils system. The coils of the inner pair are about 5 cm from the center of the system, whereas the coils of the middle pair are about 10 cm each from that center. So the distance between the coils of different pairs is changing to provide a homogeneous field on the coils axis. The setup is placed inside the coils volume so that the cell is collinear with magnetic field axis and the cell volume stays in the center of the coil system - the volume of the lowest field inhomogeneity. The current value delivered by the power supply system of the coils was set to be 1.0 A providing the magnetic field induction  $B=8.2 \cdot 10^{-4}\text{T}$ .

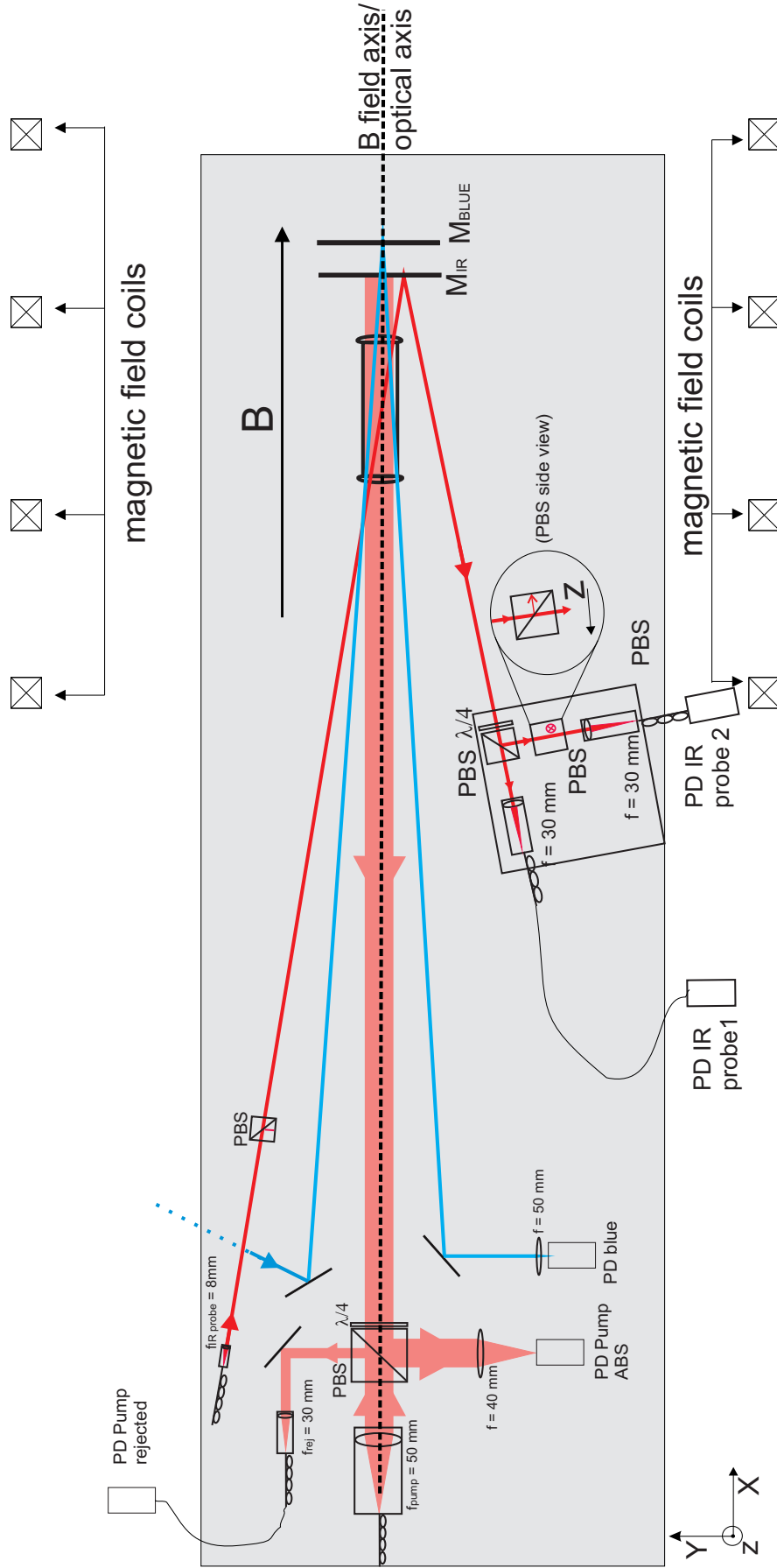


Figure 5.3: Arrangement of the optical elements for MEOB with simultaneous measurement of 465 nm laser transmission mounted on a single breadboard 120x30 cm. Pump, infra-red (IR) probe and 465 nm probe beams paths are shown. PBS: polarizing beam splitter cube,  $\lambda/4$ : quarterwave plate, PD - photodiode, M - mirror (for the IR or 465 nm wavelength),  $f$  - the value of lenses focal lengths. The polarization analyzer sits on a 10x10 cm bread board. It includes a circular analyzed PBS and 2 PD with collimating optics and fiber.

The infra-red (IR) 1083 nm pump and probe laser beams are delivered to the setup with single-mode fibers and collimated with  $f_{pump}=50$  mm plano-convex 1" and 0.5"  $f_{IRprobe} = 8$  mm anti-reflection coated lenses respectively. As the pump laser, Manlight 10 W fiber laser has been used. The  $f_{pump}$  value was chosen providing a Gaussian transverse intensity profile (with FWHM  $\approx 5$  mm) to decrease at the radial distant of the OP cell radius below 1% and above 1% of the maximum. As for the probe beam, the same as used in work of M.Batz [Bat11], power density of about  $15 \mu \text{ W/cm}^2$  has been provided by a single frequency 1083 nm DBR diode.

The pump beam linear polarization in the drawing plane is purified by the polarizing beam splitter (PBS) and orthogonal polarization is reflected at monitored for any pump laser polarization changes by the photodiode (after rejected beam part it is focused by  $f_{reject}=30$  mm lens to the light pipe  $\phi \approx 1$  mm of which the second end is placed close to the photodiode surface). After the PBS, actually glued on its outer surface, the pump beam passes the quarter-wave-plate that the axis is at  $45^\circ$  to the polarization plane of the beam. In such way the circular  $\sigma_-$  (determined in the first MEOP experiment after probe laser components - see below - signals comparison according to [BNT11]) pump beam polarization is achieved. Pump propagates along the magnetic field axis passing through the optical pumping cells windows and reflecting from the  $M_{IR}$  broadband dielectric mirror with reflectivity  $R=99.6\%$  at 1083 nm placed after the cell. After passing the OP cell for the second time the transmitted beam polarization is changed by the quarter-wave-plate back to the linear, however perpendicular to the previous linear polarization. In this way the beam is deflected by the PBS at the right angle - in opposite side than the rejected beam mentioned before. One inch  $f=40$  mm lens is focusing the transmitted beam onto the photodiode allowing the transmission observation of the pump beam during the OP process. Infra-red probe beam is also first passing through the PBS, however in that case no quarter-wave-plate is used after the cube - the polarization remains linear in the plane of the scheme. Probe beam passes the cell once - diagonally and is reflected by the same mirror  $M_{IR}$  as the pump beam. The probe beam enters the analyzer part of the setup. If one considers the linear polarization as the product of two opposite circularly polarized waves, entering the analyzer through the  $\lambda/4$  plate (also glued to PBS) results in their change into two orthogonal linear polarizations that are being separated in following PBS by the  $90^\circ$  angle. Each of resolved linearly polarized probe beams is focused by  $f = 30$  mm lens of the collimator to the 1 mm  $\phi$  light pipe, that, as in case of the rejected fraction of the pump beam, leads close to the surface of the photodiode. This solution was used due to limited space on the optical board as well as the fact that photodiodes contain elements that could introduce additional field inhomogeneity. In this way, the simultaneous observation of transmission of both circular polarizations through the cell can be performed allowing further nuclear polarization determination with the optical method described in [TBNT11]. In the simple experiment relying on the observation of the shift of the C8 and C9 due to Zeeman effect in magnetic field, determination of the probe polarizations in two detection channels was performed. Described on the Fig.5.3 PD IR probe 1 (noted also as S1 in the text) photodiode detects the linear polarization in the drawing plane coming from  $\sigma_+$  component, while the PD IR probe 2 (S2) detects the linear polarization perpendicular to the drawing plane coming from  $\sigma_-$  component. To remove about 4% of beam with horizontal linear polarization that is reflected by the cutting plane of PBS to the probe 2 photodiode of which signal should come only from the vertical one, a second PBS was put before the IR probe 2 collimator lens. The orientation (zoomed part on the analyzer part on Fig.5.3) of the PBS allows removing the light with unwanted polarization by reflecting it to the

analyzer support, while the vertical polarization passes the cube unaltered to the photodiode 2. The 465 nm laser beam is delivered to the optical board with the set of mirrors - no fiber is used. The blue beam passes the optical pumping cell twice in a V-shape path configuration. It enters the cell near its edge and propagates towards to the setup axis, leaving the cell and reaching the  $M_{IR}$  mirror (transmission  $T=43\%$  at 465 nm). The transmitted fraction of the beam is then reflected by the  $M_{blue}$  mirror placed behind the  $M_{IR}$  and comes back to the OP cell leaving it near the opposite edge of the input window. The fraction of the blue beam that is reflected from the  $M_{IR}$  also propagates through the OP cell once again along approximately the same path. 465 nm light is reflected by the mirror and focused by  $f=50$  mm lens to the photodiode (PD blue). The OP cell is mounted on the non-magnetic  $\theta - \phi$  holder allowing precise adjustment of its position with respect to the incoming pump beam. The reflected fraction of the beam is propagating again through the OP cell together with

### 5.4.3 Acquisition scheme and measurements protocols

#### 5.4.3.1 Acquisition scheme and recorded signals

The experimental setup presented on the Fig.5.3 has been coupled with the data acquisition system. The block scheme is presented on the Fig.5.4.

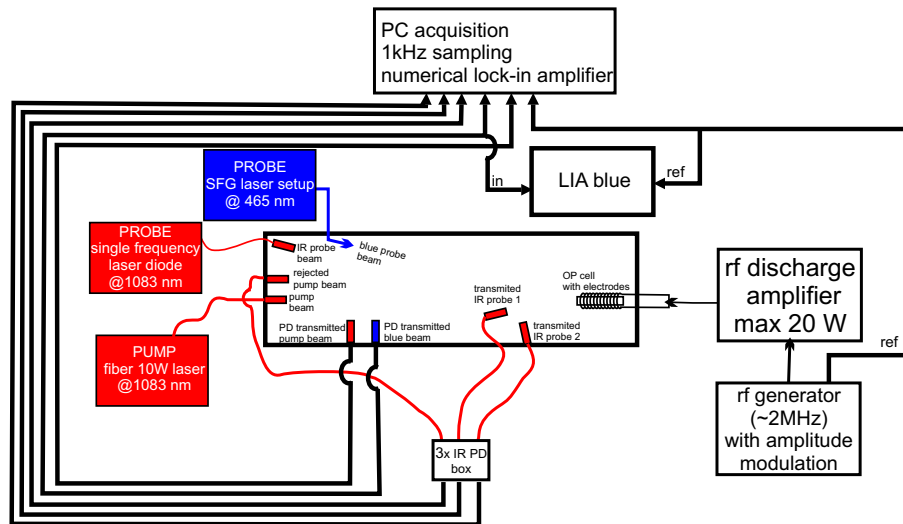


Figure 5.4: Block scheme of the measurement and acquisition system. The optical set-up inside the magnetic field coils is described in details in 5.4.2 and shown in Fig.5.3.

Intensities of both IR probes polarizations are measured by 2 of 3 photodiodes placed in common box with inlets for the fiber. The remaining infra-red dedicated photodiode detects the fraction of the pump beam of polarization component in vertical plane that is rejected by the PBS after the pump beam collimator - this allows OP incident pump beam intensity changes monitoring, related to the light polarization and power changes. The blue light probe transmission signal and the transmitted pump intensity are measured by the separate photodiodes dedicated to the visible and IR wavelengths respectively. Photodiodes signals are collected by multichannel acquisition card connected to the PC. The sampling frequency was set to 1kHz in all the experiments sampling.

A single modulation technique has been used in the experiment - amplitude of the rf discharge was modulated with the frequency of about 30 Hz allowing the increase of SNR resulting from distinction between atomic response to the resonant light excitation and the power fluctuations of the source. The modulation has the sine course with small modulation amplitude (about 20% - see below) to keep discharges at stable and constant excitation level, hence constant plasma conditions.

Modulated IR and blue probes transmission signals as well as of the pump beam can be demodulated using the numerical lock-in computer program written in Fortran by P.-J. Nacher. The detailed description of the software properties is given in [Bat11]. As the program requires the reference signal of modulation, the discharge generator TTL signal is recorded. For the blue laser tuning control, set permanently during the MEOP experiment on the top of Q(2) molecular absorption line, the photodiode signal as well as TTL reference were sent to the DSP lock-in amplifier on which the absorption signal could be observed and laser tuning performed to maximize the value if needed.

Post-processing of the raw measurement data has its advantage in the possibility of change in demodulation parameters setting to find their optimal values for each of considered signals. The regulated in this experiment user-defined parameters are: time constant, sampling (data acquisition) period, time of the offset for  $M=0$  (pump off) of the probes signal determination and phases of the recorded transmission signals. From the input data file the program generates two output files. The first contains:

- time scale of the experiment
- averaged transmitted signals of both IR probe components, blue probe and the pump beam
- magnitudes (commonly named as  $R$  in lock-in detection terminology) of demodulated signals divided by the averaged transmitted signals separately for each of above mentioned beams
- averaged rejected signal of the pump beam

For adjusted phase values (set separately for each of the demodulated signals) the second file contains:

- time scale of the experiment
- in-phase probes and pump components divided by their averaged transmitted signals
- quadrature probes and pump components divided by their averaged transmitted signals

#### **5.4.3.2 Measurements protocol**

During the MEOP performed simultaneously with the blue laser transmission systematic measurements three experimental protocols were applied allowing further extraction of interesting quantities in terms of the laser-induced relaxation rates and its correlations with the molecular species density in helium plasma. The protocols are shown on the standard chronograms on which the time courses of 1083 and 465 nm probe beams has been shown. For the clarity of the presentation, the averaged blue laser probe has been divided by the factor 2.5 as well as the ordinate axis was broken between 0.2 and 1.7 V



**(a) Probe beams absorption measurements** The protocol was developed to obtain absolute absorptions of infra-red and blue probe beams in absence of pump beam ( $M=0$ ). This provides the information about the absolute atom densities values during further MEOP tests in a chosen rf discharge settings. The recordings with use of such protocol were performed just before and after each MEOP test at single discharge condition so that the plasma stability (stability of atomic density) could be monitored over the experimental time scale.

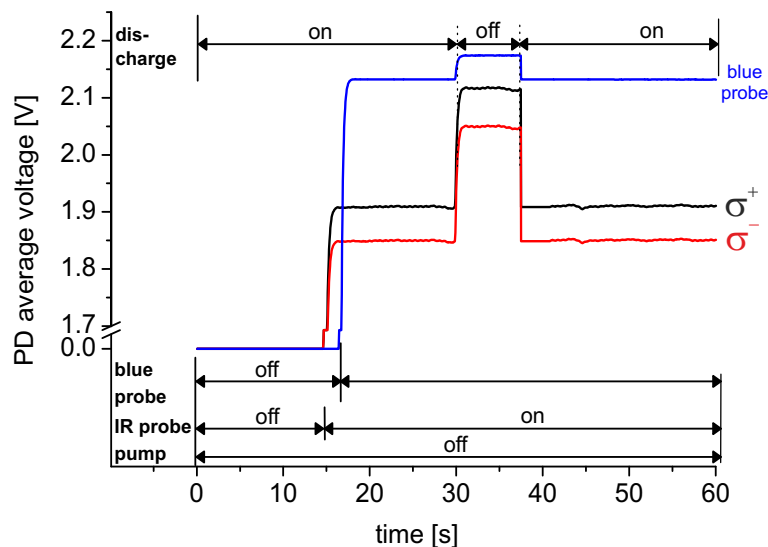


Figure 5.5: Protocol A - absorption measurement at  $M=0$ . Top: example of recorded PD signals. Bottom: time chart of the IR and blue probe beams course. Absolute values of absorptions can be computed directly from the presented signals values.

**(b) MEOP with blue experiment protocols** Two protocols of polarization build-up and decay recordings during the MEOP process in which the molecular detection has been applied are shown on the Fig.5.6 and will be described together allowing their comparison with respect to the purposes of each change.

At the beginning, for about 10 s, only the rf discharges remains ON allowing probes and pump electrical offset measurement. After that time, the probe laser is being unblocked and both component transmissions are recorded at  $M=0$  for 10 s as well - essential in further signals ratio for nuclear polarization determination at  $M \neq 0$ . Pump beam becomes unblocked - for the period depending - decreasing with the incident pump laser power - from 480 s for the lowest power of 0.1 W to 120 s at 6 W. . At this part the similarity of both protocols ends.

For the protocol B, after the steady state  $M$  value is reached the discharges are being switched off for 10 s providing the signal required to infer pump and probes absorption at  $M_{eq}$ . After switching the discharges back, the nuclear polarization builds-up again reaching the steady state value - the time of this period also depends on the incident pump power and is about 2/3 of the precedent time dedicated to polarization build-up. The pump beam is being blocked allowing decay of the polarization in presence of the discharge, so that  $T_{decay}$  can be determined with good accuracy from an exponential fit. After 90 seconds of decay a small magnet is put for a few seconds inducing strong inhomogeneity of the field causing rapid relaxation down to  $M = 0$  - then the discharges are switched off for 10 s during which signal recorded is used

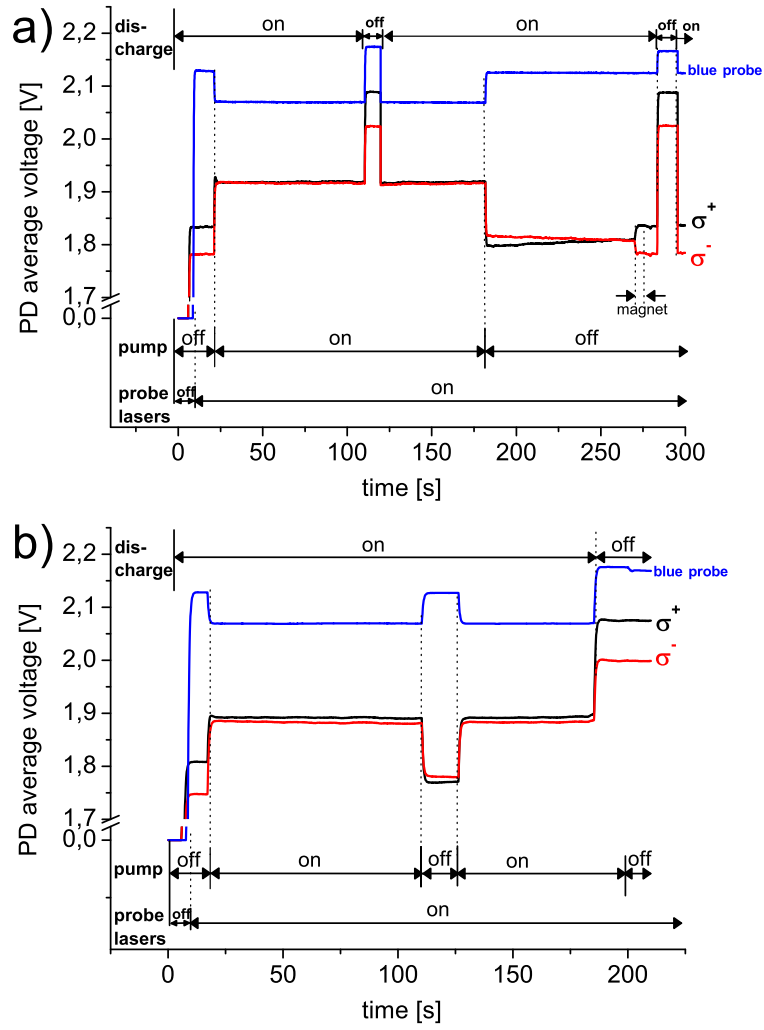


Figure 5.6: Time chart of the IR and blue probe beams course in presence of the OP light. (a) Protocol B and (b) protocol C used for investigations of MEOP dynamics.

for metastable atoms density calculation (the results serves as a control of discharge stability in each of MEOP recording performed with this protocol).

For the protocol C, after reaching  $M_{eq}$  during the build-up period, the pump beam is switched off (contrary to the switching off the discharge in protocol B). The polarization decay lasts here 30s serving as a check of the discharge conditions rather than the way of  $T_{decay}$  determination - lower accuracy on the fit to due to lower amount of points than for protocol B. After the short decay period, there is second build-up period to recover  $M_{eq}$  value at the end of which the discharges are being switched off, what is essential for pump and probes absorption calculation at the steady state nuclear polarization. 10 s after switching off the discharges the pump laser is blocked.

## 5.5 Experimental data reduction and processing

There are a few quantities that have to be extracted from the measurement data recorded using described before A,B and C protocols. They are necessary to perform any investigations on the influence of molecular helium on OP induced polarization losses. Namely they are:  $M_{eq}$  and  $T_{decay}$  - polarization value and relaxation time in absence of the OP light; absorption rates for the pump beam and the blue light at  $M = 0$  and  $M_{eq}$ , IR probe beam absorption at  $M = 0$ . In this section the method of these quantities extraction is described - first the parameters describing the MEOP and later the absorption values relying on the measurement protocol A and dedicated sequences in protocol B and C.

### 5.5.1 Polarization build-up and decay curve for $M_{eq}$ and $T_{decay}$ determination

According to the longitudinal optical method of the polarization measurement at arbitrary stage of the MEOP process (section 5.4.1.2) the absorption signals related to the transitions occurring from different sublevels  $a_i$  of atomic metastable state are required. Thus, relevant signals recorded during the B and C measurement protocols realization, are magnitudes of demodulated signals divided by the averaged transmitted signals for both probe beam polarization components  $\sigma^+$  and  $\sigma^-$ , named  $A_{\sigma^+}$  and  $A_{\sigma^-}$  [TBNT11] and eq.(5.8). For the spin temperature determination and thus the polarization value, performing the normalization of the  $\frac{A_{\sigma^+}}{A_{\sigma^-}}$  is needed in respect to the ratio value at  $M = 0$  ( $\frac{A_{\sigma^+}^{M=0}}{A_{\sigma^-}^{M=0}}$ ), which value was obtained by taking the average of divided signals of both components recorded within 10 s before turning on the pump beam (see the protocols B and C time charts 5.6). Example of the polarization build-up and relaxation obtained with protocol B measurement is shown on the graph 5.7.

The polarization value called "apparent"  $M_{app}$  is not the true value of the  $1^1S_0$  atomic state polarization as it is measured from the  $a_i$  population ratio in presence of the OP light - thus disturbed in comparison to the spin temperature distribution on which the polarization measurement method relies. The spin distribution holds true immediately after the OP light is off thus it can be inferred from the extrapolation of the decay part to the moment of removing the influence of the pumping light on plasma as shown on the fig.5.8, where the way of  $M_{eq}$  and  $T_{decay}$  determination has been shown.

The ln scale of the ordinate has been chosen as it provides the linear character of this pure exponential dependency  $M(t)$ . The linear fit is given with the red solid line and provides  $T_{decay}$  value. Extrapolation of the linear function to the time when the pump beam is being blocked (76 s) allows obtaining the  $M_{eq}$  value as a true nuclear polarization of the ground state helium atoms.

**(c) Absorption rates determination from MEOP recordings** Apart from the demodulated signals of probes and the pump beam absorptions the output files of the numerical lock-in program provides also the averaged signals from the photodiodes from which the offset was subtracted. These are used to determine the absorption values of the IR and blue probe lasers and the pump laser. Absorption values of IR probe at  $M = 0$  delivers information about absolute  $n_m$  density for certain discharge intensity. Absorptions of the 465 nm light at  $M = 0$  and  $M_{eq}$  allows investigation of molecular density increase due to the presence of OP light. The

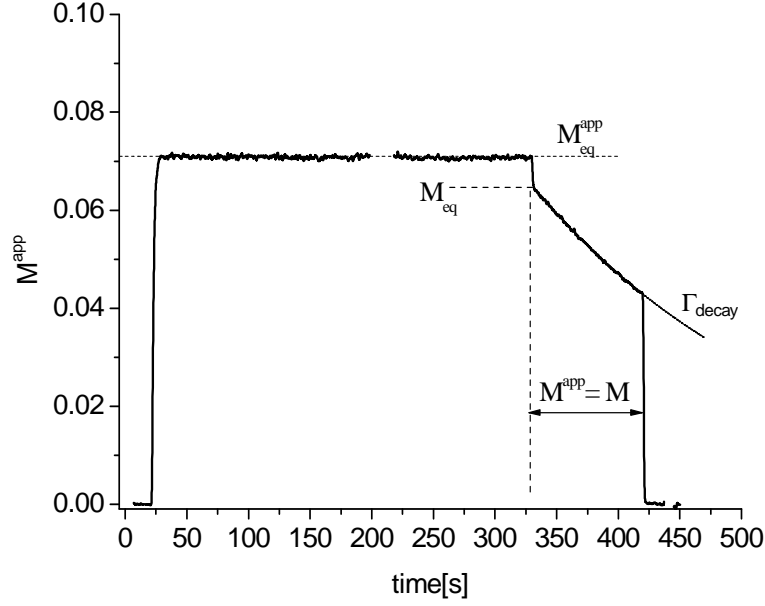


Figure 5.7: Build up and decay of polarization as a function of time for the MEOP experiment performed with protocol B (pure  $^3\text{He}$  gas,  $p = 32$  mbar, incident pump power = 1.1 W on the pumping line  $C_8$ ). The discontinuities of the presented curve correspond to the periods when the discharge was off. Apparent value of the steady-state polarization  $M^{app}$  has been marked with the dashed line. During the decay period (330-420 s) while the OP beam was blocked the true value of the polarization is obtained  $M^{app} = M$ . Recording performed for the "weak" discharges ( $n_m = 2.6 \times 10^{10} \text{ cm}^{-3}$ ,  $\Gamma_{decay} = 4.7 \times 10^{-3} \text{ s}^{-1}$ ) and 0.17 W of absorbed pump power at  $M_{eq}$  (time constant applied in the numerical demodulation  $\tau_{LIA} = 0.2$  s).

pump beam absorption at  $M_{eq}$  provides information about fraction of the incident pump power that has been deposited in the discharge plasma ( $W_{abs}^{Meq}$ ).

The way that the IR probe and pump absorption was determined in MEOP recordings is similar to that in case of blue and therefore only the latter is presented here. For the blue probe beam the rf discharge at  $M_{eq}$  and  $M = 0$  was subsequently turned off and on so that the absorbance can be determined at these polarization values. The photodiode signal before, during and after switching off the discharge was considered. The signals during the two 10 s periods before and after the discharge was off were averaged. The discharge stayed off for about 5-10 s and the photodiode signal was averaged over this period. Using these values the transmission was calculated according to expression 4.2. The periods over which the averages were taken provided the statistical accuracy on the 4th decimal place, while when the single value of the  $S_{ON}$  was taken as an average of two values - before and after switching OFF the discharges, the discrepancy were on the 3rd decimal place leading in overall relative error in the absorption value less than 1%. There was no need to subtract any offset, as it has been done by the numerical lock-in program basing on the first seconds recording when all the lasers were off.

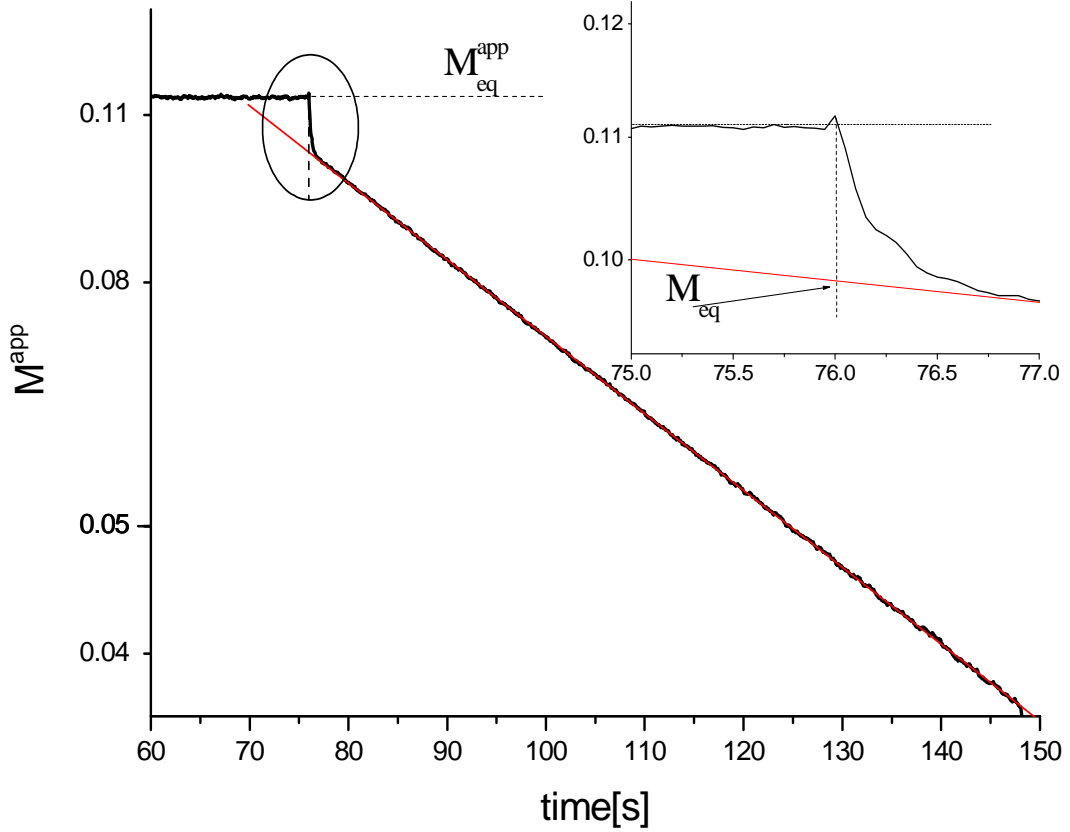


Figure 5.8: Example of polarization decay curve plotted both with semi-log scale ("strong" discharge regime,  $n_m = 1.6 \times 10^{11} \text{cm}^{-3}$ ,  $\Gamma_{\text{decay}} = 0.014 \text{s}^{-1}$ ) The red solid line represent the linear fit to the experimental data.

### 5.5.2 Metastable atoms number density determination

The details about the method of the number density of atoms in the metastable state ( $n_m$ ) determination has been well described in [Bat11, Nik10] thus only the informations relevant in terms of this work will be given.

In general the formula for  $n_m$  calculation from the transmission value  $T$  ( $\equiv 1 - Abs$ ) measured for the probe laser exactly tuned to the considered transition frequency (center of the absorption line profile), depends on the chosen transition, the gas pressure, its temperature, the magnitude of the applied magnetic field if present in the cell volume, chosen optical path of the probe beam and the value of nuclear polarization  $M$  due to inhibited Penning collisions influence that tends to decrease metastable atoms number density [Bat11]. The choice of the transition determines the used transition matrix element value (frequently noted as  $T_{ij}$  [NL85]) as well as the value of relative population of the transition initial state sublevels. For null nuclear polarization value the metastable state atoms equally populate 6 sublevels (negligibly split due to Zeeman effect at experimental 0.82 mT), what is independent of the magnetic field value. The matrix elements  $T_{ij}$ , however, are field dependent [CMN<sup>+</sup>02]. As it is reported in [ASM<sup>+</sup>04, AST<sup>+</sup>05, Abb05, Nik10, CMN<sup>+</sup>02] the sublevels energies of both metastable and  $2^3\text{P}$  state changes linearly with field what influences the absolute and relative positions of the absorption lines - completely changing the spectrum appearance for high enough magnetic

fields so that redefinition of the transition nomenclature is required. The temperature and the pressure dependencies comes in with the broadening effects of the absorption lines, namely Doppler and collisional broadening effects respectively. In the room temperature, in which the experiments of this work has been performed, of about  $T = 300K$  the Doppler broadening expressed in Gaussian profile's FWHM is  $w_G = 1.9773$  GHz for  $^3\text{He}$ . This states the lower limit of measured linewidths that is further increased depending on the pressure of the gas inside the OP cell within the range from 0.4 GHz for 8 mbar to 3.3 GHz at 267 mbar of Lorentzian profile FWHM [Nik10]. Thus the total linewidth (of the Voigt profile being a convolution of Gaussian and Lorentzian functions) of observed line profiles was expected to be of several GHz which allows to treat the probe laser beam as a single frequency radiation due to 3 orders of magnitude lower spectral width (several MHz, monomode laser sources). The effect of the line broadening (temperature and pressure influence),  $T_{ij}$  element value (field dependency) and probed frequency can be enclosed in one single parameter called the line strength  $S(\omega/2\pi)$ . The detailed equations expressing the absorption profile function can be written as:

$$n_m(M) = \tilde{\sigma}^{-1} \frac{-\ln T}{L_{path}} \frac{1}{S(\omega/2\pi, M)}, \quad (5.9)$$

where  $T$  is the transmission of the light of frequency tuned to the  $\omega$  frequency of probed transition,  $L_{path}$  is the beam optical path, whereas  $\tilde{\sigma}$  - generic cross section of the surface dimension  $\text{m}^2$ , is given by:

$$\tilde{\sigma} = \frac{\hbar \sqrt{\pi} \alpha f}{m_e D} \quad (5.10)$$

$$\tilde{\sigma}^{-1} = 1.47105 \cdot \sqrt{T/300} \cdot 10^{15} \text{m}^{-2} \quad (5.11)$$

$$(5.12)$$

$\alpha$  is the fine structure constant,  $f = 0.5392$  - the oscillator strength of the  $2^3\text{S}_1 - 2^3\text{P}$  atomic transition,  $m_e$  - mass electron,  $D = \frac{\omega_G}{2\sqrt{\ln 2}}$  is the Doppler width dependent on the gas temperature  $T$  as well as the mass of considered particle  $M_p$ :

$$D = \frac{\omega}{2\pi} \sqrt{\frac{2k_B T}{M_p c^2}}, \quad (5.13)$$

with Boltzmann constant  $k_B$  and speed of light in the vacuum  $c$ .

The value of  $S(\omega/2\pi, M)$  used in this work for probed transitions has been calculated in *Voigt* program written by P.-J.Nacher. It computes the spectrum - the line strength values in function of the frequency of the helium  $2^3\text{S}_1 - 2^3\text{P}$  transition taking into consideration the magnetic field effects on the line position, splitting, the line broadening effects (thus the baseline increase due to influence of neighboring lines is also included) and changes of the line strengths with the nuclear polarization. While for the  $n_m$  determination, the measurement of the transmission has been performed for the laser tuned to the top of the line profile, the value of  $S(\omega/2\pi, M)$  has been also taken for the maximum of absorption line of calculated spectrum.

## 5.6 Experimental results of MEOP with molecular density measurements

Described in the previous section experimental and acquisition setup allowed both dynamic and static measurements performance. By the dynamic Author means the Metastability Exchange Optical Pumping investigations of laser induced relaxation as continuation of the experiments performed in [Abb05, Bat11] with simultaneous measurements of molecular density variations in helium plasma due to presence of optical pumping light at 1083 nm. The static measurements are the investigations of molecular density change with the pump beam presence, however at null nuclear polarization value. This is obtained by continuous exposition of the cell to the strong magnetic field gradient induced by a small magnet placed on the top of OP cell. In this way the total relaxation rate  $\Gamma_R$  is equal or higher than the optical pumping rate and metastability exchange rate responsible for ground state polarization build-up. The  $\Gamma_{laser}$  increase due to the absorbed 1083 nm light power can be thus compared with the size of molecules number change. These two approaches allow to compare and check if any dependency exists between the growth of molecular density and presence (and value) or absence of nuclear polarization.

For the first tests the 32 mbar pure  $^3\text{He}$  cell was chosen. The choice of this pressure from accessible OP cells filled with the gas for the earlier purposes of MEOP investigations in low and high magnetic field, was a compromise between the SNR of the blue absorption signal (in between poor at 8 mbar and good at 66.7) and achievable nuclear polarization value in low magnetic field conditions ( $< 10\%$ ) [ASM<sup>+</sup>04, Abb05].

The investigations, however performed for a single pressure cell, were made for two different voltage amplitudes of rf discharge excitations and for various incident pump laser power values at each of discharge intensities. The pump laser was tuned to the  $C_8$  transition frequency due to, as mentioned in section 5.3 the quantum efficiency for this transition ( $\eta_{C8}$ ) does not depend on the OP light intensity nor on the nuclear polarization of the atoms. For the majority of MEOP experiments with certain pump laser power, the IR probe beam frequency was set on  $C_8$  line, however recordings with  $C_9$  were made additionally for comparison.

The result will be presented in the way that first allows the straightforward comparison with previously achieved [Abb05, Bat11] and after the new informations brought by transmission measurements with the additional frequency laser. As the performed series of measurement were made to deliver additional information about laser induced relaxation and its potential source in the presence of helium molecules in the plasma, the main variable in the experiment was the OP laser power. To relate this variable with the plasma conditions (expressed as metastable atoms number density  $n_m$  for instance) the other quantity becomes relevant, namely absorbed pump power - deposited laser power in the plasma. It is a relevant parameter related to the pump light power that comes into the angular momentum budget equation (5.3) as  $W_{abs}$ .

### 5.6.1 Discharge intensity

. As written in the introduction to this section, two different discharge conditions were studied in 32 mbar cell, namely weak and strong. The amplitude of the rf excitation in the first case was chosen so that the infra-red probe absorption in absence of the pump beam, at  $M=0$  was about 10% on  $C_8$  line what, given the geometry of the probe beam path, the cell dimensions and transition probabilities results in the  $n_m$  value of  $(3.22 \pm 0.05) \cdot 10^{10} \text{cm}^{-3}$ . The second discharge

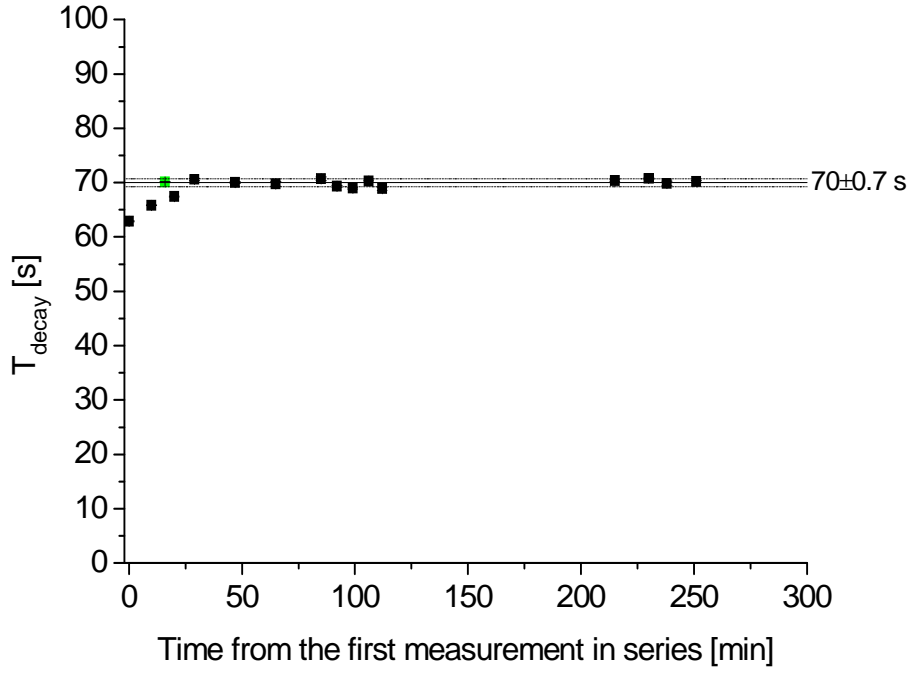


Figure 5.9: Discharge stability during 4 h series of the MEOP measurements in 32 mbar cell expressed as a stability of  $T_{decay}$  value. Regime of strong discharge (40% of IR probe,  $C_8$  absorption). Presented data results from the exponential fits to the 15 s decay recordings in the absence of pump beam within protocol C. With the line, the  $T_{decay}$  value is presented obtained from B-protocol recording where recording of the decay lasts 90 s. All the values from protocol C recordings agree within the error bars with the B-protocol value.

regime settings of rf excitation amplitude was chosen so that the absorption on  $C_8$  line was 40% - this gives the  $n_m = (1.61 \pm 0.01) \cdot 10^{11} \text{ cm}^{-3}$ .

The absorption values were checked performing the recordings with protocol A before and after the series of MEOP measurements for chosen discharge intensity.

Apart from the absorption values and thus calculated metastable atoms densities, the plasma condition indications was deduced from the value of the  $T_{decay}$  time ( $\equiv 1/\Gamma_{decay}$ ) determined from the polarization decay after the OP process was stopped. From both measurements protocols B and C  $T_{decay}$  determination is possible, however better accuracy, due to longer recording of the decay part, was obtained for B. The values of  $T_{decay}$  coming from C-protocol measurements serves as rough check of plasma condition stability from one recording to another, rather than for accurate value determination. For the weak discharge conditions  $T_{decay} = 216 \pm 0.7 \text{ s}$ , while for the strong discharge regime  $T_{decay} = 70 \pm 0.7 \text{ s}$ . Up to 4 h for weak and strong discharge conditions stability within the  $T_{decay}$  error bar is estimated from the data acquired with protocol C, what can be shown on the example of the strong discharge, where the average  $T_{decay}$  determined from recording with this protocol gave  $69 \pm 3 \text{ s}$  in good agreement with precise value from protocol B, Fig.5.9. The error bars of the values obtained from the data recorded with protocol C are mainly due to systematic error of about 10 s determined from the differences between  $T_{decay}$  obtained in B-protocol measurement for the full decay part fit of exponential function and restricted fit to the first 15 s of the decay (as this period of the decay time is for C protocol)



This is confirmed by the fair agreement of IR probe absorptions values coming from the A-protocol recordings before and after the measurement series (absolute difference up to 0.3% between absorption values before and at the end of measurement series, while absolute error of the absorption values was estimated to be 0.1%).

The discharges conditions stability allows further direct comparison of results obtained for the same rf discharge excitation voltage amplitude and its modulation while changing other experimental parameters as pump laser beam power.

The results of measured  $n_m$  value with related  $T_{decay}$  both characterizing the discharge conditions in *weak* and *strong* regime of rf excitation voltage amplitude values as well as atomic and molecular absorption values at  $M = 0$  condition are given in the table 5.2.

MEOP at 32 mbar, $^3\text{He}$ , $B=0.82$ mT		
Experimental parameters	Discharge excitation regime	
	<i>weak</i>	<i>strong</i>
atomic absorption on $C_8$ transition[%]	$10.9 \pm 0.4$	$39.8 \pm 0.2$
molecular absorption on Q(2) transition	$1.92 \pm 0.03$	$4.73 \pm 0.04$
$n_m$ [ $\text{cm}^{-3}$ ]	$(3.22 \pm 0.05) \times 10^{10}$	$(1.61 \pm 0.01) \times 10^{11}$
$T_{decay}$ [s]	$216 \pm 0.7$	$70 \pm 0.7$

Table 5.1: Parameters characterizing the discharge plasma in MEOP experiment at 32 mbar of  $^3\text{He}$ , 0.82 mT magnetic field in *weak* and *strong* regimes of excitation.

Table 5.2: Results obtained from absorption measurements at  $M=0$  and from polarization decay after MEOP (last line)

## 5.6.2 Results of MEOP - nuclear polarization values

Optical absorption method of polarization measurements delivers the information about level of nuclear polarization  $M$  at each time of the MEOP process. Just after unblocking the pump beam the polarization buildup occurs until the photon angular momentum deposition and metastability exchange transfer to the ground state are balanced by the relaxation processes, the polarization reaches steady-state value,  $M_{eq}$ . According to [BNT11] the polarization value inferred during the OP stage (when the pump beam interacts with the metastable atoms) is significantly different than for the case when the pump beam is being temporarily switched off. The presence of the pump beam perturbs the metastable atom distribution that is no more driven by the spin temperature  $1/\beta$ . So that determined polarization is called "apparent" ( $M_{app}$ ) and is out of interest, as it does not reflect the polarization of the ground state (related to the spin temperature). The "true" value of achieved polarization is inferred when the pump beam is blocked, that is after the second build up period in the protocol B and after the first in protocol C. Apart from the information about the achieved nuclear polarization - the target of the MEOP method, the  $M_{eq}$  value is necessary to determine the  $\Gamma_{laser}$  from the angular momentum budget equations (Sec.5.3).

Performed tests revealed discrepancies (of order 1% in absolute value) between obtained values of  $M_{eq}$  in two different probe tuning measurements confirm previous expectations about difficulties of using  $C_9$  as a probe transition. The values of  $M_{eq}$  are systematically lower for

$C_9$  probe than for  $C_8$  at the same value of absorbed pump power. Thus, only the results, where  $C_8$  component was probed will be shown in the results presentation of the  $M_{eq}$  dependency on absorbed OP light power 5.10.

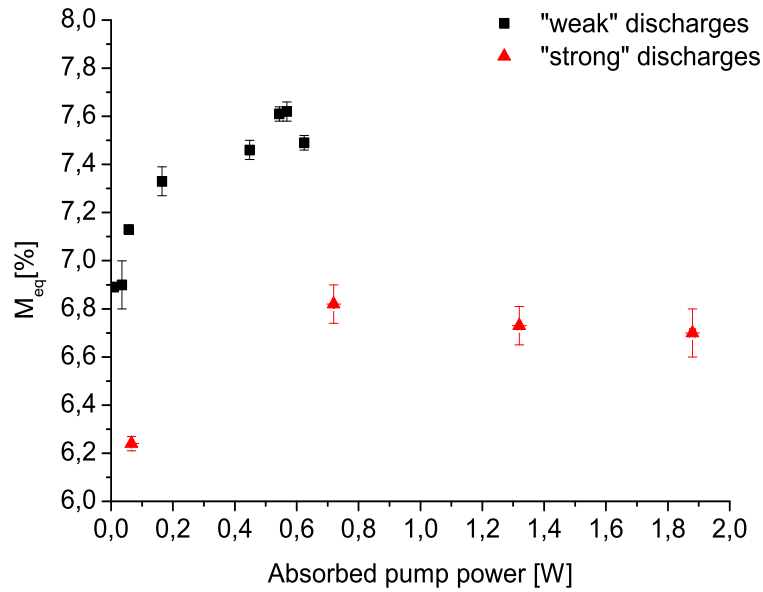


Figure 5.10: Values of  $^3\text{He}$  nuclear polarization in steady-state, obtained in the MEOP for various absorbed OP light powers for two discharge regimes: "weak" (black squares) and "strong" (red squares).  $M_{eq}$  values is presented in terms of the absorbed pump laser power at this  $M = M_{eq}$ . The values of polarization of about 6-8% are normal at 32 mbar and low magnetic field of order 1 mT [NCA<sup>+</sup>02].

In both cases of the discharges regime achieved nuclear polarization values are in agreement with the expectations (<10%) based on the previous measurements [Abb05] performed with 32 mbar cell in low field. Up to about 0.6 W of absorbed pump laser power the  $M_{eq}$  value is increasing about 9% and 7% of the lowest values at 0.04 and 0.07 W for "weak" and "strong" discharges respectively. There are no data above about 0.6 W of absorbed power for "weak" discharges. For the "strong" above 0.6 W the  $M_{eq}$  value stays at the level of 6.7% - similar behavior is expected for the first discharge regime ( $M_{eq}$  is expected to stay at the level of about 7.5%).

### 5.6.3 Light induced relaxation and molecular absorption rates at $M_{eq}$

Relying on the equations (5.4) and (5.7) laser induced relaxation rate can be determined as the parameters required in both equation, namely:  $T_{decay}$ ,  $M_{eq}$  and absorbed pump power at  $M = M_{eq} \left(1 - T_{pump}^{M=M_{eq}}\right) W_{las} \equiv W_{abs}^{M_{eq}}$ , has been obtained as shown in preceding subsections. The value of quantum efficiency in this case for 32 mbar, according to what has been written in the section 5.3, was taken as  $\eta_{C8} = 0.5$ .

The results of  $\Gamma_{laser}$  determination at two discharge regimes and for investigated pump beam powers when both IR probe and pump beams were tuned to  $C_8$  are shown together on the fig 5.11. As before, the pump beam absorbed power scale is on abscissa.

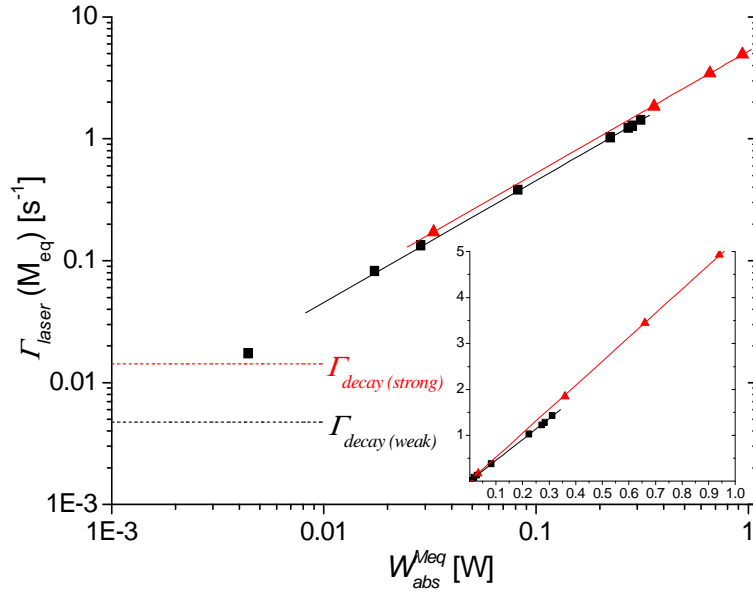


Figure 5.11: Log-log plot of laser-induced relaxation rates  $\Gamma_{laser}$  as a function of the absorbed OP beam power at  $M = M_{eq}$ . Plot in linear scale of both axis is provided in the inset. Data for two discharge regimes exhibit the same behavior: a linear increase of  $\Gamma_{laser}$  with absorbed power (the slopes obtained from the linear fit - black/red solid line - to the experimental data:  $1.018 \pm 0.013 \text{ W}^{-1}\text{s}^{-1}$  and  $1.001 \pm 0.005 \text{ W}^{-1}\text{s}^{-1}$  for weak and strong discharge respectively). Black squares/red triangles - data for "weak"/ "strong" discharge regime, black/red dashed line -  $\Gamma_{decay}$  values at these rf excitations.

The values of  $\Gamma_{laser}$  presented on the Fig5.11 are in line with the other measurement data for lower gas pressure at low field conditions and are already taken into account in comparison performed by [Bat11]. The increase of the total relaxation rate, due to  $\Gamma_{laser}$ , is up to 310 (for "weak" discharges) and 350 ("strong" discharges) times the value of the  $\Gamma_{decay}$  rate when no OP light is present. The slopes of the linear fits to the experimental data show the relative increase of  $\frac{d\Gamma_{laser}}{dW_{abs}^{Meq}}$  with the discharge strength by 15% - the difference in slopes of the linear fits is clearly visible on the graph with linear scale on abscissa and ordinate axes (inset) of the Fig.5.11.

On other hand, there are absorption measurements of the molecular species with the blue laser. Following graphs 5.12 show the change of the absorption with the absorbed IR pump power.

According to the Fig.5.12 (a), the change in the discharge intensity from "weak" to "strong" regime, causing 5 fold increase of the helium metastable  $2^3S_1$  atoms, results in the 2.5 times increase in the absolute molecular absorption signal at null absorbed 1083 nm laser power (the situation when the pump beam is off). Applying the OP light, the increase of the molecular density is noticed - linear in function of the absorbed power. The slopes for both discharges regime are similar, however it is hard to compare them quantitatively, as for the "weak" discharges data reach only 0.3 W, while for the "strong" they end up at 1 W of absorbed pump power. The comparison of the linear fits' slopes performed for the full data range for "weak" discharges (up to 0.3 W of absorbed power - black line on the 5.12; slope  $0.11 \text{ W}^{-1}$ ) and fits to the restricted data of "strong" discharges (up to 0.4 W - red - slope  $0.105 \text{ W}^{-1}$ , up to 0.2 W - blue - slope  $0.116 \text{ W}^{-1}$ ) shows the absence of a difference in the molecular density increase in function of

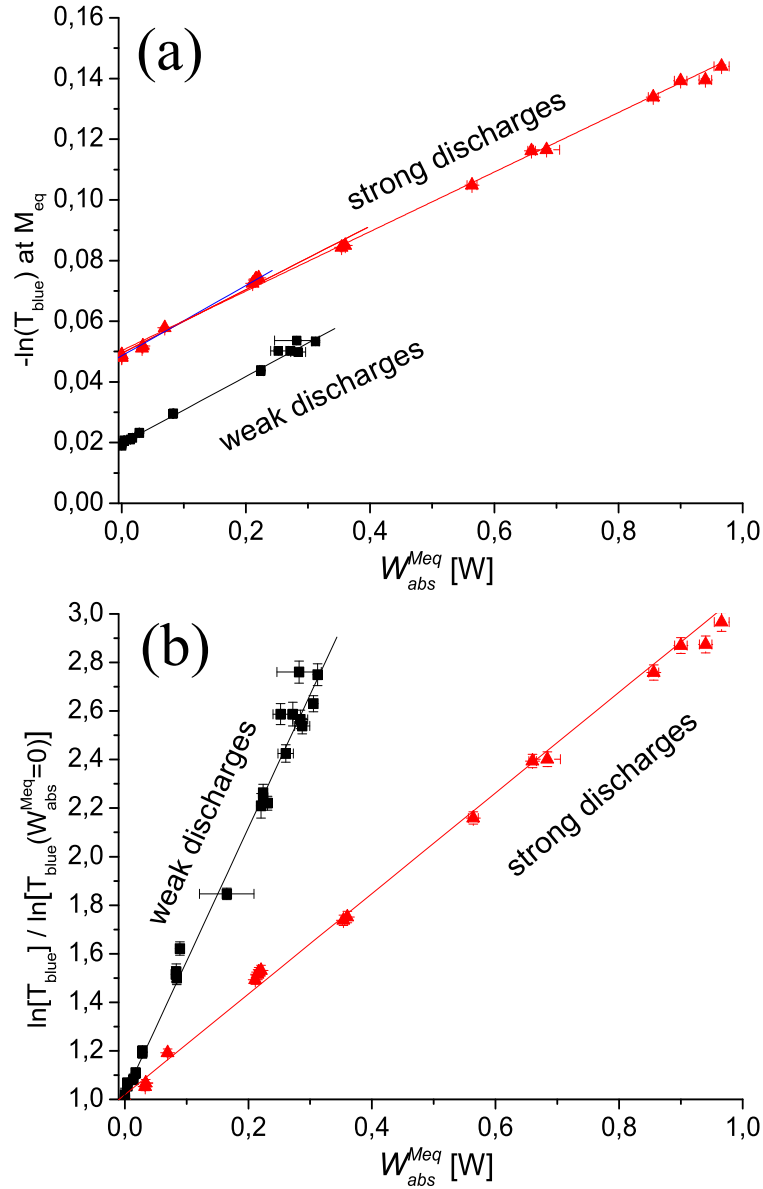


Figure 5.12: Values of  $-\ln(T_{blue})$  for 465 nm laser light tuned to Q(2) molecular transition measured at  $M_{eq}$  (32 mbar cell, blue light absorbance in MEOP experiment performed with  $C_8$  at 0.82 mT), as a function of the absorbed IR pump laser power. Red triangles / black squares - data for "strong" / "weak" discharges. Graph (a): the absolute absorbances of 465 nm light ( $-\ln(T_{blue}) \propto N_M$  - molecular density). With solid black/red/blue lines the linear fits for comparable absorption power ranges are shown in case of both discharge regimes: ("weak" full range up to 0.3 W)/("strong" up to 0.4 W)/("strong" up to 0.2 W) of absorbed pump laser power. Graph (b): Changes in absorbances (therefore in  $N_M$ ) in respect to the measured value in absence of the OP beam ( $\ln(T_{blue}(W_{abs}^{Meq} = 0))$ ). With solid lines the linear fits to the data for the two discharge regimes has been shown.

the absorbed power for the two regimes. This is in line with the previously discussed slope value of  $\Gamma_{laser}$  versus  $W_{abs}^{Meq}$  between the two discharge intensities cannot be made.

Considering the relative increase of the molecular density (Fig.5.12(b)) it is faster (about 2.5 times) for the "weak" discharge regime than for the "strong". It is a natural consequence of the  $\frac{d(-\ln T)}{dW_{abs}}$  rate equality for both regimes (fig.5.12 (a) ) and factor of 2.5×difference in absolute value of  $-\ln T_{M=0}$  - at  $M = 0$ .

Performed investigations does not allow to state that the origin of the laser induced relaxation processes can be explained only by the presence of the molecular species in helium plasma and its collisional interaction with polarized ground state atoms. The magnitude of the  $\Gamma_R = \Gamma_{decay} + \Gamma_{laser}$  increment due to presence of the OP light reaches 350 times the decay without the pump beam while the increase in the molecular density is 3 times at the highest absorbed pump beam power value of 1W. This discrepancy in two orders of magnitude between  $\Gamma_{laser}$  and molecular density change with absorbed pump power can indicate that the molecular species has minor influence on the laser induced relaxation.

In work [Abb05] it has been shown, that in the same pressure cell but at much higher magnetic field (1.5 T) the laser induced relaxation rate is about 2-3 orders of magnitude lower than observed here. This gives the possibility of performing another experiments in which the behavior of molecular density with changed absorbed pump power will be investigated. In the high field regime the interaction potential between the two helium atoms that tend to form a dimer, can be modified changing the cross section for the molecular formation process in the ternary collisions. In strong magnetic fields for example (even much stronger that order of 1 T) the binding energy between hydrogen-helium dimers is increasing with the magnetic field [HH98]. If this is also true for the helium dimer, the binding strength could promote higher molecular densities on one side but on the other could reduce the angular momentum exchange between polarized helium atom and the dimer during the collision. Results showing a simultaneous behavior of the molecular formation and laser induced relaxation rates with respect to the low field regime, could then answer to the yet unknown size of impact of helium dimers on  $\Gamma_{laser}$ .

## 5.6.4 Atomic and molecular metastable species density change with polarization

In the work of [Bat11] it has been shown (Fig. 6.18 of the referred work), that the metastable atomic species number density  $n_m$  is increasing with the square of the polarization  $M$ . For the high polarization values  $\approx 75\%$  the increase reaches even 20% of the  $n_m$  value at  $M = 0$ . As the effect decreases quadratically with  $M$ , at  $M \approx 7.5\%$ , reached in this work,  $n_m/n_m(M = 0) \leq 1$  As shown on the Fig.5.13(a), the data scatter of obtained  $n_m/n_m(M = 0)$  values during the polarization evolution in its decay part when the pump laser is switched off and no OP occurs, is about  $\pm 2.5\%$  in respect to the  $n_m/n_m(M = 0) = 1$ . This does not allow to conclude about variation of  $n_m$  with nuclear polarization value. From the other hand, considering the coupling between equation rates of both atomic and molecular metastable species, the variation of relative molecular metastable species number density  $N_M/N_M(M = 0)$  has been investigated during the polarization decay (Fig.5.13(b).)

In case of the molecular species also within the data scatter there is no indication of variation of  $N_M$  with nuclear atomic polarization.

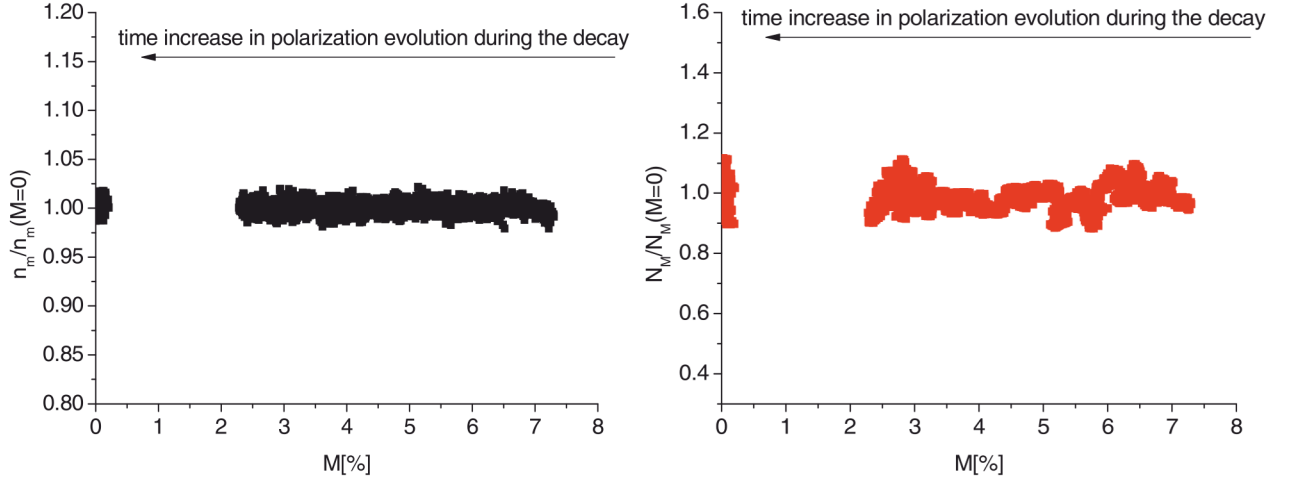


Figure 5.13: Relative change of metastable  $^3\text{He}$  atoms density (a) and of  $^3\text{He}_2^*$  density (b) with nuclear polarization  $M$  during decay. The polarization decrease is towards the origin of the horizontal axis what is reflection of the  $M$  evolution in the time domain.

Obtained in high magnetic field of order 1.5 to 2 T polarization values up to 75% at considered pressure 32 mbar of  $^3\text{He}$  gas open a possibility of performing analogous investigations in elevated magnetic field conditions so that the changes in both atomic and molecular densities is expected to exceed the level of data scatter observed in this work.

## 5.7 Absorption measurements in presence of OP pump beam at $M = 0$

Using the experimental setup presented on the graph 5.3 complementary absorption measurements has been performed. The absorption of blue, IR probe and IR pump beam has been measured for increasing power of the last one in presence of the small magnet put on the top of the OP cell. That provides high inhomogeneity of the magnetic field in the cell volume, resulting in significant relaxation rate increase to the value comparable with OP and ME rates, so that the polarization build-up process is inhibited and  $M \approx 0$ . The comparison of the blue light absorptions with earlier presented results at  $M = M_{eq}$  (Fig.5.14) allows to check if the presence of non-zero ground state polarization affects somehow their association into the molecule.

The error bars of the 465 nm absorption measurements performed at  $M = 0$  (relative errors up to 10% for "weak" and 8% for "strong" discharges) and are about 1 order of magnitude higher than those measured at  $M = M_{eq}$  (up to 1% and 0.4% respectively). This difference results from the fact that for the  $M = 0$  case the absorption was determined on the base of single values of photodiode measurement transmitted light power in presence and absence of the discharge plasma (absorber). For the  $M_{eq}$  signal levels for these two cases were determined from average on multiple points acquired during the MEOP recording when the discharges remained on and off for the time of a few tens of a second, thus in the average the total error is reduced in comparison to the error of a single value. Such discrepancy in the error values does not occur when the absorbed pump power values are compared: for "weak discharges the relative error

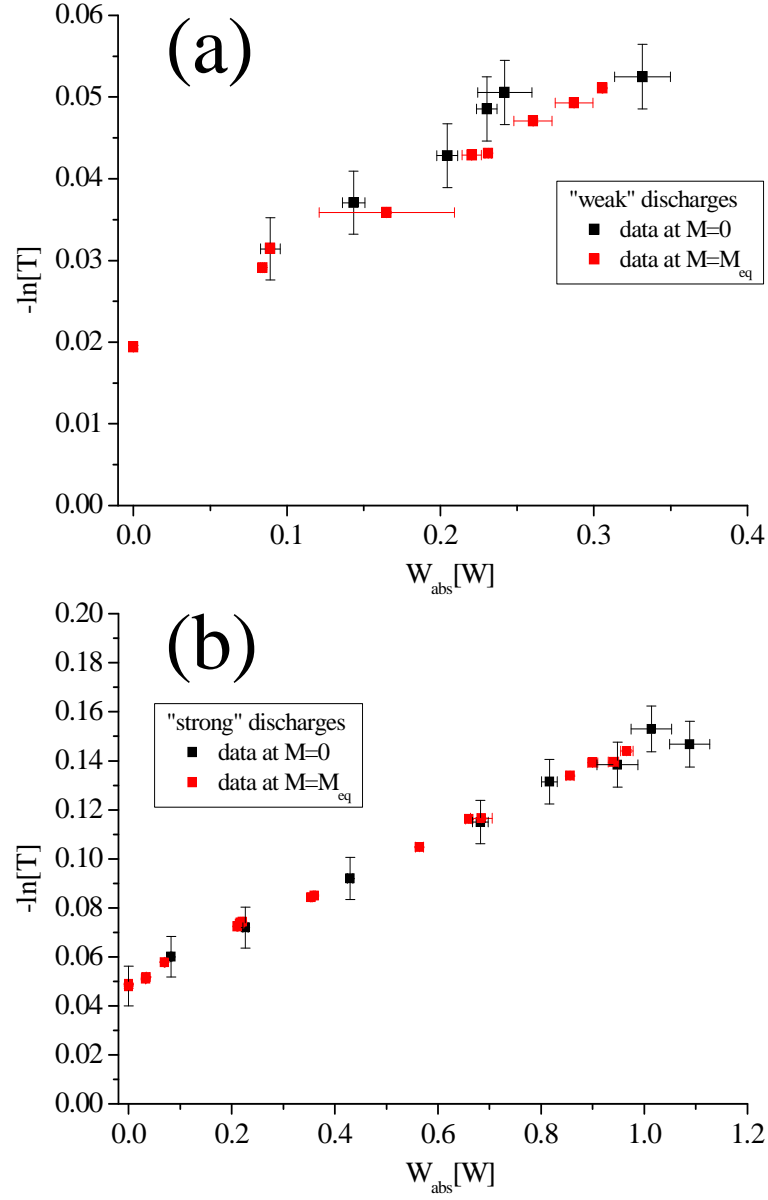


Figure 5.14: Comparison of  $-\ln(T) \propto N_M$  values measured at  $M = M_{eq}$  (red squares) and  $M = 0$  (black squares) in "weak" (a) and "strong" (b) discharge regimes in function of the absorbed pump beam power  $W_{abs}$

of  $W_{abs}$  reaches 5% for  $M = M_{eq}$  measurements and 7% at  $M = 0$ , while for the "strong" 2% and 4% respectively. In case of the measurements at  $M = 0$  the reason for such relative error magnitude is the same as it has been given for the molecular absorption error. At  $M = M_{eq}$ , in spite of the fact of averaging the data points of pump beam transmitted power recordings for the levels related to plasma presence and absence, the relative error is comparable with the value obtained for single-values measurements. This is due to higher uncertainty on the mentioned levels average value due to laser light polarization instability in that time scale of a few tens of a second and necessity of linear or quadratic functions fit for "plasma on" laser transmission signal determination. Within the uncertainty of presented data on the Fig.5.14 the molecular density does not depend on the value of nuclear polarization. At much higher values of  $M$  (tens of %) the significant (up to  $\sim 20\%$ ) increase in helium metastable atoms number density is reported [Bat11] due to inhibited, by spin conservation rules, Penning ionizing collisions in that state. Thus, the increase of the metastable molecule density is possible. This, however, can be investigated in the high magnetic field conditions where high  $M$  values at elevated pressures are achieved [Nik10].

## 5.8 Summary and the conclusions

For the first time simultaneous measurements of MEOP dynamics and molecular helium absorption were made in context of laser enhanced relaxation of polarized ground state helium atoms. The measurements and data analysis of OP were performed according to well established protocol and methods [BNT11, Bat11] providing complementary data extending the dependency of the laser induced relaxation rate  $\Gamma_{laser}$  on absorbed pump laser power per unit volume presented in [Bat11] to approximately two orders of magnitude higher absorbed pump powers per unit volume. It was achieved by using high He pressure cell of small volume normally used for optical pumping investigations at high magnetic field. In agreement with previous observations, the OP induced relaxation is observed to increase with the increase of absorbed pump laser power per unit volume ( $W_{abs}/V_{cell}$ ). In parallel, an increase of the density of metastable helium molecules was observed, however its magnitude seems to be grossly insufficient to explain the two orders of magnitude higher increase in  $\Gamma_{laser}$  value. This may indicate the minor effect of  $He_2^*$  presence in OP plasma on laser-enhanced relaxation, at least at pressure up to 32 mbar and low magnetic field. Also no effect on the metastable molecule density was observed related to the change of ground state helium atoms polarization, however, achieved values of steady-state polarization were also insufficient to allow observation of increase in the metastable helium atoms density, as that is reported in work of M. Batz [Bat11].



# Chapter 6

## Conclusion and outlook

The main objective of the present PhD work was the development of tools allowing detection of metastable helium molecules and a quantitative investigation of  $^3\text{He}_2^*$  densities in typical MEOP conditions.

To this aim a dedicated laser setup providing continuous wave emission at 465 nm and a 1.4 nm tuning range has been built, based on an original design allowing nonlinear Sum Frequency Generation from two closely lying input wavelengths. The laser features and performances have been shown to be in line with expectations and to provide a probe beam suitable for accurate absorption measurements on the  $a^3\Sigma_u^+$  state(0)-  $e^3\Pi_g$  state(0) transition. In particular, measurements of relative changes in absorption rates with high SNR could be performed on the main lines of the rotational Q branch. The laser has been mostly used to investigate room temperature pure helium-3 gas in radiofrequency plasma discharge conditions at pressures ranging from 8 to 267 mbar, but a few complementary experiments have been performed to observe the two stable isotopologues of the  $^3\text{He}_2^*$  molecule:  $^4\text{He}_2^*$  and  $(^3\text{He}-^4\text{He})^*$ . This blue laser source can serve as a tool for investigations of a variety of room temperature He plasmas but also in denser phases at low temperature, in particular in the liquid phase where  $a^3\Sigma_u^+$  is especially long-lived [TGN10]. The current laser setup, based on basic post assemblies, can be readily made more robust using more stable optomechanics components. Temperature control could be automated for improved convenience in experiments where operating wavelength must be frequently changed. A few ways to improve the output power for more demanding applications, have been discussed in [TGN10].

A number of spectroscopic observations on the  $^3\text{He}_2^*$  molecular isotopologues have been performed. The measured absorption line shapes systematically depart from the Voigt profiles expected for single lines, providing evidence of underlying structures. The knowledge of the  $e$ -state fine structure and/or the hyperfine structure of both  $a$  and  $e$  states for the dimers involving  $^3\text{He}$  is needed to quantitatively account for the observed shapes for the various isotopologues and to obtain reliable measurements of pressure broadenings. Doppler-free spectroscopy experiments might be carried out for precise measurements of the underlying line splittings. Comparisons of relative peak amplitudes at fixed rf excitation level have been performed for the accessible components of the Q branch. They indicate that in our plasma conditions thermal equilibrium is observed over the probed low-N part of the spectrum, with rotational temperatures close to gas temperatures, and allow assessment of relative abundances for the various coexisting metastable species. More systematic investigations can be performed using the described modulation techniques. Moreover the SNR of absorption measurements has been shown to be

good enough to allow quantitative monitoring of  $\text{He}_2^*$  dynamics with moderate time averaging down to a few-millibar gas pressures. Simultaneous monitoring of  $\text{He}_2^*$  and  $\text{He}^*$  absorption rates has been performed at 465 nm and 1083 nm, respectively, and, as expected, a strong correlation between steady-state values and decay rates has been observed. The dependence on gas pressure and discharge intensity can be investigated in detail and a quantitative comparison with time evolutions computed from the relevant coupled rate equations would provide strong tests of the description of the system, in terms of both leading processes and values of coefficients for the various formation, ionization, and quenching rates involved.

The quantitative monitoring of  $\text{He}_2^*$  and  $\text{He}^*$  has also been successfully combined and performed during metastability exchange optical pumping  $^3\text{He}$ . The first simultaneous measurements of the rate of additional relaxation of nuclear polarization induced by the strong 1083 nm pump laser ( $\Gamma_{\text{laser}}$ ) and of the change in  $\text{He}_2^*$  density ( $N_M$ ) have been performed at 32 mbar and 0.8 mT. First, our results complement those of a series of systematic investigations recently carried out in the same magnetic field range at lower gas pressures (0.65-2.65 mbar) [Bat11]. They confirm that the light-induced polarization loss exclusively depends on the absorbed pump power and they show that the linear increase of  $\Gamma_{\text{laser}}$  with absorbed power reported in [Bat11] holds over a gas pressure range and an absorbed power range that are both increased here by more than an order of magnitude. So far, the preliminary measurements of the correlated increases in  $\Gamma_{\text{laser}}$  and in  $N_M$  with absorbed 1083 nm light power show that the change in relaxation rate is about two orders of magnitude larger than of the molecular density. This suggests that interactions of polarized atoms with molecular species may not play a dominant role in  $^3\text{He}$  relaxation. However, more systematic measurements remain to be carried out, over the whole range of operating gas pressures and plasma conditions. Of particular interest would be investigations at higher magnetic field strengths ( $>1\text{T}$ ), where much higher nuclear polarizations can be achieved in this pressure range (in contrast with the 6-7 % achieved at 0.8 mT, polarizations up to 60% can be obtained at 32 mbar and about 25% at 267 mbar [Nik10, Col11]). If operation at high field can significantly influence the various processes occurring in the complex plasma system, it definitely modifies deeply the level structure of all metastable species and introduces hyperfine decoupling. Preliminary studies of the Zeeman effect and hyperfine decoupling, similar to those performed for the metastable atom [CMN<sup>+</sup>02], would thus need to be performed for the molecule using the blue laser. Then experiments with combined 465 nm and 1083 nm absorption measurements analogous to ours could be carried out.

# Appendix A

## Reference data on molecular helium a-e transition spectral lines

The main sources of the reference data on molecular helium  $a^3\Sigma_u^+ - e^3\Pi_g$  transition are the articles [DR50] and [BG71] both presenting the spectra for the  $^4\text{He}_2^*$  but also, in case of the first reference, for the  $^3\text{He}_2^*$ .

Following table presents the reference data for both isotopologues.

$^4\text{He}_2^* a^3\Sigma_u^+ - e^3\Pi_g$ transition lines			
N	Q branch	P branch	R branch
	Wavelength [nm]		
1	464.9772		464.3675
3	465.0670	466.0080	463.8628
5	465.2290	466.8131	463.4474
7	465.4612	467.6975	463.1216
9	465.7640	468.6613	462.8832
11	466.1361	469.7001	462.7333
13	466.5752	470.8116	462.6746
15	467.0813	471.9920	462.7021
17	467.6514	473.2370	462.8155
19	468.2836	474.5413	463.0136
21	468.9787	475.9009	463.2943
23	469.7250	477.3106	463.6550
25	470.5289	478.7658	464.0946
27	471.3824	480.2603	488.3647
29	472.2883	481.7886	465.1953
31		483.3442	465.8504
33		484.9204	—
35		486.5115	467.3563
37		488.1066	

Table A.1: Reference data on  $a-e$  transition spectrum for  $^4\text{He}_2^*$  [BG71]

${}^4\text{He}_2^* \ a^3\Sigma_u^+ - e^3\Pi_g$ transition lines						
N	Q branch		P branch		R branch	
	Wavelength [nm]	Intensity	Wavelength [nm]	Intensity	Wavelength [nm]	Intensity
1	464.9774	298	—	—	464.3672	280
2	—	—	—	—	—	—
3	465.0670	552	466.0076	182	463.8632	360
4	—	—	—	—	—	—
5	465.2288	716	466.8115	319	463.4477	389
6	—	—	—	—	—	—
7	465.4614	632	467.6964	314	463.1201	319
8	—	—	—	—	—	—
9	465.7638	536	468.6604	282	462.8828	237
10	—	—	—	—	—	—
11	466.1355	382	469.7001	222	462.7346	160
12	—	—	—	—	—	—
13	466.6327	238	470.8118	164	462.6738	40
14	—	—	—	—	—	—
15	467.0808	143			462.7018	—
16	—	—			—	—
17	467.6398	84			462.8143	—
18					—	—
19					463.0121	—

Table A.2: Reference data on  $a-e$  transition spectrum for  ${}^4\text{He}_2^*$  [DR50]

$^3\text{He}_2^* \ a^3\Sigma_u^+ - e^3\Pi_g$ transition lines						
N	Q branch		P branch		R branch	
	Wavelength [nm]	Intensity	Wavelength [nm]	Intensity	Wavelength [nm]	Intensity
0	–	–	–	–	464.7181	134
1	465.1466	69.1	–	–	464.3435	64.2
2	465.1946	318	466.0230	78	464.0001	289
3	465.2660	132	466.5167	42.4	463.6873	82.2
4	465.3609	481	467.0401	171	463.4047	262
5	465.4794	186	467.5917	125	463.1536	83.8
6	465.6218	465	468.1707	214	462.9340	229
7	465.7866	–	468.7778	72.8	462.7453	67.2
8	465.9752	396	469.4104	196	462.5878	178
9	466.1857	106	470.0695	71.4	462.4611	51.3
10	466.4199	280	470.7539	161	462.3655	119
11	466.6754	71.4	–	–	462.3006	64
12	466.9541	164	472.1948	90	462.2657	97
13	467.2541	48.3	472.9508	28.8	462.2657	97
14	467.5742	125	473.7284	61	462.2888	64
15	467.9155	27.2	474.5265	12.8	–	–
16	468.2777	56.7	475.3450	32	462.4310	24.3
17	468.6589	14.4	476.1821	6.1	462.5441	6.4
18	469.0603	30.3	477.0369	21.6	462.6871	13
19	469.4811	12.3	477.9096	3.8	462.8573	4.1
20	469.9204	13.8	478.7979	7	463.0569	5.6
21	470.3766	4.4	479.7019	2.4	463.2821	–
22	470.8515	–	480.6172	3	463.5353	3.2
23			481.5455	1.9	463.8137	–
24			482.4848	2.3	464.1144	–

Table A.3: Reference data on  $a-e$  transition spectrum for  $^4\text{He}_2^*$  [DR50]



## Appendix B

### Principle of laser absorption technique

Straightforward information about absolute density of atoms or molecules in a certain electronic state is available only through application of absorption methods. They rely on the measurement of change in the light power  $P$  passing through the volume of absorber - atomic or molecular species, provided that light frequency  $\omega_{las}$  is in the vicinity of the resonance value  $\omega_{if}$  for transition occurring between particle (atomic or molecular) initial state sublevel  $i$  and final state sublevel  $f$ . As the absorption process is considered, the initial  $i$  sublevel is the lower state, and  $f$  is the excited one. If  $P_0$  stands for light power before interaction with absorber, then value of transmission rate  $T$  is given by

$$T = \frac{P}{P_0} \quad (B.1)$$

and connected with absorption rate  $A$  in relation:

$$A = 1 - T. \quad (B.2)$$

In further considerations the power per unit surface  $dS$  perpendicular to the direction of beam propagation  $l(x, y, z)$ :

$$\frac{dP(x, y, z)}{dS} \equiv I(x, y, z), \quad (B.3)$$

which is defining the local light intensity (spatial dependency is emphasized), will show up. The coordinates  $x, y, z$  corresponds to the frame of the absorber, thus, in general, surface element  $dS$  as well as the direction of propagation can be expressed by the function of all coordinates. Of course, in the volume devoid of the absorbing species or when the radiation frequency  $\omega$  is beyond the values within the absorption line profile (see further: (a)) the value  $P_0$  implicates  $I_0$ . The local value of intensity change in function of the infinitesimal path length  $dl(x, y, z)$  (along the direction of propagation  $l$ ) of light through the absorber can be written:

$$\frac{dI(x, y, z)}{dl} = -I(x, y, z) \left( N_i(x, y, z) - \frac{g_i}{g_f} N_f(x, y, z) \right) \sigma_{if}(\omega_{las}) \quad (B.4)$$

Except obvious dependency of equation (B.4) on the initial local intensity and number of atoms in initial state sublevel per unit volume ( $N_i$   $\tilde{U}$  number density), the number density of atoms in the final state sublevel appears ( $N_f$ ) together with degeneracy factors  $g_i$  and  $g_f$  of both sublevels connected by transition. The reason for  $N_f$  presence in (B.4) is the process of

stimulated emission that is taken into account. However, if the laser beam power is small, so that population of the  $f$  sublevel is negligible compared to population of  $i$  state, as it is in case of our probe lasers, stimulated emission process can be neglected and (B.4) goes into:

$$\frac{dI(x, y, z)}{dl} = -I(x, y, z)N_i(x, y, z)\sigma_{if}(\omega_{las}) \quad (\text{B.5})$$

Apart from the assumption about the low laser power, the approximation of its monochromaticism was applied, what allows avoiding the integration about the laser frequency in eq. (B.4) and (B.5). Both laser systems - used for MEOP and blue light generation, emit laser light with spectral width of a few MHz, about two orders of magnitude less than natural absorption line broadening or collisional and Doppler broadening of a few GHz. In other words, it is assumed that all the radiation with power  $P_0$  is emitted at single chosen value of frequency  $\omega_{las}$  that can be tuned and matched to the transition frequency  $\omega_{if}$ .

Using (B.1) requires the knowledge about the value of power  $P$  and  $P_0$  which are, due to (B.3), surface integrals of  $I$  and  $I_0$  respectively. Absorption is then determined by geometrical properties and mutual relations of the laser beam power spatial profile, its path through the absorber with the geometry of absorber itself - spatial distribution of  $N_i$ . Therefore, explicit equation relating absorption requires the knowledge of the experimental setup conditions what is the matter of the chapters 4 and 5.

The factor  $\sigma_{if}(\omega_{las})$  that appears in (B.4) and (B.5) is called cross-section for absorption. After [Dem81, Hil82]:

$$\sigma_{if}(\omega) = \frac{1}{g_i} \frac{\pi\omega_{if}}{3\epsilon_0\hbar c} S_{fi} w(\omega - \omega_{fi}), \quad (\text{B.6})$$

where  $g_i$  is the degeneracy of the initial sublevel of the transition.  $S_{fi}$  is the strength of the line of the transition and  $w(\omega - \omega_{fi})$  is the line profile with the central frequency  $\omega_{fi}$ . For absorption the  $\omega \equiv \omega_{las}$ . The designation of the states:  $i$  (initial) and  $f$  (final) is matched to the absorption case  $i \rightarrow f$ . For emission, where the process occurs in the opposite direction  $i \leftarrow f$  it is denoted by reverse order of  $i$  and  $f$  in the subscript of  $S_{fi}$  than in case of the absorption:  $_{if}$ .

The line strength  $S_{fi}$  is related to the matrix element of the electric moment  $d_{fi} = \int \Psi^{f*} \hat{d} \Psi^i d\tau$  by expression:

$$S_{fi} = g_f \left| \int \Psi^{f*} \hat{d} \Psi^i d\tau \right|^2. \quad (\text{B.7})$$

$d$ , the electric dipole moment is the sum of all (electrons' and nuclei)  $e_i \vec{r}_i$  multiplicities.  $\Psi^i$  and  $\Psi^f$  are the wavefunctions of the initial and final states of the transition respectively. The integral in (B.7) is to be taken over the whole configuration space of the  $3(N\text{-particles})$  coordinates

This identity (B.7) is useful as the starting point of detailed expression for the cross-section derivation for the atoms or molecules.

### (a) Spectral line profile and line broadening

The last term in eq. (B.6):  $w(\omega - \omega_{fi})$  is the normalized line profile function centered on the transition  $i - f$  frequency  $\omega_{fi}$ . The shape of the  $w(\omega - \omega_{fi})$  reflects spectral distribution of emitted or absorbed light intensity around  $\omega_{if}$ . Non-monochromatic response of the atomic or molecular system in emission or absorption is the result of several so-called broadening processes.



The smallest one is the natural broadening, that results from the decrease of oscillation amplitude of damped oscillator to which classical model the atom or molecule can be approximated. Natural linewidth can be related to the uncertainties of energy of upper and lower states of the transition being a consequence of the uncertainty principle and their finite lifetime. According to [Dem81] the resulting line profile is given by:

$$L(\omega - \omega_{fi}) = \frac{1}{2\pi} \frac{\gamma}{(\gamma/2)^2 + (\omega - \omega_{fi})^2} \quad (\text{B.8})$$

The second broadening effect is the resultant of the Doppler effect which the absorbing particle in motion experiences. The frequency of radiation emitted (absorbed) by a particle moving with the velocity  $v$  toward the observer (in the beam direction of propagation) changes with  $v$ :

$$\omega_{fi} \rightarrow \omega_{fi} \left(1 + \frac{v}{c}\right). \quad (\text{B.9})$$

The Maxwellian velocity distribution is given by:

$$G(v) = \frac{1}{\sqrt{\pi}\bar{v}} \exp\left(-\left(\frac{v}{\bar{v}}\right)^2\right), \quad (\text{B.10})$$

where the most probable velocity  $\bar{v} = \sqrt{\frac{2kT}{m}}$  ( $k$ -Boltzmann constant,  $T$ -temperature,  $m$ -particle mass).

When both equations: (B.9) and (B.10) are combined, the Doppler broadened line profile takes form:

$$G(\omega - \omega_{fi}) = \frac{c}{\sqrt{\pi}\bar{v}\omega_{fi}} \exp\left(-\left(\frac{c(\omega - \omega_{fi})}{\bar{v}\omega_{fi}}\right)^2\right) \quad (\text{B.11})$$

The third important line broadening process is the collisions between particles when the mutual interaction, interatomic distance dependent, causes the energy shifts in the  $i$  and  $f$  levels (generally shifts are different for  $i$  than for  $f$ ). If, during the collision, no energy transfers between colliding partners occur, the collision is called *elastic*. It can additionally cause the transition frequency shift. For the inelastic collision the complete or partial internal energy transfer of between particles takes place or the energy is transferred into their translational energy. Both elastic and inelastic collisions influence on the line profile are described by the Lorentzian function [Dem81] as in the eq. (B.8). When the contributions from elastic and inelastic collisions to the line broadening are noted as:  $\gamma^{el}$  and  $\gamma^{inel}$ , writing  $\Gamma = \gamma + \gamma^{el} + \gamma^{inel}$  the eq. (B.8) can be rewritten:

$$L(\omega - \omega_{fi}) = \frac{1}{2\pi} \frac{\Gamma}{(\Gamma/2)^2 + (\omega - \omega_{fi})^2}. \quad (\text{B.12})$$

In general, if no special Doppler-free techniques are applied, both collisional and Doppler effects has to be considered simultaneously what results in the total lineshape to be the convolution of Lorentzian and Gaussian functions, the Voigt profile. The convolution of the two functions is defined as:

$$w(x) \equiv (f * g)(x) = \int_{-\infty}^{\infty} f(t)g(x-t)dt \quad (\text{B.13})$$

Applying this definition to the  $G(\omega - \omega_{fi})$  and  $L(\omega - \omega_{fi})$  functions one obtains:

$$w(\omega - \omega_{fi}) \equiv (G * L)(\omega - \omega_{fi}) = \frac{c\Gamma}{2\omega_{fi}\bar{v}\pi^{3/2}} \int_{-\infty}^{\infty} \frac{\exp\left(-\left(\frac{ct}{\omega_{fi}\bar{v}}\right)^2\right)}{(\Gamma/2)^2 + (\omega - \omega_{fi} - t)^2} dt. \quad (\text{B.14})$$

After the substitutions:

$$y = \frac{ct}{\omega_{fi}\bar{v}}, \quad (\text{B.15a})$$

$$w_G = 2\sqrt{\ln(2)}\frac{\omega_{fi}\bar{v}}{c}, \quad (\text{B.15b})$$

$$w_L = \Gamma, \quad (\text{B.15c})$$

the line profile being a consequence of broadening processes discussed here is given by:

$$w(\omega - \omega_{fi}) = 2\ln(2)\frac{1}{\pi^{3/2}}\frac{w_L}{w_G^2} \int_{-\infty}^{\infty} \frac{\exp(-y^2)dy}{\left(\frac{2\sqrt{\ln(2)}(\omega - \omega_{fi})}{w_G} - y\right)^2 + \left(\sqrt{\ln(2)}\frac{w_L}{w_G}\right)^2} \quad (\text{B.16})$$

$w_G$  and  $w_L$  are the angular frequency full width at half maximum (FWHM) of the Gaussian and Lorentzian profiles contributing to overall Voigt profile half-width of the transition line.

Considering the angular frequency dependency of (B.16) it is clear that the profile has the maximum  $w(0)$  at  $\omega = \omega_{fi}$  and is symmetric at around this value. This translates into the fact that the highest absorption of radiation occurs when the light frequency is tuned to the transition frequency  $\omega_{las} = \omega_{fi}$  and decreases as the difference  $\omega_{las} - \omega_{fi}$  increases.

# Appendix C

## Sellmeier equation and dispersion coefficients for PP-KTP

There are several approaches to the refractive indexes determination in function of the wavelength for KTP material within reported literature sources [KT02] - [FBP<sup>+</sup>00]. [FHH<sup>+</sup>87,FASR99, KEOH01] are using standard Sellmeier equation relating the refractive index with  $\lambda$  as follows:

$$n = \sqrt{A + \sum_i \frac{B_i}{1 - C_i \lambda^{-2}} - D \lambda^2} \quad (\text{C.1})$$

The parameters  $A$ ,  $B_i$ ,  $C_i$  and  $D$  are given in the following table C.1 for the  $n_z$  component relevant in this work. It has to be mentioned that references using up to  $i=1$ ,  $i=2$  or  $i=3$  expansions respectively thus different number of coefficients are needed in calculations.

Following references includes also the temperature dependency of the nonlinear crystal on the refractive index. They based on the Sellmeier equation with additional terms responsible for the crystal temperature variation.

Introduced by [FBP<sup>+</sup>00] equation for  $n_z(\lambda, T)$  is given by:

$$n_z(\lambda, T) = \sqrt{A + \beta(T^2 - 400) + \frac{B_1 + \delta(T^2 - 400)}{\lambda - C_1 \phi(T^2 - 400)} - [D + \rho(T^2 - 400)] \lambda^2} \quad (\text{C.2})$$

Coefficient for $n_z$	[FHH <sup>+</sup> 87]	[FASR99]	[KEOH01]
$A$	2.25411	2.12725	1
$B_1$	1.06543	1.18431	1.71645
$B_2$	-	0.6603	0.5924
$B_3$	-	-	0.3226
$C_1$	0.05486	$5.14852 \times 10^{-2}$	0.013346
$C_2$	-	100.00507	0.06503
$C_3$	-	-	67.1208
$D$	0.02140	$9.68956 \times 10^{-3}$	0.01133

Table C.1: Coefficients of the Sellmeier equation for the  $n_z$  refractive index component reported in [FHH<sup>+</sup>87, FASR99, KEOH01]

Coefficient for $n_z$	[FBP <sup>+</sup> 00]	[KT02]	[EA03]	
$A$	3.3134	4.59423	$n_1(\lambda)$	$n_2(\lambda)$
$B_1$	0.05694	0.06206		
$B_2$	-	110.80672		
$C_1$	0.05657	0.04763		
$C_2$	-	86.12171		
$D$	0.01682	-		
$\beta \times 10^{-7}$	-1.1327	-18.97	99.587	-0.11882
$\delta \times 10^{-7}$	1.6730	366.77	99.228	1.0459
$\phi \times 10^{-7}$	-0.1601	-292.2	-89.603	-0.98136
$\rho \times 10^{-7}$	0.52833	92.21	41.01	0.31481

Table C.2: Coefficients of the Sellmeier equation for the  $n_z$  refractive index component reported in [FBP<sup>+</sup>00, KT02, EA03]

In [KT02] the refractive index dependency on the wavelength at  $T=20^\circ\text{C}$  has been taken as:

$$n_z = \sqrt{A + \sum_{i=1}^2 \frac{B_i}{\lambda^2 - C_i}}, \quad (\text{C.3})$$

with the temperature derivative useful for  $T \neq 20^\circ\text{C}$ :

$$\frac{dn_z}{dT} = \beta + \frac{\delta}{\lambda} + \frac{\phi}{\lambda^2} + \frac{\rho}{\lambda^3} \quad (\text{C.4})$$

with coefficients of both equations (C.3) and (C.4) given in the table C.2.

[EA03] reference delivers the parabolic dependency of the refractive index on the temperature in the following form:

$$\Delta n(\lambda, T) = n_1(\lambda)(T - 25) + n_2(\lambda)(T - 25)^2 \quad (\text{C.5a})$$

$$n_i(\lambda) = \beta + \frac{\delta}{\lambda} + \frac{\phi}{\lambda^2} + \frac{\rho}{\lambda^3} \quad (\text{C.5b})$$

with coefficients given explicitly in the C.2 for different for  $n_1$  and  $n_2$  in separate columns. The result of the equation (C.5a) for  $n_z$  index calculation for KTP has to be added to the result of calculations performed using (C.1) with coefficients from the C.1 - column of [FASR99] reference.

# Appendix D

## Constants

The constants used in this work together with the reference sources are given below. There are both fundamental constants as well as molecular constants for  $^4\text{He}_2^*$  and  $^3\text{He}_2^*$ .

$c = 2.99792458 \times 10^8 \text{ m/s}$	speed of light in vacuum [NIS06]
$\epsilon_0 = 8.854187817 \times 10^{-12} \text{ F m}^{-1}$	permittivity of free space [NIS06]
$\alpha = 7.2973525376(50) \times 10^{-3}$	fine structure constant [NIS06]
$h = 6.62606896(33) \times 10^{-34} \text{ J s}$	Planck constant [NIS06]
$\hbar = 1.054571628(53) \times 10^{-34} \text{ J s}$	Planck constant $h/2\pi$ [NIS06]
$k_B = 1.3806504(24) \times 10^{-23} \text{ J/K}$	Boltzmann constant [NIS06]
$m_e = 9.10938215(45) \times 10^{-31} \text{ kg}$	electron mass [NIS06]
$u = 1.660538782 \times 10^{-27} \text{ kg}$	atomic mass unit [NIS06]
$a_0 = 0.52917721092(17) \times 10^{-10} \text{ m}$	Bohr radius [NIS06]
$f = 0.5391$	oscillator strength of the $2^3\text{S}_1 - 2^3\text{P}$ transition [WSG66, Dra96]

(b) Molecular constants

Molecular constant designation	$^4\text{He}_2^*$		$^3\text{He}_2^*$
	[BG71]	[DR50]	[DR50]
	[cm <sup>-1</sup> ]		
	$a^3\Sigma_u^+$ state		
$B_e$	7.703	7.698	10.222
$B_0$	7.589	7.587	10.046
$D_0 \times 10^{-4}$	5.60	5.47	9.76
$\alpha_e$	0.228	0.217	0.3465
$\gamma_e \times 10^{-2}$	-0.46	-0.95	-1.06
$\omega_e$	1808.5	1811.2	2085.65
$\omega_e x_e$	38.2	39.2	51.83
$T_e$	21549.95	21549.54	21549.79
$e^3\Pi_g$ state			
$B_e$	7.283	-	9.664
$B_0$	7.1728	7.17	9.495
$D_0 \times 10^{-4}$	5.22	5.05	9.08
$\alpha_e$	0.2215	-	0.3346
$\gamma_e \times 10^{-2}$	-0.13	-	-0.47
$\omega_e$	1721.1	1724.6	1982.95
$\omega_e x_e$	34.7	36	46.44

Table D.1: Molecular constants for  $^4\text{He}_2^*$  and  $^3\text{He}_2^*$  reported in [BG71] and [DR50] respectively.

# Bibliography

- [Abb05] M. Abboud, *Pompage optique de l' helium-3 a forte pression dans un champ magnetique de 1.5 Tesla*, Ph.D. thesis, Universite Pierre et Marie Curie Paris, 2005.
- [ARM<sup>+</sup>97] A. Arie, G. Rosenman, V. Mahal, A. Skliar, M. Oron, M. Katz, and D. Eger, *Green and ultraviolet quasi-phase-matched second harmonic generation in bulk periodically-poled KTiOPO<sub>4</sub>*, Optics Communications **142** (1997), no. 4–6, 265 – 268.
- [ASM<sup>+</sup>04] M. Abboud, A. Sinatra, X. Maitre, G. Tastevin, and P.-J. Nacher, *High nuclear polarization of <sup>3</sup>He at low and high pressure by metastability exchange optical pumping at 1.5 T*, Europhysics Letters **68** (2004), no. 4, 480–486.
- [AST<sup>+</sup>05] M. Abboud, A. Sinatra, G. Tastevin, P.-J. Nacher, and X. Maître, *Metastability Exchange Optical Pumping of Helium-3 at High Pressures and 1.5 T: Comparison of Two Optical Pumping Transitions*, Laser Physics **15** (2005), no. 4, 475–479.
- [Bat11] M. Batz, *Metastability exchange optical pumping of <sup>3</sup>He gas up to 30 mT: Efficiency measurements and evidence of laser-induced nuclear relaxation*, Ph.D. thesis, Universite Pierre et Marie Curie Paris and Johannes Gutenberg-Universität Mainz, 2011.
- [BC03] J.M. Brown and A. Carrington, *Rotational spectroscopy of diatomic molecules*, Cambridge molecular science series, Cambridge University Press, 2003.
- [BG71] C.M. Brown and M.L. Ginter, *Spectrum and structure of the He<sub>2</sub> molecule VI. Characterization of the states associated with the UAO's 3pΠ and 2s*, Journal of Molecular Spectroscopy **40** (1971), no. 2, 302 – 316.
- [BK68] G. D. Boyd and D. A. Kleinman, *Parametric Interaction of Focused Gaussian Light Beams*, Journal of Applied Physics **39** (1968), no. 8, 3597–3639.
- [BNT11] M. Batz, P. J. Nacher, and G. Tastevin, *Fundamentals of metastability exchange optical pumping in helium*, Journal of Physics: Conference Series **294** (2011), no. 1, 012002.
- [BO27] M. Born and R. Oppenheimer, *Zur Quantentheorie der Molekeln*, Annalen der Physik **389** (1927), no. 20, 457–484.
- [BTL85] D Bloch, G Trenec, and M Leduc, *Isotope shift of the 2<sup>3</sup>S<sub>1</sub> – 2<sup>3</sup>P transition in helium*, Journal of Physics B: Atomic and Molecular Physics **18** (1985), no. 6, 1093.

- [BV89] John D. Bierlein and Herman Vanherzeele, *Potassium titanyl phosphate: properties and new applications*, J. Opt. Soc. Am. B **6** (1989), no. 4, 622–633.
- [CBB<sup>+</sup>78] J. Chevalleyre, A. Bouvier, A. Bouvier, S. Ayoub, and J. Janin, *Determination of the vibration-rotation interaction factor for He<sub>2</sub> transitions*, Journal of Physics B: Atomic and Molecular Physics **11** (1978), no. 7, 1227.
- [CMN<sup>+</sup>02] E. Courtade, F. Marion, P.-J. Nacher, G. Tastevin, K. Kiersnowski, and T. Dohnalik, *Magnetic field effects on the 1 083 nm atomic line of helium*, The European Physical Journal D - Atomic, Molecular, Optical and Plasma Physics **21** (2002), 25–55, 10.1140/epjd/e2002-00176-1.
- [Col11] G. Collier, *Metastability Exchange Optical Pumping (MEOP) of <sup>3</sup>He in situ*, Ph.D. thesis, Jagiellonian University in Krakow, 2011.
- [Cou01] E. Courtade, *Pompage optique de I<sup>ŝ</sup> helium dans des conditions non-standard*, Ph.D. thesis, Universite Paris XI, 2001.
- [Cur13] W. E. Curtis, *A New Band Spectrum Associated with Helium*, Proc. R. Soc. Lond. A **89** (1913), 146–149.
- [Dem81] W. Demtröder, *Laser Spectroscopy Basic Concepts and Instrumentation*, Springer-Verlag, Berlin Heidelberg New York, 1981.
- [DGD77] J.-F. Delpech, J.-C. Gauthier, and F. Devos, *Electronic and rotational energy relaxation in molecular helium: Observation of reactive collisions by isotope-selective laser excitation*, The Journal of Chemical Physics **67** (1977), no. 12, 5934–5941.
- [DMCL76] R. Deloche, P. Monchicourt, M. Cheret, and F. Lambert, *High-pressure helium afterglow at room temperature*, Phys. Rev. A **13** (1976), 1140–1176.
- [DR50] G. H. Dieke and E. S. Robinson, *The Molecular Spectrum of He<sup>3</sup>*, Phys. Rev. **80** (1950), 1–5.
- [Dra96] G.W.F. Drake, *Atomic, molecular, & optical physics handbook*, AIP Press, 1996.
- [DRLL71] J Dupont-Roc, M Leduc, and F Laloë, *New value for the metastability exchange cross section in helium*, Physical Review Letters **27** (1971), no. 8, 467–470.
- [Dun32] J. L. Dunham, *The Energy Levels of a Rotating Vibrator*, Phys. Rev. **41** (1932), 721–731.
- [EA03] Shai Emanuelli and Ady Arie, *Temperature-Dependent Dispersion Equations for KTiOPO<sub>4</sub> and KTiOAsO<sub>4</sub>*, Appl. Opt. **42** (2003), no. 33, 6661–6665.
- [EADL88] F. Emmert, H. H. Angermann, R. Dux, and H. Langhoff, *Reaction kinetics of the He(2P) and the He<sub>2</sub><sup>\*</sup>(a,v) states in high-density helium*, Journal of Physics D: Applied Physics **21** (1988), no. 5, 667.
- [FASR99] K. Fradkin, A. Arie, A. Skliar, and G. Rosenman, *Tunable midinfrared source by difference frequency generation in bulk periodically poled KTiOPO<sub>4</sub>*, Applied Physics Letters **74** (1999), no. 7, 914–916.



- [FBP<sup>+</sup>00] Jean-Philippe Fève, Benoît Boulanger, Olivier Pacaud, Isabelle Rousseau, Bertrand Ménaert, Gérard Marnier, Philippe Villeval, Christophe Bonnin, G. M. Loiacono, and D. N. Loiacono, *Phase-matching measurements and Sellmeier equations over the complete transparency range of KTiOAsO<sub>4</sub>, RbTiOAsO<sub>4</sub>, and CsTiOAsO<sub>4</sub>*, J. Opt. Soc. Am. B **17** (2000), no. 5, 775–780.
- [FHH<sup>+</sup>87] Tso Yee Fan, C. E. Huang, B. Q. Hu, R. C. Eckardt, Y. X. Fan, Robert L. Byer, and R. S. Feigelson, *Second harmonic generation and accurate index of refraction measurements in flux-grown KTiOPO<sub>4</sub>*, Appl. Opt. **26** (1987), no. 12, 2390–2394.
- [FLW68] W. A. Fitzsimmons, N. F. Lane, and G. K. Walters, *Diffusion of He( $2^3S_1$ ) in Helium Gas;  $2^3S_1 - 1^1S_0$  Interaction Potentials at Long Range*, Phys. Rev. **174** (1968), 193–200.
- [FMJB92] M.M. Fejer, G.A. Magel, D.H. Jundt, and R.L. Byer, *Quasi-phase-matched second harmonic generation: tuning and tolerances*, IEEE Journal of Quantum Electronics **28** (1992), no. 11, 2631–2654.
- [GB70] Marshall L. Ginter and Rubin Battino, *Potential-Energy Curves for the He<sub>2</sub> Molecule*, The Journal of Chemical Physics **52** (1970), no. 9, 4469–4474.
- [Gel09] S. Geltman, *Ritz variational treatment of the 4 He trimer*, EPL (Europhysics Letters) **85** (2009), no. 3, 33001.
- [GG70] M. A. Gusinow and R. A. Gerber, *Diffusion Coefficient of He<sub>2</sub>( $^3\Sigma_u^+$ )*, Phys. Rev. A **2** (1970), 1973–1975.
- [GGMD76] J. C. Gauthier, J. P. Geindre, J. P. Moy, and J. F. Delpech, *Electronic and rotational energy relaxation in molecular helium*, Phys. Rev. A **13** (1976), 1781–1786.
- [GS03] H. Ghafouri-Shiraz, *Distributed feedback laser diodes and optical tunable filters*, John Wiley, 2003.
- [GWC<sup>+</sup>09] W. Guo, J. D. Wright, S. B. Cahn, J. A. Nikkel, and D. N. McKinsey, *Metastable Helium Molecules as Tracers in Superfluid  $^4\text{He}$* , Phys. Rev. Lett. **102** (2009), 235301.
- [Her50] H. Herzberg, *Molecular Spectra and Molecular Structure: I. Spectra of Diatomic Molecules*, 2nd ed., Van Nostrand Reinhold Company, 1950.
- [HH98] JS Heyl and Lars Hernquist, *Hydrogen and helium atoms and molecules in an intense magnetic field*, PHYSICAL REVIEW A **58** (1998), no. 5, 3567–3577.
- [Hil82] Robert C. Hilborn, *Einstein coefficients, cross sections,  $f$  values, dipole moments, and all that*, American Journal of Physics **50** (1982), no. 11, 982–986.
- [HNB95] I. Hazell, A. Norregaard, and N. Bjerre, *Highly Excited Rotational and Vibrational Levels of the Lowest Triplet States of He<sub>2</sub>: Level Positions and Fine Structure*, Journal of Molecular Spectroscopy **172** (1995), no. 1, 135 – 152.

- [HW98] H. Haken and H.C. Wolf, *Fizyka molekularna z elementami chemii kwantowej*, 2nd ed., Wydawnictwo Naukowe PWN SA, Warszawa, 1998.
- [JSW<sup>+</sup>04] Sandra Johansson, Stefan Spiekermann, Shunhua Wang, Valdas Pasiskevicius, Fredrik Laurell, and Katrin Ekvall, *Generation of turquoise light by sum frequency mixing of a diode-pumped solid-state laser and a laser diode in periodically poled KTP*, Opt. Express **12** (2004), no. 20, 4935–4940.
- [KB90] Martin Kristensen and Nis Bjerre, *Fine structure of the lowest triplet states in He<sub>2</sub>*, The Journal of Chemical Physics **93** (1990), no. 2, 983–990.
- [KEOH01] M. Katz, D. Eger, M. B. Oron, and A. Hardy, *Refractive dispersion curve measurement of KTiOPO<sub>4</sub> using periodically segmented waveguides and periodically poled crystals*, Journal of Applied Physics **90** (2001), no. 1, 53–58.
- [KT02] Kiyoshi Kato and Eiko Takaoka, *Sellmeier and Thermo-Optic Dispersion Formulas for KTP*, Appl. Opt. **41** (2002), no. 24, 5040–5044.
- [KTZ<sup>+</sup>90] A. Köymen, F.-C. Tang, X. Zhao, F.B. Dunning, and G.K. Walters, *Multiple activation energies for conversion of He(2<sup>3</sup>S) atoms to He<sub>2</sub>(a<sup>3</sup>Σ<sub>u</sub><sup>+</sup>) molecules in ternary collisions*, Chemical Physics Letters **168** (1990), no. 5, 405 – 409.
- [LMK<sup>+</sup>93] Fei Luo, George C. McBane, Geunsik Kim, Clayton F. Giese, and W. Ronald Gentry, *The weakest bond: Experimental observation of helium dimer*, The Journal of Chemical Physics **98** (1993), no. 4, 3564–3567.
- [LMV74] W. Lichten, M. V. McCusker, and T. L. Vierima, *Fine structure of the metastable a<sup>3</sup>Σ<sub>u</sub><sup>+</sup> state of the helium molecule*, The Journal of Chemical Physics **61** (1974), no. 6, 2200–2212.
- [LW78] W. Lichten and T. Wik, *Fine structure of the metastable a<sup>3</sup>Σ<sub>u</sub><sup>+</sup> state of the helium molecule. Further results*, The Journal of Chemical Physics **69** (1978), no. 1, 98–100.
- [MC77] G. Myers and A. J. Cunningham, *Rate measurements of reactions of helium metastable species at atmospheric pressures. II. He<sub>2</sub>(2<sup>3</sup>Σ<sub>u</sub><sup>+</sup>) in pure afterglows*, The Journal of Chemical Physics **67** (1977), no. 5, 1942–1947.
- [MN94] D.C. Morton and L. Noreau, *A compilation of electronic transitions in the CO molecule and the interpretation of some puzzling interstellar absorption features*, The Astrophysical Journal Supplement Series **95** (1994), no. 1, 301–343.
- [Mor29] Philip M. Morse, *Diatomic Molecules According to the Wave Mechanics. II. Vibrational Levels*, Phys. Rev. **34** (1929), 57–64.
- [MSZ<sup>+</sup>08] Emmanuel Mimoun, Luigi De Sarlo, Jean-Jacques Zondy, Jean Dalibard, and Fabrice Gerbier, *Sum-frequency generation of 589 nm light with near-unit efficiency*, Opt. Express **16** (2008), no. 23, 18684–18691.

- [NCA<sup>+</sup>02] P. J. Nacher, E. Courtade, M. Abboud, A. Sinatra, G. Tastevin, and T. Dohnalik, *Optical Pumping of Helium-3 at High Pressure and Magnetic Field*, Acta Physica Polonica B **33** (2002), 2225–2235.
- [Nik10] A. Nikiel, *POLARYZACJA <sup>3</sup>He W WARUNKACH ROZERWANIA SPRZĘŻENIA STRUKTURY NADSUBTELNEJ*, Ph.D. thesis, Jagiellonian University Krakow, 2010.
- [NIS06] NIST, *CODATA Internationally recommended values of the Fundamental Physical Constants*, 2006.
- [NL85] Nacher, P.J. and Leduc, M., *Optical pumping in <sup>3</sup>He with a laser*, J. Phys. France **46** (1985), no. 12, 2057–2073.
- [NTSL94] S. Neeser, R. Tietz, M. Schulz, and H. Langhoff, *Lifetime of the He<sub>2</sub>(e), He<sub>2</sub>(d) and He<sub>2</sub>(f) states*, Zeitschrift für Physik D Atoms, Molecules and Clusters **31** (1994), 61–65, 10.1007/BF01426580.
- [OL77] J. J. Olivero and R. L. Longbothum, *Empirical fits to the Voigt line width: A brief review*, Journal of Quantitative Spectroscopy and Radiative Transfer **17** (1977), no. 2, 233–236.
- [PBB<sup>+</sup>01] M. Peltz, U. Bäder, A. Borsutzky, R. Wallenstein, J. Hellström, H. Karlsson, V. Pasiskevicius, and F. Laurell, *Optical parametric oscillators for high pulse energy and high average power operation based on large aperture periodically poled KTP and RTA*, Applied Physics B: Lasers and Optics **73** (2001), 663–670, 10.1007/s003400100733.
- [Pek34] C. L. Pekeris, *The Rotation-Vibration Coupling in Diatomic Molecules*, Phys. Rev. **45** (1934), 98–103.
- [Phe55] A. V. Phelps, *Absorption Studies of Helium Metastable Atoms and Molecules*, Phys. Rev. **99** (1955), 1307–1313.
- [RBBB88] S.A. Rogers, C.R. Brazier, P.F. Bernath, and J.W. Brault, *Fourier transform emission spectroscopy of the b<sup>3</sup>Π<sub>g</sub>-a<sup>3</sup>Σ<sub>u</sub><sup>+</sup> transition of He<sub>2</sub>*, Molecular Physics **63** (1988), no. 5, 901–908.
- [Ris96] William P. Risk, *Phase-matching characteristics of periodically poled KTP*, Non-linear Frequency Generation and Conversion, vol. 2700, SPIE, 1996, pp. 78–84.
- [SBG<sup>+</sup>85] Birger Ståhlberg, Valery M. Baev, Gerhard Gaida, Holger Schroder, and Peter E. Toschek, *Laser intracavity absorption spectroscopy of He<sub>2</sub>(a<sup>3</sup>Σ<sub>u</sub><sup>+</sup>)*, J. Chem. Soc., Faraday Trans. 2 **81** (1985), 207–216.
- [Sch64] A. Schadee, *The formation of molecular lines in the solar spectrum*, Bulletin of the Astronomical Institutes of the Netherlands **17** (1964), 311–357.
- [SN90] J F Su and J L Nicol, *Measurements of self broadening of the triplet line λ706.5 nm in helium*, Journal of Physics B: Atomic, Molecular and Optical Physics **23** (1990), no. 14, 2215.

- [SPB82] J. Stevefelt, J. M. Pouvesle, and A. Bouchoule, *Reaction kinetics of a high pressure helium fast discharge afterglow*, The Journal of Chemical Physics **76** (1982), no. 8, 4006–4015.
- [SR70] L.D. Scheerer and L.A. Riseberg, *Spin conservation in ionizing collisions between He( $2^3S_1$ ) metastable atoms*, Physics Letters A **33** (1970), no. 5, 325 – 326.
- [Tas00] G. Tastevin, *Optically polarized helium-3 for N.M.R. imaging in medicine*, Physica Scripta **2000** (2000), no. T86, 46.
- [Tat67] J.B. Tatum, *The Interpretation of Intensities in Diatomic Molecular Spectra*, Astrophysical Journal Supplement **14** (1967), 21 – 55.
- [TBNT11] C. Talbot, M. Batz, P. J. Nacher, and G. Tastevin, *An accurate optical technique for measuring the nuclear polarisation of  $^3\text{He}$  gas*, Journal of Physics: Conference Series **294** (2011), no. 1, 012008.
- [TGN10] G. Tastevin, B. Glowacz, and P.-J. Nacher, *Using a cw 465 nm Laser to Probe Metastable He<sub>2</sub> Molecules*, Journal of Low Temperature Physics **158** (2010), 339–345, 10.1007/s10909-009-0050-5.
- [TKO<sup>+</sup>80] Satoshi Takao, Masuhiro Kogoma, Takefumi Oka, Masashi Imamura, and Shigeyoshi Arai, *Optical absorption spectra and kinetic behavior of helium excited diatomic molecule ( $a^3\Sigma_u^+$ )*, The Journal of Chemical Physics **73** (1980), no. 1, 148–155.
- [TZL05] R. Le Targat, J.-J. Zondy, and P. Lemonde, *75% -efficiency blue generation from an intracavity PPKTP frequency doubler*, Optics Communications **247** (2005), no. 4–6, 471 – 481.
- [US82] Yea-Hwang Uang and William C. Stwalley, *The possibility of a  $^4\text{He}_2$  bound state, effective range theory, and very low energy He–He scattering*, The Journal of Chemical Physics **76** (1982), no. 10, 5069–5072.
- [WH97] Thad G. Walker and William Happer, *Spin-exchange optical pumping of noble-gas nuclei*, Rev. Mod. Phys. **69** (1997), 629–642.
- [WHD<sup>+</sup>10] Xuebin Wu, Xianru Hu, Yunchuan Dai, Chenlei Du, Shibin Chu, Leibo Hu, Jianbo Deng, and Yuanping Feng, *Quantum Monte Carlo calculated potential energy curve for the helium dimer*, The Journal of Chemical Physics **132** (2010), no. 20, 204304.
- [WPRN03] T. R. Gosnell W. P. Risk and A. V. Nurmikko, *Compact Blue-Green Lasers*, Cambridge University Press, 2003.
- [WSG66] W. L. Wiese, M. W. Smith, and B. M. Glennon, *Atomic transition probabilities, Vol.I: Hydrogen through neon – A critical data compilation*, Nat. Stand. Ref. Data Ser., NSRDS-NBS 4, U.S. Government Printing Office, Washington, D.C., 1966.

- [Yar89] David R. Yarkony, *On the quenching of helium  $2^3S$ : Potential energy curves for, and nonadiabatic, relativistic, and radiative couplings between, the  $a^3\Sigma_u^+$ ,  $A^1\Sigma_u^+$ ,  $b^3\Pi_g$ ,  $B^1\Pi_g$ ,  $c^3\Sigma_g^+$ , and  $C^1\Sigma_g^+$  states of  $He_2$* , The Journal of Chemical Physics **90** (1989), no. 12, 7164–7175.
- [ZCG<sup>+</sup>02] P. Zeppini, P. Cancio, G. Giusfredi, D. Mazzotti, A. Arie, G. Rosenman, and P. De Natale, *Generation of tunable green radiation in bulk periodically poled  $KTiOPO_4$* , Optics and Lasers in Engineering **37** (2002), no. 5, 553 – 563.
- [ZSB<sup>+</sup>93] X. Zhao, P. A. Soletsky, W. H. Bryan, F. B. Dunning, and G. K. Walters, *Temperature dependence of  $He(2^3P_J)$  reactions: Collision-induced mixing and conversion to  $He_2(^3\Pi_g)$  molecules*, Phys. Rev. A **48** (1993), 4350–4357.